quarterly

ISSN 1898-4088 (printed)
ISSN 2300-5319 (online)

2018
volume 12 no. 1

acta mechanica et automatica

CONTENTS

ABSTRACTS

Paweł Bachman, Andrzej Milecki
Investigation of Electrohydraulic Drive Control System with the Haptic Joystick

The term haptic is used to indicate the presence of force feedback from the manipulated object to the operator. One of the most commonly used haptic devices are joysticks. Such joysticks can be successfully applied also in communication with drive system, giving the human operator a feel of the output force. In the paper one axis joystick with force feedback used to control the electrohydraulic drive is proposed. In this joystick, a controlled brake with magnetorheological fluid and a small DC motor are applied. A beam with a strain gauge is used in a joystick arm, enabling the measurement of the force. In the joystick axis also a potentiometer is assembled, which measured the current arm position. In order to develop the control algorithms an electrohydraulic drive simulation and virtual model is worked out and then a haptic joystick is connected to it. The simulation results that have been obtained, enabled to design and test impedance and admittance control strategies for the system composed of haptic joystick and a real electrohydraulic drive. Finally the whole system is built, implemented and investigated in a laboratory environment. Investigations are conducted in conditions similar to real ones, in a situation where hydraulic piston touches an obstacle and the operator cannot observe this piston very accurately. Fifteen operators have been tested this way. The outcomes indicate that haptic control can improve the human feeling of forces between electrohydraulic drive and an obstacle and, thanks to this, the manual control is more accurate and safer.

Krzysztof Kęcik
Energy Recovery from a Non-Linear Electromagnetic System

The paper presents study of a pseudo-magnetic levitation system (pseudo-maglev) dedicated for energy harvesting. The idea rely on motion of a pseudo-levitating magnet in a coil's terminal. The study based on real prototype harvester system, which in the pendulum dynamic vibration absorber is applied. For some parameters, the stability loss caused by the period doubling bifurcation is detected. The coexistence of two stable solutions, one of which is much better for energy harvesting is observed. The influence of the pseudo-maglev parameters on the recovered current and stability of the periodic solutions is presented in detail. The obtained results show, that the best energy recovery occurs for the high pseudo-maglev stiffness and close to the coil resistance. The amplitude's excitation, the load resistances and the coupling coefficient strongly influence on the system's response.

Matej Urbanský, Jaroslav Homišin, Peter Kaššay, Jozef Krajňák
Measurement of Air Springs Volume using Indirect Method in the Design of Selected Pneumatic Devices

At our department, we deal with continuous tuning of torsional oscillating mechanical systems (TOMS) during their operation in terms of torsional oscillation size. Therefore, a new mobile mechanical system was built for purposes of research and presentation of the TOMS continuous tuning using extremal control method, which main advantage is that we do not need to know a mathematical model of the mechanical system. The new mobile device is equipped with a special compressed air distribution system, which important components are air springs. The air springs are modified and used as air pressure tanks with various functions in the mobile device. Therefore, it is important to know the magnitude of the air springs inner volume. This paper deals with determination of air springs volume using indirect method, which is based on the air pressure measurement and also the comparison of obtained results with the results computed from air springs manufacturer data.

Pawel Bogusz, Roman Gieleta, Marcin Konarzewski, Michal Stankiewicz
Crushing Behaviour of the PVC Foam Loaded with Beaters of Various Shapes

Statistically, at least 50% of all injuries experienced by police officers in the line of duty are due to assaults with blunt objects. Therefore, vests used by the police should provide not only good ballistic resistance, but also good protection against such threats. Foamed materials are possible to be used for body protectors or inserts of protective clothes. The effects of dynamic impact with beaters of different shapes onto behaviour of polymeric foamed material were determined. There were used four types of beaters: flat, cylindrical, edgy and cornered. Strikes with blunt objects such as a flat board, baseball bat, edgy brick, pavement brick or a sharp stone, to which a protective ware can be subjected, were simulated. The impact load was applied to the rectangular specimens, made of polyvinyl chloride foam, with a usage of a drop hammer. Plots of force versus compression for all the tested samples were obtained and analysed. The effects of impacts with beaters of different shapes onto foamed material samples were presented. A shape of the blunt object significantly influences crushing behaviour of the foamed material. The impact energy of a flat beater is absorbed effectively on a short distance, since it is spread on a relatively large surface. The cylindrical and edgy beaters did not cause fragmentation of the samples, however, on the upper surfaces of the samples, permanent deformations mapping the beaters shapes as well as some cracks occurred. An impact with a sharp object, for example, a cornered beater is very difficult to be neutralized by the foam material, because it is cumulated on a small area.

Wojciech Sikora, Krzysztof Michalczyk, Tomasz Machniewicz
Numerical Modelling of Metal-Elastomer Spring Nonlinear Response for Low-Rate Deformations

Advanced knowledge of mechanical characteristics of metal-elastomer springs is useful in their design process and selection. It can also be used in simulating dynamics of machine where such elements are utilized. Therefore this paper presents a procedure for preparing and executing FEM modelling of a single metal-elastomer spring, also called Neidhart's spring, for low-rate deformations. Elastomer elements were made of SBR rubber of two hardness values: 50°Sh and 70°Sh. For the description of material behaviour the Bergström-Boyce model has been used.

Janusz Lewandowski, Dariusz Rozumek
Numerical Analysis of Stress Intensity Factor in Specimens with Different Fillet Geometry Subjected to Bending

The article presents the maps of xx stress component and compares values of analytical and numerical calculations for the stress intensity factor range of welded specimens with fillet welds which subjected to cyclic bending. The tests were performed under constant value of moment amplitude M_a = 9.20 N·m and stress ratio R = σ_{min}/ σ_{max} = -1. The specimens were made of drag steel rod S355. The specimens were solid and welded. The numerical models were simulated with ABAQUS suite and numerical calculations performed with FRANC3D software.

Tadeusz Kaczorek
Invariant, Decoupling and Blocking Zeros of Fractional Linear Systems

The notions of invariant, decoupling and blocking zeros are extended to the fractional linear systems. It is shown that: 1) The zeros are closely connected with the controllability and observability of the linear systems and their transfer functions matrices. 2) The state vector of the fractional system for any input and zero initial conditions is independent of the input decoupling zeros of the system. 3) The output of the fractional system for any input and zero initial conditions is independent of the input-output decoupling zeros of the system.

Agnieszka Wasilewska, Jolanta Pauk, Mikhail Ihnatouski
Image Processing Techniques for ROI Identification in Rheumatoid Arthritis Patients from Thermal Images

Rheumatoid arthritis (RA) is a systemic autoimmune disease that manifests itself by joint inflammation, swelling, pain, tenderness and may involve extra-articular organs in severe cases. Joint inflammatory lesions are associated with higher temperature due to increased vascularity in the area of inflamed tissues. This papers aimed to identify heat patterns from ROIs to interpret the presence of inflammation in rheumatoid arthritis patients. The thermovisual image sequences were collected from 65 patients with Rheumatoid Arthritis (RA). Infrared images were generated by a thermal scanning camera (FLIR E60bx Systems Inc., USA). Separate recordings of left and right foot temperature changes were performed for 3 minute periods. The temperature measurement was performed at the moment right after cold water immersion (post-cooling temperature) and at the moment after thermal recovery (post-recovery temperature). The recording of 3-minute foot thermal recovery was used for analysis. Automatically identified ROI corresponds to the area of the soft tissues covering cuboid and navicular bone.

Maria Kotełko, Mirosław Ferdynus, Jacek Jankowski
Energy Absorbing Effectiveness – Different Approaches

In the paper the study of different crashworthiness indicators used to evaluate energy absorbing effectiveness of thin-walled energy absorbers is presented. Several different indicators are used to assess an effectiveness of two types of absorbing structures, namely thin-walled prismatic column with flaws and thin-walled prismatic frustum (hollow or foam filled) in both cases subjected to axial compressive impact load. The indicators are calculated for different materials and different geometrical parameters. The problem of selection of the most appropriate and general indicators is discussed.

Dominik Wojtkowiak, Krzysztof Talaśka, Ireneusz Malujda
Concept of the Hexa-Quad Bimorph Walking Robot and the Design of its Prototype

Present-day walking robots can increasingly successfully execute locomotive as well as manipulative functions, which leads to their expansion into more and more applications. This article presents the design of a hexa-quad bimorph walking robot with the ability to move at a relatively high speed in difficult terrain. It also has manipulation capabilities both at a standstill and in motion. This feature of the robot is made possible by the ability to easily change the configuration from six-legged to four-legged by elevating the front segment of its body. Presented prototype will be used in further research to develop the hexa-quad bimorph walking robot.

Eugeniusz Mańka, Małgorzata Słomion, Maciej Matuszewski
Constructional Features of Ropes in Functional Units of Mining Shaft Hoist

In this paper structural analysis of steel ropes applied in mining shaft hoists was conducted. Functions of the ropes which they fulfilled in these shaft hoists were identified. Expected operational features of ropes were indicated too. An analysis was carried out four identified groups of ropes: hoisting ropes, balance ropes, leading rope and fender ropes. Basic constructional features: geometrical and material of ropes, which they should be characterized in each of mentioned functional groups were indicated. Constructional structures of mentioned steel ropes, the most often applied in domestic mining shaft hoists were described. Observed tendencies in analyzed issues also were shown.

Bohdan Pavlyk, Markijan Kushlyk, Dmytro Slobodzyan, Igor Matvijishyn, Roman Lys, Marek Jałbrzykowski
Radiation-Stimulated Changes in the Characteristics of Surface-Barrier Al–Si–Bi Structures with Different Concentrations of Dislocations at the Crystal Surface

We report the results of studies for the radiation-stimulated changes in electro-physical characteristics of surface-barrier Al–Si–Bi structures based on p-Si. We demonstrate that the X-ray irradiation is accompanied by different processes which depend on the density of the dislocations in the original silicon crystals. A usual evolution of the existing structural defects and their radiation-stimulated ordering dominate when the concentration remains low enough. Increase in the concentration causes the increasing role of generation of additional radiation defects. Modelling of the underlying physical processes has testified that the near-contact Si layers are strained. They act as getters for the structural defects and impurities.

acta mechanica et automatica, vol.12 no.1 (2018)

Adam Wolniakowski, Andrej Gams, Lilita Kiforenko, Aljaž Kramberger, Dimitrios Chrysostomou, Ole Madsen, Konstantsin Miatliuk, Henrik Gordon Petersen, Frederik Hagelskjær, Anders Glent Buch, Aleš Ude, Norbert Krüger

Compensating Pose Uncertainties through Appropriate Gripper Finger Cutouts

The gripper finger design is a recurring problem in many robotic grasping platforms used in industry. The task of switching the gripper configuration to accommodate for a new batch of objects typically requires engineering expertise, and is a lengthy and costly iterative trial-and-error process. One of the open challenges is the need for the gripper to compensate for uncertainties inherent to the workcell, e.g. due to errors in calibration, inaccurate pose estimation from the vision system, or object deformation. In this paper, we present an analysis of gripper uncertainty compensating capabilities in a sample industrial object grasping scenario for a finger that was designed using an automated simulation-based geometry optimization method (Wolniakowski et al., 2013, 2015). We test the developed gripper with a set of grasps subjected to structured perturbation in a simulation environment and in the real-world setting. We provide a comparison of the data obtained by using both of these approaches. We argue that the strong correspondence observed in results validates the use of dynamic simulation for the gripper finger design and optimization.

DE GRUYTER
OPEN

DOI 10.2478/ama-2018-0001

acta mechanica et automatica, vol.12 no.1 (2018)

INVESTIGATION OF ELECTROHYDRAULIC DRIVE CONTROL SYSTEM WITH THE HAPTIC JOYSTICK

Paweł BACHMAN[*], Andrzej MILECKI [**]

[*]Faculty of Mechanical Engineering, University of Zielona Góra, ul. Licealna 9, 65-417 Zielona Góra, Poland
[**]Faculty of Mechanical Engineering and Management, Poznan University of Technology, ul. Piotrowo 3, 60-965 Poznań, Poland

p.bachman@iibnp.uz.zgora.pl, andrzej.milecki@put.poznan.pl

received 10 October 2016, revised 23 February 2018, accepted 26 February 2018

Abstract: The term haptic is used to indicate the presence of force feedback from the manipulated object to the operator. One of the most commonly used haptic devices are joysticks. Such joysticks can be successfully applied also in communication with drive system, giving the human operator a feel of the output force. In the paper one axis joystick with force feedback used to control the electrohydraulic drive is proposed. In this joystick, a controlled brake with magnetorheological fluid and a small DC motor are applied. A beam with a strain gauge is used in a joystick arm, enabling the measurement of the force. In the joystick axis also a potentiometer is assembled, which measured the current arm position. In order to develop the control algorithms an electrohydraulic drive simulation and virtual model is worked out and then a haptic joystick is connected to it. The simulation results that have been obtained, enabled to design and test impedance and admittance control strategies for the system composed of haptic joystick and a real electrohydraulic drive. Finally the whole system is built, implemented and investigated in a laboratory environment. Investigations are conducted in conditions similar to real ones, in a situation where hydraulic piston touches an obstacle and the operator cannot observe this piston very accurately. Fifteen operators have been tested this way. The outcomes indicate that haptic control can improve the human feeling of forces between electrohydraulic drive and an obstacle and, thanks to this, the manual control is more accurate and safer.

Key words: Electrohydraulics, Haptic, Joystick, Control, Modelling

1. INTRODUCTION

Different devices like cranes, lifts, excavators are often controlled directly by humans, which use special levers or joysticks to assign the drive position or force. In most of these applications visual and sometimes also sound signals are used by the operator as a feedback. However, for most precise tasks it would be advantageous, to have additional feedback like feeling of the force, produced by the controlled drive (Li, 2000). Having it, the operator would be able to control the system more accurately.

The term haptic is used to indicate the presence of force feedback from the manipulated object to the operator. The aim of haptic interfaces is to render the mechanical features of the object on the user. Haptic solutions can be very valuable, because they can help the human to perform tasks more effectively and more reliably (Harward, 2006). All elements the person would touch using a drive controlled by a joystick, transfer tactile impressions to a joystick and to a user. As haptic devices such elements like: joysticks, steering-wheels, mouse's, pedals etc., are most commonly used. There can also be haptic displays, gloves, dresses and different imitations of real objects like medical instruments or bow from fiddle (Adams and Hannaford, 1999).

Haptic devices have been designed and first used about 40 years ago. Since that time their different solutions and applications are described. Some of them are focused on control of different working machines in which electrohydraulic drives are used. In the article (Zarei-nia et al., 2009) the electrohydraulic drive with proportional valve and force feedback controlled by SensAble Phantom Omni haptic device is described. The investigations are carried out for two types of load and several concepts of control algorithms. The same haptic device used for a control of an excavator arm with electrohydraulic drives is described in thesis (Frankel, 2004). Analog sensors are used to measure the position of the excavator boom and the pressure in the chambers of each cylinder that is used as a feedback signal in the controller. The important part of this work, is focused on the modeling of the hydraulic excavator. The paper (Won Oh et al., 2011) described the simulation tests of a virtual excavator arm in which a special touch device is used. Authors described the simulation results when the virtual excavator arm driven by the hydraulic device affected the wall. In the paper (Park et al., 2011), a similar study for the detection of the collisions occurring in contact between the excavator bucket and environment, is presented. The information from the excavator is transmitted to the operator which used a haptic joystick. It is shown that in a traditional remote control of excavators, in which the image is obtained by a camera and presented to the user on 2D screen, the movement or the force cannot be properly assessed. This concerns especially the depth of the trench. As a solution, the dual axis haptic joystick with a small motor is proposed and successfully applied and implemented. Paper (Kontz, 2007) contains the description of the excavator control system, in which only the force acting on a bucket is measured. The operator used the haptic device type SensAble Phantom Omni. The investigations have shown that the proposed solution greatly increased the abilities of the operator, giving him additional feedback, which enabled the improvement of the excavator movements coordination. In thesis (Kontz, 2002)

DOI 10.2478/ama-2018-0001

authors presented a concept of hydraulic forklift controlled remotely by the haptic device type SensAble Phantom Desktop, which is connected to the control system by LAN and TCP/IP protocol. In the fork a sensor is mounted, which measured the force in vertical axis of the movement. The voltage signal from this sensor is used to prepare the force feedback signal. In the article (Zee, 2009) another excavators with hydraulic drives, controlled by a haptic joystick are described. Author has proposed his own design of haptic joystick using DC motors and showing the relationship between the swing of excavators arm and the joystick. In the article (Oh K. W. et al., 2008) another design of haptic joystick used to control the excavator arm is shown. In the paper (Kudomi S. et al., 2000) the concept of the master-slave haptic configuration using two hydraulic cylinders working in the impedance control system is presented. The first hydraulic drive (slave) has moved a load and the second has controlled the position of the demand device (master). The voltage signals for actuators valves are generated by the controller, which used the signals from the force sensors.

2. MODEL OF HYDRAULIC DRIVE

Electrohydraulic servo drives are used in applications requiring high forces. The basic hydraulic part consists of the hydraulic cylinder and the hydraulic amplifier, as shown in Fig. 1. The amplifier spool is moved by the electromechanical transducer, which in most cases is a proportional electromagnet.

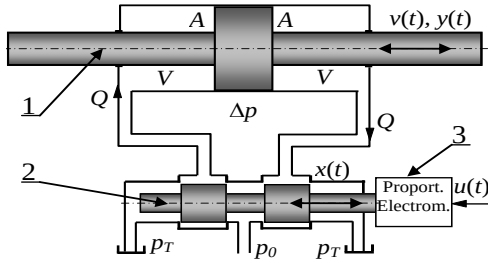

Fig. 1. Hydraulic drive: 1 – hydraulic cylinder, 2 – hydraulic valve, 3 – proportional electromagnet

From the automation point of view, the electrohydraulic drives are non-linear systems, which in many theoretical analyses are linearized. The set of linear equations describing the hydraulic part of the servo drive can be written as follows:

$$Q(t) = Q_s(t) + Q_h(t) + Q_v(t) \tag{1}$$

where: Q – valve flow, proportional (inlet and outlet), Q_s – flow balancing the flow compressibility, Q_v – cylinder absorptivity, proportional to the velocity, Q_l – leakage flow.
Substituting appropriate linear or linearized equations one obtains (Milecki and Myszkowski, 2003)

$$K_Q x(t) - K_p \Delta p(t) = \frac{V}{2E_0}\frac{d\Delta p(t)}{dt} + A\frac{dy(t)}{dt} + K_l \Delta p(t) \tag{2}$$

where: x – spool displacement, y – piston position [m], K_Q – valve flow gain [m²/s], K_p – valve flow-pressure coefficient [m⁵/(N•s)], Δp – pressure difference in a cylinder [Pa], E_0 – fluid bulk modulus [Pa], A – cylinder piston cross-sectional area [m²], K_l – leakage coefficient [m⁵/(N•s)], V – average contained volume of each cylinder chamber in a middle position of the piston [m³].

The motion of the system can be described as follows

$$m\frac{d^2y(t)}{dt} + D\frac{dy(t)}{dt} + F_L(t) = A\Delta p(t) \tag{3}$$

where: F_L – load force [N], m – mass [kg], D – viscous damping coefficient (Newtonian friction) [Ns/m].

The control valve can be described as second order system described by equation

$$\frac{d^2x(t)}{dt} = k_z\omega_z^2 u(t) - 2\zeta_z\omega_z\frac{dx(t)}{dt} - \omega_z^2 x(t) \tag{4}$$

where: k_z – the valve gain [m/V], ω_z – valve natural frequency [Hz], ζ_z – valve damping ratio, u – electromagnet input signal [V].

Basing on equations (1) ÷ (4), the electrohydraulic servo drive is described as fifth order system, consisting of valve described by second order system and cylinder described by second order element (usually oscillatory) connected serially to the integrative element. Assuming that the fluid leakage in a cylinder can be omitted, the block scheme of the drive is built and shown in Fig. 2. (Milecki and Myszkowski, 2003). Drive parameters are calculated basing on data characterizing the drive i.e.: cylinder dimensions, load, friction coefficient, oil bulk modulus etc. The valve parameters are taken from catalogue where valve step responses, frequency characteristics etc. are given. In the described here model following parameters are used:

- piston cross section area: A = 0.008 m²,
- flow coefficient: K_Q = 1.0 m²/s,
- valve flow-pressure coefficient: K_p =10⁻⁹ m⁵/Ns,
- cylinder stiffness: $2E_0/V$ = 8•10¹² Pa/m³,
- dynamic friction coefficient: D = 1000 Ns/m,
- mass: m = 200 kg.

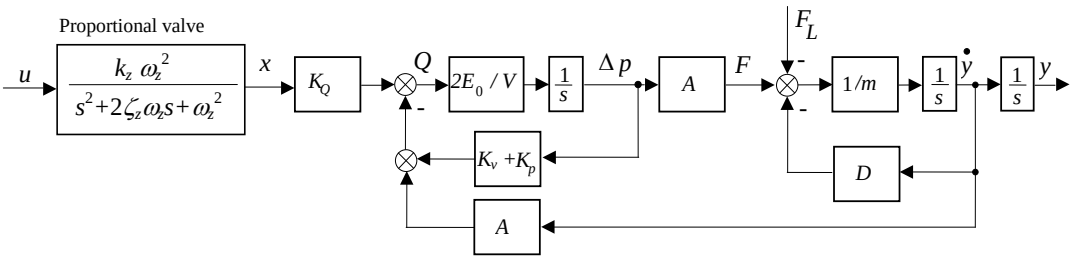

Fig. 2. Model of electrohydraulic drive

Proportional valve is described as a second order system with damping coefficient ζ_z = 1.2 and with natural frequency f_z = 16 Hz. The presented above model should be extended by adding valve control card model. Because the electronic control unit is usually very fast in comparison to the hydraulic part, at first it can be described only by a proportional element.

DOI 10.2478/ama-2018-0001

3. HAPTIC JOYSTICK AND ITS APPLICATION IN SIMULATION INVESTIGATION

In Fig. 3 the view of a one axis joystick prototype and his electronic circuits is shown. In this joystick, in order to generate the movement opposite force the rotary brake with magnetorheological (MR) fluid is used. On the brake axle, the joystick arm in the form of strain gauge load cell is mounted, which serves to measure the forces occurring on the joystick handle. On the other side of the MR brake, a potentiometer is used for measuring of the angular position. On the same axle the gear wheel with a belt is assembled to connect a DC motor.

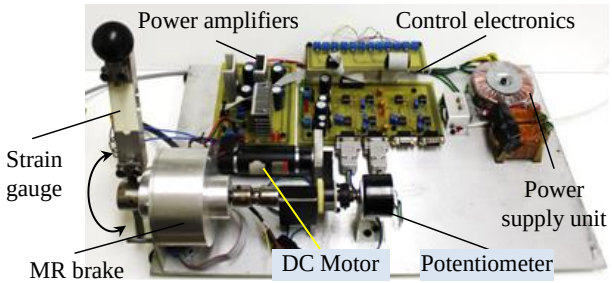

Fig. 3. The photo of the haptic joystick and its controller

The control electronic circuits include: operational amplifiers used to calibrate the joystick position and the force signals; two operational power amplifiers: one for the brake supplying and one for the motor control.

The made in Matlab-Simulink software simulation model of the described above hydraulic drive system with haptic joystick is shown in Fig. 4. It is assumed that the MR brake is modeled by the first order transfer function (with the time constant 0.01 sec.) connected serially with time delay equal to 0.05 sec. The human operator is modeled as a first order system with time constant equal to 0.1 sec. It is also assumed that the human operator control algorithm is PID like. There are two feedback loops in the model: force and position feedback. The first one is made by a haptic joystick with MR brake and the second one is made by an external cylinder piston position loop. The current position is assessed by operator's observation. The model is then connected to a virtual world thanks to special Simulink elements called VR Signal Expander and VR Sink. The first element converts simulation signal into a signal compatible with a VR Modeling Language. In case of simulation described in this article, a servo-cylinder piston displacement signal *y* is used as the VR movement simulation signal. VR Sink software includes graphic interface, combining simulation results with pictures presented in virtual reality. The Matlab VR environment includes library of a different 3D visualization objects. However, there are no hydraulic elements in this library and therefore authors have built one basing on a real servo-cylinder design principle. This simulation model was used for initial testing of the control of electrohydraulic drive.

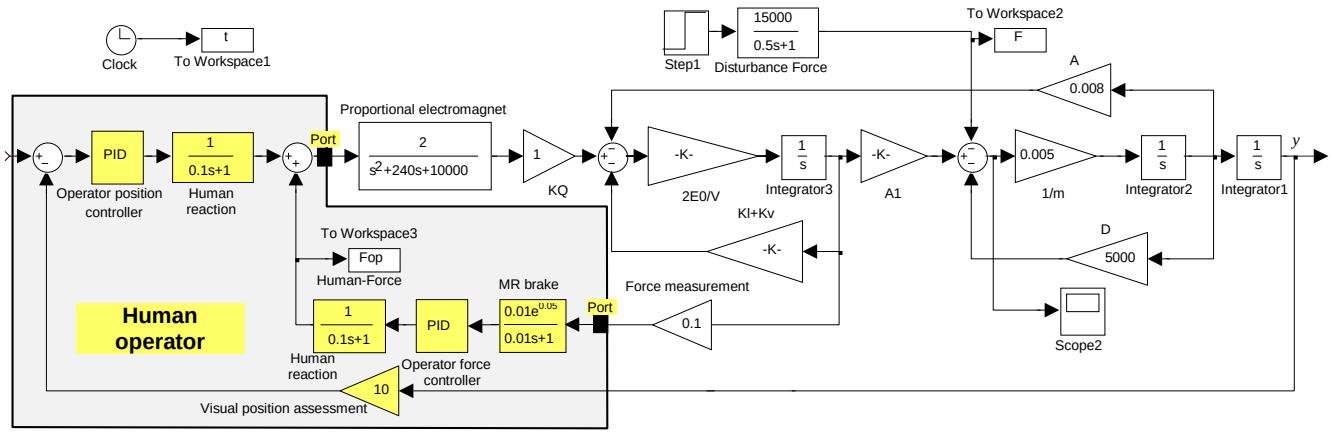

Fig. 4. Model of electrohydraulic drive

In the next step the block "Human operator" is removed from the model and replaced with the real haptic joystick, that is connected to the computer using an input/output card type RT-DAC as shown in Fig. 5. This card is controlled by toolbox software RT-CON, which is installed and used to connect the VR model of electrohydraulic drive (EHD) with the haptic joystick. Joystick input signals are: supply voltages of MR brake coil amplifier (U_{MRB}) and of DC motor (U_M). VR model output signals are: joystick arm angular position x_j measured by the potentiometer and joystick force signal F_j measured by strain gauge. In the presented system position control feedback loop is closed by the operator's eyesight (dashed line in the Fig. 5). During the investigations the PC computer with Matlab-Simulink software is used. For virtual reality presentation, a system based on VRLM environment is used.

There are two basic and dominant control methods, which may be applied when haptic joystick is used: force-command and motion command (Harward, 2006; Zhuang and Canny, 2000). When the operator's joystick motion is measured and taken as an input and the device force is fed back to the user, impedance control is applied. When the force exerted by user on a joystick arm is measured and time varying position is fed back to the operator, the method is called admittance control.

The main aim of this study is to choose an optimal control algorithm, which then will be implemented in the control system of the real electrohydraulic drive with a haptic joystick. The first investigated algorithm was admittance control, which block scheme is shown in Fig. 6. In this algorithm the drive position *y* is controlled by applied electronics and operator feels the force F_j which is proportional to the force occurring between the drive and the obstacle. In order to calculate this force two pressure sensors are installed in the cylinder chambers.

Paweł Bachman, Andrzej Milecki
DOI 10.2478/ama-2018-0001

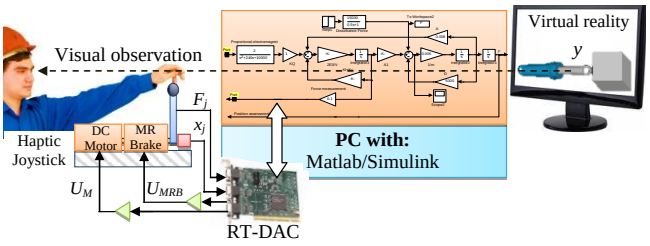

Fig. 5. The block scheme of investigation stand with real joystick

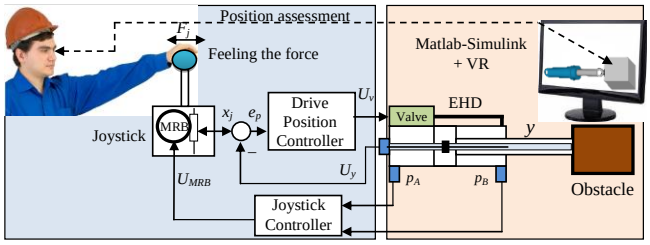

Fig. 6. Block diagram of admittance control

In the algorithm this force was calculated as pressure difference in the cylinder chambers, multiplied by controller gain coefficient. The force signal was sent as MR brake control voltage UMRF to the joystick controller.

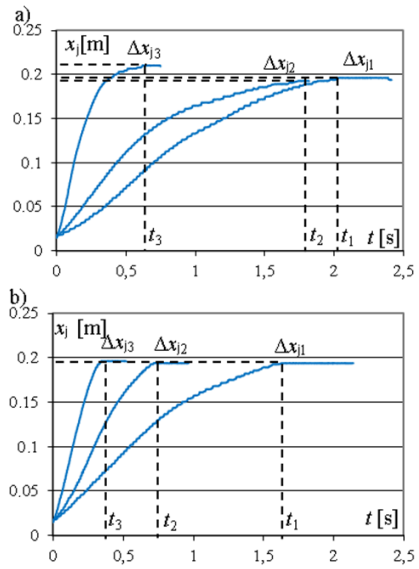

Fig. 7. The results obtained in simulation investigations of the admittance control system: a) without the feedback; b) with the force feedback

During the investigations in which simulation model and VR visualization was used, the precision of electrohydraulic drive rod positioning in touching an obstacle, depending on the speed of movement, was investigated. Virtual obstacle was placed in a distance of 0.193 m from the initial position of the piston rod. In the investigations 15 operators tried to touch smoothly the obstacle with the hydraulic cylinder piston rod. The position of the joystick arm x_j was measured and recorded during all the attempts made by operators. The best representative results obtained by a chosen operator are presented in Fig. 7. When the force feedback is disconnected (Fig. 7a), the operator is able to touch the obstacle in time t_1 = 2.05 s. In this case, the piston speed is about 0.1 m/s. If the hydraulic piston speed is about 0.2 m/s, the obstacle contact time is reduced to t_2 = 1.8 s, but position error is bigger i.e. equal to Δx_{j2} = 6 mm. At a piston speed equal to 0.5 m/s, the operator has stopped moving the joystick arm until about t_3 = 0.6 s, but in this case the position error still is the largest, and reached 19 mm. In practice, this means that the piston hit the obstacle hard. The obtained parameters are significantly improved when force feedback is switched on, as shown in Fig. 7b.

In the investigations made by different operators, the position error is not bigger than 3 mm, which occurred only for the highest speed of the movement equal to 0.8 m/s. The shortest time, in which the operator is able to touch smoothly the obstacle by the piston rod was t_3 = 0.32 s.

In Fig. 8 the scheme block diagram of impedance control is presented. In this case, the force controller is used in the drive and the operator has used his visual observation of the drive in order to generate assumed force. The force feedback is assured by pressure sensors located in cylinder chambers.

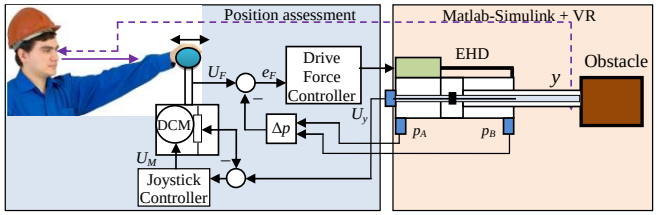

Fig. 8. Block diagram of modified impedance control algorithm

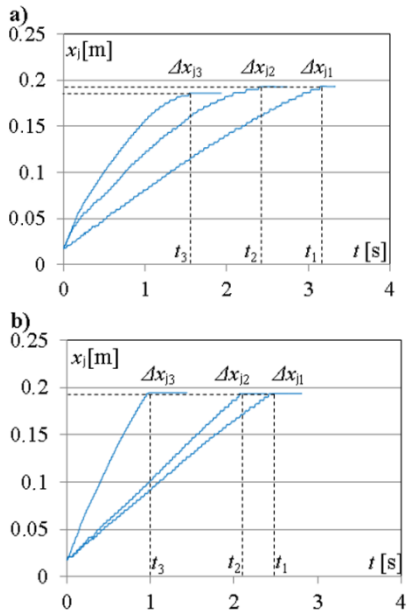

Fig. 9. The results obtained in simulation investigations of the modified impedance control algorithm a) without the feedback; b) with the force feedback

However, in order to use the haptic joystick for control of a drive with internal force feedback loop, additional solution should be used. Instead of the MR brake, the DC motor (DCM) needs to be installed in the joystick, which will set the joystick arm in a position corresponding to the current position of cylinder piston. The force on a joystick arm, measured by a strain gauge is used as an assumed signal U_F for the internal force feedback loop. The joystick arm position signal x_j is compared with the drive current position signal.

DOI 10.2478/ama-2018-0001

The difference between these two signals is used by Joystick Controller for generation of the voltage signal to DC motor installed in a joystick. So, the joystick in the impedance control system can be categorized as active. In this way in the impedance control, the human operator feels in a joystick a current drive position, and sets the required force. The DC motor tries to set the joystick arm in a position which is proportional to the piston position. In Fig. 9. the simulation results are presented, which are obtained using the described above modified impedance control.

As it was in the previous case, the results show the improvement in positioning accuracy after the introduction of the haptic feedback. The highest position error occurred at the highest piston speed.

4. INVESTIGATIONS OF THE ADMITTANCE AND IMPEDANCE CONTROL WITH THE USE OF HAPTIC JOYSTICK

In Fig. 10 the block scheme of a test stand for testing of real electrohydraulic drive controlled by the haptic joystick, is shown. It consists of three main elements: the PC which acts as a control unit, a haptic joystick with its controller and electrohydraulic drive with a load cylinder and measurement equipment.

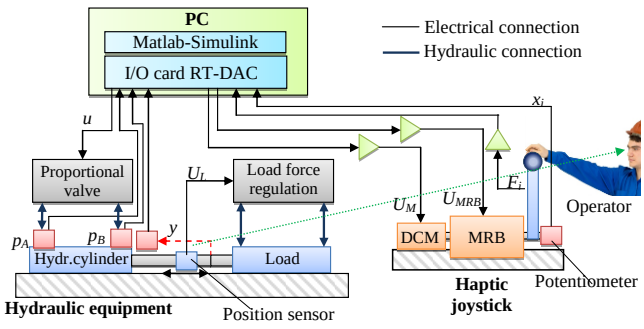

Fig. 10. The block diagram of research station for laboratory research

On the PC the program Matlab/Simulink is installed on which the implementation of control algorithm for hydraulic drive and haptic joystick is made. The controller inputs are: joystick arm position x_j and joystick arm force F_j. Basing on them, the proportional valve voltage control signal u is calculated and sent to the drive control card. In both hydraulic drive cylinder chambers the pressure sensors type MBS 1250 Danfoss with measurement range 0 – 25 MPa (0 – 250 bar) and analog output 0 – 5 V are installed and connected by RT-DAC card in the control computer. The force generated by the piston rod of hydraulic cylinder is calculated as a difference of pressures in a cylinder chamber. This pressure difference signal is also used as a feedback signal, for calculation of the magnetorheological brake voltage control signal U_{MRB}. The position of hydraulic cylinder piston is measured and additionally used for control of the proportional valve and DC motor (U_M voltage) installed in a joystick. The photo of the test stand is shown in Fig. 11.

The position of hydraulic cylinder piston is measured by the linkage sensor. Its measurement distance is equal to 1250 mm and analog output is in a range of 0-10 V. For this sensor maximum measurement parameters are: speed 10 m/s; acceleration 300 m/s^2. The measured position nonlinearity error is 0.1 %.

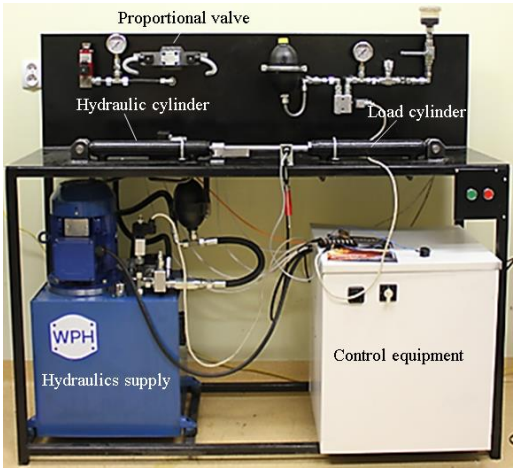

Fig. 11. The photo of hydraulic research station

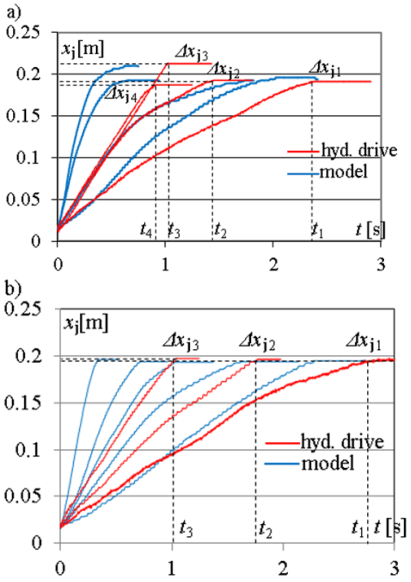

Fig. 12. Investigation results of control of electrohydraulic drive when admitance control was used: a) without the feedback; b) with the force feedback

In the empirical investigations 15 operators were involved, each of which has performed 3 tasks making 5 attempts for each task. The obstacle was located in this case 0.16 m from the initial position of the hydraulic cylinder piston rod. In Fig. 12, the best representation (obtained for one chosen operator) of all research with the use of admittance control, are presented.

In Fig. 12 the results obtained without and with admittance control are compared. In this figure curves obtained in simulation (red color) and in laboratory experiments are presented (blue color). In case when the haptic feedback is not active (Fig. 12a), during first attempt, when the velocity was about 0.8 m/s, the operator was able to touch the obstacle with an error of Δx_{j1} = 2 mm in a time t_1 = 2.34 s. In the second attempt, the velocity has increased to about 1.4 m/s and the time was reduced to t_2 = 1.4 s, without changing the positioning error. In next two attempts the velocity was about 1.8 m/s and the time was reduced to t_3 = 1.05 s and t_4 = 0.92 s. However in these two cases the positioning error was Δx_{j3} = -2 mm and Δx_{j4} = 20 mm. The characteristics obtained when the force feedback is activated are shown in Fig. 12b. It is clearly visible that for all recorded curves the positioning errors are significantly reduced. For the biggest velocity equal to about

DOI 10.2478/ama-2018-0001

0.8 m/s it is not higher than 4 mm. Also the positioning time was reduced and the best result was t_3 = 1 s which was 0.4 s faster than the time obtained when the force feedback was switched off. The comparison of curves obtained in simulation with curves obtained in real experiments have indicated close similarities of the run.

In Fig. 13 the results obtained when impedance method was applied are presented. If the haptic feedback is not activated the operator was able to touch the obstacle in an average time t_1 = 4.07 s with velocity 0.04 m/s and with positioning error equal to about 1 mm. When the velocity was increased to 0.07 m/s the positioning time was t_2 = 3.15 s. For the velocity 0.2 m/s this time was reduced to t_3 = 1.63 s, but the positioning error was Δx_{d3} = -2 mm. The results obtained when the haptic feedback was on, are shown in Fig. 13b.

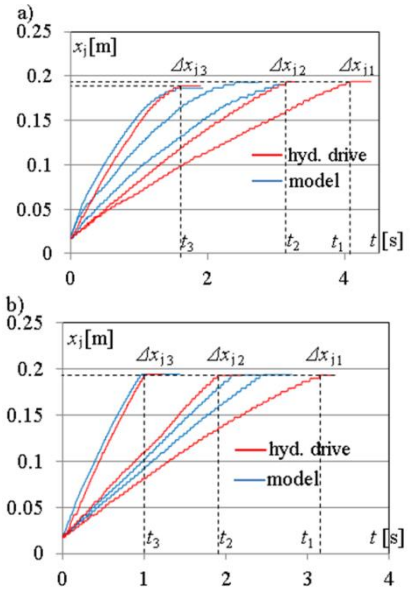

Fig. 13. Investigation results of control of electrohydraulic drive when impedance control was used: a) without the feedback; b) with the force feedback

In all attempts the positioning error was not bigger than Δx_{d3} = 1 mm, and the shortest positioning time was about t_3 = 1 s, which was of about 2.15 s faster in comparison to results obtained without a feedback. Similarly to the results obtained if admittance control is used, also in impedance control the results have been significantly improved.

5. CONCLUSION

The paper presents the results of simulation and laboratory investigations of electrohydraulic drive control made by a human operator, who used a haptic joystick. In the presented work two main control methods are considered: admittance and impedance. The theoretical control model of these two methods are described and their simulation model is proposed. The simulation investigations are focused on checking how quickly and accurately can the operator control the electrohydraulic drive during touching the obstacle by using a one-axis joystick. The obtained simulation results enable to design and build control strategies for system composed of a haptic joystick and a real electrohydraulic drive.

Finally the whole system was built, implemented and investigated in laboratory environment. The empirical investigations have shown that the use of haptic joystick improved the accuracy of touching obstacles. The biggest position errors occurred when the operator controlled the hydraulic drive without any direct feedback and had limited opportunity to observe the moving object. This situation can occur in practice, e.g. while excavator works in a deep trench and where the excavator bucket interferes with a heavy object (stone, pipe). The smallest error was recorded when the drive was controlled when the haptic feedback was switched on. Fifteen operators have participated in the simulation and experimental investigations.

The results have shown that haptic control can improve the human feeling of forces between electrohydraulic drive and an obstacle and thanks to this, the manual control can be more accurate and safer.

REFERENCES

1. **Adams R.J., Hannaford B.** (1999), Stable haptic interaction with virtual environments, *IEEE Transactions on Robotics and Automation*, 15(3), 465-474.
2. **Frankel J.G.** (2004), *Development of a Haptic Backhoe Testbed, MS thesis*, The Georgia Institute of Technology, G.W. Woodruff School of Mechanical Engineering.
3. **Harward V.** (2006), Haptic synthesis, *Proc. 8th International IFAC Symposium on Robot Control*, SYROCO, 19-24.
4. **Kontz M.E.** (2002), *Haptic Enhancement of Operator Capabilities in Hydraulic Equipment*, Masters of Science Thesis, School of Mechanical Engineering, Georgia Institute of Technology.
5. **Kontz M.E.** (2007), *Haptic control of hydraulic machinery using proportional valves*, Doctorate thesis, G.W. Woodruff School of Mechanical Engineering.
6. **Kudomi S., Yamada H., Muto T.** (2000), Development of a hydraulic master-mlave mystem for telerobotics, *Proceedings of 1st FPNI-PhD Symposium*, Hamburg, 467-474.
7. **Li P.Y.** (2000), Towards safe and human friendly hydraulics: the passive palve, *ASME Journal of Dynamic Systems, Measurement and Control*, 122(3), 402-409.
8. **Milecki A., Myszkowski A.**, (2009), Modelling of electrohydraulic servo drive used in very low velocity applications, International Journal of Modelling, *Identification and Control*, 7(3), 246-254.
9. **Oh K.W., Kim D., Hong D., Park J.-H., Hong S.** (2008), Design of a haptic device for excavator equipped with crusher, Book the 25th International Symposium on Automation and Robotics in Construction, *ISARC-2008*, Publisher Vilnius Gediminas Technical University Publishing House "Technika", 202-208.
10. **Park H.-J., Lee S., Kang S.-K., Kang M.-S., Min-Su, Han S.Ch.** (2011) Experimental study on hydraulic signal compensation for the application of a haptic interface to a tele-operated excavator, *Proceedings of the 28th ISARC*, Seoul, Korea, 298-303.
11. **Won Oh K., Kim D., Kim N., H., Hong D.** (2011), The virtual environment for force-feedback experiment of excavator using a novel designed haptic device, *Proceedings of the 28th ISARC*, Seoul, Korea, 51-56.
12. **Zarei-nia K., Goharrizi A. Y., Sepehri N., Fung Wai-keung** (2009), Experimental evaluation of bilateral control schemes applied to hydraulic actuators: a comparative study, *Transactions of the Canadian Society for Mechanical Engineering*, 33, 377-398.
13. **Zee van der L.F.** (2009), *Design of a haptic controller for excavators*, Thesis MScEng, Electrical and Electronic Engineering, University of Stellenbosch.
14. **Zhuang, Y., Canny, J.** (2000), Haptic interaction with global deformations, *Proc. IEEE Robotics and Automation Conference*, 2428-2433.

DE GRUYTER
OPEN

DOI 10.2478/ama-2018-0002

acta mechanica et automatica, vol.12 no.1 (2018)

ENERGY RECOVERY FROM A NON-LINEAR ELECTROMAGNETIC SYSTEM

Krzysztof KĘCIK*

*Department of Applied Mechanics, Lublin University of Technology, Nadbystrzycka 36, 20-618 Lublin, Poland

k.kecik@pollub.pl

received 5 April 2017, revised 26 February 2018, accepted 1 March 2018

Abstract: The paper presents study of a pseudo-magnetic levitation system (pseudo-maglev) dedicated for energy harvesting. The idea rely on motion of a pseudo-levitating magnet in a coil's terminal. The study based on real prototype harvester system, which in the pendulum dynamic vibration absorber is applied. For some parameters, the stability loss caused by the period doubling bifurcation is detected. The coexistence of two stable solutions, one of which is much better for energy harvesting is observed. The influence of the pseudo-maglev parameters on the recovered current and stability of the periodic solutions is presented in detail. The obtained results show, that the best energy recovery occurs for the high pseudo-maglev stiffness and close to the coil resistance. The amplitude's excitation, the load resistances and the coupling coefficient strongly influence on the system's response.

Key words: Magnetic Pseudo-Levitation, Energy Harvesting, Vibration, Electromagnetic Coupling, Attractor Coexistence

1. INTRODUCTION

Energy harvesting (EH) or energy scavenging (ES) is a promising and evolving field of research capable of supplying power to systems in a broad range of applications. EH can meet in many distinct technologies, including solar panels, wind turbines, kinetic motion harvesters, and thermal generators (Mann and Owens, 2010). The ES devices (harvesters) from vibration have become increasingly widespread because vibrations are everywhere. The devices can be alternative energy sources, especially for microelectromechanical systems (MEMS). The energy recovery from vibration can be achieved by several methods of transform vibration in the electric energy.

Three of the most popular method are:

- Variable Capacitance (VC) Systems,
- Piezoelectric Material (PM) Systems,
- Magnetic Induction (MI) Systems.

The VC systems transduce vibration energy through the electric fields between a parallel plate capacitor with a movable plate. The magnitude of the recovered energy from such systems is generally of the order of microwatts (Jonnalagadda, 2007). The PM systems will produce an electric field and consequently a voltage when deformed under an applied stress. The magnitude of recovered energy from these systems can vary from microwatts to watts (Beeby et al., 2006). Similarly, to the piezoelectric are a magnetostrictive material will produce a magnetic field when deformed. The MI systems also called electromagnetic systems use the motion of a permanent magnet to voltage induction across the terminals of a coil of wire. The magnet's motion creates a magnetic flux leads to the voltage flow in an electrical circuit. The magnitude of recovered energy from these systems can range up to kilowatts, and strongly depending on the size of the magnetic induction systems (Joyce, 2011).

One of the most interesting type of MI harvesters are the pseudo-maglev systems, which use the pseudo-levitation effect for energy recovery (Mann and Sims 2009; Soares at al., 2016; Sun et al., 2018). The pseudo-levitation harvesters characterize simplicity construction, lack of the dampers and the springs and reliability (Li et al., 2016; Zhou and Wang, 2017). Additionally, can be easy to modification. The pseudo-maglev term means that the magnetic levitation effect occurs with a help mechanical constraint for provides stability. A theorem due to Earnshaw (Earnshaw, 1842) proves that it is not possible to achieve magnetic static levitation using any combination of fixed magnets and electric charges. The static levitation means stable suspension of an object against gravity. From Earnshaw's theorem, at least one stable axis must be present for the system to levitate successfully. However, there are different methods for successful levitation: electromagnets, diamagnetism or superconductors (Qian, 2015; Zhu et al., 2017).

The proposed pseudo-maglev harvester is a crucial component of the laboratory harvester-absorber system, which allows to simultaneously vibration mitigation and energy recovery (Kecik, 2015; Kecik and Mitura, 2016; Kecik et al., 2017a). The detailed study of the maglev harvester helps to proper tune and find the best configuration of the system.

2. PSEUDO-MAGLEV'S HARVESTER MODEL

The pseudo-maglev harvester system consists of the permanent cylindrical levitating magnet (moving) suspended in the magnetic field. The scheme and photo of the harvester in Fig.1 are shown. The pseudo-levitation effect coming from the two fixed permanent magnets pairs, which are suitable pole oriented. Each pair of magnets having magnetic poles oriented to repelling NS-SN-NS (Fig. 1 (a)). This repel orientation of the magnets is more stable compared to attract magnet's orientation. All magnets are mounted in the cylindrical nonmagnetic tube (made from the non-magnetic Plexiglas material). The special air holes and gapes are

DOI 10.2478/ama-2018-0002

made on the tube's surface in order to air cushion reduction. Additionally, the magnet and tube surfaces were sprayed by Teflon to minimalize the friction effect.

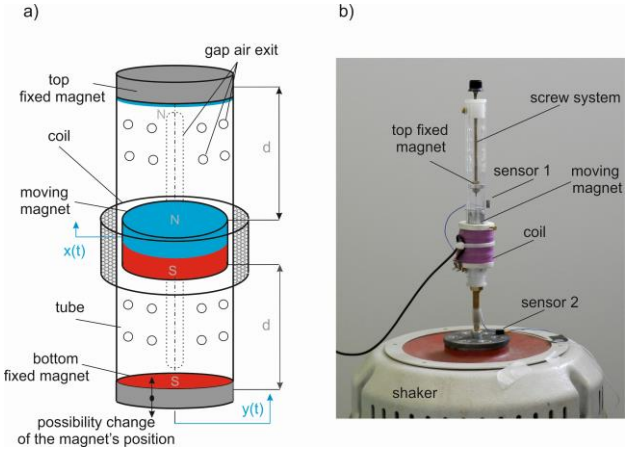

Fig. 1. Pseudo-maglev harvester: a) scheme; b) and prototype (b). This prototype device has been sent to the patent application (no. P.420720)

The small friction and air dissipation is described by the viscous damping coefficients, which were estimated from the free vibration test. The inductor is formed by winding wire around the outer surface of the tube. The distance between the moving and the fixed magnets can be change by the special screw system (see Fig. 1(b)). Modification in the bottom magnet position (parameter d (Fig.1(a)) causes change in the stiffness suspension (Mann and Sims, 2010).

The pseudo-maglev suspension model has been experimentally identified and proposed in papers (Mann and Sims, 2010; Kecik et al., 2017b), where the obtained results lead to the suspension consists of the non-linear spring and the linear damper. The electromechanical model of the maglev harvester is shown in Fig. 2(a). From a functional principle point of view, the system is similar to a shaker, but the conversion process is reversed.

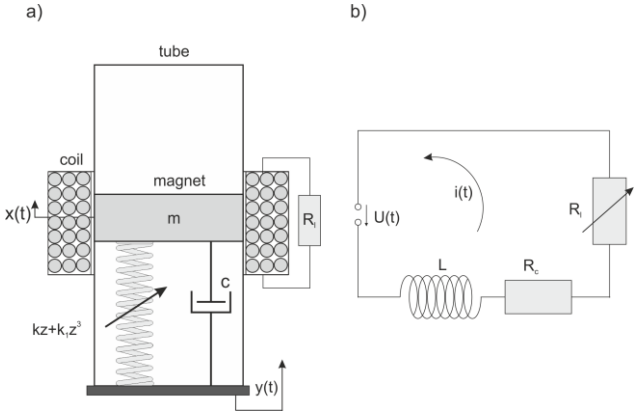

Fig. 2. Schematic diagram of the pseudo-maglev elektromechanical harvester: a) model; b) the electrical circuit

The displacement of the moving magnet from the static position denoted as $x(t)$. The $y(t)$ is the excitation of the base, assumed to be harmonic $\mathrm{y(t)} = \mathrm{Asin(\omega t)}$, where parameters A and ω are the amplitude and the frequency of excitation, respectively. The m means the magnet's mass, c is the viscous damping coefficient, k and k_1 are the linear and the non-linear stiffness components of the pseudo-maglev suspension. The magnet's oscillation induces current $i(t)$, and voltage $\mathrm{U(t)}$. The electrical circuit of the harvester is presented in Fig. 2(b). It is modelled as the inductor (coil) having the resistance R_c and the inductance L. The electrical power generated from the harvester is dissipated across the load resistor $\mathrm{R_l}$, which can be adjustable. The total resistance denoted as R means the sum of $\mathrm{R_c}$ and $\mathrm{R_l}$.

The magnetic restoring forces were calibrated from measurements of the restoring force F and separation distance d between the bottom and moving magnets with help of the simple static tests. A series of experimental measurements (black points) where the force against a separation distance between two magnets are plotted in Fig. 3.

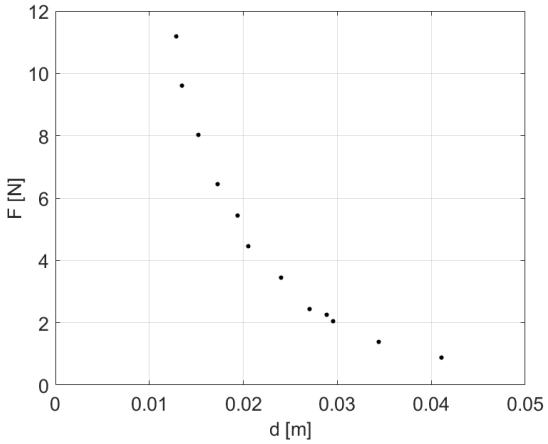

Fig. 3. The restoring force plotted as a function of the separation distance *d* between the moving and bottom magnet

Next, the experimental results (black points) were transformed into new x coordinates (circle points in Fig. 4). Because the top and bottom magnets are the same, it assumed that both forces are identical. Finally, the curve fitting technique to obtain the mathematical pseudo-maglev suspension model has been used (black line in Fig. 4). On the basis of this result a model of the complete magnetic suspension is developed.

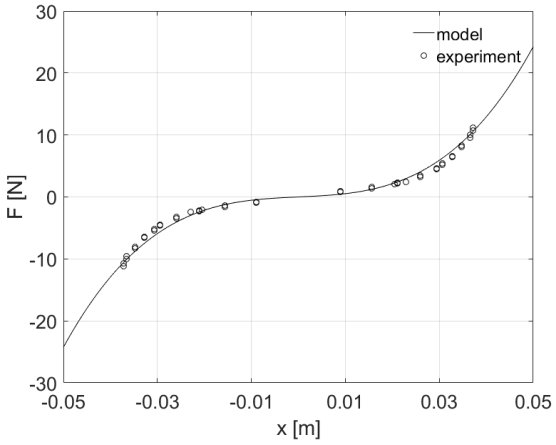

Fig. 4. The force-displacement model magnetic suspension (line) and experimental results (circle points)

DOI 10.2478/ama-2018-0002

The total restoring force is calculated as a sum of two forces leads to the monostable hard Duffing characteristics

$$F(x) = F_b(x) - F_t(x) = \sum_{n=0}^{3} \beta_n (x+d)^n - \sum_{n=0}^{3} \beta_n (d-x)^n = (2\beta_1 + 4d\beta_2 + 6d^2\beta_3)x + 2\beta_3 x^3 = kx + k_1 x^3, \quad (1)$$

where $\beta_0 - \beta_3$ are the experimental coefficients estimated from the restoring force (Fig. 3). $\mathrm{F_b(x)}$ and $\mathrm{F_t(x)}$ are the restoring repelling forces describe the relationship between the pairs of magnets (fixed bottom-moving and moving – fixed top). The linear part of the Duffing characteristics is equals $\mathrm{k} = 2\beta_1 + 4\mathrm{d}\beta_2 + 6\mathrm{d}^2\beta_3$, and the non-linear component equals $\mathrm{k_1} = 2\beta_3$. More information about pseudo-magnetic suspension identification technique can be found in (Mann and Sims, 2010; Kecik et al., 2017b), where used very similar methodology.

The mathematical analysis of the pseudo-magnetic suspension characterized by the equation (1) shows two important conclusions:

- the distance d influences on the linear stiffness, and the pseudo-maglev's resonance, only,
- the non-linear part independent on the distance separation of the magnets.

The governing equations of motion for the pseudo-maglev harvester system can be obtained from summation of all forces acting in the vertical direction (simply non-linear oscillator) and use the Kirchhoff's law for the current flow. Additionally, to simplification, the relative magnet's displacement $\mathrm{z(t)} = \mathrm{x(t)} - \mathrm{y(t)}$ is introduced:

$$m\frac{d^2z}{dt} + c\frac{\mathrm{dz}}{dt} + kz + k_1 z^3 + \alpha i + mg = -m\frac{d^2y}{dt}, \quad (2)$$

$$L\frac{\mathrm{di}}{dt} + (R_l + R_c)i - \alpha\frac{\mathrm{dz}}{dt} = 0. \quad (3)$$

The parameter α is a constant coefficient estimated from the experiment tests (called coupling coefficient). In case of vibration with the small amplitude, the α tends towards zero and the harvester can be treated as linear. Equations (2) and (3) represent two forms of the mathematical model of the non-linear pseudo-maglev harvester.

3. PARAMETER SENSITIVY ANALYSIS

Before starting the analysis, it is important to clarify goals. To have a general overview how does the electrical parameters change affect on the energy harvesting and dynamics of the pseudo-maglev system, the parametric analysis has been done. These results will allow optimal setting and optimize the harvester system. The numerical calculations have been done in AUTO 07p software (Doedel and Odelman, 2012) using the continuation technique method (pseudo-arclength continuation for following solution families), additionally verified by MATLAB 2015b. The numerical continuation is a numerical method successfully used to response and bifurcation analysis of ordinary differential equation (ODE) systems.

The simulation parameters based on the identification from the laboratory rig presented in Fig. 1(b) and equal: $\mathrm{m} = 0.09\mathrm{kg}$, $\mathrm{c} = 0.054\mathrm{Ns/m}$, $\mathrm{k_1} = 160000\mathrm{N/m^3}$, $\mathrm{R_c} = 1.20\mathrm{k\Omega}$, $\mathrm{L} = 1.460\mathrm{H}$, $\alpha = 60\mathrm{Vs/m}$. The numerical simulation starts from the fixed point: $\mathrm{z(t)} = 0\mathrm{m}, \dot{\mathrm{z}}(\mathrm{t}) = 0\mathrm{m/s}$, $\mathrm{i(0)} = 0\mathrm{A}$, and from the periodic solution for coexistence solution detection. The numerical calculations have been performed for the frequency range from $\omega = 10\mathrm{rad/s}$ to $\omega = 100\mathrm{rad/s}$, so that the amplitude of excitation force changes along the resonance curves.

3.1. Amplitude influence analysis

The exemplary resonance curves of the magnet and the recovered current versus frequency ω for the various amplitude of excitation A are shown in Fig. 5 and 6, respectively. These diagrams show maximal value of the magnet's displacement max(z) and the maximal recovered current max(i).

The black line corresponds to the case where the excitation amplitude equals $\mathrm{A} = 0.005\mathrm{m}$, the blue line to $\mathrm{A} = 0.01\mathrm{m}$, and the green line to $\mathrm{A} = 0.014\mathrm{m}$. The bifurcation points are labelled as: SN (saddle-node bifurcation) and PD (period doubling bifurcation). The stable periodic solutions are marked by the solid line, while the dashed-dotted line denotes the unstable solutions.

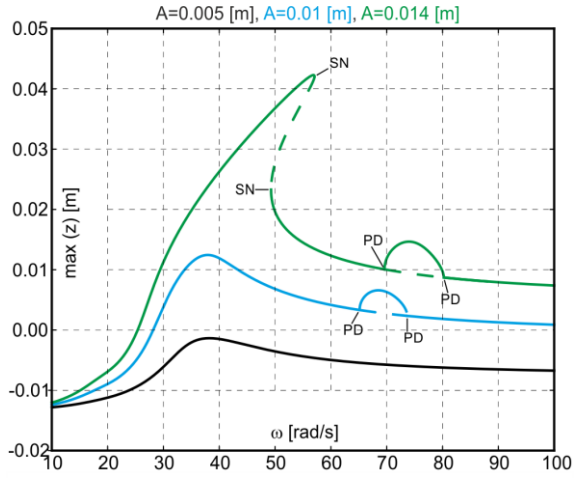

Fig. 5. Resonance curves of the magnet, for k=38.7N/m and R=2.3kΩ

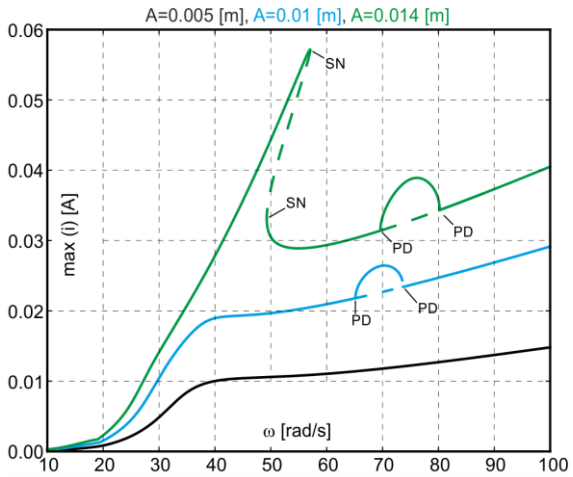

Fig. 6. Recovered current for the various excitation amplitude, for k=38.7N/m and R=2.3kΩ

DOI 10.2478/ama-2018-0002

The resonance peak is observed near the frequency $\omega \approx 40\mathrm{rad/s}$, but for the higher excitation amplitudes, shape of the resonance curve is distorted (hardening behaviour is observed). The maximal recovered current obtained for the high amplitude of excitation $\mathrm{A} = 0.014\mathrm{m}$ and equals $\mathrm{i} = 0.06\mathrm{A}$. Generally, two times greater amplitude causes two times current increase. Moreover, for the higher excitation amplitude, coexistence of two solutions occurs. For frequency range of $\omega \approx 65 - 75\mathrm{rad/s}$ (for $\mathrm{A} = 0.01\mathrm{m}$) and $\omega \approx 70 - 80\mathrm{rad/s}$ (for $\mathrm{A} = 0.014\mathrm{m}$), one stable and one unstable solution are observed.

The new stable solution characterizes change in the vibration period, caused by the PD bifurcation. The period increases from $\mathrm{T} = 0.9\mathrm{s}$ to $\mathrm{T} = 0.18\mathrm{s}$. This situation is clearly presented in Fig. 7, for the frequency $\omega = 70\mathrm{rad/s}$, (black line).

For the large value of A, the resonance curve shape is distorted and exhibits two stable periodic solutions (top and bottom branches, Fig. 5 and 6). One of these solutions shows higher energy output.

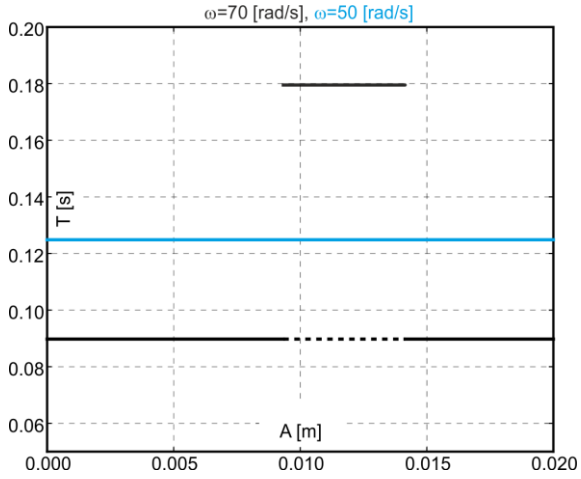

Fig. 7. The change of the magnet vibration period. The black line represents the period doubling bifurcation behaviour

The maximal recovered current equals about $\mathrm{i} = 0.06\mathrm{A}$ from the top branch, while $\mathrm{i} = 0.03\mathrm{A}$ from the bottom curve. These solutions depend on the initial conditions of the pseudo-maglev system (initial displacement $\mathrm{z}(0)$ and velocity $\dot{\mathrm{z}}(0)$). This effect is called foldover and is characteristic for the non-linear resonances.

The coexistence of two stable solutions are confirmed by the basin of attraction (Fig. 8). Basin of attraction is the set of initial conditions leading to long-time behaviour that approaches that attractor. The red colour with attractor no. 2 denotes the periodic solution corresponding to the bottom branch, while the yellow colour (and its attractor no. 1) corresponds to the top branch of hardening characteristic presented in Fig. 5. One can easily notice that the BA represents by the yellow colour is dominant. The solution from top branch is much better for the energy harvesting. Therefore, the influence of the electrical parameters is crucial from practical point of view.

Exemplary time series of the pseudo-levitating magnet for $\omega = 50\mathrm{rad/s}$ is presented in Fig. 9. The blue line means the solution represented by the top branch, while the red line denotes solution from the bottom branch (see, Fig. 5). Note, that both signals have periodic nature.

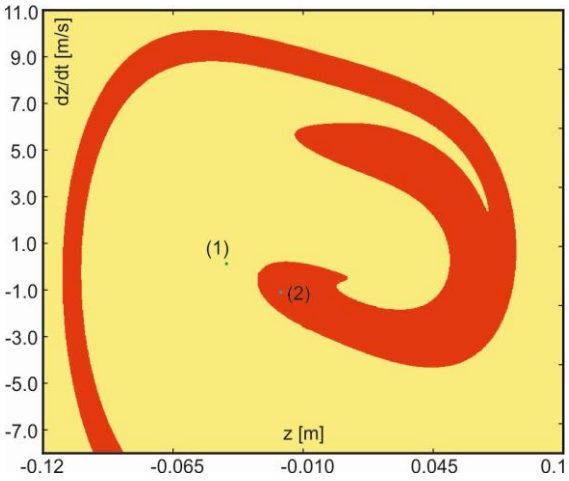

Fig. 8. Basins of attraction for parameters ω=50rad/s and A=0.014m: (1) attractor of the top branch, (2) attractor of the bottom branch

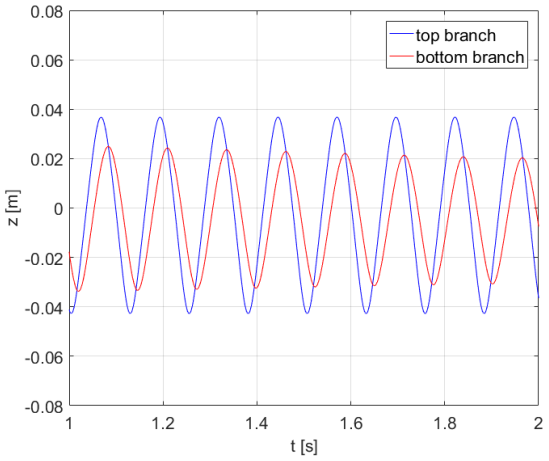

Fig. 9. The magnet vibration vs. time of the top (blue line) and bottom branch (red line), for parameters: ω=50rad/s, A=0.014m

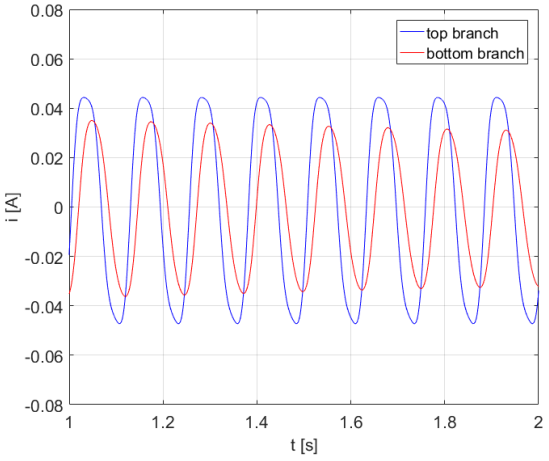

Fig. 10. The recovered current vs. time of the top (blue line) and bottom branch (red line), for parameters: ω=50rad/s, A=0.014m

DOI 10.2478/ama-2018-0002

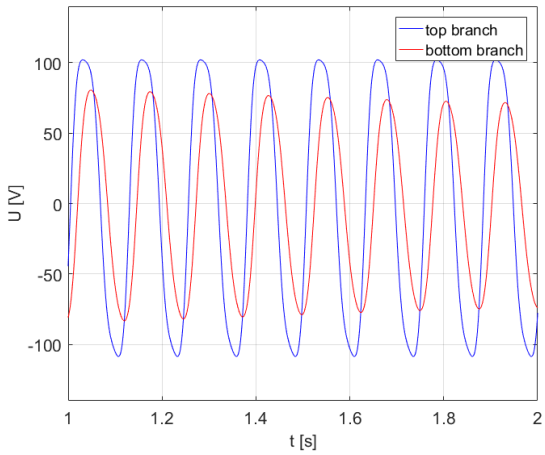

Fig. 11. The recovered voltage vs. time of the top (blue line) and bottom branch (red line), for parameters: ω=50rad/s, A=0.014m

Additionally, the displacement of the vibration centre is observed. This displacement is a result of the magnet's gravitation force, included in equation (2). Of course, the displacement depends on the pseudo-maglev stiffness.

The recovered voltage U and the instantaneous power P extracted from the magnet's vibrations can be computed from simple formulas (Mann and Sims, 2009)

$$U = iR_l, \quad P = i^2 R_l. \tag{4}$$

The recovered current and the voltage versus time in Fig. 10 and 11 are presented, respectively. The maximal current value from the top branch equals $\mathrm{i} = 0.045\mathrm{A}(\mathrm{U} \approx 100\mathrm{V})$, while from the bottom is $\mathrm{i} = 0.03\mathrm{A}(\mathrm{U} \approx 80\mathrm{V})$.

Analysing both time series can be concluded that recovered power from the bottom branch equals $\mathrm{P} = 2.65\mathrm{W}$, while from the top branch is $\mathrm{P} = 5.53\mathrm{W}$. The recovered current and voltage have periodic course, also. The frequency of the magnet's vibration and the recovered current (and voltage) have the same vibration's period.

3.2. Pseudo-maglev suspension influence

The pseudo-magnetic levitation stiffness can be easy modified by the parameter d in the real system. However, the modification also changes the linear resonance of the magnet. The vibration amplitude and amount of the recovered energy strongly depends on parameter k (Fig. 12). For small stiffness $\mathrm{k} = 10\mathrm{N/m}$ the maximal magnet's amplitude equals $\mathrm{z} = 0.025\mathrm{m}$ and the recovered current equals $\mathrm{i} = 0.045\mathrm{A}$. If the stiffness increases, then the resonance curve exhibit non-linear resonance with the foldover effect. Additionally, the period doubling (PD) region disappears.

For the low frequency level, the parameter k practically does not influence on the recovered current level. However, increase of k, in higher frequency level the recovered energy is larger (Fig. 13), especially close to the resonance peak ($\omega = 40 - 60\mathrm{rad/s}$). For the small pseudo-maglev stiffness $\mathrm{k} = 10\mathrm{N/m}$, the higher level of recovered energy occurs in the PD region ($\omega \approx 55 - 85\mathrm{rad/s}$). Interestingly, to this region, that the magnet's oscillation is similar to the vibration in the resonance peak.

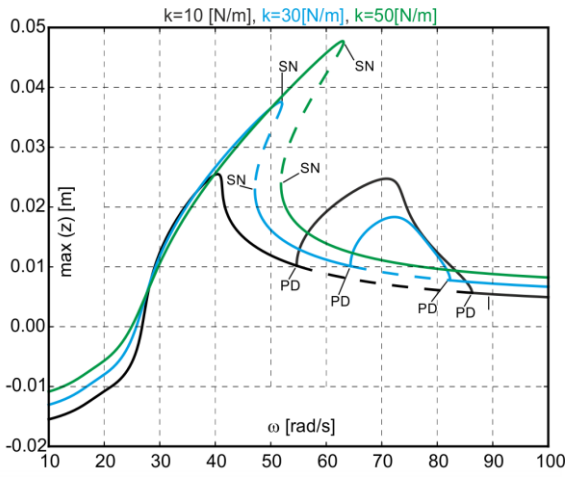

Fig. 12. Resonance curves for various pseudo-maglev stiffness *k*, for parameters: R=2.3kΩ, A=0.014m

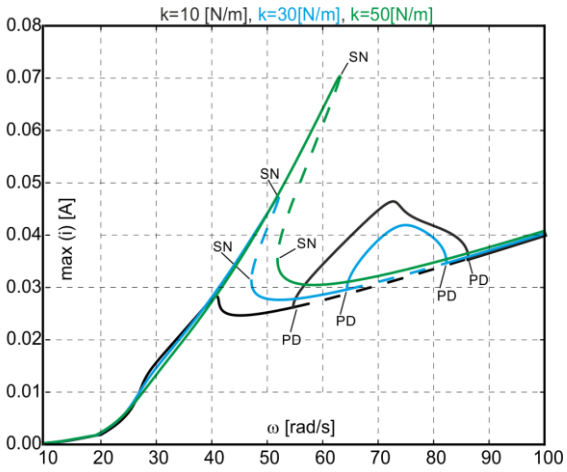

Fig. 13. Recovered current for various pseudo-maglev stiffness *k*, for parameters: R=2.3kΩ, A=0.014m

This means that is possible to rise of the recovered energy level without increase of the magnet's oscillation. Note, that the large magnet's oscillations can cause the magnet jump from the coil, but this case was not analysed.

3.3. Resistance load influence

The resonance curves for the pseudo-levitating magnet and the recovered current under the load resistance influence R are shown in Fig. 14 and 15, respectively. The black line corresponds to the case where the total resistance is $\mathrm{R} = 2.0\mathrm{k\Omega}$, the blue line to $\mathrm{R} = 2.4\mathrm{k\Omega}$, and the green to $\mathrm{R} = 2.8\mathrm{k\Omega}$. Analysing and comparing the results in both diagrams, it can conclude that resistance R may introduce new solutions. For some parameters, two stable periodic solutions and the loss of the stability caused by PD bifurcation are observed. As expected, the highest recovered energy for the $\mathrm{R} = 2.4\mathrm{k\Omega}$ is observed. This means, that the load resistance should be close to the coil resistance $\mathrm{R_c} = 1.2\mathrm{k\Omega}$. Increase of R causes that period doubling region is growing. It can see that for small value of ω the resistance practically does not effect on the magnet's amplitude and the recovered energy.

DOI 10.2478/ama-2018-0002

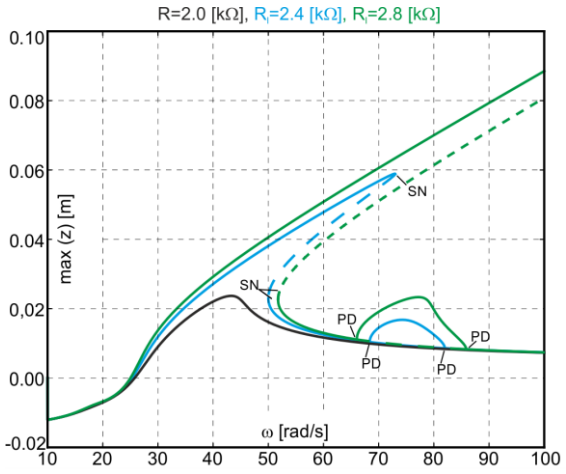

Fig. 14. Resonance curves for the various total resistances, for parameters: k=38.7N/m and A=0.014m

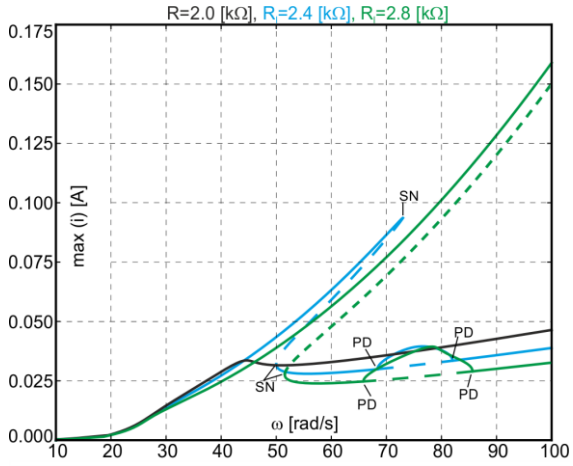

Fig. 15. Recovered current for various total resistances, for parameters: k=38.7N/m, A=0.014m

3.4. Coil inductance influence

The coil inductance L is one of the fundamental parameters describing the coil design. The L characterizes this behavior of a inductor and is defined in terms of that opposing electromotive force or its generated magnetic flux and the corresponding electric current. The inductance of a circuit depends on the geometry of the current path as well as the magnetic permeability of nearby materials. In our study assumed that the coil inductance is constant, not depends on the magnet's position during current flow. However in most coils terminals have ferromagnetic cores, therefore the inductance will vary with core reluctance, and depends on core length and cross section (and material), positioning and shape (Gomand et al., 2007).

Influence of the coil inductance is shown in Fig. 16 and Fig. 17. The black line corresponds to $\mathrm{L} = 0.1\mathrm{H}$, blue line to $\mathrm{L} = 1.46\mathrm{H}$ and green line to $\mathrm{L} = 5.0\mathrm{H}$. The small values of the inductance (usually typical in real practice) has a negligible effect on the response of the pseudo-maglev system and the energy recovery level.

The influence is visible only for the higher value of the inductance and higher frequency of excitation ($\omega > 50\mathrm{rad/s}$), where the increase of recovered energy is observable.

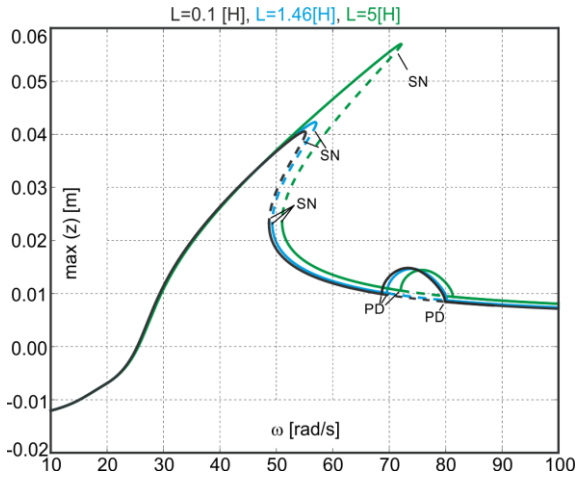

Fig. 16. Resonance curves for various coil inductance, for parameters: R=2.3kΩ, k=38.7N/m and A=0.014m

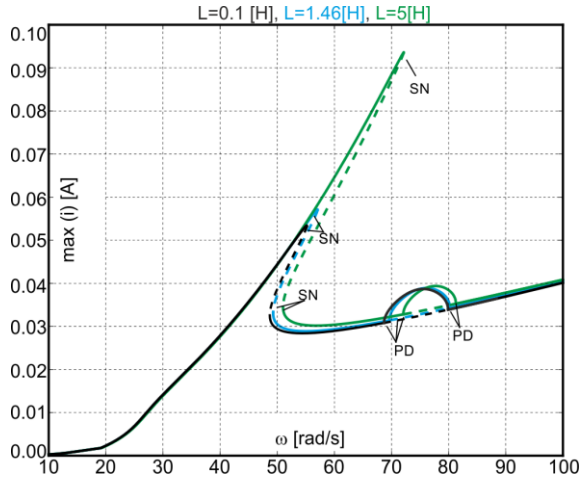

Fig. 17. Recovered current for tvarious coil inductance, for parameters: R=2.3kΩ, k=38.7N/m, A=0.014m

3.5. Coupling coefficient influence

The next studied parameter is the coupling coefficient (inductive coefficient). This parameter depends on the magnet position in the coil and construction of the harvester. However, the paper (Kecik et al., 2017b) shows, that constant coupling coefficient value can be accepted, if it is properly chosen.

The blue line shows the resonance curves obtained for $\alpha = 60\mathrm{Vs/m}$ and it is value chosen from the experiment based on the static tests and calculated from Faraday's law. If the coefficient increases, then the magnet's amplitude and the recovered energy are significantly reduced (green lines in Fig. 18 and 19). Otherwise, if the coefficient decreases, then magnet's amplitude and the recovered current have higher level and the PD region expanded. This means that α plays role of the electrical damping. Interestingly, that for the low frequency, three stable solution are observed (nearly $\omega \approx 85\mathrm{rad/s}$).

In many papers (Williams and Yates, 1996; Beeby et al., 2006; Olaru et al., 2014), the inductance L is neglected, then the coupling coefficient α is additional damping comes from the electrical circuit. Often researchers have treated the magnetic flux density as uniform over the coil volume and constant over the

DOI 10.2478/ama-2018-0002

magnet's entire range of motion and this factor depends on the magnitude of the magnetic flux and the length of wire composing the coil (Mitcheson et al., 2004; Mitcheson, 2005; Bedekar, 2009).

The new model of the coupling coefficient and compared it with the classical approach is presented in paper (Kecik et al., 2017b).

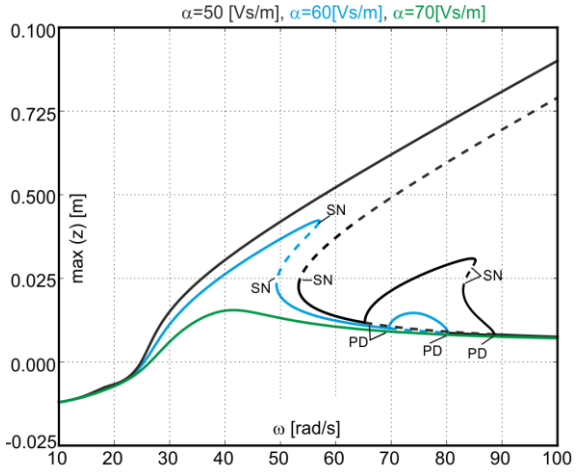

Fig. 18. Resonance curves for various coupling coefficient, for parameters: R=2.3kΩ, k=38.7N/m, A=0.014m

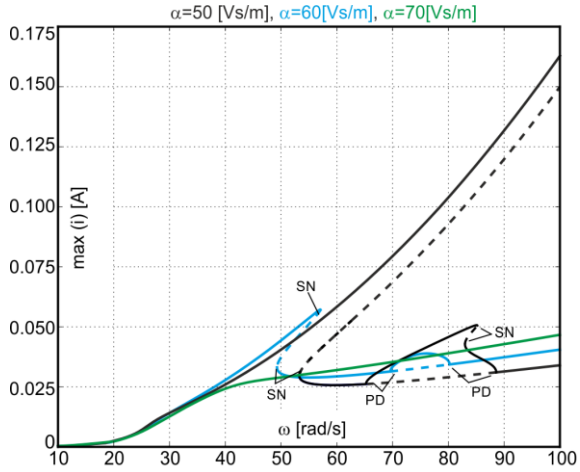

Fig. 19. Recovered current for various coupling coefficient, for parameters: R=2.3kΩ, k=38.7N/m, A=0.014m

4. CONCLUSIONS AND FINAL REMARKS

The paper presents numerical study of the prototype electromagnetic pseudo-levitation harvester. The influence of the main system's parameters on the recovered current and dynamics of the moving magnet have been presented.

The obtained results show interesting behaviour especially for the higher level of excitation, like the stability loss, the period doubling bifurcation and the attractor coexistence. The maximal recovered current equals about $\mathrm{i} = 0.17\mathrm{A}$, what corresponds to the power about $\mathrm{P} = 66\mathrm{W}$.

The load resistance and the coupling coefficient similarly influence on the system's response, causes bending the resonance curves (hardening behaviour) and the foldover effect is observed. The coupling coefficient strongly influences on the recovered current level, therefore should be proper estimated.

For the higher frequency, the coexistence or two or more periodic solutions are possible. The coexistence of solution is promising from the energy harvesting point of view, because one solution (top branch) recover even six times more energy.

The electrical parameters of the pseudo-maglev harvester system can be applied to energy harvesting of small devices and the magnet's vibration control.

The next step will be experimental verification of the obtained results and elaboration the control methods to jump from the lower to high energy input solution. Additionally, the optimization problem will be studied.

REFERENCES

1. **Bedekar V., Oliver J., Priya S.** (2009), Pen harvester for powering a pulse rate sensor, *Journal of Physics D: Applied Physics*, 42(10), 105105.
2. **Beeby S., Tudor M., White N.** (2006), Energy harvesting vibration sources for microsystems applications, *Measurement Science and Technology*, 17(12), 175-195.
3. **Beeby S.P., Torah R.N. Tudor M.J.** (2008), Kinetic energy harvesting. *ACT Workshop on Innovative Concepts. ESA-ESTEC*, 17, 1-10.
4. **Doedel E., Oldeman B.** (2012), Auto-07p: Continuation and bifurcation software for ordinary differential equations, *Concordia University, Montreal*, 1–266.
5. **Earnshaw S.** (1842). On the nature of the molecular forces which regulate the constitution of the luminiferous ether, *Transactions of the Cambridge Philosophical Society,* 7, 97–112.
6. **Gomand J., Remy G., Tounzi A., Barre P.J., Hautier J.P.** (2007), Impact of permanent magnet field on inductance variation of a PMLSM, European *Conference on Power Electronics and Applications*, 1-10.
7. **Jonnalagadda A.S.** (2007) *Magnetic induction systems to harvest energy from mechanical vibrations*, PhD thesis, Massachusetts Institute Engineering.
8. **Joyce S.** (2011) *Development of an electromagnetic energy harvester for monitoring wind turbine blades*, PhD thesis, Virginia Polytechnic.
9. **Kecik K.** (2015) Dynamics and control of an active pendulum system, *International Journal of Non-linear Mechanics*, 70, 63-72.
10. **Kecik K., Brzeski P., Perlikowski P.** (2017a) Non-linear dynamics and optimization of a harvester absorber system, *International Journal of Structural Stability and Dynamics*, 17(9), 1-15.
11. **Kecik K., Mitura A.** (2016), Nonlinear dynamics of a vibration harvest-absorber system. Experimental Study, *Springer Proceedings in Mathematics & Statistics, Dynamical Systems: Modelling*, 181, 197-208.
12. **Kecik K., Mitura A., Lenci S., Warminski J.** (2017b), Energy harvesting from a magnetic levitation system, *International Journal of Non-linear Mechanics*, 94, 200-206.
13. **Li Y.J., Dai Q., Zhang Y., Wang H., Chen Z., Sun R.X., Zheng J., Deng C.Y., Deng Z.G.** (2016), Design and analysis of an electromagnetic turnout for the superconducting Maglev system Physica C: *Superconductivity and its Applications*, 528, 84-89.
14. **Mann B., Sims N.** (2010), On the performance and resonant frequency of electromagnetic induction energy harvesters, *Journal of Sound and Vibration*, 329(1-2), 1348–1361.
15. **Mann B.P. Sims N.D.** (2009), Energy harvesting from the nonlinear oscillations of magnetic levitation, *Journal of Sound and Vibration*, 319(1-2), 515–530.
16. **Mann B.P., Owens B.A.** (2010), Investigations of a nonlinear energy harvester with a bistable potential well, *Journal of Sound and Vibration* 329, 1215-1226.
17. **Mitcheson P.D.** (2005), *Analysis and optimisation of energy-harvesting micro-generator systems*, University of London.

DOI 10.2478/ama-2018-0002

18. **Mitcheson P.D., Green T.C., Yeatman E.M., Holmes A.S.** (2004), Architectures for vibration-driven micropower generators, *Journal of Microelectromechanical Systems*, 13(3), 429-440.
19. **Olaru R., Gherca R., Petrescu C.** (2014), Analysis and design of a vibration energy harvester using permanent magnets, *Revue Roumaine des Sciences Techniques - Serie Electrotechnique*, 59(2), 131–140.
20. **Qian N., Zheng B., Gou Y., Chen P., Zheng J., Deng Z.** (2015), Study on the effect of transition curve to the dynamic characteristics of high-temperature superconducting maglev, *Physica C: Superconductivity and its Applications*, 519, 34-42.
21. **Soares S.M.P., Ferreira J.A.F., Simoes J.A.O., Pascoal R., Torrao J., Xue X., Furlani E.P.** (2016), Magnetic levitation-based electro-magnettic energy harvesting: a semi-analytical non-linear model for energy transduction, *Scientific Reports* 6, Article ID 18579.
22. **Sun R., Zheng J., Zheng B., Qian N., Li J., Deng Z.** (2018), New magnetic rails with double-layer Halbach structure by employing NdFeB and ferrite magnets for HTS maglev, *Journal of Magnetism and Magnetic Materials*, 445, 44-48.
23. **Williams C., Yates R.** (1996), Analysis of a micro-electric generator for microsystems, *Sensors and Actuators A: Physical,* 52 (1-3) 8–11.
24. **Zhou D, Yu P., Wang L, Li J.** (2017), An adaptive vibration control method to suppress the vibration of the maglev train caused by track irregularities, *Journal of Sound and Vibration*, 408(10), 331-350.
25. **Zhu H., Khiang Pang Ch., Joo Teo T.** (2017), Analysis and control of a 6 DOF maglev positioning system with characteristics of end-effects and eddy current damping, *Mechatronics*, 47, 183-194.

Acknowledgments: This work was financially supported under the project of National Science Centre according to decision no. DEC-2013/11/D/ST8/03311.

DE GRUYTER
OPEN

DOI 10.2478/ama-2018-0003

acta mechanica et automatica, vol.12 no.1 (2018)

MEASUREMENT OF AIR SPRINGS VOLUME USING INDIRECT METHOD IN THE DESIGN OF SELECTED PNEUMATIC DEVICES

Matej URBANSKÝ[*], Jaroslav HOMIŠIN[*], Peter KAŠŠAY[*], Jozef KRAJŇÁK[*]

[*]Faculty of Mechanical Engineering, Technical University of Košice, Letná 9, 040 01, Košice, Slovakia

matej.urbansky@tuke.sk, jaroslav.homisin@tuke.sk, peter.kassay@tuke.sk, jozef.krajnak@tuke.sk

received 14 April 2016, revised 27 February 2018, accepted 2 March 2018

Abstract: At our department, we deal with continuous tuning of torsional oscillating mechanical systems (TOMS) during their operation in terms of torsional oscillation size. Therefore, a new mobile mechanical system was built for purposes of research and presentation of the TOMS continuous tuning using extremal control method, which main advantage is that we do not need to know a mathematical model of the mechanical system. The new mobile device is equipped with a special compressed air distribution system, which important components are air springs. The air springs are modified and used as air pressure tanks with various functions in the mobile device. Therefore, it is important to know the magnitude of the air springs inner volume. This paper deals with determination of air springs volume using indirect method, which is based on the air pressure measurement and also the comparison of obtained results with the results computed from air springs manufacturer data.

Key words: Air Tank Volume Determination, Indirect Method, Air Pressure Measurement

1. INTRODUCTION

At our department, we deal for a long time with tuning and continuous tuning of torsional oscillating mechanical systems (TOMS) during their operation in terms of torsional oscillation size (Homišin, 2002, 2014; Homišin and Kaššay, 2014; Grega, 2014). For the TOMS with continuous tuning during their operation we use pneumatic flexible shaft couplings (pneumatic torsional oscillation tuners, thereinafter „pneumatic tuners“) developed in our department. Torsional stiffness of the pneumatic tuners can be changed by air pressure adjusting in their pneumatic elements.

Resonances from individual harmonic components of excitation (Fig. 1) can be ejected from operational speed range (OSR) of the mechanical system by suitable value of torsional stiffness k ($k_2 < k_1 < k_3$) and herewith the value of dynamic component MD of transmitted load torque can be reduced (Dresig and Holzweißig, 2007; Baworski et al., 2015; Czech et al. 2014; Czech, 2014; Haľko and Pavlenko, 2012; Handrik et al., 2014; Łazarz et al., 2009; Sapietová and Dekýš, 2016; Wojnar, 2010).

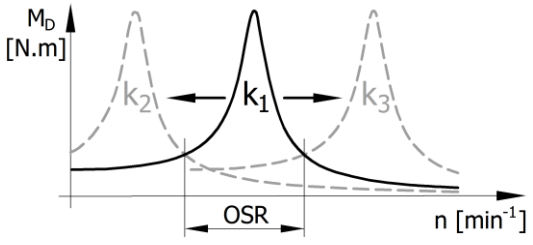

Fig. 1. Mechanical system tuning principle

One of the continuous tuning methods is the application of extremal control – experimental optimization, which main advantage is that we do not need to know a mathematical model of the mechanical system. The extremal control gives us the possibility to minimize the value of dangerous torsional vibration in the TOMS during their operation by adapting the dynamic properties of the system to actual operating parameters and failures (Homišin, 2002, 2014; Homišin and Kaššay, 2014).

Therefore, the new mobile mechanical system (Fig. 2) was built for research and presentation of the TOMS with continuous tuning using extremal control method. The new mobile device is equipped with a special compressed air distribution system, which important components are air springs. Air springs have wide range of use (Kohl and Pešík, 2016; Pešík and Němeček, 1997; Sturm and Pešík, 2017). In this case, the air springs are modified and used as air pressure tanks with various functions in the mobile device. Therefore, it is important to know the magnitude of the air springs inner volume. This paper deals with determination of air springs volume using indirect method, which is based on the air pressure measurement and also the comparison of obtained results with the results computed from air springs manufacturer data.

2. DESCRIPTION OF THE NEWLY BUILT MOBILE MECHANICAL SYSTEM

In Fig. 2 we can see that the basic part of this newly built mobile device is a torsional oscillating mechanical system (TOMS). This TOMS consists of 3-phase asynchronous electromotor MEZ 4AP132M-4 (nominal power 7.5 kW at 1450 min^{-1}) (1), whose rotation speed is continuously vector-controlled by the frequency converter Sinamics G120C (2). Electromotor drives the 3-cylinder piston compressor ORLIK 3JSK-75 (3) through the pneumatic tuner of type 4-2/70-T-C (4). The compressor has no flywheel;

DOI 10.2478/ama-2018-0003

hence it has a higher dynamic impact. The mentioned TOMS is situated on a rigid frame, which is flexibly mounted on a mobile platform (5). The next component situated on the mobile platform is the electronic extremal control system called ESLER (6) and its accessories (e.g. sensors, actuators, etc.). Current level of the ESLER function is in detail described in Homišin and Urbanský, (2015).

The main part of the mobile platform (5) is the special compressed air distribution system (in detail described in Urbanský and Kaššay, 2015), which important components are four air springs of type Rubena 340/3 (Fig. 3). These modified air springs, used as air pressure tanks, have the following functions:

- a compressed air storage for the pneumatic tuner inflation – 3 interconnected air springs,
- compressor delivery pipe volume compensation for properly adjustment of compressor delivery pressure and thereby also TOMS load – 1 air spring.

Fig. 2. The newly built mobile device for extremal control presentation: 1 – electromotor MEZ 4AP132M-4, 2 – frequency converter Sinamics G120C, 3 – piston compressor ORLIK 3JSK-75, 4 – pneumatic tuner 4-2/70-T-C, 5 – mobile platform, 6 – electronic extremal control system

Fig. 3. The mobile platform with 4 air springs Rubena 340/3

3. COMPUTATION OF THE AIR SPRINGS VOLUME FROM MANUFACTURER DATA

The following data were available for air springs volume computation (Rubena, 2016):

- air spring volume V_{Hstat} at static height H_{stat} (installation height); V_{Hstat} = 14900 cm^3 = 0.0149 m^3;
- theoretic force-stroke dependencies at constant air pressures in the air spring.

For our purposes, in Fig. 4 we can see that the stroke S equals to zero at minimal operating height H_{min}; and S = 200 mm at maximal operating height H_{max}.

In Fig. 5 we can see the dependence of the effective area of the air spring A_{ef} on the air spring stroke S, obtained from above mentioned theoretic force-stroke dependence at constant air pressure in the air spring. This dependence can be described with the following polynomial:

$$A_{ef} = -0.6438 \cdot S^2 - 0.0564 \cdot S + 0.0726 \ . \tag{1}$$

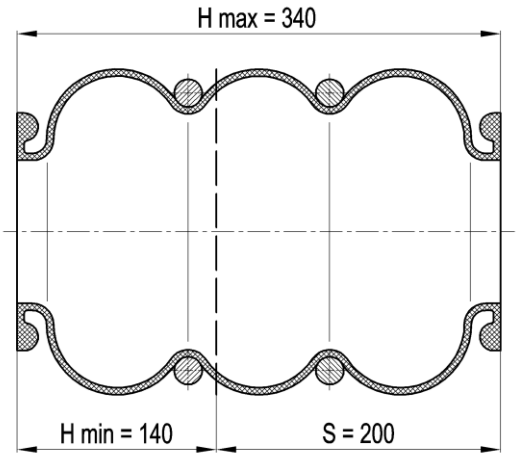

Fig. 4. The air spring stroke

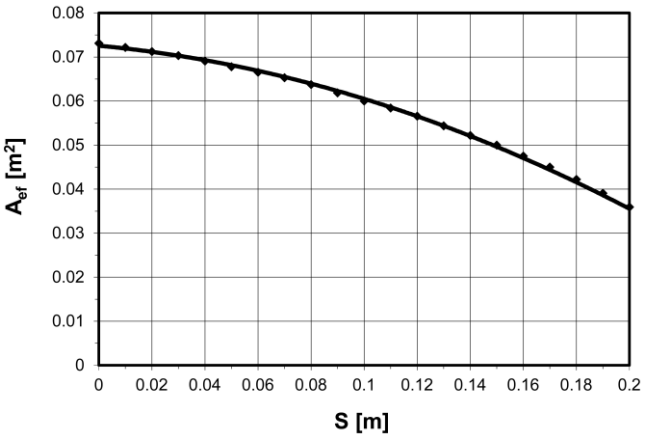

Fig. 5. The dependence of the effective area of the air spring A_{ef} on the air spring stroke S

The axial force F of air spring at its certain stroke can be computed as follows:

$$F = p_p \cdot A_{ef} \ \text{[N]} \ , \tag{2}$$

where p_p [Pa] is an air overpressure in the air spring. Axial stroke of the air spring dS causes an air spring inner volume change dV.

The relation between the mechanical work of axial force and the work of compressed air inside the air spring is defined as follows:

$$F dS = p_p dV. \tag{3}$$

Using a substitution of equation (2) in equation (3) and additional modification of equation (3) we obtain following equation (4):

DOI 10.2478/ama-2018-0003

$$A_{ef}dS = dV \Rightarrow V = \int_0^S A_{ef}dS \ . \tag{4}$$

Using a substitution of equation (1) in equation (4) we obtain the following equation (5) for the air spring volume computation:

$$V = -\frac{1}{3}\cdot 0.6438\cdot S^3 - \frac{1}{2}\cdot 0.0564\cdot S^2 + 0.0726\cdot S + C \ , \tag{5}$$

where an integration constant C = 0.00814 is computed so that air spring volume V_{Hstat} = 0.0149 m³ is at static height H_{stat}.

4. DETERMINATION OF THE AIR SPRINGS VOLUME USING INDIRECT METHOD

In our case, all air springs are installed to maximal installation height H_{max} (Fig. 4). From equation (5) we can compute that in our case, the 1 air spring volume value is V_{Hmax} = 0.01986 m³.

In praxis we observe that with increasing air pressure in air spring at constant stroke, the rubber-textile coat of the air spring stretches up to a certain point. It results in the air spring volume which increases with increasing air pressure in the air spring.

We also have used an indirect method for the determination of air springs volume. This method is based on the air pressure equalization between known and unknown volume, whereby isothermal process was considered (Klenovčanová, 2007).

As the known volume was chosen air pressure tank (1) with inner volume of 0.3 m³ (300 l) (Fig. 6).

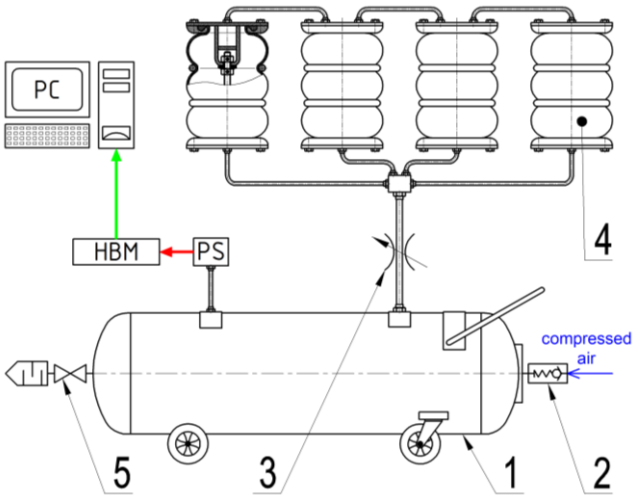

Fig. 6. Devices used for measurement: 1 – pressure tank, 2 – backflow valve, 3 – throttle valve, 4 – air spring, 5 – ball lock valve

Compressed air streams into the pressure tank through backflow valve (2) and it can be deflated using a ball lock valve (5). Four air springs (4) are interconnected and connected with the pressure tank through delivery piping with throttle valve (3). Pressure sensor (PS) (type Meret TSZ, measuring range 0 to 1 MPa, combined fault – linearity, hysteresis and reproducibility = 0.1% of measuring range, in our case 1 kPa) (Meret, 2017) senses air pressure value in the pressure tank and the measuring equipment HBM Quantum X sends a data to PC.

The measurement principle scheme is shown in Fig. 7. From the figure results the following equations:

$$V = V_1 + V_2 \ ; \ V = V_1' + V_2' \ ; \ V_1 + V_2 = V_1' + V_2' \ , \tag{6}$$

$$p_1 \cdot V_1 = p \cdot V_1' \ ; \ p_2 \cdot V_2 = p \cdot V_2' \ ; \ V_1 + V_2 = \frac{p_1}{p}\cdot V_1 + \frac{p_2}{p}\cdot V_2 \tag{7}$$

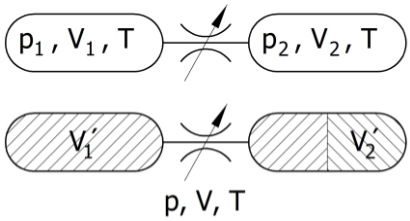

Fig. 7. Scheme of measurement principle

By modification of equation (7) we obtain the following equations:

$$V_1 \cdot \left(1 - \frac{p_1}{p}\right) = V_2 \cdot \left(\frac{p_2}{p} - 1\right) \ ; \ V_1 \cdot \left(\frac{p - p_1}{p}\right) = V_2 \cdot \left(\frac{p_2 - p}{p}\right), \tag{8}$$

$$V_2 = V_1 \cdot \left(\frac{p - p_1}{p_2 - p}\right) , \tag{9}$$

$$V_2 = V_1 \cdot \left(\frac{p_p + p_a - p_{p1} - p_a}{p_a - p_p + p_a}\right) , \tag{10}$$

where p_p [Pa] is an air overpressure after air pressure equalization, p_{p1} [Pa] is an air overpressure in the pressure tank, p_a [Pa] is atmospheric pressure (101325 Pa), V_1 is inner volume of the air pressure tank (0.3 m³), V_2 is inner volume of the four interconnected air springs and piping. By modification of equation (10) we obtain the following equation:

$$V_2 = V_1 \cdot \left(\frac{p_{p1} - p_p}{p_p}\right) . \tag{11}$$

In order to maximize measurement accuracy, it is advisable to observe the following rules:

- the whole measurement device should be pressure-tight as good as possible (i.a. Scully, 2015),
- considering the isothermal process, it is important to wait long enough for p_p and p_{p1} values consolidation (Abbas et al., 2011; Massey, 2006),
- it is necessary to use very accurate pressure sensor,
- it is necessary to know the accurate value of known volume.

In Fig. 8 we can see the results of realized measurements. It was executed 9 measurements at p_{p1} = 400, 450, 500, 550, 600, 650, 700, 750 and 800 kPa. The volume of 1 air spring V_{Hmax} at maximal installation height H_{max} is computed without the piping volume. In the figure we can see that the value of V_{Hmax} increases degressively with increasing p_p values according to equation:

$$V_{H\max} = -8.463\cdot 10^{-6}\cdot p_p^2 + 1.207\cdot 10^{-2}\cdot p_p + 15.256 \ . \tag{12}$$

This fact is probably caused by extensibility of the air springs rubber-textile coat in radial direction, because the air spring is rigid in axial direction.

DOI 10.2478/ama-2018-0003

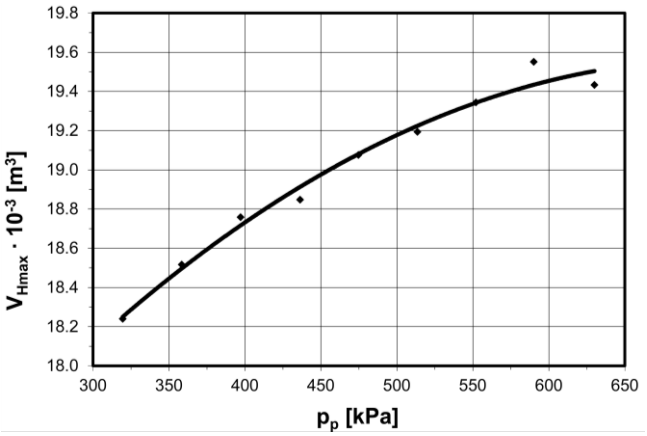

Fig. 8. One air spring volume value V_{Hmax} dependent on air overpressure p_p in the air spring.

5. CONCLUSIONS

Comparing the air spring volume values we can see that values of V_{Hmax} shown in Fig. 8 approximate at higher p_p values to the reference value $V_{Hmax} = 0.01986$ m^3 computed from equation (5). All by us measured values of V_{Hmax} are smaller than the reference value. This is probably caused by the facts that inside of our air springs are in addition excessive stroke prohibitive components.

The accuracy of measured results is difficult to evaluate, because we have not accurate results measured by another method and the volume of air springs is not constant, as we can see at air springs inflation. Therefore, it is advisable to verify the accuracy of given method by measuring of both known volumes.

In order to maximize measurement accuracy, it is advisable to observe the rules mentioned in previous chapter 4. We could say that these rules are simultaneously disadvantages of the given measurement method. Advantage of the method is that we could determine approximate (inner) volume of intricate shaped objects.

REFERENCES

1. **Abbas R., Ihmels C., Enders S., Gmehling J.** (2011), Joule–Thomson coefficients and Joule–Thomson inversion curves for pure compounds and binary systems predicted with the group contribution equation of state VTPR, *Fluid phase equilibria,* 306, 181-189.
2. **Baworski A., Garbala K., Czech P., Witaszek K.** (2015), Estimation of the ability to use a mass of air from a moving vehicle in wind turbine propulsion, *Scientific Journal of Silesian University of Technology, Series Transport,* 88, 5-17.
3. **Czech P.** (2014), Conception of use vibroacoustic signals and neural networks for diagnosing of chosen elements of internal combustion engines in car vehicles*, Scientific Journal of Silesian University of Technology, Series Transport,* 82, 51-58 (in Polish).
4. **Czech P., Wojnar G., Burdzik R., Konieczny Ł., Warczek J.** (2014), Application of the discrete wavelet transform and probabilistic neural networks in IC engine fault diagnostics, *Journal of Vibroengineering*, 16, 1619-1639.
5. **Dresig H., Holzweißig F.** (2007), *Dynamics of Machines,* Springer, Berlin Heidelberg (in German).
6. **Grega R.** (2014), Examination of applicated pneumatic flexible coupling and its effect on magnitude of vibrations in drive of belt conveyer, *Scientific Journal of Silesian University of Technology. Series Transport*, 85, 21-25.
7. **Haľko J., Pavlenko S.** (2012), Analytical suggestion of stress analysis on fatigue in contact of the cycloidal - vascular gearing system, *Scientific Journal of Silesian University of Technology. Series Transport*, 76, 63-66.
8. **Handrik M., Vaško M., Kopas P., Sága M.** (2014), Effective finite element solution and post-processing for wide load spectrum, *Communications,* 16(3A), 19-26.
9. **Homišin J.** (2002), *New types of pneumatic flexible shaft couplings: development, research, application,* Vienala, Košice (in Slovak).
10. **Homišin J.** (2014), New methods for tuning of mechanical systems during operation in steady state, *Scientific Journal of Silesian University of Technology. Series Transport*, 85, 49-55.
11. **Homišin J., Kaššay P.** (2014), Experimental verification of the possibility using pneumatic flexible shaft couplings for the extremal control of torsional oscillating mechanical system, *Diagnostyka*, 15(2), 7-12.
12. **Homišin J., Urbanský M.** (2015), Partial results of extremal control of mobile mechanical system, *Diagnostyka*, 16(1), 35-39.
13. **Klenovčanová A.** (2007), *Thermomechanics,* Faculty of mechanical engineering, Technical University of Košice (in Slovak).
14. **Kohl O, Pešík L.** (2016), Evaluation of a driver's seat's dynamic properties, *Scientific Journal of Silesian University of Technology. Series Transport*, 91, 59-69.
15. **Łazarz B., Wojnar G., Madej H., Czech P.** (2009), Evaluation of gear power losses from experimental test data and analytical methods, *Mechanika*, 80(6), 56-63.
16. **Massey, B.** (2006), *Mechanics of fluids,* Taylor and Francis, London.
17. **Meret** (2017), Pressure transmitters type TSZ with a sensor with metal diaphragm. Accessed: 13.04.2016. Available at: http://www.meret.sk/en/produkty/meranie-tlaku/snimace-tlaku/snimace-tlaku-typu-tsz/
18. **Pešík L., Němeček P.** (1997), Monitoring of vibration of machines with an elastic support, *Insight*, 39, 566-568.
19. **Rubena** (2016)**,** Rubber-textil products, air springs. Accessed: 31.03.2016. Available at: http://www.rubena.cz/air-springs/t-659/.
20. **Sapietová A., Dekýš V.** (2016) Dynamic analysis of rotating machines in MSC.ADAMS, *Procedia Engineering*, 136, 143-149.
21. **Scully, L.** (2015)**,** Make pneumatic connections air tight. Accessed: 13.04.2016. Available at: http://www.hydraulicspneumatics.com/fittings-couplings/make-pneumatic-connections-air-tight/
22. **Sturm M., Pešík L.** (2017), Experimental determination and simulation of spring-tensions under working conditions of a vibrating bowl feeder, *Acta Mechanica et Automatica*, 11, 243-246.
23. **Urbanský M., Kaššay, P.** (2015), The new realized mobile device for extremal control research and presentation, *Scientific Journal of Silesian University of Technology. Series Transport*, 89, 173-178.
24. **Wojnar G.** (2010), Using of torsional vibrations velocity for the detection of toothed wheels' fault, *Scientific Journal of Silesian University of Technology. Series Transport*, 66, 123-128.

This paper was written in the framework of grant projects: VEGA 1/0473/17 "*Research and development of technology for homogeneous charge self-ignition using compression in order to increase engine efficiency and to reduce vehicle emissions*", KEGA 041TUKE-4/2017 "*Implementation of new technologies specified for solution of questions concerning emissions of vehicles and transformation of them into the educational process in order to improve quality of education*" and PhD. Student's and Young Researcher 's Project: "*Solution of a control system element for mechanical systems continuous tuning*".

DE GRUYTER
OPEN

DOI 10.2478/ama-2018-0004

acta mechanica et automatica, vol.12 no.1 (2018)

CRUSHING BEHAVIOUR OF THE PVC FOAM LOADED WITH BEATERS OF VARIOUS SHAPES

Paweł BOGUSZ*, Roman GIELETA*, Marcin KONARZEWSKI*, Michał STANKIEWICZ*

*Department of Mechanics and Applied Computer Science Faculty of Mechanical Engineering, Military University of Technology
00-908 Warszawa 46, ul. Gen. Witolda Urbanowicza 2, Poland

pawel.bogusz@wat.edu.pl, roman.gieleta@wat.edu.pl, michal.stankiewicz@wat.edu.pl, marcin.konarzewski@wat.edu.pl

received 30 January 2017, revised 27 February 2018, accepted 3 March 2018

Abstract: Statistically, at least 50% of all injuries experienced by police officers in the line of duty are due to assaults with blunt objects. Therefore, vests used by the police should provide not only good ballistic resistance, but also good protection against such threats. Foamed materials are possible to be used for body protectors or inserts of protective clothes. The effects of dynamic impact with beaters of different shapes onto behaviour of polymeric foamed material were determined. There were used four types of beaters: flat, cylindrical, edgy and cornered. Strikes with blunt objects such as a flat board, baseball bat, edgy brick, pavement brick or a sharp stone, to which a protective ware can be subjected, were simulated. The impact load was applied to the rectangular specimens, made of polyvinyl chloride foam, with a usage of a drop hammer. Plots of force versus compression for all the tested samples were obtained and analysed. The effects of impacts with beaters of different shapes onto foamed material samples were presented. A shape of the blunt object significantly influences crushing behaviour of the foamed material. The impact energy of a flat beater is absorbed effectively on a short distance, since it is spread on a relatively large surface. The cylindrical and edgy beaters did not cause fragmentation of the samples, however, on the upper surfaces of the samples, permanent deformations mapping the beaters shapes as well as some cracks occurred. An impact with a sharp object, for example, a cornered beater is very difficult to be neutralized by the foam material, because it is cumulated on a small area.

Key words: Polymeric Foams, Polyvinyl Chloride Foam, Hitting With A Blunt Object, Energy Absorption, Impact Tests, Experimental Mechanics

1. INTRODUCTION

Bulletproof and knife-proof vests are manufactured for specific applications that determine their structure. Types of threats depend on the environment and a kind of service. Statistically, at least 50% of all injuries experienced by police officers in the line of duty is a consequence of attacks with blunt objects, such as a baseball bat, stone, bricks and a flat board. 35% of all injuries is due to attacks with a knife or other sharp objects, whereas only up to 15% of injuries occurs during attacks with firearms (Cook, 2008). Therefore, the vest should not only provide good ballistic resistance, but also good protection against the risks of injuries caused by attacks with a blunt object, knife or other sharp tools. The paper is focused on analysis of blunt objects impact hazards.

Typically, strong fibreglass/aramid, ultra-high-molecular-weight polyethylene (UHMWPE) and high strength-steel or ceramic-based materials are used in structures of protective clothing inserts.

Foamed materials are possible to be used materials for designing protective clothes as well as developing bulletproof and knife-proof vests. The cellular construction of the foam materials provides not only lightweight capability, but also a deformation mechanism that allows for efficient absorption of energy. Fig. 1 shows a typical curve of standard foamed aluminium obtained by compressing a cubic specimen quasi-statically along one direction. The curve exhibits three definite regions: linear elasticity, plateau and densification. At low strains, the behaviour is linear elastic, with a slope equal to the Young modulus of the foam.

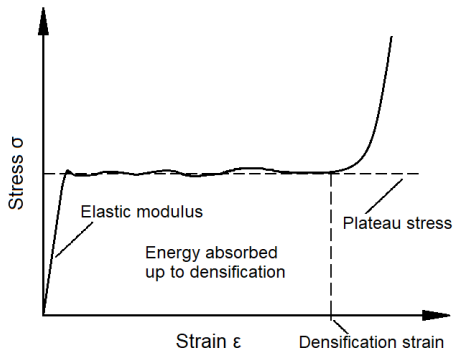

Fig. 1. The static compression curve for standard foamed material (Ashby et al., 2000; Avalle et al., 2001)

A small amount of energy is absorbed in this region. As the load increases, the foam cells begin to collapse by elastic buckling, plastic yielding or brittle crushing, depending on the mechanical properties of the cell walls (Ashby et al., 2000; Avalle et al., 2001). The most effective part of the curve is up to a so-called densification strain, for which pores of the foam are mostly closed. In this region, a stress value is approximately on a constant level or increases gradually. What allows for large energy absorption at

DOI 10.2478/ama-2018-0004

an almost constant load is a long plateau of the stress-strain curve. After closing the pores, force starts to increase rapidly, as in the case of the solid uniform material. During unloading the foam, the stress depends non-linearly on the strain (Avalle et al., 2001).

In Avalle et al. (2001), an efficiency diagram method is presented to obtain synthetic diagrams useful to characterize the material and to help design energy absorbing components for the three tested materials. The energy absorption characteristics have been examined for three polymeric foams (expanded polypropylene EPP, polyurethane foam PUR and a blend of polyamide reinforced with modified polyphenylene and polystyrene PS/PA foams). Also, the mechanical properties of the foams at room temperature have been experimentally evaluated in both static and impact loading conditions.

A polyvinyl chloride (PVC) foam is extensively used in sandwich structures as a lightweight core and is combined with different face layers, e.g. aluminium, fibre glass composite, polypropylene, plywood or others. Several studies have been undertaken to experimentally characterize the impact properties of PVC foams.

Objectives studied in Mahfuz et al. (2006) included, among others, investigation of behaviour of PVC foam materials at strain rates ranging from quasi-static to around 2000 s^{-1}. Room temperature response, strain rate sensitivities and failure characteristics have been determined for various density foams. The performed investigation showed that with the increase in the strain rate, a moderate increase in the compressive strength of the foams occurs. At quasi-static and high strain rate regimes, the increased temperature led to degradation of strength and stiffness. This degradation, however, increased with the density of the core (Mahfuz et al., 2006).

In paper Zhang et al. (2012), a methodology for characterising the elastic properties of Divinycell PVC H100 foam at elevated temperatures is proposed. The focus is on determination of reliable values of the tensile and compressive moduli and Poisson's ratio based on the strain data obtained using digital image correlation (DIC). The design of the specimens and loading jigs are developed and assessed in terms of introduction of the uniform strain. The tests conducted at elevated temperatures ranging from 20°C to 90°C showed that the material is highly anisotropic with stiffness of 50% less in the plane of the foam sheet compared to the through thickness direction. A nonlinear reduction in Young's modulus is obtained with a significant degradation occurring above 70°C, losing more than half of the room temperature stiffness – 130 to 55 MPa at 90°C. The Poisson's ratio remains stable at different temperatures – 0.43 on average (Zhang, 2012).

The uniaxial compressive responses of two PVC foams (Divinycell H100 and H250) and balsa wood ProBalsa LD7 have been measured within strain rates ranging from 10^{-4} s^{-1} to $4x10^{3}$ s^{-1}. These materials are extensively used as cores for composite light-weight structures capable of providing impact and blast protection. The high strain rate compression tests were performed using a Split Hopkinson Pressure Bar. The compressive yield strength of the H250 PVC foam and balsa wood doubles when the strain rate is increased from quasi-static rates to rates in the order of $10^{3}s^{-1}$. In contrast, the H100 PVC foam displays only a small elevation in uniaxial compressive strength (about 30%) for the same increase in the strain rate (Tagarvielli et al., 2008).

Divinycell PVC H100 foam was also the subject of the research in papers (Chen and Hoo Fatt, 2013; Hoo Fatt and Chen, 2015; Hoo Fatt et al., 2017). In Chen and Hoo Fatt (2013), cyclic material tests were done to obtain both out-of-plane and in-plane compression and shear material properties after foam yielding. The ratio of out-of-plane to in-plane stiffness and yield strength for the PVC H100 was found to be approximately 3/2 in both the compression and shear modes. After viscoplastic yielding, the foam underwent permanent damage and exhibited hysteresis, mainly in the form of viscoelasticity.

A phenomenological constitutive model for Divinycell PVC H100 foam undergoing crushing and hysteresis under cyclic compression loading was developed in Hoo Fatt and Chen (2015). The PVC H100 foam exhibited strain-rate dependency of a damage mode and hysteresis. The damage that occurred in the foam after yielding was fixed at a given strain amplitude and progressed with increasing the strain amplitude (the pattern of Mullins). A damage initiation criterion based on critical compressive strain was proposed. A standard model, an elastic spring in parallel with Maxwell element, was used to describe viscoelastic behaviour before and after damage.

In Hoo Fatt et al. (2017), a precise constitutive foam model, which can be used to predict crushing behaviour, energy absorption and damping properties of structural polymeric foams, was developed. To determine the multi-axial, elastic-plastic and hysteresis characteristics of Divinycell PVC H100 foam, several experiments was carried out. The foam exhibited elastic-plastic response followed by viscoelastic hysteresis in compression, shear and combined compression and shear. A Tsai-Wu plasticity model, including combined kinematic and isotropic hardening, was developed to accurately describe multiaxial yielding of the foam.

Plasticized PPVC is widely utilized, for example, in automotive industry, as part of an energy absorbing structure of a car body. In Bernard et al. (2015), an influence of a wide range of strain rate on the mechanical response and mechanical properties of PPVC composed of 50% of PVC, 40% of plasticizers and 10% of additives was investigated using normalized thicknesses of different samples: 1.0, 1.25 and 1.5. The experimental results indicate that the mechanical properties, especially at high strain rates, are different for the various thicknesses. Considering all the investigations, the elastic modulus and yield stress are greater for the higher thickness (Bernard et al., 2015).

In Loung et al. (2013), a set of closed-cell polyvinyl chloride (PVC) foams with different densities is studied for compressive response. The results show that the mechanical properties depend on the foam density and are strain rate sensitive. The compressive strength and modulus increase with the foam density. Similarly to other publications, it has been found that within the quasi-static strain rate regime, compressive strength of PVC foams at $10^{-1}s^{-1}$ can be up to 50% higher than at $10^{-4}s^{-1}$. At strain rates of 2000 s^{-1}, the strength can be 200% higher than the quasi-static values noted at $10^{-4}s^{-1}$. The peak and plateau strengths are dependent on the foam density. Foams with higher density provide better properties. The absence of experimentally measured mechanical properties in the intermediate strain rate range of 1–500 s^{-1} is observed for PVC foams. The main failure mechanisms are buckling and plastic deformation of cell walls leading to foam compaction. Cell wall buckling is clearly observed in high density foams, whereas low density foams demonstrate wrinkling and stretching of cell faces (Loung et al., 2013).

To support development of sandwich composite failure models, a series of PVC material tests were performed in Loup et al. (2005) to characterize foam core material response under quasi-static and dynamic tension loading. Material stress-strain response was found to be highly nonlinear and dependent on the

DOI 10.2478/ama-2018-0004

loading orientation relative to the axis of the foam sheet. At low to moderate strain rates, less than 150 s^{-1}, tension strength and modulus increased, whereas ultimate strain at failure decreased (Loup et al., 2005).

The failure behaviour of a PVC closed-cell cellular foam under a multiaxial state of stress was investigated in Gtoutos et al. (2001). The uniaxial compressive, tensile, and shear stress-strain curves along the in-plane and through-the-thickness directions were obtained. A series of multiaxial tests including strip, thin-wall ring and thin-wall tube specimens under combined tension/compression, torsion, and internal pressure was performed. As a result of these tests, biaxial strength in the in-plane and through-the-thickness directions was obtained. The results were in good agreement with the Tsai-Wu failure criterion (Gtoutos et al., 2001).

The aim of the paper is to determine the crushing resistance of rectangular samples of HEREX C70.130, made of polyvinyl chloride closed-cell foam, to the effects of impact with blunt objects of different shapes. This core material is intended to be used for many lightweight sandwich structures subjected to dynamic or static loads. The material may be used for rotor blades and turbine generator housings in wind turbines, in the structure of skis, snowboards or surfboards, fuselage, wing and interiors of aircrafts, and others (Alan Composites, 2016). Closed-cell foams are used in marine vessels and ground transportation applications due to their compressive energy absorption capabilities, especially, as a core material in sandwich composites (Luong et al., 2013).

Tab. 1. Material properties for HEREX C70.130 foamed material (Alan Composites, 2016)

Average properties	Norm	Units	Value
Tensile strength in the plane	DIN 53455	MPa	3.8
Tensile modulus in the plane	DIN 53457	MPa	115
Compressive strength perpendicular to the plane	ISO 844	MPa	2.6
Compressive modulus perpendicular to the plane	DIN 53421	MPa	155
Shear strength	ISO 1922	MPa	2.3
Shear modulus	ASTM C393	MPa	50

The detailed material strength properties for the HEREX C70.130 foamed material are presented in Tab. 1. The material is described as a rigid, closed-cell foam. It is characterised with a high stiffness and a strength to weight ratio. The foam is used as a core material for lightweight sandwich structures (Alan Composites, 2016) and provides great resistance to chemicals. It does not absorb water and it's purchasing cost is relatively low.

The tactical and technical assumptions of the protective clothes are based on the adequate standards. There are many standards for the classification of soft and hard ballistic performance. The primary task of ballistic inserts is to stop the projectile. The second issue is to limit deflection of the body armour, which can cause non-penetrating injuries to internal organs, referred to as a blunt trauma. The vests, especially for uniformed services, should also protect from knife blades, needle-shaped objects, shrapnel, and blunt heavy objects.

Typical standards present tests for verification of ballistic performance. The most popular is the US National Bureau of Justice's NIJ standard 0101.06 (2008) and NIJ standard 0101.04 (2000). The NIJ standard has been developed primarily for users of uniformed services, not military ones and, therefore, it is specific to pistol-type hazards. It divides the ballistic protection into five classes of resistance - Level IIA, II, IIIA, III, IV. The latest version of 2008 is NIJ 0101.06 standard (2008) and is very restrictive, especially in terms of a test run and an expensive certification procedure, therefore, most manufacturers make their ballistic protection products in compliance with the earlier NIJ 0101.04 standard (2000). According to level IIIA, for the new soft ballistic test, resistance to 9 mm is performed using Parabellum bullet with a lead core weighted 8 g and a impact speed of 436 m/s or with 0.44-inch Magnum bullet with a mass of 15.6 g and impact speed of 436 m/s. The maximum deflection arrow can be up to 44 mm.

In the MIL-STD-622F (1997) standard, the FQ/PD 07-05 specification, the ballistic resistance of the soft panels was set to withstand impact of three 9 mm Parabellum FMJ bullets with a mass of 8.0 g fired at 464.2 m/s. Maximal deflection of the material after the impact is allowed to be 44 mm.

The Polish Ballistic Standard PN-V-87000:2011 (2011) was developed based on STANAG 2920 adopted by NATO. According to K2 level, bulletproof performance can be verified by measuring resistance to a 7.62x25 mm lead core bullet fired from TT gun. The maximum deflection arrow may be 40 mm, which is more restrictive than the American standards.

The second parameter, according to which the vests are tested, is the shrapnel resistance verifying whether the cover stops a so-called "standard shrapnel" with a mass of 1.10 g at different speeds. For example, according to PN-V-87000, the O3 class of shrapnel resistance, defines a standard shrapnel as a 1.1 g fragment with speed from 600 to 675 m/s. This also conforms to the NATO standard STANAG 2920.

In standard MIL-STD-622F (1997), restrictions were set to stop fragments of weight from 0.12 g to 1.01 g moving at a speed of 563.8 to 826 m/s.

The basis for the resistance against knife and/or spike piercing is the NIJ Standard-0115.00 (2000), Stab Resistance of Personal Body Armor (2000), which describes a research method for the stab resistance of ballistic packages. According to this standard, a free-falling sabot system, with a knife blade or spike attached, strikes the ballistic package lying motionless on a deformable surface. The protection level 2 defines the sabot kinetic energy to be 33 J with maximum penetration of 7 mm or 50 J with maximum penetration of 20 mm, in both cases for striking angles of 90° or 45°. Piercing-by-needle resistance is evaluated with a needle-shaped arrow blown at a speed of more than 50 m/s, from a distance of 5 m.

Blunt and/or heavy objects resistance, which is the scope of this article, is the subject of the British Standard BS 7971-8 (2003). The standard presents guidelines for protective clothing and equipment performance to be used in violent situations. It adopts a value of 20 J for impact energy as a basis for the research. An average value of the transferred force should not exceed 4 kN and none of the individual forces should exceed 6 kN.

The next standards presented are not directly related to the military or even non-military uniformed services, however, they contain guidelines for protection of body parts from different injuries.

The Polish PN-EN 1621-2: 2014-03 (2014): Motorcyclists' protective clothing against mechanical impact – Part 2: Motorcyclists' back protectors – Requirements and test methods is based on the EU standard EN 1621-2: 2014. The document sets the loading energy at the level of 50 J with accuracy of ±1.5 J. The beater

DOI 10.2478/ama-2018-0004

mass is set to 5000±50 g. Therefore, the impact energy is greater than in the case of BS 7971-8 standard. The standard proposes two protection levels. Protection level 1: the average value of transmitted force not greater than 18 kN, single impact force not greater than 24 kN. Protection level 2: the average value of transmitted force not greater than 9 kN, single impact force not greater than 12 kN.

Requirements and test methods for protective clothing for hockey on the grass goalkeepers and players in the field are described in PN-EN 13546:2008 (2008). It sets standards for protection of the most vulnerable and exposed parts of a body, e.g. arms, chest, foot, genitals. The area of the heart has five levels of protection: level 1 – energy 5 J, level 2 – energy 20 J, level 3 – energy 30 J, level 4 – energy 40 J, level 5 – energy 50 J, similar as in the case of the PN-EN 13546 (2008).

Standard PN-EN 13277-1 (2002) introduces requirements for protective equipment for martial arts. In this case, impact energy of a beater is limited to 12 J. The maximum weight of the loading beam is 2.5 ±0.025 kg. The maximum transferred energy cannot exceed 3 kN.

PN-EN 13158 (2010) presents requirements and evaluation methods for protective clothing for horse riders and those working with horses. According to the standard, a flat beater should have energy levels of 25 to 35 J. An average value of the transmitted force should be less than 25 kN, none of the individual values should exceed 30 kN.

As presented in the literature review, the highest value of the impact energy from blunt objects and different injuries for the protective equipment to withstand is 50 J.

2. RESEARCH METHODOLOGY

The paper presents an investigation of PVC foam crushing behaviour tests. The tests were performed on a drop hammer presented in Fig. 2. The testing bed design allows setting an appropriate impact energy through control of a dropping height or a dropping beam weight. It allows measuring the impact force, displacement, and dropping height automatically. The force is measured with a piezoelectric sensor Piezotronics PCB M200C50 operating within the range of 222.4 kN. The sensor is mounted under the support plate of the hammer. A beam movement, corresponding to a specimen compression, is measured by a laser triangular sensor. Beaters with different shapes can be mounted to the beam.

Prior to the proper tests with a drop hammer, the impact energy parameter for the foamed material tests was determined during an additional experimental research. The research was based on throwing or hitting with various blunt objects by a few adult people. The different types of blunt objects used in the evaluations are presented in Fig. 3. There were used: pavement stones, small and big bricks, small and big rocks. Also, striking with a baseball bat was covered in the tests. Five people performed each type of test. The experiment was recorded with a high-speed camera to measure velocity of thrown objects or striking with a baseball bat. Special marks were placed on the objects to evaluate velocity using Digital Image Correlation method (DIC) – Fig. 4. Afterwards, a kinetic energy for each blunt object was calculated. All results were averaged and the statistical averaged kinetic energy of throwing/striking with blunt objects was measured It was determined to be 195 J.

Fig. 2. A specimen placed on the support plate of the drop hammer with a flat beater installed on the beam

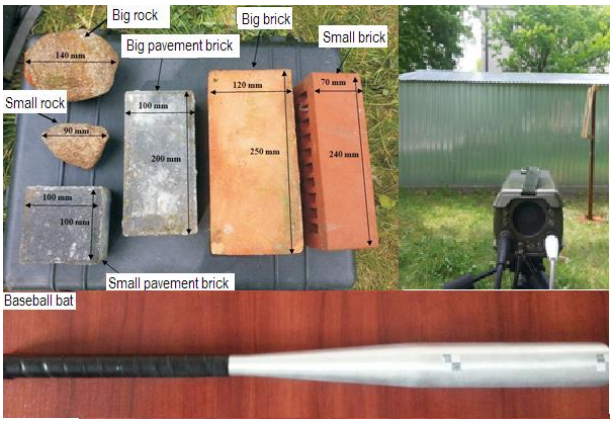

Fig. 3. Blunt objects and baseball bat used in the kinetic energy evaluation test with high-speed camera

The adopted averaged value of the kinetic energy–obtained from the additional tests is more than ten times greater than the potential energy set in the testing standards considering loading with blunt instruments. The British Standard BS 7971-8 (2003) adopts a value of 20 J as a basis for the research, whereas Polish PN-EN 1621-2 (2014) sets the loading energy at the level of 50 J. Those values appear to be low when compared to possible treats experienced by police officers in the line of duty.

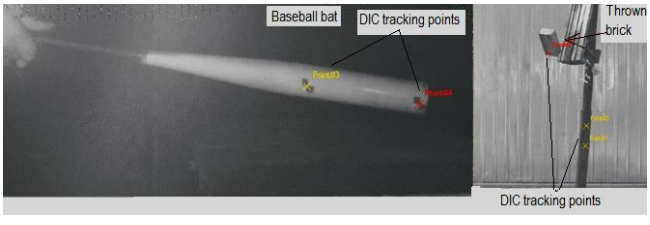

Fig. 4. Evaluation of velocity and kinetic energy of blunt objects thrown and baseball bat strike, using tracking points of Digital Image Correlation method

A dynamic impact load was applied using beaters with different shapes. Four types of beaters were prepared: flat, cylindrical, edgy and cornered. A flat beater, presented in Fig. 5a), has dimensions of 70x70 mm and simulates an attack with flat objects

DOI 10.2478/ama-2018-0004

such as boards. A baseball bat is modelled using a cylinder with a diameter of 55.2 mm and length of 70 mm – Fig. 5b). An edgy beater (Fig. 5c) has the following dimensions: height – 40 mm, the base – 45x80 mm. The fourth one, presented in Fig. 5d), is a cornered beater. Its base is an equilateral triangle with side length of 68.7 mm and height of 40 mm. The last two beaters are to simulate attacks with edged bricks, crushed pavement stones or sharp stones.

The dropping height of the hammer beam for each sample was determined in such a manner that the potential energy was equal to 195 J. The total mass of the beam of the drop hammer with a beater installed was equal to 15 kg. To achieve the desired impact energy, the dropping height was set to 1325 mm. The impact speed was equal to about 5 m/s. The experimental conditions correspond to the strain rate of about 10^2 s^{-1}. According to majority of the literature, i.e. (Mahfuz et al., 2006; Zhang et al., 2012; Luong et al., 2013; Loup et al., 2005), PVC foam crushing force is sensitive to a strain rate increase compared to the static tests.

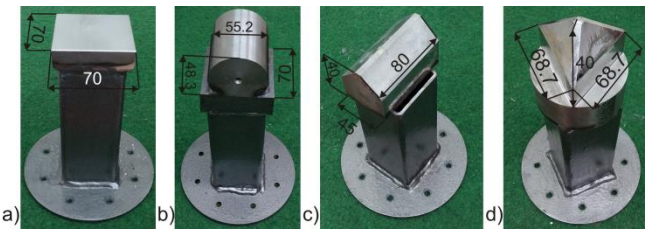

Fig. 5. The beaters used in the study of the PVC foam crushing resistance: a) flat; b) cylindrical; c) edgy; d) cornered

Rectangular samples of HEREX C70.130 with dimensions of 70x70x40 mm and density of 130 kg/m^3 were prepared. The actual average density was equal to 139 kg/m^3. The samples were cut, using a water jet machine, from a raw factory-prepared PVC foam sheet of 40 mm height. The samples were loaded in through-thickness direction, wherein the material has the best properties (Zhang et al., 2012). A sample placed on the testing bed equipped with a flat beater is shown in Fig. 2.

In the case of flat, cylindrical and cornered beaters, five samples were tested. However, in the case of the edgy beater, six samples were evaluated.

In the initial tests, load of 100% was applied, which means that the beam with an appropriate beater was dropped from the maximum height (1325 mm). In the cases where the impact energy was too high, and an impact caused sample fragmentation, the drooping height was gradually reduced for another samples by 20%, and if it did not prevent fragmentation, it was reduced by 50% of the initial height.

It should be noted that the test does not reflect real conditions of the human body protection against strikes with blunt objects. This is due to firmly stiff steel backplate of the testing bed, on which the samples were set during the tests. However, the paper presents the most disadvantageous condition in which crushing behaviour under impact of objects of various shapes can be observed.

Based on the obtained data, the graphs of force versus compression for all tested samples were evaluated, analysed and compared. The presented force curves were determined until the maximum compression of the samples was reached. The area under the curves represents the absorbed energy which was also calculated for each sample.

3. RESULTS OF THE RESERCH

The crushing behaviour and energy absorption performance of the tested PVC foam are very dependent on the shape of the striking object. The samples of foam material after the tests with a flat beater are shown in Fig. 6. None of the tested samples underwent fragmentation. On the top surfaces of the samples, permanent and evenly distributed deformations occurred. The impact energy of a flat beater is absorbed effectively on a relatively short distance, compared to the tests of other beaters, since the impact is spread on a relatively large surface.

The detailed results of the impact tests are covered in Tab. 2, which presents impact speed of the hammer beam, displacement covering sample compression, maximum crushing force, average crushing force and energy absorbed by the specimens. The absorbed energy was calculated as an area below the force-displacement curves. The averaged values were calculated and are presented in the last row of Tab. 2.

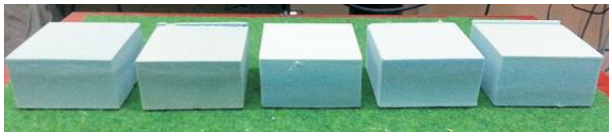

Fig. 6. Samples after the tests with a flat stamp

Tab. 2. Results of the impact tests for flat beater impact

Dropping height [%]	Impact speed [m/s]	Displace place-ment [mm]	Maxi-mum force [kN]	Aver-aged force [kN]	Ab-sorbed energy [kJ]
100	5.1	8.8	25.7	20.8	182.9
100	5.1	9.3	26.0	20.5	190.3
100	5.1	9.3	25.2	20.4	189.9
100	5.1	9.5	24.8	20.0	189.7
100	5.1	9.8	24.3	19.3	189.6
Average:	**5.1**	**9.4**	**25.2**	**20.2**	**188.5**

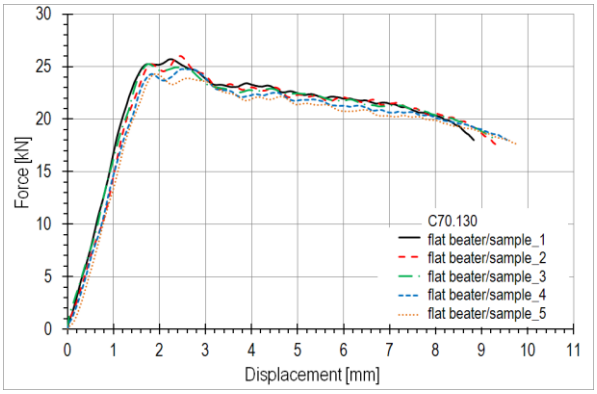

Fig. 7. Force-displacement curves obtained in the flat beater tests

In Fig. 7, the force-displacement curves obtained in the flat beater tests for all five specimens are presented. The compression curves are presented to the moment of the maximum specimen compression. The results are repeatable as shapes of the curves are very similar to each other. After a linear force increases and reaches its maximal value, which is equal to about 25 kN,

DOI 10.2478/ama-2018-0004

a gradual decrease occurs when the beater decelerates. Both the maximum and the average transferred crushing force exceed the values proposed in most standards regarding blunt object impacts or injury resistance. This is due to a relatively high initial energy and a stiff steel backplate of the testing bed. The averaged absorbed energy for all tests is equal to 188.5 J. Most energy of the impact was absorbed by the foam.

The samples crushed with a cylindrical beater are presented in Fig. 8. As it can be observed in the photo, samples did not undergo any fragmentation. However, on the top surfaces of the foamed materials, some semi-circular deformations and small cracks were formed.

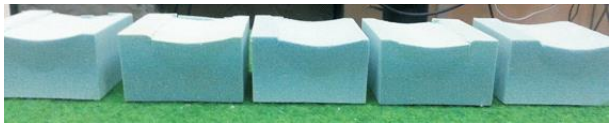

Fig. 8. Samples crushed with a cylindrical beater

Tab. 3 presents quantities of the energy absorbed obtained for the cylindrical beater. The maximum transferred force was equal to 16 kN and averaged force – 12.2 kN. The averaged absorbed energy is equal to 185.8 J, which means that almost 96% of the impact energy was absorbed by the specimens. PVC foam is slightly less effective in counteracting the rounded-shaped object strike compared to a flat object impact. Only a small amount of energy would be transferred to the protected object.

In the crushing plots obtained during the cylindrical beater impacts, presented in Fig. 9, the crushing force increases smoothly along with deflection, which is due to a gradual increase of the contact area of the beater with the sample in the crushing zone. The maximum force is significantly less than for a flat beater and it occurs at the end of the impact; however, displacement is almost twice as high. The impact energy is absorbed in a longer distance, due to a smaller cross section area of the beater. The 40 mm-thick foam is capable resisting this kind of threat without being fragmented.

Tab. 3. Results of impact tests for cylindrical beater impact

Dropping height [%]	Impact speed [m/s]	Displacement [mm]	Maximum force [kN]	Averaged force [kN]	Absorbed energy [kJ]
100	4.9	15.1	16.5	12.4	187.2
100	4.9	15.3	15.8	12.3	188.4
100	4.8	15.3	15.9	11.9	182.2
100	4.9	15.1	15.8	12.4	187.3
100	4.9	15.2	15.9	12.1	183.9
Average:	**4.9**	**15.2**	**16.0**	**12.2**	**185.8**

For samples loaded with an edgy beater, presented in Fig. 10, different degrees of destruction for various samples were observed. Therefore, in this case, the tests for six samples were made. Samples no. 2 and no. 4-6 (last four samples shown in Fig. 10) did not undergo fragmentation. There were permanent deformations shaped in the form of the beater and cracks present along the specimens; however, the samples resisted the test without any fragmentation. In the case of the first two specimens presented in Fig. 10 (samples no. 1 and 3), the load of the dropping hammer caused some significantly large cracks clearly visible in the picture. Parts of the samples, separated with the cracks through the whole height, were stuck to the rest of the sample parts only on small fragments. Permanent deformations of the surfaces in the shape of the cylindrical beater are also clearly visible. Despite the occurrence of large cracks, piercing through the thickness was not observed.

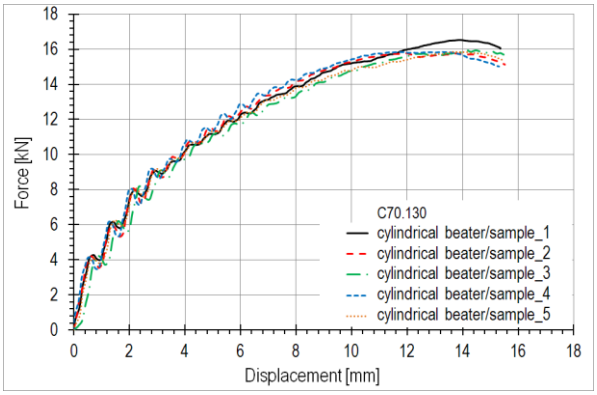

Fig. 9. Force-displacement curves obtained in the cylindrical beater tests

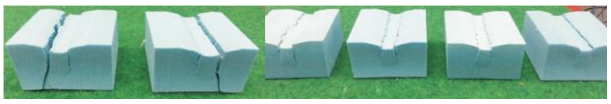

Fig. 10. Samples crushed with an edgy beater

The results of the crushing tests for an edgy beater impact are presented in Tab. 4. The maximum crushing force was equal to 14.2 kN and the averaged crushing force – 9.2 kN. Both values are even less than in the case of the cylindrical beater and the resulting displacement of the specimens is greater. On average, almost 89% of the impact energy of the edgy beater was absorbed by the foam, which means that the rest of the energy would be transferred to the protected object causing injuries. A smaller amount of the impact energy of the hammer beam was absorbed on the longer distance.

Tab. 4. Results of impact tests for edgy beater impact

Dropping height [%]	Impact speed [m/s]	Displacement [mm]	Maximum force [kN]	Averaged force [kN]	Absorbed energy [kJ]
100	5.0	18.5	14.3	9.2	170.4
100	5.0	19.1	14.1	9.3	177.6
100	5.0	18.1	13.9	8.9	160.2
100	5.0	19.6	14.3	9.4	184.4
100	5.0	18.4	14.5	9.4	172.2
100	5.0	18.9	14.2	9.2	173.8
Average:	**5.0**	**18.8**	**14.2**	**9.2**	**173.1**

Fig. 11 shows a graph of the impact compression with an edgy beater for six samples. In this scenario, a cross section of the beater hitting the specimen gradually increases during the impact, which results in a linear force increase and crushing distance extension. Elongation of the crushing displacement is an adverse phenomenon, due to limited thickness of the protective

DOI 10.2478/ama-2018-0004

material. The 40 mm-thick PVC foam is not sufficient to withstand the threat caused by a sharp object.

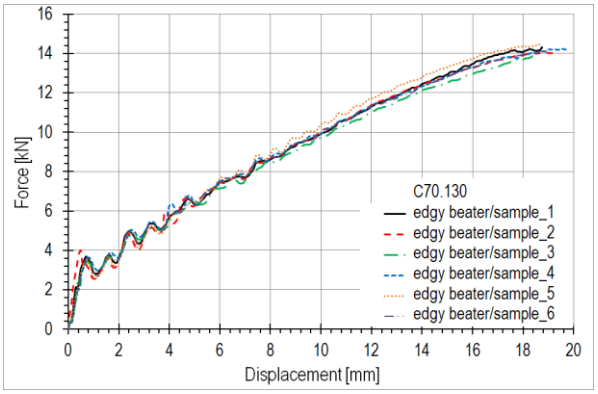

Fig. 11. Force-displacement curves obtained in the edgy beater tests

Based on the experience obtained in previous investigations, in the case of the cornered beater strike, the level of the initial dropping height of the hammer beam was reduced by 20% of the basic value (to 1060 mm). It corresponds to dropping energy of 156 J. After the first two tests, it was found that the samples were pierced through by the cornered beater and completely defragmented (first two samples presented in Fig. 12). For the remaining samples, the dropping height was limited to 50% of the maximum height (97.5 J). These samples were not torn apart. Permanent and deep deformation mapping the shape of the cornered beater is observed on the surfaces of these samples. Fig. 12 presents all samples after the tests.

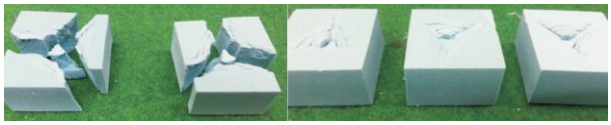

Fig. 12. Samples crushed with a cornered beater

Tab. 5. Results of impact tests for cornered beater impact

Dropping height [%]	Impact speed [m/s]	Displace placement [mm]	Maximum force [kN]	Averaged force [kN]	Absorbed energy [kJ]
80	4.3	24.7	10.6	5.1	124.8
80	4.3	26.0	10.9	5.3	138.5
50	3.4	21.7	8.7	4.1	88.7
50	3.4	22.1	8.7	4.1	91.2
50	3.4	22.0	8.7	4.1	89.7
Average:	**3.4**	**21.9**	**8.7**	**4.1**	**89.9**

In Tab. 5, the results of the crushing tests with a cornered beater are shown. The averaged values were calculated based only on the last three specimens, which were hit from the level of 50% of the total height and these rows are marked grey. Comparing the absorbed energy from the impact tests with a flat beater and the last scenario, only a small amount of the energy was absorbed by the foamed material hit with a cornered beater. This is due to a strongly sharp shape of the beater. A load is cumulated on a small area, which leads to a considerably low crushing force observed during the tests.

The graphs illustrating the force progress are presented in Fig. 13. The maximum force is reached at the end of the trials. A low level of crushing force at the beginning means that the crushing distance necessary to absorb all of impact energy can potentially be greater than the thickness of the protective layer. The last scenario of impact with cornered blunt elements (corners of brick or stones) is the most difficult for the foamed material to withstand and effectively protect against the threat.

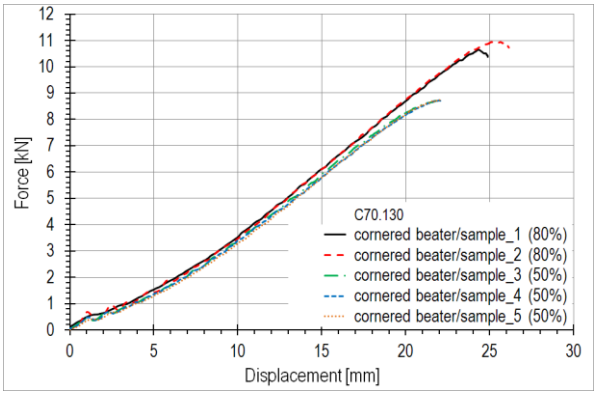

Fig. 13. Force-displacement curves obtained in the cornered beater tests

The selected specimens of scenarios evaluated in the impact tests with beaters of different shapes are compared on the graph in Fig. 14. The area under the curves represents the energy absorbed by the samples. It is clearly illustrated how significantly the shape of the blunt object influences the behaviour of the foamed material. The PVC foam materials can easier withstand flat object strikes and absorb more impact energy, while sharp objects impacts are very difficult to resist. The average crushing force is low; therefore, impact energy cannot be neutralized sufficiently by the foam. The average force of the flat beater impact (20 kN) is 5 times greater than the corresponding average force of the cornered beater impact (4.1 kN). The impact energy is cumulated on a very small area of the impact zone.

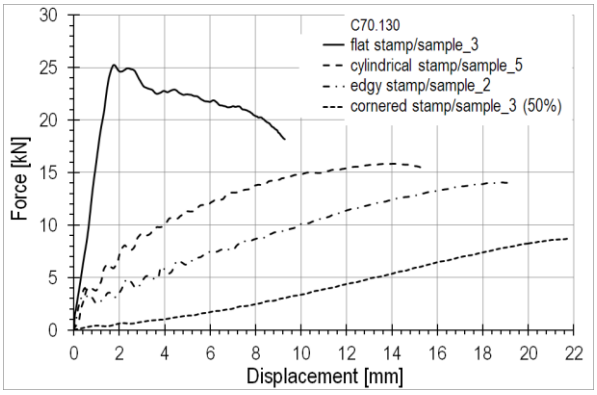

Fig. 14. Comparison of force-displacement curves for all types of crushing tests

4. CONCLUSIONS

The following conclusions of the study of the PVC foam material behaviour under load simulating the impact of a blunt object have been drawn:

1) The results for crushing tests of impact with different beaters

DOI 10.2478/ama-2018-0004

cannot be directly compared because a cross section area and a shape were different for each beater shape; however, general conclusions can be derived;

2) The impact energy of a flat beater is absorbed very effectively. For this case, a path of compression was considerably short. There were permanent but uniform deformations over the entire surfaces of the samples. The foam protects from flat blunt object strikes effectively;
3) The cylindrical and edgy beaters did not cause fragmentation of samples; however, the impact energy was absorbed in a considerable longer distance, compared with a flat beater. On the upper surfaces of the samples, permanent deformations mapping the beaters shapes as well as some cracks occurred;
4) The foamed material was able to absorb only a small amount of the impact energy of the cornered beater. To avoid fragmentation of the samples, the dropping height was reduced by 50%. On the top surfaces of the specimens, some deep cavities and cracks appeared. Those kinds of threats are very dangerous and difficult to be neutralized by the foam;
5) A shape of the blunt object significantly influences the behaviour of the foamed material. Flat objects cause the foamed material to absorb more energy and, thus, to be more effective, while sharp objects impacts are very difficult to be neutralized;
6) In the case of stiff foamed material like PVC foam investigated in the paper, edgy and cornered objects can cause cracks and defragmentation of the material during an impact;
7) It is shown that an averaged value of the kinetic energy obtained from the additional tests is more than ten times greater than the potential dropping energy set in the testing standards considering loading with blunt objects;
8) The test of throwing the blunt objects of different shapes and striking with a baseball bat allowed establishing an impact energy value for the test using beaters with different shapes. The potential energy for the main tests was equal to 195 J.

The paper covers the study of the crushing effects of impact load of the foamed material with beaters of different geometry, simulating an attack with blunt objects, such as: flat board, baseball bat, edgy bricks, pavement stones or stones.

REFERENCES

1. **Alcan Composites** (2016), *Sandwich Technology, Data sheet, Herex C70 universal structural foam*, C70DATASHEET.pdf www.alcanairex.com, Alcan Airex AG, Switzerland.
2. **Ashby M. F.** et al. (2000), *Metal foams – a design guide*, Butterworth-Heinemann, Oxford, UK.
3. **Avalle M., Belingardi G., Montanini R.** (2001), Characterization of polymeric structural foams under compressive impact loading by means of energy-absorption diagram, *International Journal of Impact Engineering*, 25(5), 455-472.
4. **Bernard C.A., Bahlouli N., Wagner-Kocher C., Ahzi S., Remond Y.** (2015), Impact behaviour of an innovative plasticized poly(vinyl chloride) for the automotive industry; *The European Physical Journal Conferences Web of Conferences 94*, DYMAT, Lugano, Switzerland.
5. **British Standards Institution** (2003), *BS 7971-8 – Protective clothing and equipment for use in violent situations and in training. Blunt trauma torso, shoulder, abdomen and genital protectors. Requirements and test methods*, BSI, UK, 2003.
6. **Chen L., Hoo Fatt M.S.** (2013), Transversely isotropic mechanical properties of PVC foam under cyclic loading, *J Mat Sci*, 48(19), 6786-6796.
7. **Cook W. (**2008), Designing body armour for today's police, *Technical Textiles*, 3/4, 50-53.
8. **Department of Defence Test Method Standard, MIL-STD-622F** (1997), *V50 ballistic test for armor*, Department of Defence, U.S.
9. **Gdoutos E.E., Daniel I.M., Wang K-A.** (2001), Multiaxial characterization and modeling of a PVC cellular foam, *J Thermoplast Compos Mater*, 14(5), 365–373.
10. **Hoo Fatt M.S., Chen L.** (2015), A viscoelastic damage model for hysteresis in PVC H100 foam under cyclic loading, *Journal of Cellular Plastics*, 51(3), 269–287.
11. **Hoo Fatt M.S., Jacob A. J., Tong X., MacHado-Reyes A.** (2017), Crushing behavior and energy absorption of PVC foam: an anisotropic visco-elastic-plastic-damage model, *21st International Conference on Composite Materials*, Xi'an, China, August 20-25, 2017.
12. **Loup D.C., Matteson R.C., Gielen A.W.J.** (2005), Material characterization of PVC foam under static and dynamic loading**.** In: Thomsen O.T., Bozhevolnaya E., Lyckegaard A., editors. *Sandwich structures 7: advancing with sandwich structures and materials: proceedings of the 7th international conference on sandwich structures*, Aalborg University, Aalborg, Denmark, 29–31 August 2005.
13. **Luong D.D., Pinisetty D., Gupta N.** (2013)**,** Compressive properties of closed-cell polyvinyl chloride foams at low and high strain rates: Experimental investigation and critical review of state of the art, *Composites Part B: Engineering*, 44(1), 403–416.
14. **Mahfuz H., Thomas T., Rangari V., Jeelani S. (**2006)**,** On the dynamic response of sandwich composites and their core materials, *Composites Science and Technology*, 66(14), 2465-2472.
15. **NIJ standard 0101.04** (2000), *Ballistic resistance of personal body armor*, U.S. Department of Justice, U.S.
16. **NIJ standard** 0115.00 (2000), *Stab resistance of personal body armor*, U.S. Department of Justice, U.S.
17. **NIJ standard 101.06** (2008), *Ballistic resistance of body armor*, U.S. Department of Justice, U.S.
18. **Polish Committee of Standardization** (2002), PN-EN 13277-1:2002 – Protective equipment for martial arts – Part 1: General requirements and test methods, PKN, Warsaw, (in Polish).
19. **Polish Committee of Standardization** (2008), *PN-EN 13546:2008 – Protective clothing – Hand, arm, chest, abdomen, leg, foot, and genital protectors for field hockey goal keepers, and shin protectors for field players – Requirements and test methods*, PKN, Warsaw, (in Polish).
20. **Polish Committee of Standardization** (2010), PN-EN 13158:2010 – Protective clothing – Protective jackets, body and shoulder for equestrian use: For horse riders and those working with horses, and for horse drivers – Requirements and test methods, PKN, Warsaw, (in Polish).
21. **Polish Committee of Standardization** (2011), PN-V-87000:2011 – *Lightweight ballistic shields. Bullet- and fragment-proof vests. General requirements and tests*, PKN, Warsaw, (in Polish).
22. **Polish Committee of Standardization** (2014), PN-EN 1621-2:2014-03 – Motorcyclist' protective clothing against mechanical impact, PKN, Warsaw (in Polish).
23. **Tagarielli V.L., Deshpande V.S., Fleck N.A.** (2008), The high strain rate response of PVC foams and end-grain balsa wood, *Composites Part B: Engineering*, Elsevier, 39(1), 83-91.
24. **Zhang S., Dulieu-Barton J.M., Fruehmann R.K., Thomsen O.T.** (2012), A methodology for obtaining material properties of polymeric foam at elevated temperatures. *Experimental Mechanics*, 52(1), 3–15.

Acknowledgement: The work has been accomplished under the research project: INNOTECH-K2/IN2/56/182840/NCBR/13 financed by the National Centre of Research and Development (NCBiR).

DE GRUYTER
OPEN

DOI 10.2478/ama-2018-0005 acta mechanica et automatica, vol.12 no.1 (2018)

NUMERICAL MODELLING OF METAL-ELASTOMER SPRING NONLINEAR RESPONSE FOR LOW-RATE DEFORMATIONS

Wojciech SIKORA[*], Krzysztof MICHALCZYK[*], Tomasz MACHNIEWICZ[**]

[*]Faculty of Mechanical Engineering and Robotics, Department of Machine Design and Technology,
AGH University of Science and Technology, al. Mickiewicza 30, 30-059 Kraków, Poland
[**]Faculty of Mechanical Engineering and Robotics, Department of Strength and Fatigue of Materials and Structures,
AGH University of Science and Technology, al. Mickiewicza 30, 30-059 Kraków, Poland

wosikora@agh.edu.pl, kmichal@agh.edu.pl, machniew@agh.edu.pl

received 6 June 2017, revised 28 February 2018, accepted 5 March 2018

Abstract: Advanced knowledge of mechanical characteristics of metal-elastomer springs is useful in their design process and selection. It can also be used in simulating dynamics of machine where such elements are utilized. Therefore this paper presents a procedure for preparing and executing FEM modelling of a single metal-elastomer spring, also called Neidhart's spring, for low-rate deformations. Elastomer elements were made of SBR rubber of two hardness values: 50°Sh and 70°Sh. For the description of material behaviour the Bergström-Boyce model has been used.

Key words: Bergström-Boyce Model, Neidhart's Spring, Metal-Elastomer Spring, FEM, SBR Rubber, Nonlinear Spring

1. INTRODUCTION

Nowadays, there are many different solutions for elastic elements utilized in machine design. Most basic and well known are metal springs, however there are also other alternatives. One of them is metal-elastomer spring based on Neidhart patent (Neidhart, 1951). This type of spring can be – compared to metal springs – advantageous in some applications due to significant damping properties. It relates in particular to vibrating machines, in which resonant vibrations amplitudes during run-up and run-down phase pose important problem (Cieplok, 2009). Application range of this type of metal-elastomer springs in various machines and industries constantly grows over the years. This makes justified to conduct research on them, which will lead to better understanding how they function and allow to improve their design.

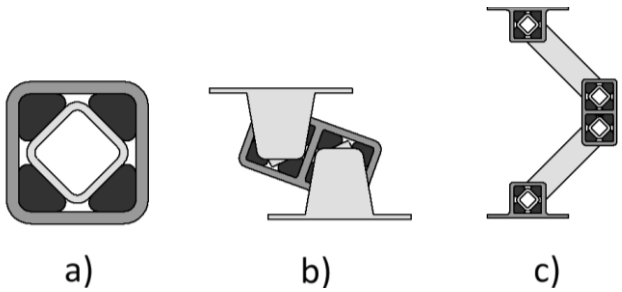

Fig. 1. Selected constructions of Neidhart's spring assemblies: a) single joint, b) two-joint support, c) four-joint support

Fig. 1 shows three different constructions of spring based on Neidhart patent. Single metal-elastomer spring shown in Fig. 1a is only capable of angular deformation, whereas two other constructions (Fig. 1b and 1c) are able to undergo linear deformation of large values, what makes them a significant competition even for helical springs. Moreover, by modifying rubber elements geometry or by changing rubber blend it is possible to change the mechanical properties of such system. Flexibility in their design proves the great potential of the metal-elastomer springs.

Proper selection of geometrical and material properties of metal-elastomer spring is essential in terms of Its application and faultless operation. To the best knowledge of authors, currently there is no analytical model in available literature, which would allow to describe relation of spring geometry and material properties of rubber with mechanical characteristics of metal-elastomer spring based on Neidhart patent. Probably the main reason behind this is that rubber parts undergo significant deformations during initial assembly and later operation of the spring. Moreover, nonlinear character of stress-strain relation of the elastomer itself also pose difficulties. Faced with described circumstances finite element method (FEM) seems to be a reasonable solution for modelling of this type of springs.

This paper presents an approach to modelling of a metal-elastomer spring using FEM. The first part describes and analyses Bergström-Boyce material model which was used to describe mechanical properties of the elastomer blends and was later utilized within FEM software. In the second part of this work the experimental tests conducted to receive empirical characteristics of metal-elastomer springs for given types of rubber have been presented. The results obtained were then used to assess accuracy of FEM modelling.

2. MATERIAL MODEL

Most of the well-known classic material models like Mooney-Rivlin (Mooney, 1940), Yeoh (1993), Gent (1996) or Arruda-Boyce (Arruda and Boyce, 1993) and others are sufficient when it comes

Wojciech Sikora, Krzysztof Michalczyk, Tomasz Machniewicz
DOI 10.2478/ama-2018-0005

to modelling static or quasi-static loading of an elastomer in typical laboratory tests with load modes like uniaxial tension, compression or simple shear. They are still commonly used and appear in literature (Diego et. al., 2017; Sikora, 2016; Ghoreishy et al., 2015). However, in practical applications, elastomer components usually undergo full cycles of loading and unloading, e.g. cylindrical rubber springs used as support in vibrating screens or feeders, displaying elastic hysteresis. Problem which arises is how to describe such behaviour, resulting from elastomer viscosity and connected with its time-dependent deformation. Mentioned above difficulty is still not completely solved and most of presented solutions are more empirical-based than analytical.

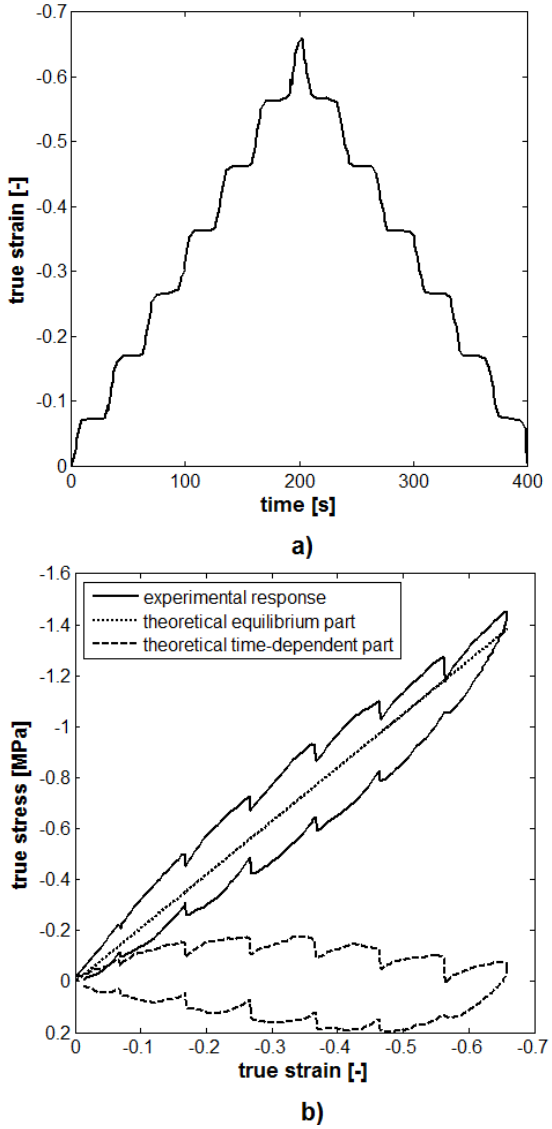

Fig. 2. Presentation of the main concept behind Bergström-Boyce model: a) load history, b) decomposition of true stress vs true strain curves into equilibrium and time dependent part. Modified plots are based on the original work from (Bergström, 1999)

The Bergström-Boyce model (Bergström and Boyce, 1998), further referred as BB model, is a constitutive model that allows to predict nonlinear and time-dependent response of elastomers. It bases on previous advancements in areas of viscosity of polymers and hyperelasticity, but tailors them into a new conception. The model is based on the assumption, that mechanical response of an elastomer consists of two parts: elastic equilibrium and time-dependent parts. This assumption comes from the experiment described in (Bergström, 1999) and presented in Fig. 2. An uniaxial compression test was conducted on a cylindrical specimen with additional relaxation periods, where strain was held at a constant value. It was observed that during relaxation, both on loading and unloading curve, recorded stress values were drifting to a theoretical line, which could be interpreted as a response in equilibrium conditions. This lead to assumption that elastomer, which is a network of polymer chains, could be treated as a system consisting of pure elastic network A and viscoelastic network B. It must be that noted this is a kind of idealization for the purpose of modelling. Those networks are responsible for, respectively, equilibrium and time-dependent parts of elastomer behaviour (Fig. 2b). If this system should be depicted using mechanical equivalents, it would look like in Fig. 3 which is similar to classic rheological Zener model (also named standard solid model). Network A is presented as single spring and network B as damper and spring connected in series. This kind of approach can be found in other material models (Kießling, 2016). Such composition has important features as it allows to portray material creep and stress relaxation phenomenon, both of which occur in elastomers and are important for a complete description of mechanical response for this type of material.

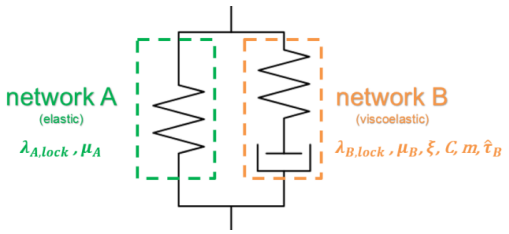

Fig. 3. Bergstrom-Boyce model concept with material parameters for each of the networks

In the present paper only strains due to mechanical deformation are considered, because all experiments have been conducted at constant, room temperature ca. 23°C. Assumption of material incompressibility is also made as it simplifies the study without leading to significant mistakes.

Classic hyperelastic material models can be illustrated as a simple spring with nonlinear characteristic, dependent on specific model. Therefore, it seems to be appropriate and correct to use one of known hyperelastic model to describe spring elements shown in Fig. 3. Those models usually have a form of an equation for strain energy density as a function of invariants of deformation tensor, which in most cases is based on phenomenological observations. Thus it is expected that application range of such models would be limited to specific materials or load modes. In the BB model author chose to use eight-chain (EC) model (Arruda and Boyce, 1993) which is motivated by a behaviour of elastomers on microstructural level. It assumes that an elementary volume of elastomer element has the shape of cube. It contains eight polymer chains attached to each of vertices of the cube and converging at its centre point. Edges of cube are orientated according to direction of principal stretches. This leads to the following equation for effective distortional stretch:

$$\bar{\lambda} = \sqrt{\frac{\lambda_1^{\,2} + \lambda_2^{\,2} + \lambda_3^{\,2}}{3}}$$

DOI 10.2478/ama-2018-0005

which is used next in the expression for stress:

$$\boldsymbol{\sigma} = \frac{\mu}{\bar{\lambda}} \cdot \frac{\mathcal{L}^{-1}\left(\frac{\bar{\lambda}}{\lambda_{lock}}\right)}{\mathcal{L}^{-1}\left(\frac{1}{\lambda_{lock}}\right)} \cdot \boldsymbol{b}'$$

where: σ – Cauchy stress tensor, μ – shear modulus [MPa], $\mathcal{L}(\mathrm{x}) = \coth(\mathrm{x}) - \frac{1}{\mathrm{x}}$ – Langevin function, $\mathcal{L}^{-1}(\mathrm{x})$ – inverse Langevin function, λ_{lock} – maximum possible stretch of a polymer chain [-], b' - deviator of left Cauchy-Green strain tensor; its symbol is small letter b to avoid confusion with network B.

The EC model is potentially more versatile than its phenomenological counterparts, because it proposes rationally justified mechanism of deformation. Material parameters $\mu, \lambda_{\mathrm{lock}}$ have to be identified experimentally. It seems that EC model is correct choice for a foundation of a more complex BB model.

Basic concept used in BB model is based on works of de Gennes (Gennes, 1971) who described motion of polymer chains inside network and called it reptation (from latin reptate – to creep). Theory of reptational motion was later further developed in (Doi and Edwards, 1986). Bergstrom brought those previous achievements closer to practical applications in his BB model (Bergström, 1999) in the form of an equation for viscous rate:

$$\dot{\gamma}_B = \gamma_0 \cdot \left(\overline{\lambda_{Bv}} - 1 + \xi\right)^C \cdot \left(\frac{\tau_B}{\sqrt{2} \cdot \hat{\tau}_B}\right)^m$$

where: $\gamma_0 = 1\left[\frac{1}{s}\right]$ - constant for units agreement, $\overline{\lambda_{Bv}}$ – viscous component of effective distortional stretch for network B, ξ – material constant [-], C – material constant [-], $\frac{\tau_B}{\sqrt{2}} = \frac{\|\boldsymbol{\sigma}'_B\|_F}{\sqrt{2}}$ – equivalent shear stress for network B [MPa], $\boldsymbol{\sigma}'_B$ - deviator of stress tensor for network B, $\|\ldots\|_F$ – Frobenius norm of a matrix, $\hat{\tau}_B$ – material constant [MPa], m – material constant [-].

To obtain specific stretch rate for viscous part the following expression (Bergström, 2015) should be used:

$$\dot{\boldsymbol{F}}_{Bv} = \dot{\gamma}_B \cdot (\boldsymbol{F}_{Be})^{-1} \cdot \frac{\boldsymbol{\sigma}'_B}{\|\boldsymbol{\sigma}'_B\|_F} \cdot \boldsymbol{F}_{Be} \cdot \boldsymbol{F}_{Bv}$$

where: $\dot{\boldsymbol{F}}_{Bv}$ – deformation rate tensor for viscous part of network B, $\boldsymbol{F}_{Be}$ – deformation tensor for elastic part of network B, $\boldsymbol{F}_{Bv}$ – deformation tensor for viscous part of network B, $\boldsymbol{\sigma}'_B$ - deviator of the stress tensor of network B.

Characterization of viscoelastic behavior of polymer network, like in case of EC model, is a result of analysis of this phenomenon and its mechanisms which has concluded in the successful attempt to describe it with mathematical formulas. Therefore it can be stated that whole BB model, both in elastic and viscoelastic part, is a model which is strongly connected with polymer mechanics theory. Thus it is versatile and has big potential for employing it for FEM computations of mechanical systems (Dal and Kaliske, 2009). BB model seems to be useful tool for modelling elastomer elements as there are publications describing its successful applications (Chouinard et al., 2009; Ghoreishy, 2014).

The BB model in the version presented in this paper has eight parameters, which have to be estimated in order to utilize it. Results of experimental tests based on which mentioned parameters were evaluated will be presented in the next section of present paper.

3. MATERIAL PARAMETERS IDENTIFICATION

Typical procedure of estimation of material parameters in hyperelastic model requires conducting a series of experimental test on standard specimens. Those tests are usually uniaxial tension, compression or simple shear. Empirically obtained force-displacement (stress-strain) curves are subsequently used for the model calibration. Next, the equation of theoretical curve for specific test should be derived from general model and fitted to empirical one. Sometimes, depending on model, one type of test is not enough to properly estimate material characteristics. Therefore, the general principle says that the more load modes are tested, the better performance of the model can be expected. This is true especially in case of phenomenological models. However, in case of BB model, because of reasons accented in previous section, in most cases one type of test should be enough to obtain satisfying results with this model.

Number of parameters which can be estimated in case of BB model is eight and it makes this model a bit sophisticated and difficult to calibrate. Referring to its original author (Bergström, 1999) some of those parameters can be specified before actual experiments. It is suggested that λ_{lock} for both A and B networks can be assumed to be the same. Another one, ξ, is constant which task is to prevent singularity when $\overline{\lambda_{\mathrm{Bv}}} \to 1$ (undeformed state) and is usually taken as 0.0001. This reduces number of model parameters to six and simplifies fitting operation. Even though, it is still a six dimensional optimization problem, because fitting can be also treated as minimization of difference between experimental and theoretical results where material parameters are decision variables. Possibility of getting stuck during optimization process in some local minima exists. Therefore it is advisable to use algorithms incorporating stochastic elements, which are able to break out of local minimas. The estimation of BB model parameters in this paper was carried out with a help of a genetic algorithm.

Theoretical formula for uniaxial compression of cylindrical specimen according to BB model consists of three basic equations: stress of the network A, stress of the network B and viscous stretch rate of the network B. All following formulas were derived for uniaxial loading of incompressible material. Deformation gradient F for this specific loading mode is:

$$\boldsymbol{F} = \begin{bmatrix} \lambda & 0 & 0 \\ 0 & \frac{1}{\sqrt{\lambda}} & 0 \\ 0 & 0 & \frac{1}{\sqrt{\lambda}} \end{bmatrix}$$

where: **F** – deformation gradient, λ – principal stretch along compression axis [-].

Deformation gradient F can be written also as the product of elastic and viscous parts:

$$\boldsymbol{F} = \boldsymbol{F}_A = \boldsymbol{F}_B = \boldsymbol{F}_{Be} \cdot \boldsymbol{F}_{Bv}$$

Stress in both networks for uniaxial load, per EC model is expressed by (Bergström, 1999):

$$\sigma_A = \frac{\mu_A}{\overline{\lambda_A}} \cdot \frac{\mathcal{L}^{-1}\left(\frac{\overline{\lambda_A}}{\lambda_{A,lock}}\right)}{\mathcal{L}^{-1}\left(\frac{1}{\lambda_{A,lock}}\right)} \cdot \left(\lambda_A^2 - \frac{1}{\lambda_A}\right)$$

Wojciech Sikora, Krzysztof Michalczyk, Tomasz Machniewicz
DOI 10.2478/ama-2018-0005

$$\sigma_B = \frac{\mu_B}{\overline{\lambda_{Be}}} \cdot \frac{\mathcal{L}^{-1}\left(\frac{\overline{\lambda_{Be}}}{\lambda_{B,lock}}\right)}{\mathcal{L}^{-1}\left(\frac{1}{\lambda_{B,lock}}\right)} \cdot \left(\lambda_{Be}^2 - \frac{1}{\lambda_{Be}}\right)$$

and stretch rate for viscous part in network B:

$$\dot{\lambda}_{Bv} = \dot{\gamma}_0 \cdot \left(\overline{\lambda_{Bv}} - 1 + \xi\right)^C \cdot \left(\frac{1}{\sqrt{3}} \cdot \frac{\sigma_B}{\hat{\tau}_B}\right)^m \cdot \sqrt{\frac{2}{3}} \cdot \lambda_{Bv}$$

where: $\lambda_A = \lambda_B = \lambda$, $\overline{\lambda_A} = \sqrt{\frac{{\lambda_A}^2 + \frac{2}{\lambda_A}}{3}}$, $\overline{\lambda_{Bv}} = \sqrt{\frac{{\lambda_{Bv}}^2 + \frac{2}{\lambda_{Bv}}}{3}}$,

$\overline{\lambda_{Be}} = \sqrt{\frac{{\lambda_{Be}}^2 + \frac{2}{\lambda_{Be}}}{3}}$, λ_{Be} – elastic part of stretch in the network B, λ_{Bv} – viscous part of stretch in the network B, $\lambda_{A,lock} = \lambda_{B,lock} = \lambda_{lock}$.

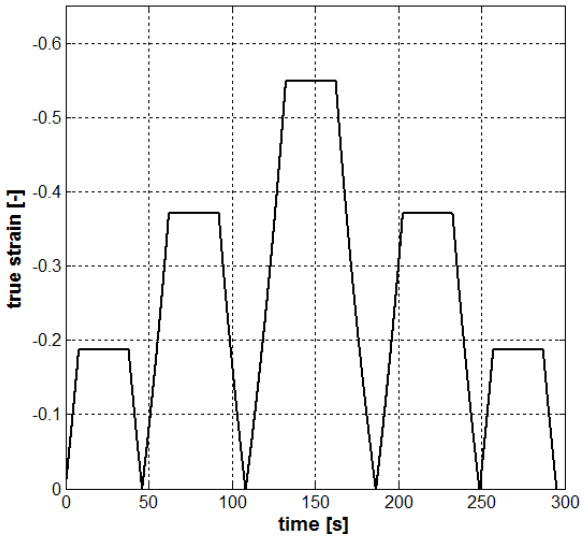

Fig. 4. Load sequence used for the calibration of BB model

Experimental tests were conducted on cylindrical specimens of 30 mm diameter and 14 mm height. Specimens were made from SBR (styrene-butadiene rubber) in two hardness variants: 50 °ShA and 70 °ShA (Shore hardness type A). It should be noted that also a 90°ShA SBR rubber was initially planned for experiments but it proved to be too stiff for its effective utilisation in metal-elastomer spring thus it was omitted. Samples underwent uniaxial compression on universal testing machine. Registered results were later used for evaluating parameters of BB model.

In Fig. 4 is shown a time history of applied load in test which was utilized to calibrate BB model. It consists of five consecutive cycles with changing maximum true strain. At peak strain in each of them there is a relaxation period where strain is held at a constant value. Characteristic feature of elastomers is stress relaxation in time. Incorporating relaxation effect into material testing of elastomers make it easier to describe viscoelastic effects using BB model. Before executing calibration test from Fig. 4 rubber samples underwent mechanical conditioning which allowed to stabilize their mechanical response and significantly reduce Mullins effect. Fitting results are shown in Fig. 5. Received results presents satisfactory coincidence with experimental tests. Calibration test performed for an only single strain rate was sufficient because next experiments on metal-elastomer springs were conducted with relatively low speeds. Elastomer hardening due to deformation rate magnitude which was employed during springs tests (far below 1Hz) was not significant.

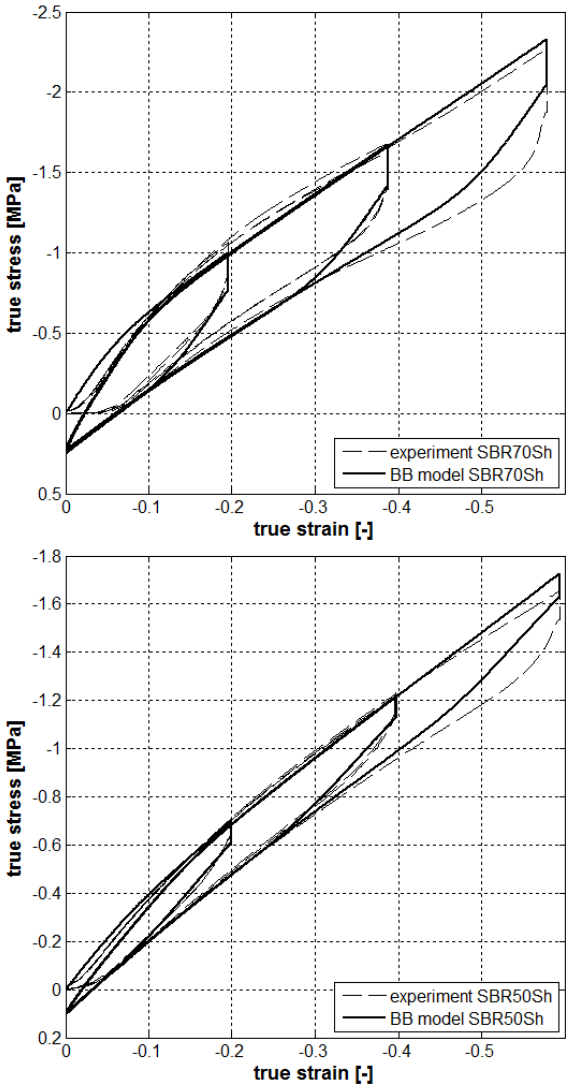

Fig. 5. Results of fitting BB model to experimental curves for materials SBR 70°Sh and SBR 50°Sh

4. EXPERIMENTAL TESTS AND FEM SIMULATIONS

To validate results of the FEM simulations there must be conducted a series of experimental tests on metal-elastomer springs which would serve later as a reference for assessment. A single elastic joint (Fig. 1a) is a torsion spring, thus it must be loaded with moment of force or angular displacement. Therefore, a simple apparatus which allows to adapt a typical universal test machine to perform such kind of experiment was designed and assembled. It is shown in Fig. 6 and it consists of rack (2) and pinion gear (3) that is fixed on the shaft (4). It allows to convert linear to angular motion (comparatively force to moment). Shaft itself was supported by two bearings (6) that were fixed to the device frame. Tested joint (5) was pushed onto shaft and then fixed in place. Load has been applied through testing machine jaws (1) which hold rack and allows to move it vertically. Force inflicted on rack and its displacement were recorded by a testing machine software and were converted later to angle and moment respectively. The

DOI 10.2478/ama-2018-0005

rotary inertia of the whole system does not influence adversely the results of experiments due to quasi-static character of displacements.

Three types of tests with varying load sequence were performed. Plots showing angle vs time history for each of them are shown in Fig. 7. Fig. 7a represents a symmetrical cyclic loading with 30° rotation clockwise and counter-clockwise, consisting of three full cycles. It explores the whole rotational working range of the joint. Second load sequence, presented in Fig. 7b, is in close proximity to the loads which undergo metal-elastomer springs in the most of applications. It starts with initial load, 15° in this case, and then oscillates around it with amplitude equal to 5°. Initial static load represents the force associated with the weight of the machine. Later comes the working load in the form of vibration/oscillations. This test involves full four load cycles. The last type of loading sequence, presented on Fig. 7c, consists of three consecutive cycles with increasing true strain value.

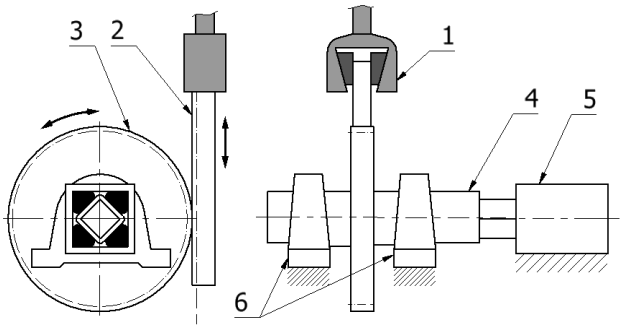

Fig. 6. Diagram of apparatus for testing metal-elastomer springs: 1 – grips, 2 – rack, 3 – pinion gear, 4 – shaft, 5 – tested spring, 6 – support bearings

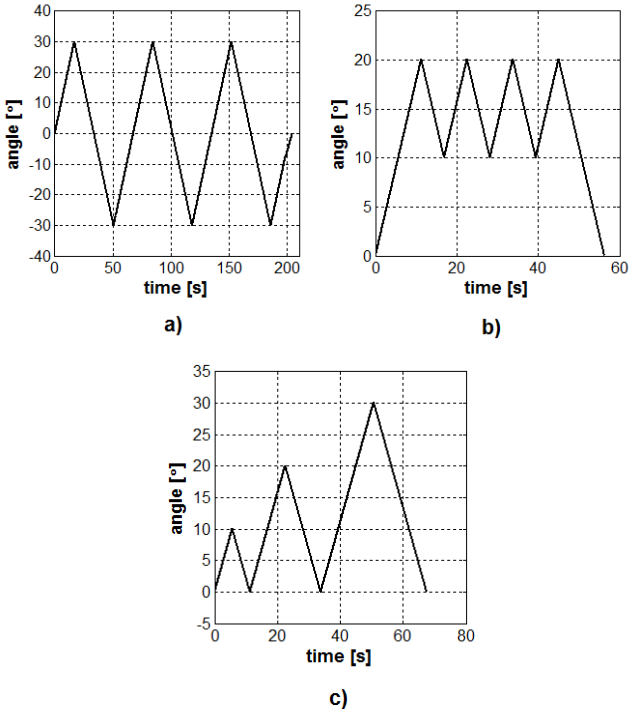

Fig. 7. Load sequences used in FEM simulations and experimental test of metal-elastomer springs

FEM simulations were conducted with the help of Ansys Mechanical APDL. The prepared solid model consists, like its real-life counterpart, of three parts: outer square tube, elastomer cylinder and inner square tube. Dimensions of spring's elements are shown in Fig. 8. Elastomer elements before assembly had cylinder shape of 12mm in diameter and 40mm length. Due to three symmetry planes which can be found in the considered spring, only 1/8 of assembly model was considered in simulations, replacing missing parts of model with proper boundary conditions (Fig. 8). Boundary conditions for the simulation were assumed to be identical like in experimental tests, i.e. element (1) in Fig. 9 was fixed and element (3) was constrained in such a way, that it could only rotate around main axis, as it is shown in Fig. 9. The result of each simulation was a moment reaction on element (3) as function of time and rotation angle. Bodies (1) and (3) were treated as rigid and (2) as flexible.

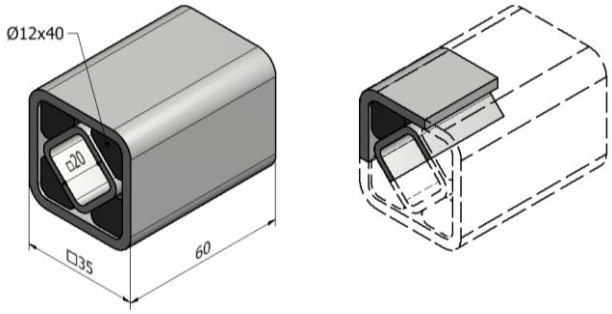

Fig. 8. Reduction of model size due to existing symmetry planes

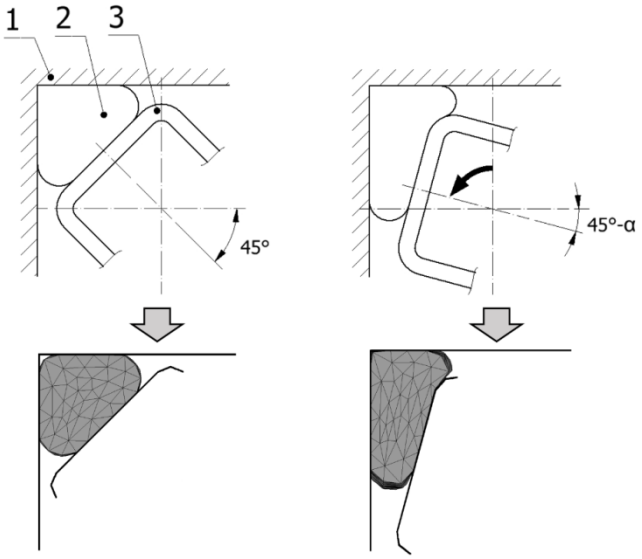

Fig. 9. Schematic of FEM simulation. 1 – outer square tube, 2 – elastomer, 3 – inner square tube

Mechanical response of metal-elastomer springs, due to rubber properties, is slightly changing during initial load cycles, mainly because of softening effect. Thus, before actual experiments, springs were mechanically conditioned to stabilize their response. Thanks to that the third cycle from experimental load sequences in Fig.7a and Fig. 7b was representing equilibrium state response and therefore was taken in to the comparison between experimental results and FEM simulations.

Wojciech Sikora, Krzysztof Michalczyk, Tomasz Machniewicz
DOI 10.2478/ama-2018-0005

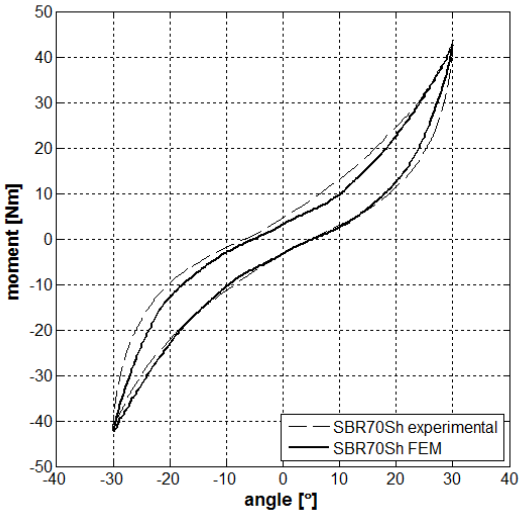

load sequence **a** for SBR 70°Sh

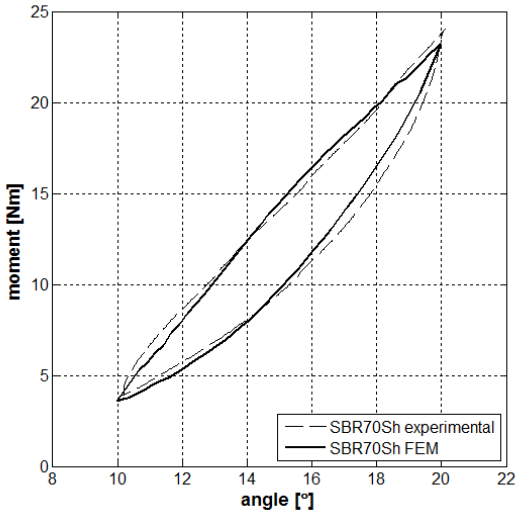

load sequence **b** for SBR 70°Sh

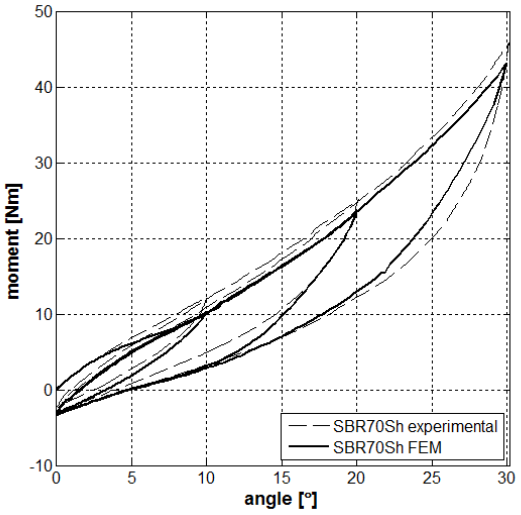

load sequence **c** for SBR 70°Sh

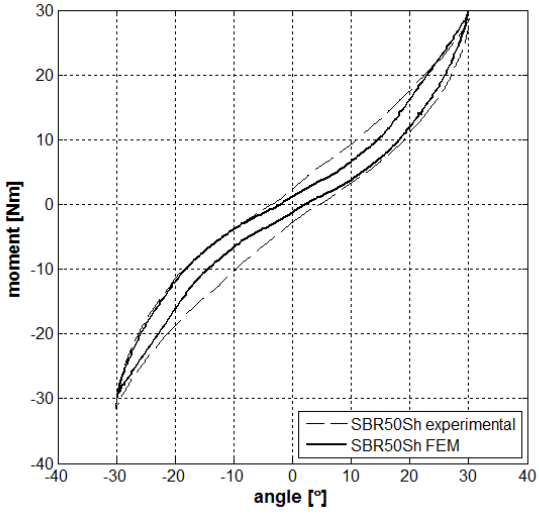

load sequence **a** for SBR 50°Sh

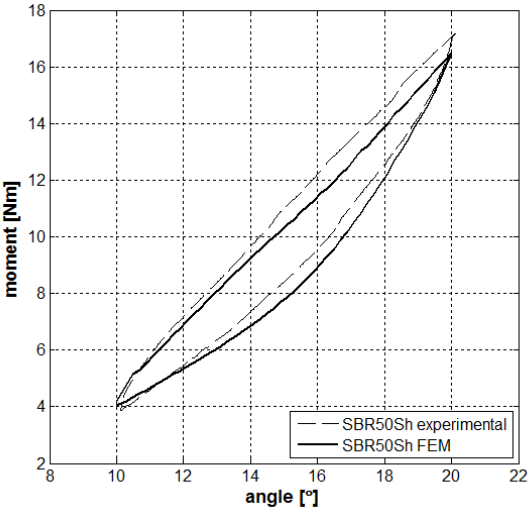

load sequence **b** for SBR 50°Sh

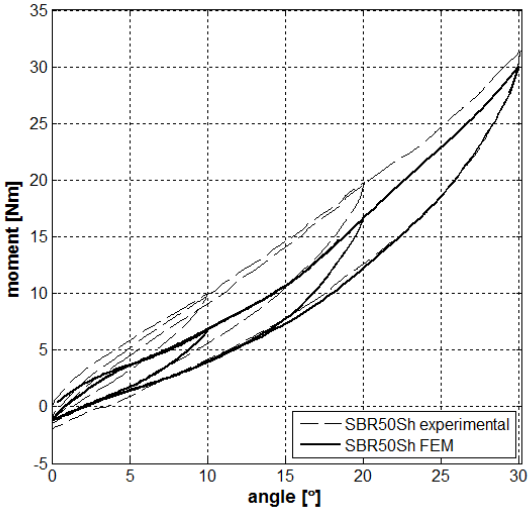

load sequence **c** for SBR 50°Sh

Fig. 10. Comparison between experimental tests and FEM simulations results

DOI 10.2478/ama-2018-0005

5. RESULTS

Comparison between experimental and FEM simulation results is shown in Fig. 10. Considering first specimen, i.e. spring containing elastic elements made of SBR 70 °ShA rubber, it can be seen, that numerical simulation provides quite accurate results, coincident with experimental characteristics. Maximum values of moment for each of load sequences from Fig. 7a-c are very similar, with slight deviation around 2% to 6%. The shape of the experimental curves are well represented by the simulated ones. However, slight deviations in the size of elastic hysteresis can be observed in each sequence. Sample with softer rubber, SBR 50°Sh, shows at the other hand more significant discrepancy. General shape of FEM curves for load sequence from Fig. 7a and 7c have a slightly lower compliance with experimental test results than the ones for the tougher rubber It can also be observed, that hysteresis loop for load sequence in Fig.7b, obtained from experimental tests is significantly narrower than the area obtained from FEM simulations.

Considering that FEM simulation and experiment conditions were identical for both rubber types, the source of noted differences is the material itself. From mechanical point of view these two rubber compositions differ only by Shore hardness. However, rubber hardness is a collective effect of its chemical composition – i.e. base rubber blend and additives and fillers. It can be observed that BB model exhibits lower accuracy, when describing behaviour of soft rubber blends in complicated loading cases.

6. CONCLUSIONS

This paper presents a numerical FEM modelling of metal-elastomer spring nonlinear response for low-rate deformations. It describes an outline of Bergstrom-Boyce hyperelastic model used later in numerical calculations and a method for its material parameters identification. Experimental tests were performed for two types of SBR rubber with different hardness, i.e. 70°ShA and 50°ShA. Load-deformation curves obtained from FEM simulations were compared with empirical results acquired with the help of custom made apparatus on universal testing machine.

The main aim of this work was to evaluate possibilities of modelling of metal-elastomer springs at low deformation rates. For the reason that rubber elements undergo large deformations during assembly and later during operation of such spring, analytical means of description seemed to be difficult to apply in this case. Alternative solution was FEM simulation. Obtained numerical results were assessed by comparing them with curves obtained from empirical tests. Simulations performance were different for both of tested materials. Metal-elastomer spring containing elastic elements made of SBR 70°ShA behaved similarly during experiment and FEM simulation. There was slight difference in peak values of moment and elastic hysteresis but in general it can be summarized as successful attempt. Evaluation of simulation for SBR 50°ShA is notably worse than in previous case. The main problem which occurred is visible discrepancy in elastic hysteresis reproduction.

Hardness of the rubber used in considered metal-elastomer springs which are available on the market is around 70°ShA. Modifications of the spring stiffness is in most cases realised by changing dimensions of rubber elements, while rubber hardness remain unchanged. Softer SBR blend was included in this work for the purpose of evaluation performance of BB model in FEM simulations.

Further work should concern influence of deformation rate on mechanical characteristics of metal-elastomer springs and possibilities of modelling it with FEM.

REFERENCES

1. **Arruda E.M., Boyce M.C.** (1993), A three-dimensional constitutive model for the large stretch behavior of rubber elastic materials, *Journal of the Mechanics and Physics of Solids*, 41 (2), 389-412.
2. **Bergström J.S.** (1999), *Large strain time-dependent behavior of elastomeric materials*, Ph.D. thesis, MIT.
3. **Bergström J.S.** (2015), *Mechanics of solid polymers: theory and computational modeling*, William Andrew, San Diego, USA.
4. **Bergström J.S., Boyce M.C.** (1998), Constitutive modeling of the large strain time-dependent behavior of elastomers, *Journal of the Mechanics and Physics of Solids*, 46, 931-954.
5. **Chouinard, P., Proulx, S., Lucking Bigué J.P., Plante, J.** (2009), Design of an antagonistic bistable dielectric elastomer actuator using the Bergstrom-Boyce constitutive viscoelastic model, presented at *33rd Mechanisms and Robotics Conference*, 2009, San Diego, CA, USA.
6. **Cieplok G.** (2009), Verification of the nomogram for amplitude determination of resonance vibrations in the run-down phase of a vibratory machine, *Journal of Theoretical and Applied Mechanics*, 47, 295-306.
7. **Dal H., Kaliske M.** (2009), Bergström–Boyce model for nonlinear finite rubber viscoelasticity: theoretical aspects and algorithmic treatment for the FE method*, Computational Mechanics*, 44, 809–823.
8. **Diego S., Casado J. A, Carrascal I., Ferreno D., Cardona, J., Arcos R.** (2017), Numerical and experimental characterization of the mechanical behavior of a new recycled elastomer for vibration isolation in railway applications, *Construction and Building Materials*, 134, 18-31.
9. **Doi M., Edwards S.F.** (1986), *The theory of polymer dynamics*. Oxford University Press, Oxford.
10. **Gennes P.G.** (1971), Reptation of a polymer chain in the presence of fixed obstacles, *The Journal of Chemical Physics*, 55 (2), 572-579.
11. **Gent A. N.** (1996), A new constitutive relation for rubber, *Rubber Chemistry and Technology*, 69, 59-61.
12. **Ghoreishy M.H.R., Firouzbakht M., Naderi G.** (2014), Parameter determination and experimental verification of Bergström-Boyce hysteresis model for rubber compounds reinforced by carbon black blends. *Materials and Design*, 53, 457–465.
13. **Ghoreishy M.H.R., Naderi G., Roohandeh B.** (2015), An experimental investigation on the degradation effect of ozone on hyperelastic behavior of an NR/BR blend, *Iranian Polymer Journal*, 24(12), 1015-1024.
14. **Hossain M., Vu D.K., Steinmann P.** (2012), Experimental study and numerical modelling of VHB 4910 polymer, *Computational Materials Science*, 59, 65-74.
15. **Kießling R., Landgraf R., Scherzer R., Ihlemann J.** (2016), Introducing the concept of directly connected rheological elements by reviewing rheological models at large strains*, International Journal of Solids and Structures*, 97-98, 650-667.
16. **Mooney M.** (1940), A theory of large elastic deformation, *Journal of Applied Physics*, 11(9), 582-592.
17. **Neidhart H.** (1951), *Elastic joints*, US patent 2 712 742.
18. **Sikora W., Michalczyk K., Machniewicz T.** (2016), A study of the preload force in metal-elastomer torsion springs, *Acta Mechanica et Automatica*, 10(4), 300-305.
19. **Yeoh O.H.** (1993), Some forms of the strain energy function for rubber, *Rubber Chemistry and Technology*, 66(5), 754-771.

Acknowledgements: This work is supported by AGH University of Science and Technology under research program no. 15.11.130.598.

DOI 10.2478/ama-2018-0006

NUMERICAL ANALYSIS OF STRESS INTENSITY FACTOR IN SPECIMENS WITH DIFFERENT FILLET GEOMETRY SUBJECTED TO BENDING

Janusz LEWANDOWSKI*, Dariusz ROZUMEK*

*Faculty of Mechanical Engineering, Department of Mechanics and Machine Design, Opole University of Technology, ul. Mikołajczyka 5, 45-271 Opole, Poland

janusz210@wp.pl, d.rozumek@po.opole.pl

received 5 April 2017, revised 28 February 2018, accepted 5 March 2018

Abstract: The article presents the maps of xx stress component and compares values of analytical and numerical calculations for the stress intensity factor range of welded specimens with fillet welds which subjected to cyclic bending. The tests were performed under constant value of moment amplitude M_a = 9.20 N·m and stress ratio R = σ_{min}/ σ_{max} = -1. The specimens were made of drag steel rod S355. The specimens were solid and welded. The numerical models were simulated with ABAQUS suite and numerical calculations performed with FRANC3D software.

Key words: Numerical Method, Fatigue Crack Growth, Bending

1. INTRODUCTION

Dynamically increasing competitiveness in quality, economy and consumer expectations force producers to optimize production in the way that products are of top quality and costs are maximally reduced at the same time. The problem of cost-effectiveness in production process concerns all industries. Engineering industry has no possibility to conduct research since they are expensive; therefore it cooperates with research institutions/centers (e.g. universities) to verify the structural solutions. In these centers the numerous research are conducted on the specimens with static and dynamic load to answer questions about strength and life. Experimenting with specimens on strength testing machines is expensive and time-consuming. The specimens are only in the simple shapes. Nevertheless, the results of the experiments give knowledge about the behavior of elements, material, welded joints, etc. in the real environment, considering all limitations of the tested element or the material structure (Carpinitieri et al., 2005; Zhi-Gang et al., 2012; Shang et al., 2015; Pakandam and Varvani-Farahani, 2010; Balitskii and Kostyuk, 2009; Rozumek and Marciniak, 2012; Poutiainen and Marquis, 2006; Benachour et al., 2008; Niklas, 2014; Rozumek, 2009). Nowadays, the numerical calculations are commonly performed together with experiments. These calculations provide for the analysis of stress, strain and displacement of the structures which are of different complexity and dimension and working under constant and variable loads (Tanaka et al., 2014; Ferro et al., 2016; Lewandowski and Rozumek, 2016). The crucial point is that numerical calculations do not reflect fully the behavior of the material or structure (Rusiński, 2002; Duchaczek and Mańko, 2012). The reason for this is that many simplifications are introduced into the calculation, such as:: the size of a single finite or boundary element (from which a construction model was made), the adoption of a perfectly isotropic material, the adoption of faulty initial assumptions (points of application and load values, etc.). The numerical calculations performed by people without basic knowledge of the subjects give sometimes completely erroneous results. Therefore, the results of the numerical calculations are often verified by experimental results.

The aim of the paper is to analyze the stress intensity factor and values of experimental (analytical) and numerical calculations for the stress intensity factor range of welded specimens with different fillet geometry subjected to cyclic bending.

2. SUBJECT OF STUDY

The analytical and numerical calculations were performed on the basis of three types of specimens made of S355 steel i.e., the solid specimen and the of welded specimens with fillet welds (concave and convex). Shapes and dimensions of the specimens are presented in Fig. 1 (solid specimen, specimens with concave and convex welds), and mechanical properties are given in Tab. 1.

Tab. 1. Monotonic mechanical properties of S355 steel

Yield stress, σ_y (MPa)	Ultimate stress, σ_u (MPa)	Elongation, A_5 (%)	Young's modulus, E (GPa)	Poisson's ratio v
357	535	21	210	0.30

Hand-made welds were made based on the TIG method using the inert gas shielding (Argon) for protection. The theoretical stress concentration factor in the solid specimen under bending K_t = 1.38 was estimated with use of the model (Kocańda and Szala, 1985; Rozumek and Macha, 2009).

Fig. 2 presents the microstructure of the solid specimen

DOI 10.2478/ama-2018-0006

material and the parent material (for welded specimens) of S355 steel. This material has a fine-grained ferritic-perlitic structure (Lewandowski and Rozumek, 2016).

Chemical composition of the tested S355 steel shown in the Tab. 2.

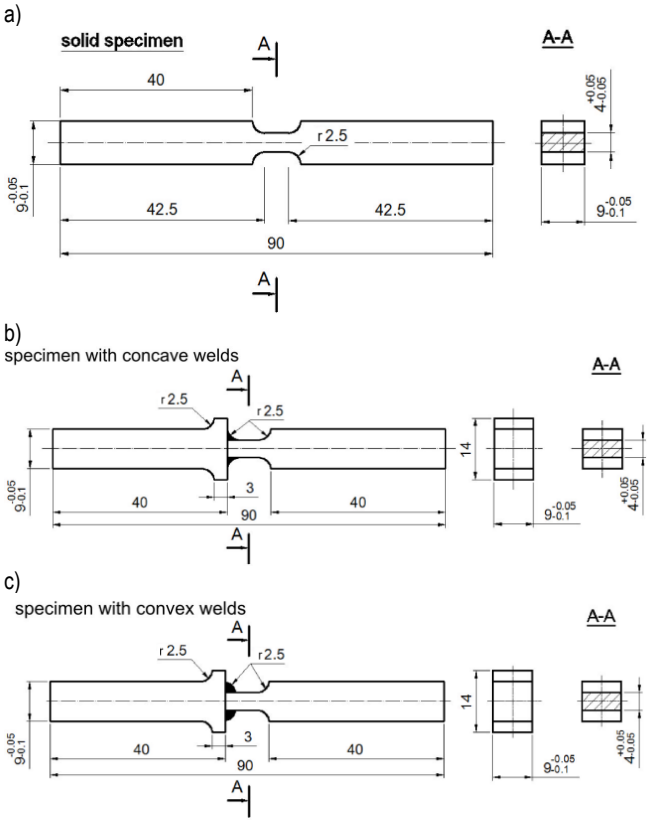

Fig. 1. Shapes and dimensions of specimens: (a) solid specimen, (b) specimen with concave welds, and (c) specimen with convex welds, dimensions in mm

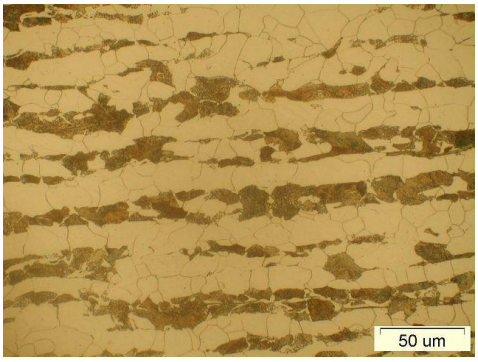

Fig. 2. The microstructure of the base material (magnification 500x)

Tab. 2. Chemical composition (in wt%) of S355 steel

C	Mn	Si	P	S	Cr	Ni	Cu	Fe
0.2	1.49	0.33	0.023	0.024	0.01	0.01	0.035	Bal.

The analytical and numerical calculations were performed for bending specimens at constant value of moment amplitude M_a = 9.20 N·m. The tests was carried out at loading frequency 28.4 Hz and stress ratio R = -1. Fig. 3 presents the method how the specimens were fixed and loaded.

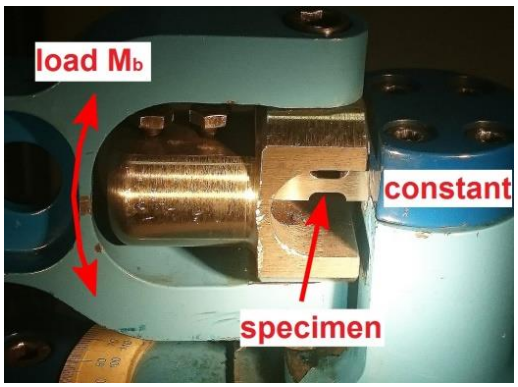

Fig. 3. Method of restrained and specimens loaded

3. NUMERICAL COMPUTATIONS

3.1. Description of the software for numerical computations

The numerical models were simulated with ABAQUS suite which applies finite element method (FEM). Besides building the model the program allows analysis of stress, strain and displacement and visualization of the results in a form of diagrams or maps. The limitation of ABAQUS is the lack of the tool for simulating cracks or cracks growth. Therefore, the FRANC3D software was chosen for that purpose (Faszynka et al., 2016; www.cfg.cornell.edu/software/software.htm). The program performs calculations based on the boundary element method (BEM). The capabilities of the program allow, among other things, for simulating crack growth by the given value and calculating stress intensity factors. For numerical calculations with ABAQUS program three test samples without cracks were made. These models served as a base for further calculations. The first numerical calculations were performed, which resulted in stress maps (σxx component of stress tensor) for the analyzed specimens without cracks. Then the files with models were transported to FRANC3D, where the cracks a = 0.10 mm long on the top surface, on the top of the notch were simulated. These cracks run perpendicular to the length of the specimen. Finite element mesh was made of tetrahedrons. The side length of the single element for solid specimens and for the specimens with concave welds was 0.25 mm, and for specimens with concave welds of 0.37 mm. However, in the stress concentration zones and in the crack growth, the size of the element side was 0.03 mm (Rusiński, 2002; Faszynka et al., 2016). Fig. 4 presents simulated cracks for the analyzed specimens: solid specimens with concave and convex welds.

After cracks simulation (crack initiation), FRANC3D software calculates the stress intensity factors for the given crack lengths. Next, models with cracks 0.10 mm long were transferred to ABAQUS to perform numerical calculations to get the stress maps for the analyzed specimens.

At the subsequent stages, repeatedly another cracks growth in length were simulated using FRANC3D and stress intensity factors were calculated as well as the stresses using the ABAQUS were calculated. The important rule applied for the research was that the lengths of cracks calculated numerically related to the lengths of the cracks recorded during the experiments. Fig. 5 presents the example specimens with cracks: the solid specimens with the crack a = 1.70 mm long, the specimen with concave welds and the crack a = 1.44 mm long, and the specimen with the convex weld and crack a = 1.48 mm long. FRANC3D software

calculates the stress intensity factor according to Eq. (1) taking into account the specimen shapes. In the area of developing cracks, the sizes FE mesh was concentrated to obtain the most accurate calculation. Numerical calculation error when changing the element size did not exceed 5%.

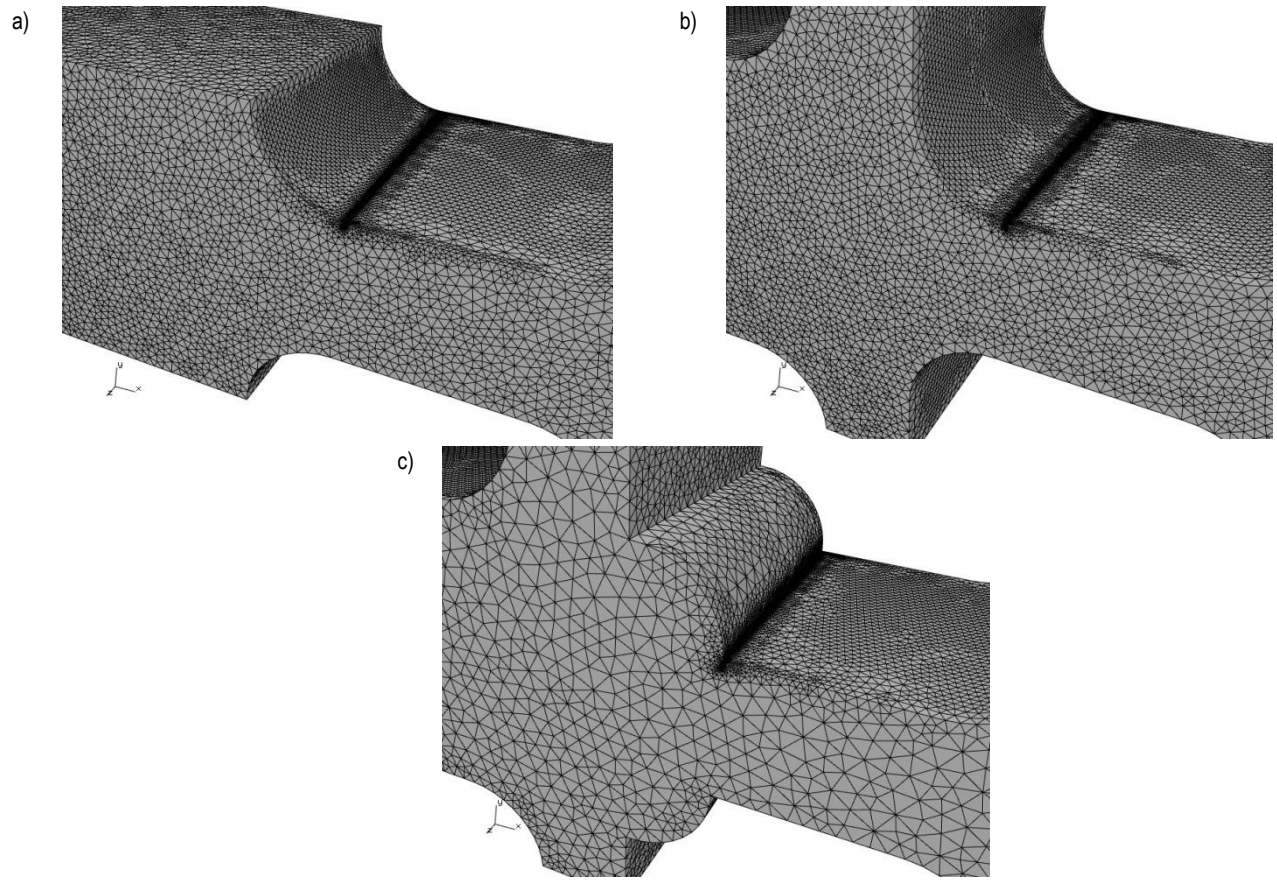

Fig. 4. Crack initiation (a = 0.10 mm) of specimens: a) solid, b) with concave welds, and c) with convex welds

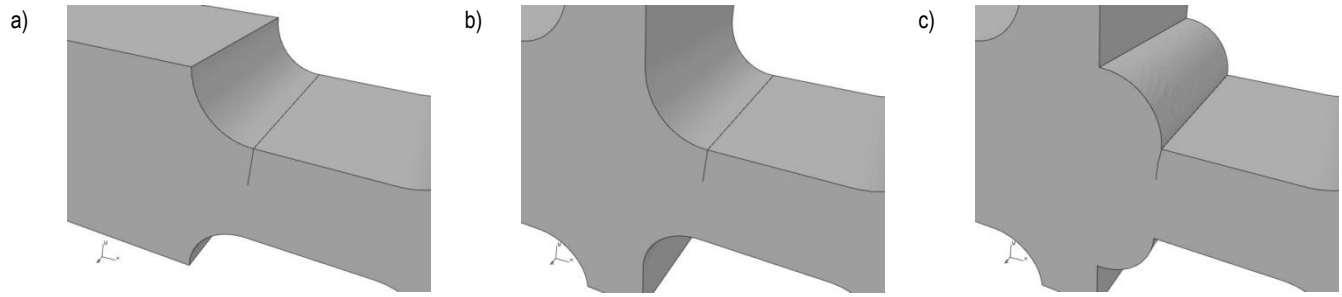

Fig. 5. Specimens with numerical calculation cracks: a) solid, b) with concave welds, and c) with convex welds

3.2. The results of numerical computations

The results of the numerical calculations are presented in the forms of stress maps (σ_{xx} component of stress tensor) for three specimen models. Fig. 6 presents specimens without cracks. Fig. 7 presents stresses maps for models with cracks of length: the solid specimen a = 1.70 mm, the specimen with concave welds a = 1.44 mm and the specimen with the convex weld a = 1.48 mm.

The subsequent cracks growth was calculated numerically. The values of lengths related to the lengths and directions the cracks run, which were reported during the experiments. Cracks in the specimens tested experimentally run evenly in the cross section of the specimens. The cracks growth in a similar way in the specimens calculated numerically. The values of stresses calculated numerically relate to the values reported during the experiment, which proves that the applied calculation method was correct. Fig. 8 presents results of calculations numerically for the stress intensity factors range.

In numerical calculations, a uniform structure of material is assumed. The differences in properties occurring in the heat affected zone were not taken into account.

DOI 10.2478/ama-2018-0006

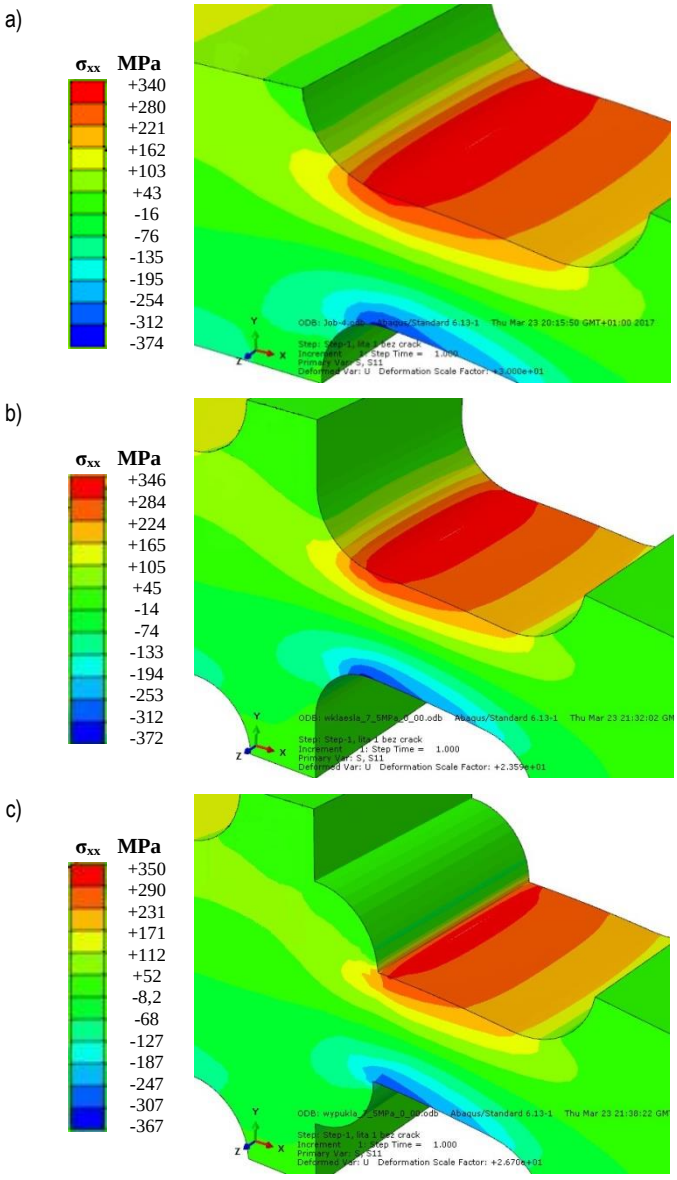

Fig. 6. Distribution of stresses (σ_{xx} component of stress tensor) in models without cracks: a) solid, b) with concave welds, c) with convex welds

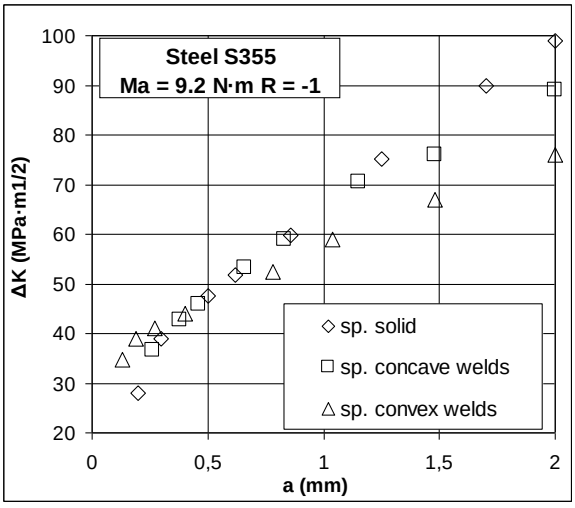

Fig. 8. Stress intensity factor range vs. cracks length calculated numerically

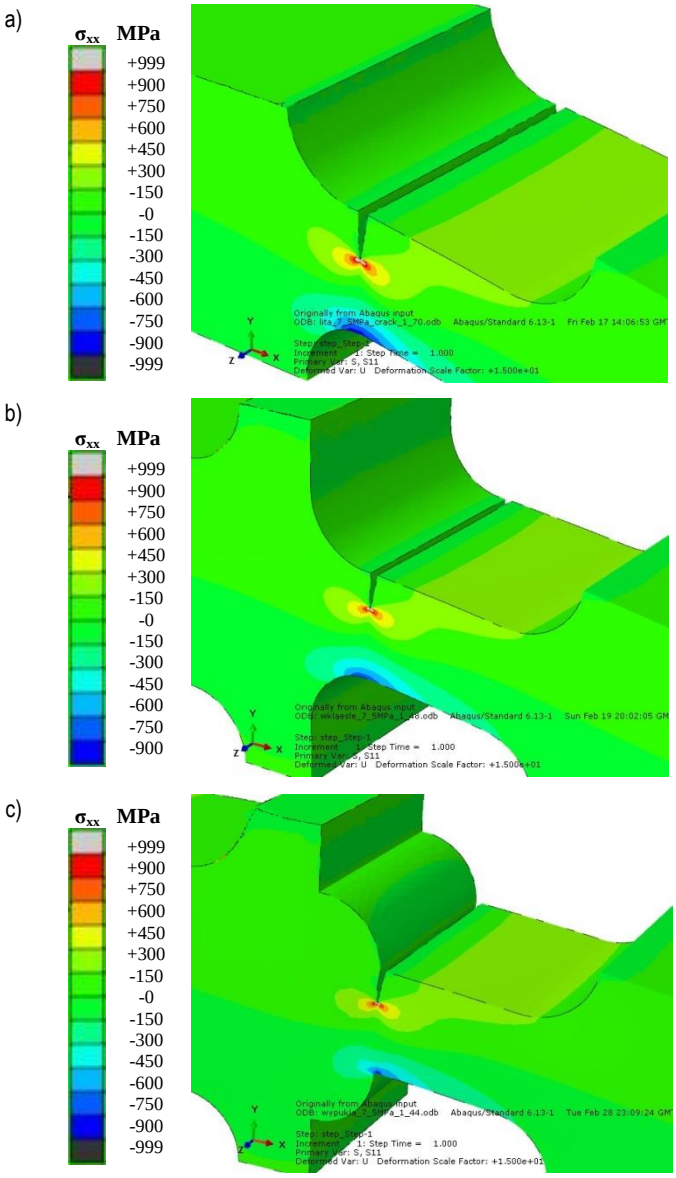

Fig. 7. Distribution of stresses (σ_{xx} component of stress tensor) in models with cracks length: a) solid a = 1.70 mm, b) with concave welds a = 1.44 mm, c) with convex welds a = 1.48 mm

4. ANALITYCAL CALCULATIONS

4.1. Methodology of conducting computations

Analytical calculations concentrated mainly on the values of stress intensity factor (SIF and its ranges) for the tested specimens with growing crack. Using the Eq. (1), the stress intensity factors were calculated for the individual crack lengths.

$$\Delta K = M_k \cdot Y \cdot \Delta\sigma \cdot \sqrt{\pi a} \tag{1}$$

where: $\Delta\sigma$ – stress range, MPa, a – crack length, mm, M_k – magnification function taking into account of the welded structure.

The specimen was subjected to bending, so the stresses deciding about demage of the specimen are derived from the stress tensor σ_{xx}. For the calculation in Eq. (1), $\Delta\sigma = \sigma_{max}$ (according to the literature (Kocańda and Szala, 1985)) was taken, i.e. in our case $\Delta\sigma = \sigma_{xx}$.

In order to explain the size of *w* and *h* of the weld and designations for equations (1) - (5), added Fig. 9.

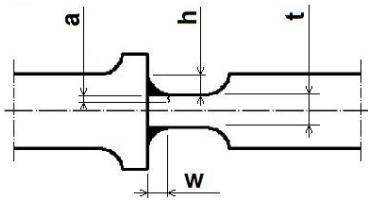

Fig. 9. Size of w and h of the weld and designations for equations (1) - (5)

Correction function Y for ΔK including shape and load of specimens was obtained from the Eq. (Rozumek and Macha, 2009)

$$Y = 5/\sqrt{20-13(a/t)-7(a/t)^2} \tag{2}$$

To calculate stress intensity factor and its ranges for welded specimens the additional correction function were applied. This function included structure and shape of welds in the analyzed specimens. The function M_k including the structure of the welded joints is identified (for this specimen) by using the equation (3, 4, and 5) (Hobbacher, 2008):

$$M_k = B \cdot \left(\frac{a}{t}\right)^k \tag{3}$$

where: a - crack length, mm, t - specimen thickness, mm.

$$B = 0.8068 - 0.1554\left(\frac{h}{t}\right) + 0.0429\left(\frac{h}{t}\right)^2 + 0.0794\left(\frac{w}{t}\right) \tag{4}$$

where: h - weld height, mm, w - weld width, mm t - specimen thickness, mm.

$$k = -0.1993 - 0.1839\left(\frac{h}{t}\right) + 0.0495\left(\frac{h}{t}\right)^2 + 0.0815\left(\frac{w}{t}\right) \tag{5}$$

4.2. Results of analytical calculations

Analytical calculations provided values for stress intensity factor range ΔK for solid, concave and convex welds specimens. The results are presented in Fig. 10.

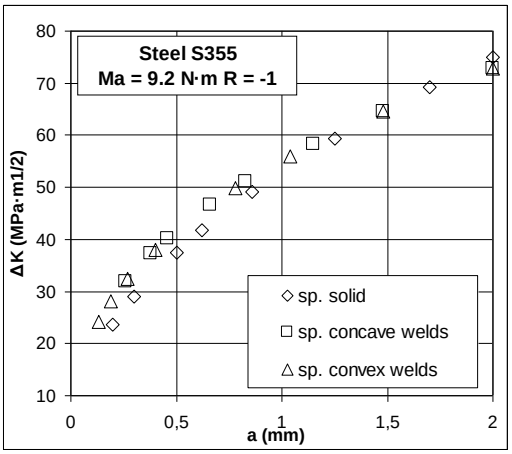

Fig. 10. Stress intensity factor range calculated analytically

5. COMPARISON OF NUMERICAL CALCULATION WITH ANALYTICAL

Figs. 11-13 presents the comparison of values for the stress intensity factor ranges ΔK obtained independently (numerically and analytically). Fig. 11 presents comparative results for solid specimens, Fig. 12 – the results for specimens with concave welds and Fig.13 - the results for specimens with convex welds.

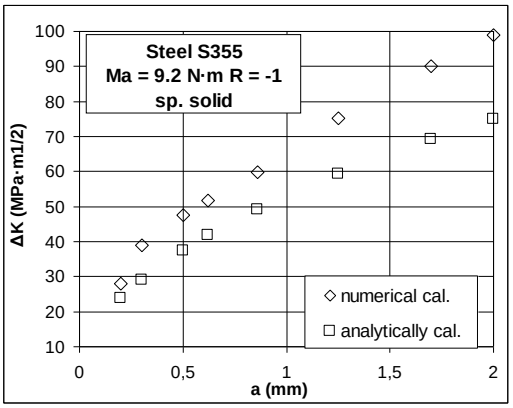

Fig. 11. Comparison of the values stress intensity factor range in crack length function calculated analytically and numerically for solid specimens

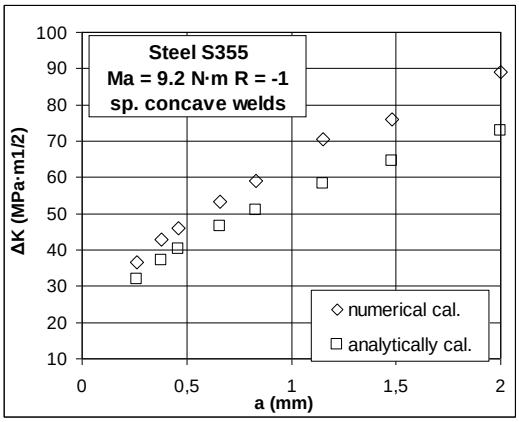

Fig. 12. Comparison of the values stress intensity factor range in crack length function calculated analytically and numerically for concave welds

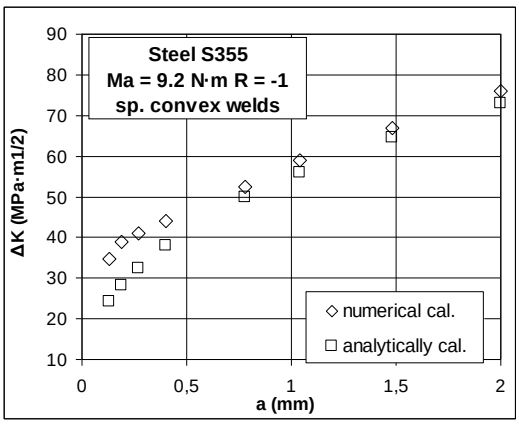

Fig. 13. Comparison of the values stress intensity factor range in crack length function calculated analytically and numerically for convex welds

DOI 10.2478/ama-2018-0006

The graphs show that the results are similar for the initial crack lengths. For the crack lengths of maximum 1 mm, the differences in values for solid specimens did not exceed 15 %, for specimens with concave welds – 13% and for specimens with convex welds – 5%. Whereas for the crack lengths up to 1.2 mm the differences in values for solid specimens did not exceed 19 %, for specimens with concave welds – 17% and for specimens with convex welds – 5.5%. For the bigger crack lengths the values are more diverging. It may be concluded then, that with the applied calculation method the results obtained numerically and analytically are similar within a certain range, in that case up to a = 1.2 mm. For more conformity of the results the calculation method should be modified by including certain correction coefficients. Based on Figs. 11 to 13 we can observe a slightly higher values of ΔK for numerical calculations. The authors believe that both methods can be applied without significant errors. Numerical calculations should be based on previous experimental studies to ensure the reliability of the results obtained. Numerical SIF calculation takes into account geometrical differences of specimens, because the dependences ΔK-a are different (Figs. 11-13). Thus, numerical method is more properly for SIF calculation of different geometry specimens.

6. CONCLUSIONS

On the basis of obtained results of numerical and analytical calculations the following conclusions can be formulated:

1. Correctly built numerical models provide good results which are similar to results obtained in experiments or analytical calculations.
2. The applied analytical formulas gave similar results to those obtained from numerical calculations for the crack lengths up to 1 mm.
3. The best compatibility of the results was obtained for welded specimens with convex welds. The error for the crack lengths up to 1.2 mm did not exceed 5.5%.
4. The biggest differences between results are for the solid samples. The error for the crack lengths up to 1.2 mm did not exceed 19%.
5. The authors paper believe that both methods can be applied without significant errors. In the case of numerical calculations should be based on previous experimental studies to ensure the reliability of the results obtained. Numerical SIF calculation takes into account geometrical differences of specimens, because the dependences $\Delta K - a$ are different (Figs. 11-13), therefore the authors propose this method.

REFERENCES

1. **Balitskii O.I., Kostyuk I.F.** (2009), Strength of welded joints of Cr-Mn steels with elevated content of nitrogen in hydrogen-containing media, *Materials Science*, 45, 97-107.
2. **Benachour M., Benguediab M., Hadjoui A., Hadjoui F., Benachour N.** (2008), Fatigue crack growth of a double fillet weld, *Computational Materials Science*, 44, 489–495.
3. **Carpinteri A., Brighenti R., Huth H.J., Vantadori S.** (2005) Fatigue growth of a surface crack in a welded T-joint, *Int. J. Fatigue*, 27, 59–69.
4. **Duchaczek A., Mańko Z.** (2012), Assessment of direct method of calculating stress intensity factor, *Journal of Science of the gen. Tadeusz Kosciuszko Military Academy of Land Forces*, 3 (165), 336-346 (in Polish).
5. **Faszynka S., Lewandowski J., Rozumek D.** (2016), Numerical analysis of stress and strain in specimens with rectangular cross-section subjected to torsion and bending with torsion, *Acta Mechanica et Automatica,* 10, 5-11.
6. **Ferro P., Berto F., James M.N.** (2016), Asymptotic residual stresses in butt-welded joints under fatigue loading, Theoretical and Applied *Fracture Mechanics*, 83, 114-124.
7. **Hobbacher A.** (2008), *Recommendations for fatigue design of welded joints and components*, International Institute of Welding, doc. XIII-2151r4-07/XV-1254r4-07,Paris, France.
8. **Kocańda S., Szala J.,** (1985), *Basics of fatigue calculations*, *PWN*, Warsaw (in Polish).
9. **Lewandowski J., Rozumek D.** (2016), Cracks growth in S355 steel under cyclic bending with fillet welded joint, *Theoretical and Applied Fracture Mechanics*, 86, 342–350.
10. **Niklas K.** (2014), Calculations of notch stress factor of a thin-walled spreader bracket fillet weld with the use of a local stress approach, *Engineering Failure Analysis*, 45, 326–338.
11. **Pakandam F., Varvani-Farahani A.** (2010), A comparative study on fatigue damage assessment of welded joints under uniaxial loading based on energy methods, *Procedia Engineering*, 2, 2027–2035.
12. **Poutiainen I., Marquis G.(**2006), A fatigue assessment method based on weld stress, *International Journal of Fatigue*, 28, 1037–1046.
13. **Rozumek D.** (2009), Influence of the slot inclination angle in FeP04 steel on fatigue crack growth under tension, *Materials & Design*, 30 1859-1865.
14. **Rozumek D., Macha E.** (2009), J-integral in the description of fatigue crack growth rate induced by different ratios of torsion to bending loading in AlCu4Mg1, *Mat.-wiss. u. Werkstofftech.,* 40 (10), 743-749.
15. **Rozumek D., Marciniak Z.** (2012), Fatigue properties of notched specimens made of FeP04 steel, *Materials Science*, 47, 462-469.
16. **Rusiński E.** (2002*), Principles of designing load-bearing structures of automobile vehicles*, Wrocław University of Science and Technology, Wrocław (in Polish).
17. **Shang Y., Shi H., Wang Z., Zhang G.** (2015), In-situ SEM study of short fatigue crack propagation behavior in a dissimilar metal welded joint of nuclear power plant, *Materials & Design*, 88, 598-609.
18. **Tanaka S., Kawahara T., Okada H.** (2014), Study on crack propagation simulation of surface crack in welded joint structure, *Marine Structures*, 39, 315-334.
19. www.cfg.cornell.edu/software/software.htm.
20. **Zhi-Gang X., Tao C., Xiao-Ling Z.** (2012), Fatigue strength evaluation of transverse fillet welded joints subjected to bending loads, *Int. J. Fatigue*, 38, 57–64.

DE GRUYTER
OPEN

DOI 10.2478/ama-2018-0007

INVARIANT, DECOUPLING AND BLOCKING ZEROS OF FRACTIONAL LINEAR SYSTEMS

Tadeusz KACZOREK*

*Faculty of Electrical Engineering, Białystok University of Technology, ul. Wiejska 45D, 15-351 Białystok, Poland

kaczorek@ee.pw.edu.pl

received 14 June 2017, revised 1 March 2018, accepted 6 March 2018

Abstract: The notions of invariant, decoupling and blocking zeros are extended to the fractional linear systems. It is shown that: 1) The zeros are closely connected with the controllability and observability of the linear systems and their transfer functions matrices. 2) The state vector of the fractional system for any input and zero initial conditions is independent of the input decoupling zeros of the system. 3) The output of the fractional system for any input and zero initial conditions is independent of the input-output decoupling zeros of the system.

Key words: Fractional, Linear, System, Invariant, Decoupling, Blocking Zero

1. INTRODUCTION

The notion of controllability and observability and the decomposition of linear systems have been introduced by Kalman (1960, 1963). These notions are the basic concepts of the modern control theory (Antsaklis and Michel, 2006; Kaczorek, 1993; Kailath, 1980; Rosenbrock, 1970; Wolovich, 1974; Valcher, 1977). They have been also extended to positive linear systems (Farina and Rinaldi, 2000; Kaczorek, 2011a). The positive circuits and their reachability has been investigated in (Kaczorek, 2011a; Kaczorek and Rogowski, 2015) and controllability and observability of electrical circuits in (Kaczorek, 2011c; Kaczorek and Rogowski, 2015).

The reachability of linear systems is closely related to the controllability of the systems. Specially for positive linear systems, the conditions for the controllability are much stronger than for the reachability (Kaczorek, 2002, 2016). Tests for the reachability and controllability of standard and positive linear systems are given in Kaczorek (2002, 2008) and in Kaczorek and Rogowski (2015). The positivity and reachability of fractional continuous-time linear systems and electrical circuits have been addressed in (Kaczorek, 2008, 2011a, 2013d; Kaczorek and Rogowski, 2015). The finite zeros of positive discrete-time and continuous-time linear systems have been investigated in Tokarzewski (2011a, 2011b) and the decoupling zeros of positive discrete-time linear systems and positive electrical circuits in Kaczorek (2010, 2013b).

The positive linear systems consisting of n subsystems with different fractional orders has been analyzed in Kaczorek (2011b). Some recent interesting results in the fractional systems theory and its applications can be found in Dzieliński Sierociuk and Sarwas (2009) and in Kaczorek (2017b). The constructability and observability of standard and positive electrical circuits in Kaczorek (2013a). The stability of fractional systems has been analysed in (Busłowicz, 2008; Dzieliński and Sierociuk, 2008; Kaczorek, 2008, 2009).

The invariant, decoupling and blocking zeros of linear positive systems and electrical circuits have been addressed in Kaczorek (1993, 2017b).

In this paper the notions of invariant zeros, decoupling zeros and blocking zeros of linear systems will be extended to the fractional linear systems. The paper is organized as follows. In section 2 the elementary operations and Smith canonical form of polynomial matrices are recalled. Basic definitions and theorems concerning the invariant, decoupling and blocking zeros of fractional linear systems are presented in section 3. Concluding remarks are given in section 4.

The following notation will be used: $\Re$ is the set of real numbers, $\Re^{n\times m}$ represents the set of $n \times m$ real matrices, $\Re^{n\times m}[s]$ denotes the set of $n \times m$ polynomial matrices with real coefficients, C is the field of complex numbers, I_n is the $n \times n$ identity matrix.

2. ELEMENTARY OPERATIONS AND SMITH CANONICAL FORM OF POLYNOMIAL MATRICES

Definition 1. (Kaczorek, 1993) The following operations on polynomial matrices are called elementary row (column) operations:

- Multiplication of the i-th row (column) by scalar (number) c. This operation will be denoted by $L(i \times c)(R(i \times c))$.
- Addition to the i-th row (column) of the j-th row (column) multiplied by any polynomial $b(s)$. This operation will be denoted by $L(i + j \times b(s))(R(i + j \times b(s)))$.
- Intercharge of the i-th and j-th rows (columns). This operations will be denoted by $L(i, j)(R(i, j))$.

Applying the elementary row and column operations to identity matrices we obtain unimodulary matrices. The elementary row (column) operations are equivalent to premultiplication (postmultiplication) of the matrix by suitable unimodular matrices (Kaczorek 1993). The elementary row and column operations do not change the rank of the matrices.

DOI 10.2478/ama-2018-0007

Definition 2. (Gantmacher, 1988, Kaczorek, 1993) The polynomial matrix:

$$A_S(s) = \begin{bmatrix} a_1(s) & 0 & \cdots & 0 & 0 & \cdots & 0 \\ 0 & a_2(s) & \cdots & 0 & 0 & \cdots & 0 \\ \vdots & \vdots & \ddots & \vdots & \vdots & \ddots & \vdots \\ 0 & 0 & \cdots & a_r(s) & 0 & \cdots & 0 \\ 0 & 0 & \cdots & 0 & 0 & \cdots & 0 \\ \vdots & \vdots & \ddots & \vdots & \vdots & \ddots & \vdots \\ 0 & 0 & \cdots & 0 & 0 & \cdots & 0 \end{bmatrix} \in \Re^{m\times p}[s] \quad (1)$$

is called the Smith canonical form of the polynomial matrix $\mathrm{A(s)} \in \Re^{\mathrm{m\times p}}[\mathrm{s}]$, where $\mathrm{a_1(s)}$, $\mathrm{a_2(s)}$, ..., $\mathrm{a_r(s)}$ are nonzero invariant polynomials (with leading coefficients equal to 1) of the matrix $\mathrm{A(s)}$ such that $\mathrm{a_i(s)|a_{i+1}(s)}$ ($\mathrm{a_i(s)}$ divides $\mathrm{a_{i+1}(s)}$ with zero remainder) for $\mathrm{i} = 1,\ldots,\mathrm{r}-1$ and $\mathrm{r} = \mathrm{rankA(s)}$.

The invariant polynomials $\mathrm{a_1(s)}$, $\mathrm{a_2(s)}$, ..., $\mathrm{a_r(s)}$ of the matrix $\mathrm{A(s)}$ are uniquely determined by:

$$a_k(s) = \frac{D_k(s)}{D_{k-1}(s)} \text{ for } k = 1,\ldots,r\ (D_0(s) = 1), \quad (2)$$

where $\mathrm{D_k(s)}$ is the greatest common divisor of all of the $\mathrm{k}\times\mathrm{k}$ minors of the matrix $\mathrm{A(s)}$.

The equivalent polynomial matrices have the same greatest common divisors $\mathrm{D_k(s)}$ (Kaczorek, 1993).

3. INVARIANT, DECOUPLING AND BLOCKING ZEROS OF FRACTIONAL LINEAR SYSTEMS

Consider the fractional linear system (Kaczorek, 2011d):

$$\frac{d^\alpha x(t)}{dt^\alpha} = Ax(t) + Bu(t),\ 0 < \alpha < 1 \quad (3a)$$

$$y = Cx, \quad (3b)$$

where:

$$_0D_t^\alpha f(t) = \frac{d^\alpha f(t)}{dt^\alpha} = \frac{1}{\Gamma(1-\alpha)}\int_0^t \frac{\dot{f}(\tau)}{(t-\tau)^\alpha}d\tau, \quad (3c)$$

is Caputo definition of the fractional derivative of α order, $\dot{\mathrm{f}}(\tau) = \frac{\mathrm{df}(\tau)}{\mathrm{d}\tau}$, $\Gamma(\mathrm{x}) = \int_0^\infty \mathrm{t}^{\mathrm{x}-1}\mathrm{e}^{-\mathrm{t}}\mathrm{dt}$, $\mathrm{Re(x)} > 0$ is the Euler gamma function and $\mathrm{x} = \mathrm{x(t)} \in \Re^{\mathrm{n}}$, $\mathrm{u} = \mathrm{u(t)} \in \Re^{\mathrm{m}}$, $\mathrm{y} = \mathrm{y(t)} \in \Re^{\mathrm{p}}$ are the state, input and output vectors and $\mathrm{A} \in \Re^{\mathrm{n\times n}}$, $\mathrm{B} \in \Re^{\mathrm{n\times m}}$, $\mathrm{C} \in \Re^{\mathrm{p\times n}}$.

The system matrix of the linear system (3) is defined by:

$$S(\lambda) = \begin{bmatrix} I_n\lambda - A & B \\ C & 0 \end{bmatrix} \in \Re^{(n+p)\times(n+m)}[\lambda],\ \lambda = s^\alpha \quad (4)$$

Let the matrix:

$$S_S(\lambda) = \begin{bmatrix} \mathrm{diag}[p_1(\lambda) & \cdots & p_r(\lambda)] & 0 \\ 0 & & & 0 \end{bmatrix} \in \Re^{(n+p)\times(n+m)}[\lambda] \quad (5)$$

be the canonical Smith form of the system matrix (4), where $\mathrm{p_1(\lambda)}$, ..., $\mathrm{p_r(\lambda)}$ are the invariant polynomials satisfying the condition $\mathrm{p_i(\lambda)|p_{i+1}(\lambda)}$ for $\mathrm{i} = 1,\ldots,\mathrm{r}-1$ and $\mathrm{r} = \mathrm{rankS(\lambda)}$.

The invariant polynomials are determined by:

$$p_k(\lambda) = \frac{D_k(\lambda)}{D_{k-1}(\lambda)} \text{ for } k = 1,\ldots,r\ (D_0(\lambda) = 1). \quad (6)$$

From (6) we have:

$$p(\lambda) = p_1(\lambda)\ldots p_r(\lambda) = \frac{D_1(\lambda)}{D_0(\lambda)}\frac{D_2(\lambda)}{D_1(\lambda)}\ldots\frac{D_r(\lambda)}{D_{r-1}(\lambda)} = D_r(\lambda). \quad (7)$$

The polynomial $\mathrm{p(\lambda)}$ is called the invariant zero polynomial of the system (3).

Definition 3. The zero of the polynomial $\mathrm{p(\lambda)}$ is called the invariant zero of the system (3.1).

Theorem 1. (Kaczorek, 1993) If $\mathrm{m} = \mathrm{p}$ and the matrix (4) has full rank then:

$$p(\lambda) = \det S_S(\lambda) = c\det S_S(\lambda), \quad (8)$$

where $\mathrm{c} = \mathrm{detL(\lambda)detR(\lambda)}$ since $\mathrm{L(\lambda)}$ and $\mathrm{R(\lambda)}$ are unimodular matrices of elementary row and column operations.

Theorem 2. If $\mathrm{m} = \mathrm{p}$ then:

$$p(\lambda) = \det\begin{bmatrix} I_n\lambda - A & -B \\ C & 0 \end{bmatrix} = \det[I_n\lambda - A]\det T(\lambda), \quad (9)$$

where:

$$T(\lambda) = C[I_n\lambda - A]^{-1}B. \quad (10)$$

Proof. It is easy to see that:

$$\begin{bmatrix} I_n & 0 \\ -C[I_n\lambda - A]^{-1} & I_p \end{bmatrix}\begin{bmatrix} I_n\lambda - A & -B \\ C & 0 \end{bmatrix} = \begin{bmatrix} I_n\lambda - A & -B \\ 0 & T(\lambda) \end{bmatrix} \quad (11)$$

and:

$$\det\left\{\begin{bmatrix} I_n & 0 \\ -C[I_n\lambda - A]^{-1} & I_p \end{bmatrix}\begin{bmatrix} I_n\lambda - A & -B \\ C & 0 \end{bmatrix}\right\} = \det\begin{bmatrix} I_n\lambda - A & -B \\ 0 & T(\lambda) \end{bmatrix} \quad (12a)$$

since:

$$\det\begin{bmatrix} I_n & 0 \\ -C[I_n\lambda - A]^{-1} & I_p \end{bmatrix} = 1. \quad (12b)$$

□

Consider the submatrix:

$$S_1(\lambda) = [I_n\lambda - A \quad B] \quad (13)$$

of the system matrix (4).

Definition 4. (Kaczorek, 1993) A number $\mathrm{z} \in \mathrm{C}$ for which:

$$\mathrm{rank}[I_n z - A \quad B] < n \quad (14)$$

is called the input decoupling (i.d.) zero of the fractional system (3).

Let the matrix:

$$S_{1S}(\lambda) = [\mathrm{diag}[\bar{p}_1(\lambda) \quad \cdots \quad \bar{p}_n(\lambda)] \quad 0] \in \Re^{n\times(n+m)}[\lambda] \quad (15)$$

be the canonical Smith form of the matrix (13).

Note that $\mathrm{z} \in \mathrm{C}$ is an i.d. zero of the system (3) if and only if z is a zero of the polynomial:

$$\bar{p}(\lambda) = \bar{p}_1(\lambda)\ldots\bar{p}_n(\lambda). \quad (16)$$

DOI 10.2478/ama-2018-0007

Therefore, the i.d. zeros of the system are the zeros of the polynomial (16). The system has no i.d. zeros if and only if $\bar{p}(\lambda) = 1$, i.e. the matrix $S_1(\lambda)$ has the canonical Smith form $[I_n \quad 0]$. The i.d. zeros represent unreachable modes of the system (3) (Kaczorek, 1993).

The number of i.d. zeros n_1 of the system (3) is equal to the rank defect of its reachability (controllability) matrix, i.e.

$$n_1 = n - \text{rank}R_n, \tag{17}$$

where:

$$R_n = [B \quad AB \quad \cdots \quad A^{n-1}B]. \tag{18}$$

Theorem 3. (Kaczorek 1993) The state vector x of the fractional system (3) for any input $u(t)$ and zero initial state $x(0) = 0$ is independent of the i.d. zeros of the system.

Consider the submatrix:

$$S_2(\lambda) = \begin{bmatrix} I_n\lambda - A \\ C \end{bmatrix} \tag{19}$$

of the system matrix (4).

Definition 5. (Kaczorek 1993) A number $z \in C$ for which:

$$\text{rank}\begin{bmatrix} I_n z - A \\ C \end{bmatrix} < n \tag{20}$$

is called the output-decoupling (o.d.) zero of the fractional system (3).

Let the matrix:

$$S_{2S}(\lambda) = \begin{bmatrix} \text{diag}[\hat{p}_1(\lambda) \quad \cdots \quad \hat{p}_n(\lambda)] \\ 0 \end{bmatrix} \in \Re^{(n+p)\times n}[\lambda] \tag{21}$$

be the canonical Smith form of the matrix (19).

Note that $z \in C$ is an o.d. zero of the system (3) if and only if z is a zero of the polynomial:

$$\hat{p}(\lambda) = \hat{p}_1(\lambda)\ldots\hat{p}_n(\lambda). \tag{22}$$

Therefore, the o.d. zeros of the system are the zeros of the polynomial (22). The system has no o.d. zeros if and only if $\hat{p}(\lambda) = 1$, i.e. the matrix $S_2(\lambda)$ has the canonical Smith form $\begin{bmatrix} I_n \\ 0 \end{bmatrix}$. The o.d. zeros represent unobservable modes of the system (3) (Kaczorek, 1993).

The number of o.d. zeros n_2 of the system (3) is equal to the rank defect of its observability matrix, i.e.

$$n_2 = n - \text{rank}O_n, \tag{23}$$

where:

$$O_n = \begin{bmatrix} C \\ CA \\ \vdots \\ CA^{n-1} \end{bmatrix}. \tag{24}$$

Theorem 4. (Kaczorek, 1993) The output y of the fractional system (3) for any input $u'(t) = Bu(t)$ and zero initial condition $x(0) = 0$ is independent of the o.d. zeros of the system.

Definition 6. (Kaczorek, 1993) A number $z \in C$ for which both conditions (14) and (20) are satisfied is called the input-output decoupling (i.o.d.) zero of the fractional system (3).

Therefore, $z \in C$ is an i.o.d. zero if and only if it is both an i.d. zero and an o.d. zero of the system.

The number of i.o.d. zeros n_{io} of the fractional system (3) is equal to:

$$n_{io} = n - \text{rank}R_n - \text{rank}O_n + \text{rank}O_nR_n. \tag{25}$$

Definition 7. (Kaczorek, 1993) A number $z \in C$ is called a blocking zero of the system (3) if:

$$C[I_n z - A]_{ad}B = 0, \tag{26}$$

where $[I_n z - A]_{ad}$ is the adjoint matrix.

If (26) is satisfied for all λ then by definition the system has no blocking zeros.

Theorem 5. (Kaczorek, 1993) A number $z \in C$ is an uncontrollable and/or unobservable mode of the system if and only if z is a blocking zero of the system.

Theorem 6. If the transfer function matrix:

$$T(\lambda) = C[I_n\lambda - A]^{-1}B = 0 \tag{27}$$

then:

$$O_nR_n = 0, \tag{28}$$

where O_n and R_n are defined by (24) and (18), respectively.

Proof. Note that if (27) holds then:

$$CA^kB = 0 \text{ for } k = 0,1,\ldots,n-1. \tag{29}$$

Using (24), (18) and (29) we obtain:

$$\begin{aligned} O_nR_n &= \begin{bmatrix} C \\ CA \\ \vdots \\ CA^{n-1} \end{bmatrix}[B \quad AB \quad \cdots \quad A^{n-1}B] \\ &= \begin{bmatrix} CB & CAB & \cdots & CA^{n-1}B \\ CAB & CA^2B & \cdots & CA^nB \\ \vdots & \vdots & \ddots & \vdots \\ CA^{n-1}B & CA^nB & \cdots & CA^{2(n-1)}B \end{bmatrix} = 0. \end{aligned} \tag{30}$$

This completes the proof. □

Theorem 7. Let for the fractional system (3) the condition (27) be satisfied. Then:

1. the pair (A,B) is unreachable if $C \neq 0$,
2. the pair (A,C) is unobservable if $B \neq 0$.

Proof. From (13) we have:

$$C[B \quad AB \quad \cdots \quad A^{n-1}B] = 0 \tag{31}$$

and:

$$\text{rank}[B \quad AB \quad \cdots \quad A^{n-1}B] < n \tag{32}$$

if $C \neq 0$. Therefore, the pair (A,B) is unreachable.

Similarly, from (30) we have:

$$\begin{bmatrix} C \\ CA \\ \vdots \\ CA^{n-1} \end{bmatrix} B = 0 \tag{33}$$

and:

$$\text{rank}\begin{bmatrix} C \\ CA \\ \vdots \\ CA^{n-1} \end{bmatrix} < n \tag{34}$$

if $B \neq 0$. Therefore, the pair (A,C) is unobservable. □

DOI 10.2478/ama-2018-0007

Example 1. Consider the electrical circuit shown in Fig. 1 with given resistances R_1, R_2, R_3, R_4, inductance L, capacitance C and voltage source e.

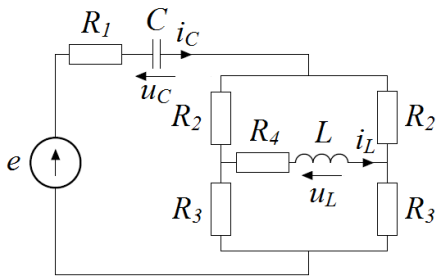

Fig. 1. Electrical circuit of Example 1

Knowing that $\mathrm{i_c} = \mathrm{C}\frac{\mathrm{d}^\alpha \mathrm{u_C}}{\mathrm{dt}^\alpha}$, $\mathrm{u_L} = \mathrm{L}\frac{\mathrm{d}^\alpha \mathrm{i_L}}{\mathrm{dt}^\alpha}$ and using Kirchhoff's laws we may write the equations:

$$e = RC\frac{d^\alpha u_C}{dt^\alpha} + u_C, R = R_1 + \frac{R_2+R_3}{2},$$
$$R_4 i_L + L\frac{d^\alpha i_L}{dt^\alpha} = 0. \tag{35}$$

As the output y we choose:

$$y = i_L. \tag{36}$$

The equations (35) and (36) can be rewritten in the form:

$$\frac{d^\alpha}{dt^\alpha}\begin{bmatrix} u_C \\ i_L \end{bmatrix} = A_2\begin{bmatrix} u_C \\ i_L \end{bmatrix} + B_2 e, y = C_2\begin{bmatrix} u_C \\ i_L \end{bmatrix}, \tag{37a}$$

where:

$$A_2 = \begin{bmatrix} -\frac{1}{RC} & 0 \\ 0 & -\frac{R_4}{L} \end{bmatrix}, B_2 = \begin{bmatrix} \frac{1}{RC} \\ 0 \end{bmatrix}, C_2 = [0 \quad 1]. \tag{37b}$$

The transfer function of the electrical circuit is:

$$T(\lambda) = C_2[I_2\lambda - A_2]^{-1}B_2$$
$$= [0 \quad 1]\begin{bmatrix} \lambda + \frac{1}{RC} & 0 \\ 0 & \lambda + \frac{R_4}{L} \end{bmatrix}^{-1}\begin{bmatrix} \frac{1}{RC} \\ 0 \end{bmatrix} = 0 \tag{38}$$

for all values of R_1, R_2, R_3, R_4, L and C.

The electrical circuit with (37b) is unreachable and unobservable since the matrices:

$$R_2 = [B_2 \quad A_2B_2] = \begin{bmatrix} \frac{1}{RC} & -\frac{1}{(RC)^2} \\ 0 & 0 \end{bmatrix},$$
$$O_2 = \begin{bmatrix} C_2 \\ C_2A_2 \end{bmatrix} = \begin{bmatrix} 0 & 1 \\ 0 & -\frac{R_4}{L} \end{bmatrix} \tag{39}$$

have only one nonzero column and one nonzero row, respectively. From (39) we have:

$$O_2R_2 = \begin{bmatrix} 0 & 1 \\ 0 & -\frac{R_4}{L} \end{bmatrix}\begin{bmatrix} \frac{1}{RC} & -\frac{1}{(RC)^2} \\ 0 & 0 \end{bmatrix} = \begin{bmatrix} 0 & 0 \\ 0 & 0 \end{bmatrix}. \tag{40}$$

From (14) and (37b) we obtain:

$$\mathrm{rank}[I_n z - A_2 \quad B_2] = \mathrm{rank}\begin{bmatrix} z + \frac{1}{RC} & 0 & \frac{1}{RC} \\ 0 & z + \frac{R_4}{L} & 0 \end{bmatrix} = 1 \tag{41}$$

Therefore, by Definition 4 the electrical circuit has one input-decoupling zero $z_1 = -\frac{R_4}{L}$.

From (14) and (37b) we have:

$$\mathrm{rank}\begin{bmatrix} I_n z - A_2 \\ C_2 \end{bmatrix} = \mathrm{rank}\begin{bmatrix} z + \frac{1}{RC} & 0 \\ 0 & z + \frac{R_4}{L} \\ 0 & 1 \end{bmatrix} = 1 \tag{42}$$

and by Definition 5 the electrical circuit has also one output-decoupling zero $z_2 = -\frac{1}{RC}$.

Therefore by Definition 5 the electrical circuit has no input-output decoupling zeros since $\mathrm{z_1} \neq \mathrm{z_2}$.

From (42) it follows that the electrical circuit has no blocking zeros since (38) holds for all λ.

4. CONCLUDING REMARKS

The notions of invariant, decoupling and blocking zeros have been extended to the fractional linear systems. The relationship between the decoupling zeros and the controllability and observability of the fractional linear systems has been shown. It has been also shown that if the transfer matrix is zero then the product of the observability and controllability matrices is zero matrix (Theorem 6) and if the product is zero then the pair (A, B) is unreachable if $\mathrm{C} = 0$ and the pair (A, C) is unobservable if $\mathrm{B} = 0$ (Theorem 7). The considerations can be extended to the positive fractional linear systems and electrical circuits.

REFERENCES

1. **Antsaklis E., Michel A.** (2006), *Linear Systems*, Birkhauser, Boston.
2. **Busłowicz M.** (2008), Stability of linear continuous-time fractional order systems with delays of the retarded type, *Bull. Pol. Acad. Sci. Tech.*, 56(4). 319-324.
3. **Dzieliński A., Sierociuk D.** (2008), Stability of discrete fractional order state-space systems, *Journal of Vibrations and Control*, 14(9-10), 1543-1556.
4. **Dzieliński A., Sierociuk D., Sarwas G.** (2009), Ultracapacitor parameters identification based on fractional order model, *Proc. European Control Conference*, Budapest, Hungary, 196-200.
5. **Farina L., Rinaldi S.** (2000), *Positive Linear Systems: Theory and Applications*, J. Wiley & Sons, New York.
6. **Gantmacher, F.R.** (1988), *The theory of matrices*, AMS Chelsea Publishing, Rhode Island.
7. **Kaczorek T.** (1993), *Linear Control Systems*, vol. 1, J. Wiley, New York.
8. **Kaczorek T.** (2002), *Positive 1D and 2D Systems*, Springer-Verlag, London.
9. **Kaczorek T.** (2008), Practical stability of positive fractional discrete-time linear systems, *Bull. Pol. Acad. Sci. Tech.*, 56(4), 313-317.
10. **Kaczorek T.** (2009), Asymptotic stability of positive fractional 2D linear systems, *Bull. Pol. Acad. Sci. Tech.*, 57(3), 289-292.
11. **Kaczorek T.** (2010), Decoupling zeros of positive discrete-time linear systems, *Circuits and Systems*, 1, 41-48.

DOI 10.2478/ama-2018-0007

12. **Kaczorek T.** (2011a), Positive electrical circuits and their reachability, *Archives of Electrical Engineering*, 60(3), 283-301.
13. **Kaczorek T.** (2011b), Positive linear systems consisting of n subsystems with different fractional orders, *IEEE Trans. Circuits and Systems*, 58(6), 1203-1210.
14. **Kaczorek T.** (2011c), Positivity and reachability of fractional electrical circuits, *Acta Mechanica et Automatica*, 5(2), 42-51.
15. **Kaczorek T.** (2011d), *Selected Problems of Fractional Systems Theory*, Springer-Verlag, Berlin.
16. **Kaczorek T.** (2013a), Constructability and observability of standard and positive electrical circuits, *Electrical Review*, 89(7), 132-136.
17. **Kaczorek T.** (2013b), Decoupling zeros of positive electrical circuits, *Archives of Electrical Engineering*, 62(4), 553-568.
18. **Kaczorek T.** (2017a), Invariant, decoupling and blocking zeros of positive linear electrical circuits with zero transfer matrices, *Circuits, Systems, and Signal Processing*, 36(11), 4716-4728.
19. **Kaczorek T.** (2017b), Specific properties of invariant, decoupling and blocking zeros of positive linear electrical circuits with zero transfer matrices, Proc. of SPIE, 104451C.
20. **Kaczorek T., Rogowski K.** (2015), *Fractional Linear Systems and Electrical Circuits, Studies in Systems*, Decision and Control, vol. 13, Springer.
21. **Kailath T.** (1980), *Linear systems*, Prentice Hall, Englewood Cliffs, New York.
22. **Kalman R.** (1960), On the general theory of control systems, *Proc. First Intern. Congress on Automatic Control*, London, UK: Butterworth, 481-493.
23. **Kalman R.** (1963), Mathematical description of linear systems, *SIAM J. Control*, 1(2), 152-192.
24. **Rosenbrock H.** (1970), *State-space and multivariable theory*, J. Wiley, New York.
25. **Tokarzewski J.** (2011a), Finite zeros of positive linear discrete-time systems, *Bull. Pol. Acad. Sci. Tech.*, 59(3), 287-292.
26. **Tokarzewski J.** (2011b), Finite zeros of positive continuous-time systems, *Bull. Pol. Acad. Sci. Tech.*, 59(3), 293-298.
27. **Valcher M.E.** (1977), On the initial stability and asymptotic behaviour of 2D positive systems, *IEEE Trans. on Circuits and Systems – I*, 44(7), 602-613.
28. **Wolovich W.A.** (1974), *Linear Multivariable Systems*, Springer-Verlag, New York.

Acknowledgment: The studies have been carried out in the framework of work No. S/WE/1/2016 and financed from the funds for science by the Polish Ministry of Science and Higher Education.

DE GRUYTER
OPEN

DOI 10.2478/ama-2018-0008 acta mechanica et automatica, vol.12 no.1 (2018)

IMAGE PROCESSING TECHNIQUES FOR ROI IDENTIFICATION IN RHEUMATOID ARTHRITIS PATIENTS FROM THERMAL IMAGES

Agnieszka WASILEWSKA[*], Jolanta PAUK[*], Mikhail IHNATOUSKI[**]

[*]Faculty of Mechanical Engineering, Department of Automatic Control and Robotics, Bialystok University of Technology, ul. Wiejska 45C, 15-351 Bialystok, Poland
[**]Scientific and Research Department, Yanka Kupala State University of Grodno, Grodno, Belarus

a.wasilewska@doktoranci.pb.edu.pl, j.pauk@pb.edu.pl, mii_by@mail.ru

received 2 October 2017, revised 5 March 2018, accepted 9 March 2018

Abstract: Rheumatoid arthritis (RA) is a systemic autoimmune disease that manifests itself by joint inflammation, swelling, pain, tenderness and may involve extra-articular organs in severe cases. Joint inflammatory lesions are associated with higher temperature due to increased vascularity in the area of inflamed tissues. This papers aimed to identify heat patterns from ROIs to interpret the presence of inflammation in rheumatoid arthritis patients. The thermovisual image sequences were collected from 65 patients with Rheumatoid Arthritis (RA). Infrared images were generated by a thermal scanning camera (FLIR E60bx Systems Inc., USA). Separate recordings of left and right foot temperature changes were performed for 3 minute periods. The temperature measurement was performed at the moment right after cold water immersion (post-cooling temperature) and at the moment after thermal recovery (post-recovery temperature). The recording of 3-minute foot thermal recovery was used for analysis. Automatically identified ROI corresponds to the area of the soft tissues covering cuboid and navicular bone.

Keywords: Dynamic Thermography, Image Processing, Segmentation, Inflammation

1. INTRODUCTION

Rheumatoid arthritis (RA) is a systemic autoimmune disease that manifests itself by joint inflammation, swelling, pain, tenderness and may involve extra-articular organs in severe cases (Cojocaru, 2010). The disease majorly involves the small joints of the hand and feet (Gabriel, 2001). Early diagnosis of RA is necessary as uncontrolled disease progression may lead to bone destructions and disabilities. Joint inflammatory lesions are associated with higher temperature due to increased vascularity in the area of inflamed tissues (Fernández, 2015). Thus, joint temperature comprises a promising diagnostic parameter in identifying rheumatoid arthritis. Owing to the fact that every object, including human skin, emits infrared radiation, these pathological changes can be observed with the use of Infrared thermography (IT): an imagining technique that enables detecting this emission (Tattersall, 2016). This method has received a great deal of particular attention in science and medical practice for several decades (Jones, 1998).Infrared thermography, when compared to temperature measured by contact probes, gives a distribution over a surface instead of a scalar value (Ludwig, 2014). This method of temperature measurement enables to map body surface temperature remotely (Lahiri, 2012). Its low price and non-invasiveness are primary reasons to explore the diagnostic potential of this method. In medicine usefulness of IT has been first noticed after observation of asymmetric hot spots and vascularity in thermal breast images of patients with breast cancer. The diagnostic basis of IR thermography in clinical use is the increased vascularity of pathological lesions, e.g. inflammation or neoplasms, which results in the rise of skin temperature and these changes can be detected by infrared camera (Ring, 1998). The dynamic procedure includes the application of specific stimuli, e.g. local cooling or heating on measured object. Afterwards, the evolution of surface temperature distribution is registered during the transitional process. These changes are recorded as dynamic thermogram or a sequence of thermal images. Wasilewska noted that due to additional time information and minimal dependency on external and host conditions dynamic thermography presents certain advantages over static IT (Wasilewska, 2017). In active thermography, surface temperature reacts to applied cold excitation, and these changes depend on the internal structure and inform about thermal properties of the analysed material, which poses a significant value in diagnosing subcutaneous tissues abnormalities, especially tumours and inflammatory lesions (Kaczmarek, 2016). Due to safety issues, the shape of thermal stimulus and its exposition time should be controlled. In human examinations, to avert biofeedback and reduce the influence of thermoregulatory process, no more than one-minute exposition is recommended (Kaczmarek, 2016). Wasilewska and Pauk suggested applying 5-second cooling period in dynamic IT examinations of rheumatoid arthritis lesions as it provides discernible effects and safety examination conditions (Wasilewska, 2017). In literature, scientists indicate different medical praxis of active thermography, e.g. Purslow et al. used active thermography to analyze the effect of contact lens wear on dynamic ocular surface temperature (Purslow, 2005). Several authors presented the usefulness of active thermography in skin burn diagnostics (Renkielska, 2006; Renkielska, 2014), evaluation of cardiosurgery and post-cardiosurgery wound healing (Nowakowski, 2014; Nowakowski, 2015), plastic surgery (John, 2016) or skin cancer (Herman, 2011). Thermal images lack shape and precise limits (Afshar, 2017). Infrared thermograms are usually captured in a large area,

DOI 10.2478/ama-2018-0008

then the unnecessary regions and background from the thermogram images before further processing should be removed (Dey, 2017). In the aims of ROI extraction from the thermal infrared image, the ROI segmentation should be performed to partition the thermal image into multiple segments as a set of pixels or superpixels (Bezerra, 2013). After segmentation, features extraction specifies the quantifiable property of the thermal image. Typical measurements are: minimum and maximum temperatures and region statistics, e.g. averages and standard deviations (Barcelos, 2014). This papers aimed to identify heat patterns from ROIs to interpret the presence of inflammation in rheumatoid patients.

2. METHODS

2.1 Thermovisual images acquisition

The thermovisual image sequences were collected from 65 patients with Rheumatoid Arthritis (RA). None of the participants had a health condition, which would impact study outcome. Inclusion criteria for patients recruited for the study included: age above 18 years old, the duration of treatment above 1 year. All subjects received full information about the study before giving signed consent. The ethical committee approved the study (Medical University of Bialystok, Poland). Infrared images were generated by a thermal scanning camera (FLIR E60bx Systems Inc., USA). The camera was calibrated by the manufacturer for reproducibility and accuracy of readings. The image resolution was 320×240 pixels. The patients stayed in seated position for 10 minutes in the examination room before the registration began. The camera was mounted on a standard camera tripod located at 1.0 meter from the skin surface. Experiments demonstrated that the most convenient cooling method for the foot is the application of ice water for 5 seconds. It cooled the skin by about 5-70C below its initial normal temperature. Separate recordings of left and right foot temperature changes were performed for 3 minute periods. The temperature measurement was performed at the moment right after cold water immersion (post-cooling temperature) and at the moment after thermal recovery (post-recovery temperature). The ambient temperature during measurements was 23°C, relative humidity 55%. Fig.1 and Fig. 2 demonstrate thermal images post-cooling and post-recovery. Thermal recovery registration was accomplished simultaneously for healthy and unhealthy parts of the skin.

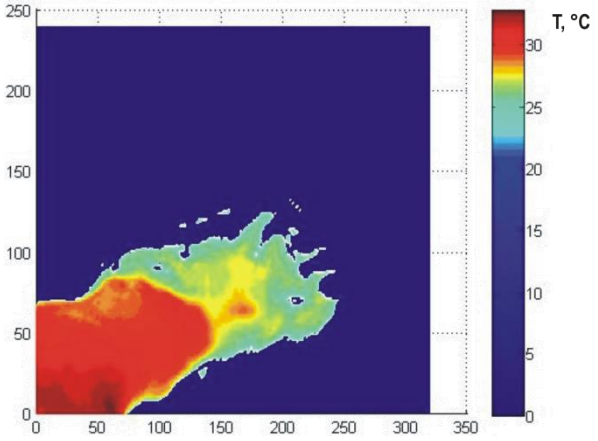

Fig. 1. Thermal image post-cooling

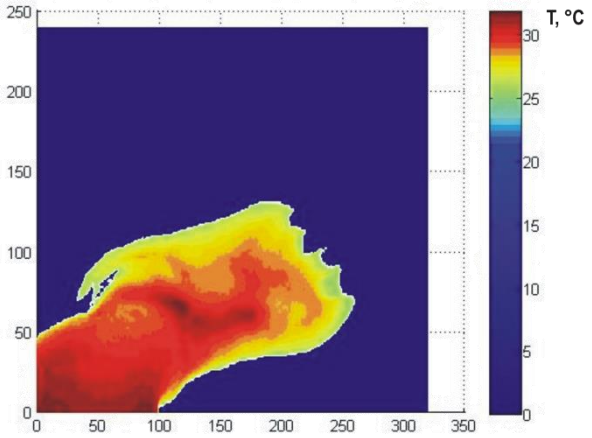

Fig. 2. Thermal image post-recovery

There are definite differences between post-cooling and post-recovery temperature distributions in the dorsal part of RA patient's foot ($p<0.05$).

2.2 Image processing and analysis

The recording of 3-minute foot thermal recovery was used for analysis. The last frame's temperature distribution diagram was generated. It was bimodal with a first maximum in the standard temperature of background and second maximum in the standard temperature of the body. The local minimum between the first and second maximums was found, and it comprised the level of thresholding. Thresholding technique was used to isolate foot in the thermal image. Arithmetical mean of the temperature of the foot was calculated starting from the first frame up to the last frame. The images were segmented on the basis of a multidimensional matrix of joint occurrence of attributes (W) (Kovalev, 1996). An arbitrary pair of pixels (i, j) given by indices $(i = (x_i, y_i)$, $j = (x_j, y_j))$ on a 2D space was analysed to construct a matrix of attributes. The distance between the pixels was $d(i,j)$. The brightness levels of the pixels were designated by $I(i)$, $I(j)$. The luminance gradient modules were calculated as follow:

$$G(i) = \sqrt{G_x^2(i) + G_y^2(i)}, \quad (1)$$

$$G(j) = \sqrt{G_x^2(j) + G_y^2(j)}. \quad (2)$$

The components of the gradient vectors were calculated as follow:

$$G_x = K_x \otimes I\big(NB(x,y)\big), \quad (3)$$

$$G_y = K_y \otimes I\big(NB(x,y)\big), \quad (4)$$

where: $NB(x,y)$ – neighbourhood of the analysed pixel (size 3x3 or more). The masks of the convolution operation were Prewit, Sobel or Hummel (Zucker, 1981). The angle between the directions of the luminance gradient vectors in 2D space was calculated:

$$A(i,j) = \arccos\big(g(i) \times g(j)\big), \quad (5)$$

where: $g(i)$, $g(j)$ are normalised gradient vectors.

The six-dimensional matrix of joint occurrence of attributes combines all the listed features:

DOI 10.2478/ama-2018-0008

$$W = \left\| w\left(I(i), I(j), G(i), G(j), A(i,j), d(i,j)\right)\right\|. \quad (6)$$

The size of the matrix of attributes was equal to the number of pixel combinations of the image:

$$C = \frac{N!}{2(N-2)!}, \quad (7)$$

where: N is a number of pixels.

The matrix of attributes was divided into classes ($f: W \rightarrow \prod(W)$) using the function (Ihnatouski, 2000):

$$f \rightarrow \min|W_k \times W_l|. \quad (8)$$

The partitioning of the matrix of attributes into classes can be considered complete if for all $W_k(k, l = 1,2,\ldots,C)$ performed:

$$W_k \cap W_l = 0(\forall k, l). \quad (9)$$

2.3 Statistical Analysis

Descriptive statistics of maximum, minimum and mean temperatures were used for primary data analysis. Data were tested for normality with the Shapiro-Wilk test and comparisons were computed using paired-samples t-tests. Statistical analysis was performed using Statistics 13.5, and the statistical significance was set at $p<0.05$.

3. RESULTS

Sixty-five RA patients of both genders were analysed to perform this research work. Foot thermograms in the frontal view were taken with the FLIR E60bx camera, making a total of 130 thermal scan images. The ROI (Figs: 3,4,5) and the shin were two hottest places in the last frame. These two areas have been picked out. Then the shin area bordering on the margin of the image has been deselected. Fig. 3 presents ROI with maximal temperature selected from the first frame which corresponded to the moment right after cooling procedure.

ROI with maximal temperature (Fig. 5) was also appointed for the last image of thermal recovery registration which corresponded to steady –state temperature.

After selecting areas covered by pathological process, the area of healthy part of foot was determined. Fig. 4 presents inflamed and healthy area in the same thermal image.

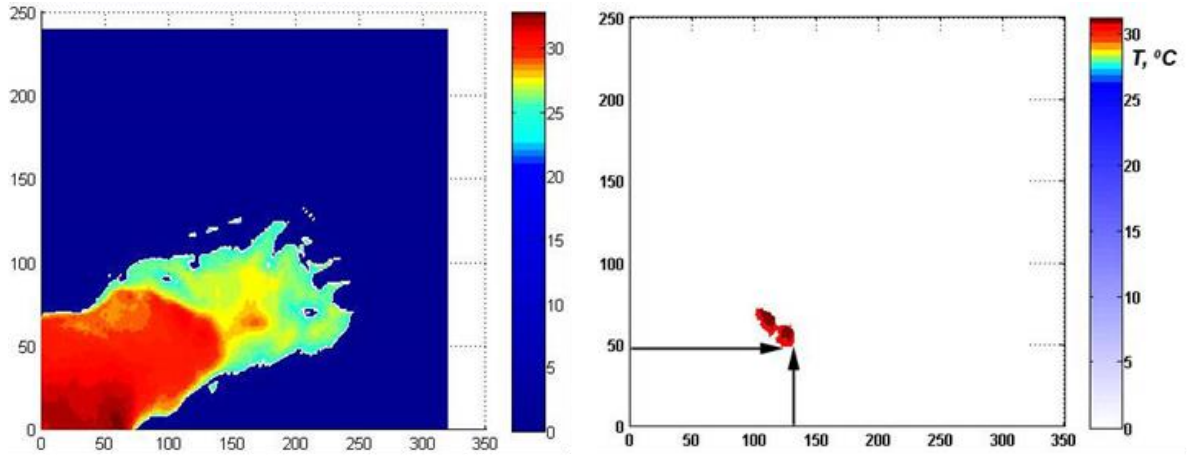

Fig. 3. ROI with Tmax from the first frame

The simultaneous rewarming process of pathological tissues and healthy tissues foregrounded the thermal differences between affected and healthy tissues. Automatically identified ROI corresponds to the area of the soft tissues covering cuboid and navicular bone. According to the scale alongside presented thermal images, selected ROI strikes as being the warmest place at the moment after cooling as well as in the moment after thermal recovery. However, after returning to baseline temperature, the area particularly affected by the disease is significantly warmer and more apparent. Fig. 6 presents the plot of temperature rise as a function of time for ROI area. Arithmetical mean of the temperature of dorsal metatarsal veins of the foot has been calculated starting from the first up to last frames.

The sample parameter values obtained from the measurements of the temperature [°C] in ROI for RA patients are presented in Tab. 1. Additionally, the difference between the inflamed (ROI) and healthy parts of the skin was determined.

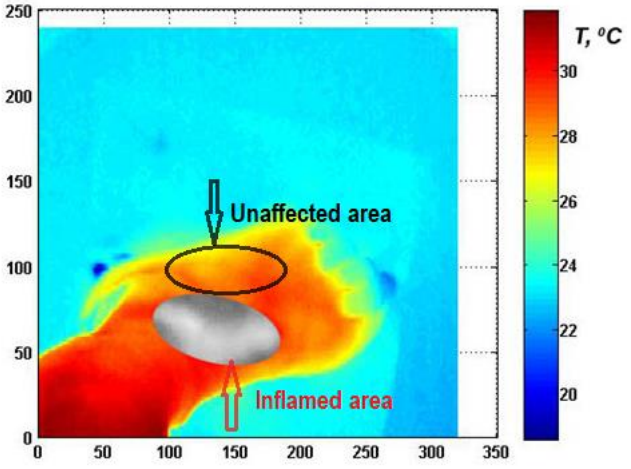

Fig. 4. The ROI post-recovery

Agnieszka Wasilewska, Jolanta Pauk, Mikhail Ihnatouski DOI 10.2478/ama-2018-0008

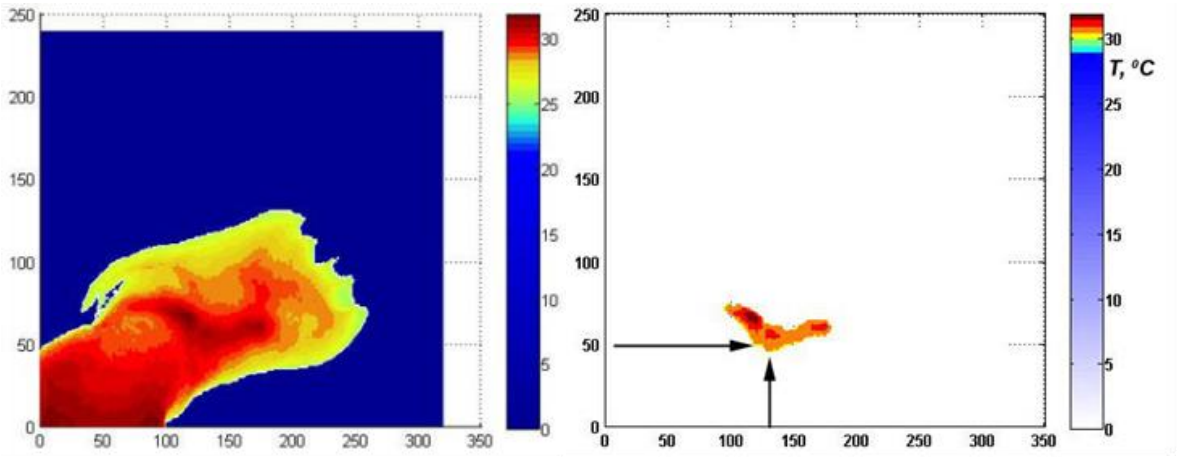

Fig 5. ROI with Tmax from last frame

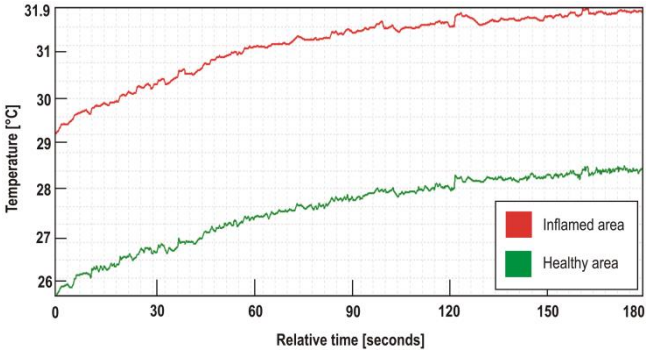

Fig. 6. Thermal response of the skin in the ROI area

Tab. 1. The set of parameters for the inflammation and healthy skin

Temperature	Inflammed area		Healthy area		Difference in post-cooling temperature between inflamed area vs healthy skin	Difference in post-recovery temperature between inflamed area vs healthy skin
	Post-cooling	Post-recovery	Post-cooling	Post-recovery		
Minimum	23.60	25.60	20.40	23.50	2.31*	2,22*
Maximum	30.20	33.80	28.20	32.10		
Mean (SD)	27.81 (1.93)	30.61 (1.84)	25.53 (1.89)	28.42 (1.83)		

*p<0.05

The results show several regularities. The difference in post-cooling temperature between inflamed area and healthy tissues is statistically significant with the higher temperature for the prior ($p<0.05$). Similarly, statistically significant difference between inflamed and healthy part of the foot occurs also in post-recovery temperature, with the higher temperature for the abnormal tissues ($p<0.05$). The post-recovery temperature is higher for the inflamed part as well as for healthy part of the skin when compared to the post-cooling temperature, with the higher temperature for the abnormal tissues ($p<0.05$). The post-recovery temperature is higher for the inflamed part as well as for healthy part of the skin when compared to the post-cooling.

4. CONCLUSIONS

The analysis of thermal images usually includes the manual or semi-automatic extraction of ROI provided by commercial software. In this study, we developed a method which allows identifying automatically a region of interest (ROI) on thermal images based on proposed segmentation algorithm. Results revealed statistically significant differences between inflamed and healthy area in post cooling temperature as well as in post recovery temperature. Thus, the method can be used in effective assessment of inflammation in RA patients.

REFERENCES

1. **Afshar S., Sheehan M.** (2017), Applying infrared thermography and image analysis to dilute 2-phase particulate systems: Hot Particle Curtains, *Energy Procedia*, 110, 408-413.
2. **Barcelos Z.E., Caminhas W.M., Ribeiro E., Pimenta E.M., Palhares R.M.** (2014), A combined method for segmentation and registration for an advanced and progressive evaluation of thermal images, *Sensors,* 14, 21950-21967.
3. **Bezerra H.G., Attizzani G.F., Sirbu V., Musumeci G., Lortkipanidze N., Fujino Y., Wang W., Nakamura S., Erglis A., Guagliumi G., Costa M.A.** (2013), Optical coherence tomography versus intravascular ultrasound to evaluate coronary artery disease and percutaneous coronary intervention, *JACC Cardiovasc Interv.,* 6(3), 228-36.
4. **Cojocaru M., Cojocaru I.M., Silosi I., Vrabie C.D., Tanasescub R.,** (2010), Extra-articular manifestations in rheumatoid arthritis; *Maedica (Buchar),* 5(4), 286–291.
5. **Dey N., Ashour A.S., Chakraborty S., Banerjee S., Gospodinova E., Gospodinov M., Hassanien A.E.** (2017), Watermarking in biomedical signal processing, Intelligent Techniques in Signal Processing for Multimedia Security, Dey N, Santhi V (eds); *Springer International Publishing*, 345 -369.
6. **Fernández-Cuevas I., Bouzas Marins J.C., Arnáiz Lastras J., Gómez Carmona P.M., Piñonosa Cano S., García-Concepción M.A., Sillero-Quintana M.** (2015), Classification of factors influencing the use of infrared thermography in humans: a review, *Infrared Physics & Technology* 71, 28–55.
7. **Gabriel S.E.** (2001), The epidemiology of rheumatoid arthritis, *Rheum Dis Clin North Am*., 27(2), 269–81.
8. **Herman C., Pirtini Cetingul M.** (2011, Quantitative visualization and detection of skin cancer using dynamic thermal imaging, *J. Vis. Exp.*, 51, 1-4.

DOI 10.2478/ama-2018-0008

9. **Ihnatouski M.I.** (2000), Methods of segmentation of AFM and STM images. Recognition and description of cluster surface objects in the nanoscale *IV Belarusian seminar on scanning probe microscopy (SPM-4). V.A. Belyi Metal Polymer Research Institute*: 122-126.
10. **John H.A., Niumsawatt V., Rozen W.M., Whitaker I.S.** (2016), Clinical applications of dynamic infrared thermography in plastic surgery: a systematic review, *Gland Surg*, 5(2), 122-132.
11. **Jones B.F.** (1998), A re-appraisal of the use of infrared thermal image analysis in medicine, *IEEE Trans Med Imaging*, 17,1019–27.
12. **Kaczmarek M., Nowakowski A.** (2016), Active IR-thermal imaging in medicine, *J Nondestruct Eval*, 35(19), 1-16.
13. **Kovalev V., Petrou M.** (1996), Multidimensional co-occurrence matrices for object recognition and matching, *Graphical Models and Image Processing*., 58(3), 187-197.
14. **Lahiri B.B., Bagavathiappan S., Jayakumar T.** (2012), Medical applications of infrared thermography, A review, *Infrared Physics & Technology,* 55(4), 221-235.
15. **Ludwig N., Formenti D., Gargano M., Alberti G.** (2014), Skin temperature evaluation by infrared thermography: comparison of image analysis methods, *Infrared Physics & Technology,* 62,1-6.
16. **Nowakowski A., Siondalski P., Moderhak M., Kaczmarek M.** (2014), Problems of cardiosurgery wound healing evaluation, *Proceedings of QIRT*, 1–9.
17. **Nowakowski A., Siondalski P., Moderhak M., Kaczmarek M.** (2015), A new diagnostic method for evaluation of cardiosurgery wound healing*, JQIRT*, 1–16.
18. **Purslow C., Wolffsohn J.S., Santodomingo-Rubido J.** (2005), The effect of contact lens wear on dynamic ocular surface temperature, *Contact Lens & Anterior Eye,* 28, 29–36.
19. **Renkielska A., Kaczmarek M., Nowakowski A., Grudzinski J., Czapiewski P., Krajewski A., Grobelny I.** (2014), Active dynamic infrared thermal imaging in burn depth evaluation, *J. Burn Care Res*, 35(5), 294–303.
20. **Renkielska A., Nowakowski A., Kaczmarek M., Ruminski J.** (2006), Burn depths evaluation based on active dynamic IR thermal imaging—a preliminary study, *Burns,* 32, 867–875.
21. **Ring E.F.J.** (1998), Progress in the measurement of human body temperature, *IEEE Eng Med Biol*, 17, 19–24.
22. **Tattersall G.J.** (2016), Infrared thermography: non-invasive window into thermal physiology, *Comp Biochem Physiol A Mol Integr Physiol*, 202, 78-98.
23. **Wasilewska A.** (2017), Advantages of active over passive thermography in terms of applying in medicine, *Scientific and didactic equipment*, 22(2), 88-93.
24. **Wasilewska A., Pauk J.** (2017), Safety conditions in dynamic IT examinations of rheumatoid arthritis lesions, *Scientific and didactic equipment*, 22(3), 205-214.

Acknowledgements: The work has been accomplished under the research project No. MB/WM/19/2016 financed by the Bialystok University of Technology.

DE GRUYTER
OPEN

DOI 10.2478/ama-2018-0009

ENERGY ABSORBING EFFECTIVENESS – DIFFERENT APPROACHES

Maria KOTEŁKO[*], Mirosław FERDYNUS[**], Jacek JANKOWSKI[*]

[*]Faculty of Mechanical Engineering, Department of Strength of Materials, Lodz University of Technology,
90-924 Łódź, Stefanowskiego 1/15, Poland
[**]Department of Machine Construction and Mechatronics, Lublin University of Technology,
20-618 Lublin, Nadbystrzycka 36, Poland

maria.kotelko@p.lodz.pl, m.ferdynus@pollub.pl, jacek.jankowski@p.lodz.pl

received 24 May 2017, revised 8 March 2018, accepted 14 March 2018

Abstract: In the paper the study of different crashworthiness indicators used to evaluate energy absorbing effectiveness of thin-walled energy absorbers is presented. Several different indicators are used to assess an effectiveness of two types of absorbing structures, namely thin-walled prismatic column with flaws and thin-walled prismatic frustum (hollow or foam filled) in both cases subjected to axial compressive impact load. The indicators are calculated for different materials and different geometrical parameters. The problem of selection of the most appropriate and general indicators is discussed.

Key words: Thin-Walled Structure, Energy Absorber, Impact, Absorbing Effectiveness

1. INTRODUCTION

Since demands of general public of the safe design of components of vehicles, ships, etc. have increased substantially in the last few decades, a new challenge appeared to design special structural members which would dissipate the impact energy in order to limit the deceleration and finally to stop a movable mass (e.g. vehicle) in a controlled manner. Such a structural member termed energy absorber converts totally or partially the kinetic energy into another form of energy. One of the possible design solutions is the conversion of the kinetic energy of impact into the energy of plastic deformation of a thin-walled metallic structural member. There are numerous types of energy absorbers of that kind that are cited in the literature (Alghamdi, 2001). Namely, there are steel drums, thin tubes or multi-corner columns subject to compression, compressed frusta (truncated circular cones), simple struts under compression, sandwich plates or beams (particularly honeycomb cells) and many others. Among all those design solutions, mentioned above, thin-walled metal tubes are widely used as energy absorption systems in automotive industry due to their high energy absorption capability, easy to fabricate, relatively low price and sustainability at collapse. A designer of any impact attenuation device must meet two main, sometimes contrary, requirements: the initial collapse load has to be not too high in order to avoid unacceptably high impact velocities of the vehicle. On the other extreme, the main requirement is a possibly highest energy dissipation capacity, which may not be achieved if the collapse load of the impact device is too low. The latter may result in dangerously high occupant "ride down" decelerations.

Thus, maximizing energy absorption and minimizing peak to mean force ratio by seeking for the optimal design of these components are of great significance. There are several crashworthiness indicators (Jones, 2003; Kotełko, 2010) used to evaluate the crashworthiness of the energy absorbing structure (energy absorber): energy absorption (EA), peak crushing force (PCF), mean crushing force (MCF), crash load efficiency (CLE), stroke efficiency (STe). These indicators allow one to compare energy absorption capability within one particular material and one structural geometry (design solution). Thus, an alternative energy absorbing effectiveness factor was introduced recently by Jones (2010), which is supposed to enable a selection of most proper material and design solution of an energy absorbing structure.

2. ENERGY ABSORBING EFFECTIVENESS INDICATORS – OVERVIEW

As mentioned above, there are several crashworthiness indicators used to evaluate the crashworthiness of the energy absorbing structure (energy absorber). The typical crushing force – displacement curve for a thin-walled member subjected to axial impact is shown in Fig.1.

$$EA(d_x) = \int_0^{d_x} F(x)dx \tag{1}$$

where d_x is a crushing distance (see Fig.1).

The factor , which directly indicates absorbing effectiveness is the energy absorbed (EA) given by relation (1), or specific energy (energy per unit mass) S_e , given by (2), where m is a mass of the absorber.

$$S_e = \frac{EA}{m} \tag{2}$$

Since the reduction of an initial peak crushing force (PCF) is mostly desirable from biomechanical reasons, this factor is an important indicator of the absorber effectiveness.

The mean crushing force (MCF – Fig.1.) for a given crushing deformation d_x is calculated as:

DOI 10.2478/ama-2018-0009

$$MCF = \frac{EA(d_x)}{d_x} \tag{3}$$

Crash load efficiency is defined as a mean crushing force (MCF) to peak crushing force (PCF – see Fig.1) ratio:

$$CLE = \frac{MCF}{PCF} \cdot 100\% \tag{4}$$

The CLE factor should be as close to 100% as possible in practice and CLE of an ideal energy absorber is 100%.

Another crashworthiness indicator is the stroke efficiency, which represents the deformation capacity of an absorber. Stroke efficiency $\mathrm{St_e}$ is defined as follows:

$$St_e = \frac{L_o - U}{L_o} \cdot \tag{5}$$

where: L_o – initial length (characteristic dimension) of the member [mm], U – maximum shortening (maximum characteristic deformation) of the member. The most desirable is the lowest value of this factor, corresponding to the highest value of the crushing distance.

A combination of the CLE and the stroke efficiency was defined by Hanssen et al. (2000) as total efficiency TE to assess the whole performance of an energy absorber. It is a dimensionless number and is given by

$$TE = CLE \times St_e \tag{6}$$

However, this total efficiency does not include the factor of the weight of the structures and therefore another index was introduced by Zhang et al. (2009), who proposed to divide the total efficiency by the mass. This factor is defined it as specific total efficiency and expressed as follows:

$$STE = \frac{TE}{m} = \frac{CLE \times St_e}{m} \tag{7}$$

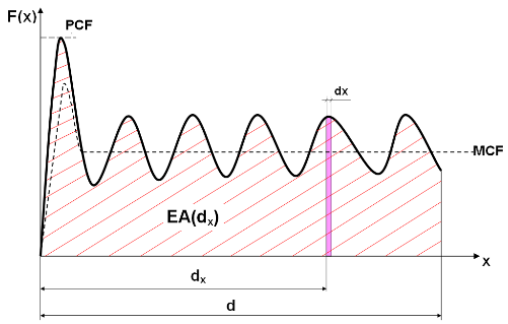

Fig. 1. Exemplary load-shortening diagram of thin-walled column under axial impact

All indicators, mentioned above express an absorber characteristics within one specific structural geometry and one absorber's material. The first indicator, which included the material factor was introduced by Pugsley and Jones (2003), termed structural efficiency and defined as:

$$\eta = \frac{MCF}{A \cdot \sigma_0} \tag{8}$$

where: σ_0 – yield stress, A – area of the absorber cross-section.

Any comparisons between the characteristics of energy absorbers, made from different materials are difficult using indicators, mentioned above , to some extent except structural efficiency given by (8). Thus, a new alternative approach to the assessment of energy absorbing effectiveness has been proposed by Jones (2010). He proposed the factor defined as:

$$\Psi_0 = \frac{\text{total elastic and plastic energy absorbe } d \text{ by a absorber}}{\text{energy absorbed in the same volume of material specimen up to failure in tension}}$$

In the case of axial crushing, Jones derived an approximate relation determining this factor as follows (Jones, 2010):

$$\Psi_0 = \frac{3mv^2}{8\sigma_0 A \delta_f \varepsilon_R} \tag{9}$$

where: m – mass of impactor, v – initial impact velocity, σ_0 – yield stress, A – area of the absorber cross-section, δ_f – final axial displacement (shortening), ε_R – rupture strain.

In the case of foam filled structure, the denominator in (9) incorporates energy of the same volume of foam material tensile test specimen, as follows:

$$\Psi_0 = \frac{3mv^2}{8\delta_f \varepsilon_R (\sigma_0 A_s + \sigma_f A_f)} \tag{10}$$

where: σ_f – yield stress of the foam material, $\mathrm{A_s}$ – area of the shell (face sheet), $\mathrm{A_f}$ – area of the foam.

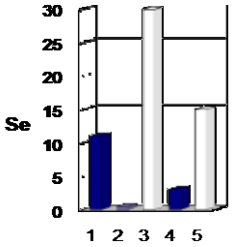

Fig. 2. Specific energies (Se) for selected energy absorbers (1 – top hat, 2 – plain channel, 3 – crushing tube, 4 – hydraulic device, 5 – aluminum honeycomb)

A direct measure of the absorber's effectiveness, energy absorbed during crushing process, can be compared within one type of absorber's structure, material, etc. A comparison of specific energy absorbed by different types of absorbers is shown in Fig. 2. As shown, the most effective is a circular thin-walled tube. Thus, since early 60ties of XXth Century, the majority of the studies were devoted to this type of energy absorber, made of mild steel (Jones, 2003). However, in more recent years, investigators have examined prismatic tubes of various cross-sectional shapes, made of different materials (high strength steel, aluminum, etc.), also filled with different foam materials.

Another alternative solution are flaws or dents acting as triggers. A trigger may induce the most desirable crushing (collapse) mode, leading to higher energy absorption and mean to peak crushing force ratio. Very few published papers deal with tubular structures with dents or other flaws (Ferdynus et al., 2016, 2018). An interesting solution has been presented by Yang (2017). The subject of investigation was the crushing behavior of a thin-walled circular tube with internal gradient grooves. The authors fabricated stainless steel thin-walled tube with preset internal circumferential rectangular groove defects using SLM 3D printing method. They observed double buckling-splitting crushing mode. Empty and foam-filled circumferentially grooved thick-walled circular tubes under axial low velocity impact were investigated theoretically and experimentally by Darvizeh et al. (2017).

A different concept of energy absorbing structures represent compressed thin-walled frusta (truncated circular cones or prisms) (Alghamandi, 2001; Mołdawa and Kotełko, 2016), currently used as impact attenuation members in car structures, mainly due to the reduction of the peak crushing load in relation to parallelepi-

DOI 10.2478/ama-2018-0009

ped. There are relatively few published results, concerning this type of energy absorbing members (Fredynus et al., 2016; Mołdawa and Kotełko, 2016). Ei-Sobky et al. (2001) investigated crushing behavior of conical truncated frusta. They analyzed influence of boundary conditions on the peak and mean crushing load. Very recently, Sarkabiri et al. (2015) published the results of multi-objective crashworthiness optimization of thin-walled conical groove tubes filled with polyurethane foam. They stated , that the conical angle reduces the peak crushing force, however it reduces also the absorbed energy.

3. SUBJECTS OF THE COMPARATIVE STUDY

The aim of the present study was a comparative analysis of energy absorption capability of selected thin-walled energy absorbers (prismatic columns under axial impact) expressed by selected crash-worthiness indicators. Subjects of the analysis were prismatic thin-walled tubes with flaws (Fredynus et al., 2016, 2018) and prismatic, hollow and foam filled thin-walled frusta (Fredynus et al., 2016; Mołdawa and Kotełko, 2016), shown in (Fig. 2).

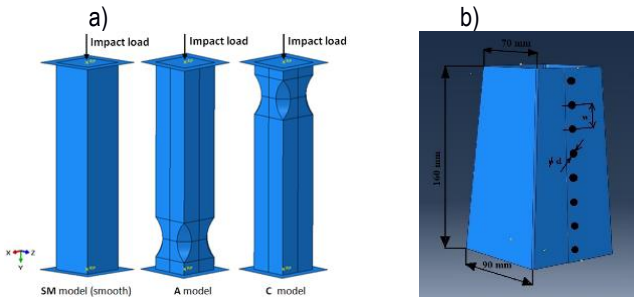

Fig. 3. Energy absorbing structures: a) – prismatic thin-walled tube with flaws (dents) (Jones, 2010), b) – prismatic thin-walled frustum (Fredynus et al., 2016; Mołdawa and Kotełko, 2016)

In the first case (Fig. 3a), the subject of investigation was a thin-walled square section aluminum tube with four indentations in the corners. The tubes of dimensions 70x2 and height l=335 mm were investigated. The dents geometry was characterized by the main radius R=50 mm and relative dent depth with respect to the dimension b of main diagonal (Fig. 3) of the column cross-section (from 5% up to 30%). Dents were made at the bottom of the column or at the top. The models with the dents at the bottom of the column were designated by the symbols from A05_X to A30_X, where the first number stands for the relative depth of the dent (in percent) and X stands for the distance of the dent from the bottom (Fig. 4). The column with smooth walls (without dents) was designated as SM. In the second case (Fig. 3b), the subject of investigation was a thin-walled prismatic frustum on square foundation of constant edge length a = 90 mm and height h =160 mm, hollow or foam-filled.

4. CRASHWORTHINESS COMPARATIVE ANALYSIS

The comparative analysis was focused on the following indicators: peak crushing force (PCF), mean crushing force (MCF), crash load efficiency (CLE), stroke efficiency (Ste) and alternative energy absorbing effectiveness factor ψ_0 .

4.1. PCF and CLE

The comparison of decrease of PCF in examined absorbers is shown in Fig. 4 and 5. Fig.4 shows load-shortening diagrams for flawed prismatic columns. The maximum decrease in PCF amounts about 25%. Fig. 5 shows corresponding diagrams for hollow frusta of different frustum angle. The decrease of PCF is more significant and amounts up to 50%. Diagrams of CLE for absorbers under investigation are shown in Fig. 6 and 7 Also this indicator reaches higher values for hollow frusta. CLE indicator does not differ significantly for different materials. The maximum for steel flawed column is about 36%, while for aluminium column – 39%. Maximum CLE for both steel and aluminium hollow frustum is about 70%. The decrease of PCF and increase of CLE are main advantages of both examined absorbers.

Foam filling of frusta for examined materials (steel and aluminum) did not affect either PCF or CLE (Fig. 14).

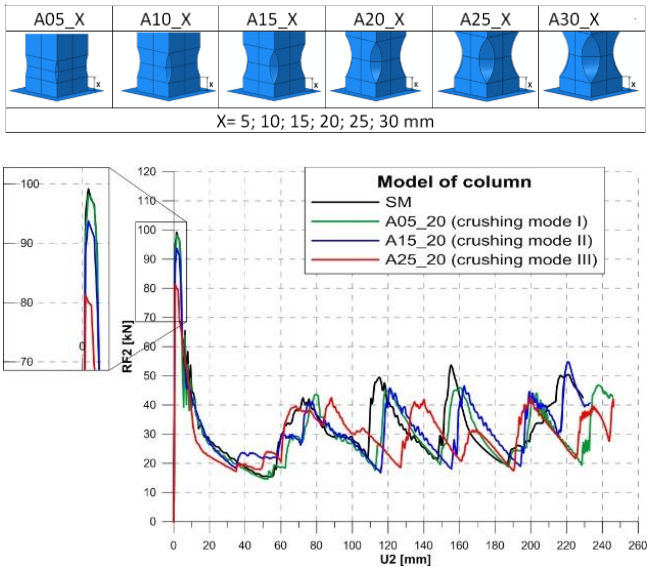

Fig. 4. Load-shortening diagrams for columns A exhibiting three different crushing modes (constant value of X=20 mm); v_0=10 m/s, impactor mass m= 200 kg (Ferdynus et al., 2016)

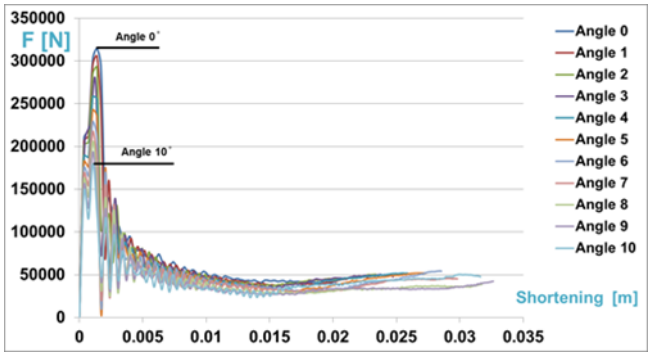

Fig. 5. Load shortening diagrams for hollow thin-walled frustum of different frustum angle; = 0.8 mm, v_0 = 6.2 m/s, impactor mass m= 50kg (Mołdawa and Kotełko, 2016).

DOI 10.2478/ama-2018-0009

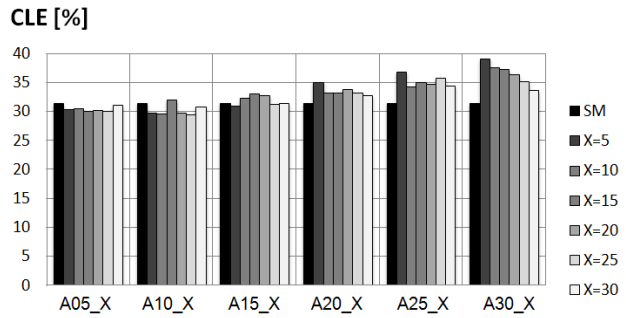

Fig. 6. Flawed prismatic thin-walled steel columns: crash load efficiency (CLE) v_0=10 m/s, impactor mass m= 200 kg (Ferdynus et al., 2018)

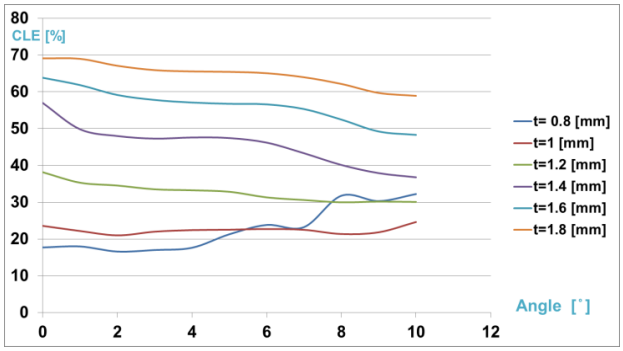

Fig. 7. Steel hollow frustum: Crash load efficiency (CLE); v_0 = 6.2 m/s, impactor mass m= 50kg (Mołdawa and Kotełko, 2016)

4.2. Stroke efficiency

Comparison of the stroke efficiency (measure of deformation capacity) for two types of absorbers under investigation give diagrams in Figs. 8 and 9.

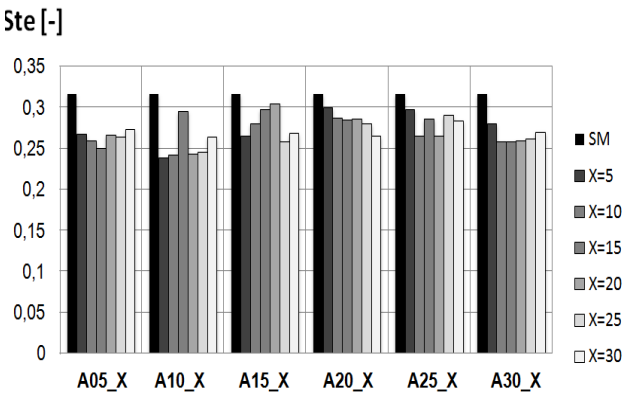

Fig. 8. Flawed prismatic thin-walled steel columns: stroke efficiency (Ste), v0=10 m/s, impactor mass m= 200 kg (Ferdynus et al., 2018)

In the contrary to CLE the stroke efficiency is lower (more optimal) for flawed columns in comparison with hollow frusta. It also depends much more significantly on the absorber's material. It is related not only to the material stiffness, but also to differences in failure modes (see Fig. 11 and 12). Fig. 11 and 12 (load-shortening diagrams) show the difference in structural behaviour of examined absorbers made of steel and aluminium. In the case of hollow frusta stroke efficiency is less sensitive to the material.

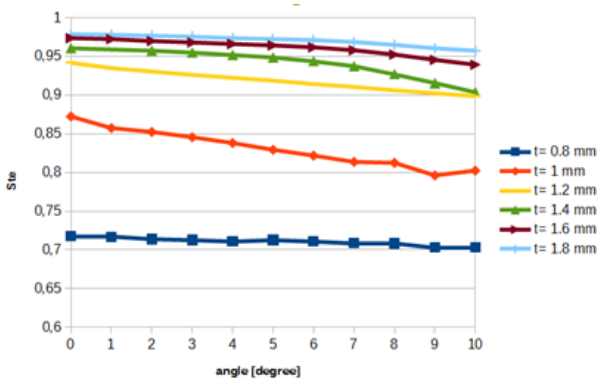

Fig. 9. Steel hollow frustum: stroke efficiency (Ste); v0 = 6.2 m/s, impactor mass m= 50kg (Mołdawa and Kotełko, 2016)

Stroke efficiency for foam filled frustum, because of increased structural stiffness, is higher in comparison with hollow frustum (Fig.14).

Fig. 10 shows maps of crash load efficiency (CLE) (Fig.10a) and stroke efficiency (Ste) (Fig. 10b) for flawed columns with different relative dent depth and dent position [8], obtained from FE simulations. As it is presented, optimal values of these two indicators (the highest CLE and lowest Ste) are obtained for different magnitudes of dent depth and position. Thus, using different effectiveness factors in optimization procedure, we may obtain different solutions.

a)

b)

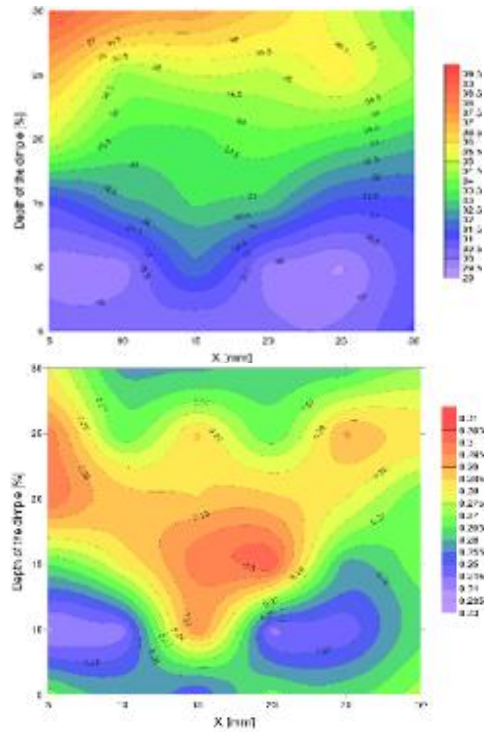

Fig. 10. Two crashworthiness indicators for flawed prismatic aluminium thin-walled columns: a) crash load efficiency (CLE), b) stroke efficiency (Ste) (Ferdynus et al., 2018)

Tables 1 and 2 show, that all crashworthiness indicators mentioned above, particularly CLE and Ste, depend on an impact energy and, on the other extreme (at constant impact energy) on the initial impact velocity. It also induces the question about an adequate effectiveness measure to be still open.

DOI 10.2478/ama-2018-0009

4.3. Energy absorbing effectiveness factor – alternative approach

An alternative energy absorbing effectiveness factor was introduced by Jones (2010), in order to enable a selection of most proper material and design solution of an energy absorbing structure. Its main advantage is a possibility of comparing energy effectiveness not only within one structural design solution, but among different types of energy absorbing structures as well. As shown in Tabs. 1 and 2, this effectiveness factor does not depend significantly on an impact energy or initial velocity, which makes this effectiveness measure more general.

Tab. 3 contains values of effectiveness factor ψ_0 for considered two types of energy absorbing structures.

Tab. 1. Crashworthiness indicators for flawed prismatic steel columns, at constant initial impact velocity v_0 = 10 m/s

impact energy [kJ]	Mass m [kg]	PCF	MCF [kN]	CLE [%]	Ste	Ψ_0
7.5	150	171.895	53.283	30.997	0.580	3.60
10	200	172.105	49.611	28.826	0.399	3.63
15	300	172.286	56.006	32.508	0.200	3.78
20	400	172.379	69.057	40.061	0.135	4.66

Tab. 2. Crashworthiness indicators for flawed prismatic steel columns, at constant impact energy EA=14 kJ

V [m/s]	Mass [kg]	PCF [kN]	MCF [kN]	CLE [%]	Ste [%]	Ψ_0
2	7000	138.433	49.085	35.458	0.150	3.32
4	1750	150.381	49.835	33.139	0.162	3.36
6	777.78	158.747	51.122	32.203	0.183	3.46
8	437.50	168.787	52.270	30.968	0.207	3.56
10	280	189.54	54.249	28.622	0.228	3.64

Tab. 3. Energy absorbing effectiveness factor ψ_0

Type of absorber	Material/ Yield stress [MPa]	Mass of impactor [kg]/ Initial velocity [m/s]	ψ_0
Hollow parallelpiped α=0°	Steel /590	50/6	0.78
Hollow frustum α=2°	Steel/590	50/6.2	0.76
Hollow frustum α=5°	Steel/590	50/6.2	0.76
Hollow frustum α=10°	Steel/590	50/6.2	0.72
Hollow frustum α=10°	Aluminium/175	50/6.2	2.79
Foam filled frustum α=5°	Steel/590 Polypropylene/-	50/6.2	1.36
smooth column	Aluminium/175	200/10	2.77
Flawed column A30_5	Aluminium/175	200/10	2.64
Flawed column A30_5	Steel/165	200/10	3.72

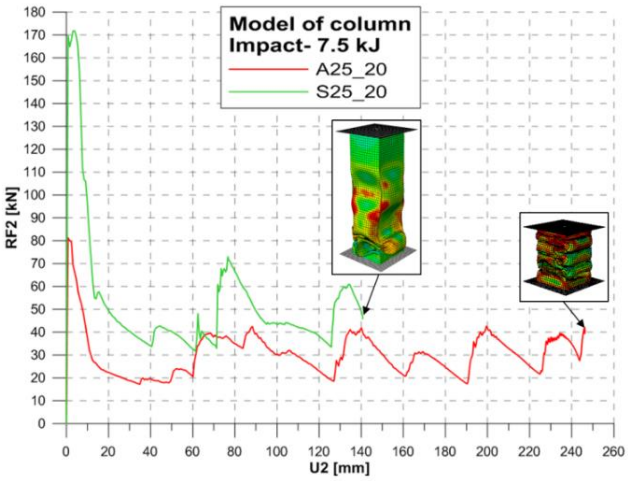

Fig. 11. Load-shortening diagrams of flawed prismatic thin-walled steel and aluminium columns; v0=10 m/s, impactor mass m= 200 k

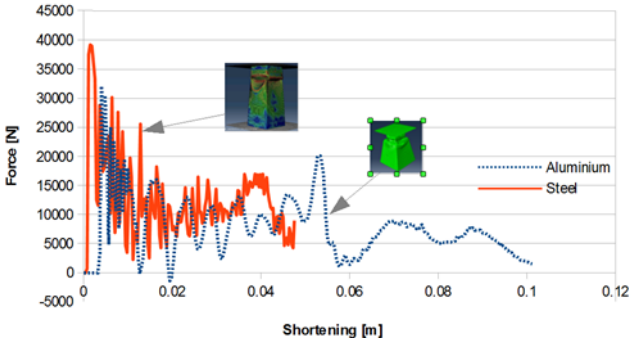

Fig. 12. Load-shortening diagrams of thin-walled steel and aluminium frusta; v0=6.2 m/s, impactor mass m= 50 kg

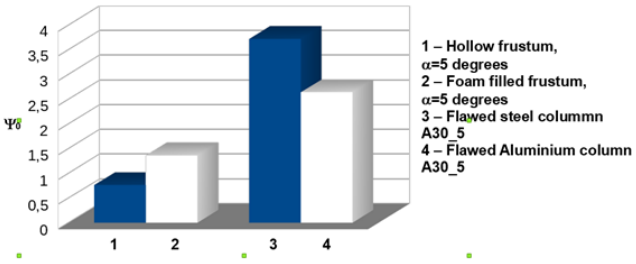

Fig.13. Energy absorbing effectiveness factor Ψ_0 for two examined types of absorbers - comparison

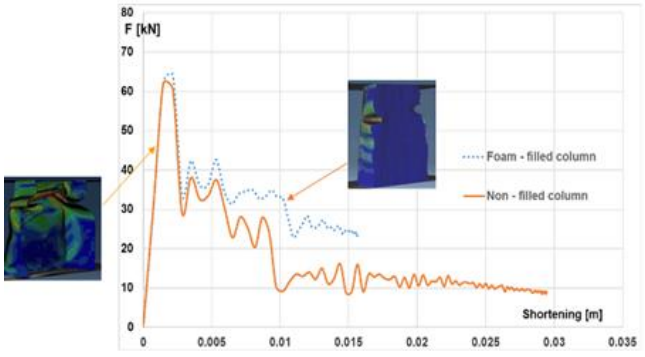

Fig. 14. Load-shortening diagrams for thin-walled hollow and foam filled frustum; steel metal sheet, polypropylene filling; v0=6.2 m/s, impactor mass m= 50 kg

DOI 10.2478/ama-2018-0009

5. FINAL REMARKS

Higher values of energy absorbing effectiveness factor ψ_0 have been obtained for flawed tubes (Fig.1a) in comparison with thin-walled frusta (Fig.1b). However, within one type of absorbing structure this factor does not indicate the best solution. For example, PCF or CLE indicators, very important from biomechanical point of view, are higher for flawed column than for smooth column (Fig. 1a) and higher for frustum, than for parallelepiped (Fig. 1b), in the contrary to the effectiveness factor ψ_0 (Tab. 3). Thus, it may be concluded, that the energy absorbing effectiveness factor ψ_0 may be used in a preliminary analysis, leading to a selection of an absorber's type. After this initial selection, within one type of absorbing structure, other crashworthiness indicators, particularly important for specific absorber's purposes, should be taken into account. However, appropriate general indicator (or indicators) of energy absorption capability is still an open question and demands further comparative analysis.

REFERENCES

1. **Alghamdi A.A.A**. (2001), Collapsible impact energy absorbers: an overview, *Thin-Walled Struct*, 39, 189-213.
2. **Darvizeh A., Meshkinzar A., Alitavol M., Rajabierhard R.** (2017), Low velocity impact of empty and foam filled circumferentially grooved thick-walled circular tubes, T*hin-Walled Struct.*, 110, 97-105.
3. **Ei-Sobky H., Singace A.A., Petsios R. .** (2001), Mode of collapse and energy absorption characteristics of constrained frusta under axial impact loading. *Int.J.Mech.Sci.,* 43, 743-757.
4. **Ferdynus M., Kotełko M.,Kral J.** (2018) Energy absorption capability numerical analysis of thin-walled prismatic tubes with corner dents under axial impact, accepted for publication, *Maintenance and Reliability*, v.20 (2), 248-255
5. **Ferdynus M**., **Kotełko M., Mołdawa A.** (2016), Prismatic tubular thin-walled members as energy absorbers, chapter in *Statics, dynamics and stability of structures*, (series of monographs) ed. by R.J. Mania, Lodz University of Technology, 4, 178-195.
6. **Hanssen A.C., Langseth M., Hopperstad O.S.** (2000), Static and dynamic crushing of circular aluminium extrusions with aluminium foam filler, *International Journal of Impact Engineering*, 24(5), 475–507.
7. **Jones N.** (2003), *Structural Impact*, Cambridge University Press.
8. **Jones N**. (2010), Energy absorbing effectiveness factor, *Int. J. of Impact Engineering*, 37, 754-765.
9. **Kotełko M.** (2010), *Load-capacity and mechanisms of failure of thin-walled structures* (in Polish), WNT, Warszawa.
10. **Mołdawa A., Kotełko M.** (2016), Impact behaviour of spot-welded thin-walled frusta, *Acta Mechanica et Automatica*, 10 (4), 280-284
11. **Sarkabiri B., Jahan A., Rezvani M.** (2015), Multi-objective crashworthiness optimization of thin-walled conical groove tubes filled with polyurethane foam, *3 rd Polish Congress of Mechanics, 21 st International Conference of Computer Methods in Mechanics*, 947-948.
12. **Zhang X., Cheng G., Zhang H.** (2009), Numerical investigations on a new type of energy-absorbing structure based on free inversion of tubes, *Int. J. of Mechanical Sciences*, 51, 64-76.
13. **Zhe Y., You Y., Wei Y., Huang Ch.** (2017), Crushing behaviour of a thin-walled circular tube with internal gradient grooves fabricated by SLM 3D printing, *Thin-Walled Struct.*, 111, 1-8.

DE GRUYTER
OPEN

DOI 10.2478/ama-2018-0010

CONCEPT OF THE HEXA-QUAD BIMORPH WALKING ROBOT AND THE DESIGN OF ITS PROTOTYPE

Dominik WOJTKOWIAK*, Krzysztof TALAŚKA*, Ireneusz MALUJDA*

*Chair of Basics of Machine Design, Faculty of Machines and Transport,
Poznan University of Technology, ul. Piotrowo 3, 60-965 Poznań, Poland

dominik.wojtkowiak@put.poznan.pl, krzysztof.talaska@put.poznan.pl, ireneusz.malujda@put.poznan.pl

received June 2017, revised 16 March 2018, accepted 20 March 2018

Abstract: Present-day walking robots can increasingly successfully execute locomotive as well as manipulative functions, which leads to their expansion into more and more applications. This article presents the design of a hexa-quad bimorph walking robot with the ability to move at a relatively high speed in difficult terrain. It also has manipulation capabilities both at a standstill and in motion. This feature of the robot is made possible by the ability to easily change the configuration from six-legged to four-legged by elevating the front segment of its body. Presented prototype will be used in further research to develop the hexa-quad bimorph walking robot.

Key words: Walking Robot, Hexa-Quad, Bimorph, Hexapod, Quadruped

1. INTRODUCTION

There have been significant advances in scientific and technical aspects of walking robots. The changes are noticeable both in design of robot components and motion control. Increasingly advanced designs, varying in size, come to life. To put their legs in motion a broad range of actuators are used - from electric and combustion motors to pneumatic and hydraulic actuators to those using intelligent materials. Modern walking robots can not only move in difficult, rough terrain and different types of surface (ice, sand, etc.), but also climb vertical walls (Saunders et al., 2006) or move under water (Kim and Jun, 2014). Algorithms of motion control and advanced sensors allow generating quick gaits, retaining stability in nearly every condition and even providing movement continuity in case of damaging one of the robot legs (Ignaki, 1998). More and more often walking robots gain motion autonomy thanks to artificial neural networks. This way they acquire machine learning capabilities and artificial intelligence.

Locomotive capabilities of walking robots are well described in scientific literature of the subject. Much less focus is placed on manipulative functions, which walking robots can execute as effectively as locomotive functions. This is what lies behind the concept of the hexa-quad bimorph walking robot whose objective is to combine both functions. The term bimorphism in the context of walking robots means properties that enable two configurations within one design, with no need for changeovers. The concept of the hexa-quad bimorph walking robot came to life following the attempt to design an autonomous walking robot with two key properties:

- the ability to move in difficult terrain with the highest speed possible,
- the ability to manipulate objects both in motion and at a standstill.

Depending on its size, this type of walking robots can have multiple applications, both military (space exploration, scouting and bomb disposal) and civil (mining and forestry).

While analysing the existing, present-day design solutions for walking robots what can be found is partial, but not complete, execution of the functional properties of hexa-quad bimorph walking robots.

Lewinger (2005) presented the design of six-legged walking robot, called BILL-Ant, capable of manipulating objects. In designing the robot, the biological template of the insect, namely the ant, was used. According to the author's assumption, this robot can automatically move on uneven surfaces and manipulate objects in its environment. The robot's advanced locomotive capabilities are owed to six legs with three active degrees of freedom. This type of design makes it possible for the robot foot to reach any point in the working space of the leg. The design element that allows object manipulation is the robot's head, which is equipped with the grabbing device in the form of mandibles. Thanks to three degrees of freedom the robot's head can effectively manipulate the object. The main limitation for this type of design is the unfavourable distribution of weight, which leads to easy destabilization and poor manipulation capabilities while in motion.

The group of walking robots that are successful in executing the locomotive function in difficult terrain while moving at sufficiently high speeds, are designs characterized by a segmented body with active or passive joints. Tang (2015) presented the design of the modular multi-legged walking robot consisting of three or more identical segments. Each segment has one pair of legs with merely one degree of freedom. Between particular segments there is a single axial revolute joint allowing their mutual rotational movement around the vertical axis of the robot. This made it possible to achieve quick gait despite using only a small number of drives. In turn, Bartsch (2012) presented the design of a walking robot with a two-segment body with a controllable joint placed between the segments. The joint allows rotational movement around the axis lateral to the direction of robot move-

DOI 10.2478/ama-2018-0010

ment. This makes it possible to generate gait algorithms allowing motion through uneven terrain. However, none of these designs executes manipulative functions.

In Kim's work (2014) the design of a six-legged walking robot whose main functional feature was movement under water was presented. The robot was called Little Crabster. Its design is typical for a hexapod with a rigid body, which ensures its gait is quick and statically stable. The robot has front legs executing both locomotive and manipulative functions. To manipulate objects a gripping device extends out of its leg. This type of solution is used to work on objects rather than to move them. It follows from the need to keep the machine's centre of gravity within the support polygon. The problem was partially solved by leaving at least one leg in the support phase, which significantly reduces manipulation capabilities. Placing an extendable gripping device inside the leg requires sufficient space, which means this solution can only be implemented in larger robots.

The next example of a walking robot construction which can fulfill analyzed properties is LAURON V presented by Roennau (2014). Its legs have four independent joints each in order to cope with steep inclines and large obstacles as well as to manipulate objects by using the front legs. It has autonomy of operation, robustness, terrain adaptability and large payload capacity, which makes it highly suitable to for field applications. However, shifting the center of mass can be achieved only by the angular configuration of the legs, which means it will be difficult to control its position during manipulation in motion.

Another interesting construction was presented by Boston Dynamics and was called SpotMini. It is a quadruped with an optional robotic arm ended with a precise gripper which is mounted on the top of the front part of its body. Because its kinematics is biologically inspired it can easily move in rough terrain like a real animal. On the other hand, during the gait generation it is necessary to use dynamic stable gaits instead of static ones in order to achieve full maneuverability.

The last design with traces of bimorphism is the robot MANTIS designed within the LIMES project and presented by Manz (2013). During its operation the robot can assume either of two postures - the locomotive or the manipulative one. This design offers extremely good stability parameters and manipulation capabilities. However, the solution requires high power drives as the rotation of the entire body is necessary. Additionally, the robot design necessitates that object manipulation takes place at a standstill. It also has a negative impact on surmounting obstacles in motion.

Other traces of bimorphism can be also noticed in (Kalouche 2015), where the reconfigurable legged robot with series-elastic actuators was introduced. This type of construction consists of multiple modules that can be easily adapted to quadruped, hexapod or biped configuration. This way, by proper configuration, we can gain the robot locomotion and manipulation abilities.

The objective of this paper is presenting the concept of the hexa-quad bimorph six-legged walking robot, which combines the advantages of the above mentioned designs and eliminates their imperfections. Moreover the goal was to show the construction of the prototype research model, which can be used in further tests in order to develop the idea of a hexa-quad bimorph walking robot by formulating mathematical and physical models. These models can make it possible to describe the design and motion control algorithms as well as the process of designing walking robots capable of executing the above mentioned functions and applications.

2. THE DESIGN OF THE HEXA-QUAD BIMORPH SIX-LEGGED WALKING ROBOT

2.1. The kinematic structure of the hexa-quad bimorph walking robot

The kinematic structure of the hexa-quad bimorph walking robot is presented in Fig. 1. The construction consists of three-segment body containing the front segment 1, the middle segment 2 and the rear segment 3. Between the front segment and the middle segment there is an active double axial joint 7, which allows the rotation of the front segment relative to the vertical axis Z and the lateral axis X. The rear segment is connected with the middle segment with an active single axial joint, which allows its rotation around the vertical axis Z. Each body segment is assigned only one pair of limbs. The locomotive legs, whose only function is executing robot motion in space, are attached to the middle and rear segments. Front legs, apart from basic locomotive functions, are also used to manipulate objects. They are - as a result - manipulative and locomotive legs. Additionally, the hexa-quad bimorph six-legged walking robot is equipped with an extendable weight system 8 built into the rear body segment. Its purpose is making regulation of the robot's centre of gravity possible (Wojtkowiak, 2017).

Bimorphism of this type of design has to do with its ability to move easily from hexapod configuration to quadruped configuration or the other way around. Both robot configurations are presented in Fig. 2 and Fig. 3.

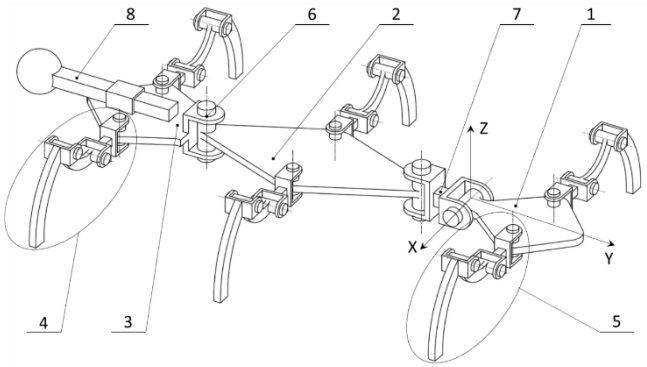

Fig. 1. Design schematic of the hexa-quad bimorph six-legged walking robot: 1 – front body segment, 2 – middle body segment, 3 – rear body segment, 4 – locomotion leg, 5 – locomotion and manipulation leg, 6 – single axial joint, 7 – double axial joint, 8 – movable weight system; X – lateral axis, y – longitudinal axis, Z – vertical axis

The assumption is that in this configuration the robot should achieve the highest possible speed while moving through uneven terrain. The number of legs in the basic configuration, that is the one where all the robot legs are used to generate gait, is predicated mainly on the need for the static stability of gait in both configurations. To meet this criterion, the robot needs to have at least six legs, which means that in the alternative configuration it will move on four legs. Choosing a larger number of legs would allow higher speeds of statically stable gaits but it would significantly reduce the weight and size of the robot and greatly complicate both the design and motion control algorithms (Todd, 1985).

DOI 10.2478/ama-2018-0010

Fig. 2. 3D model of the hexa-quad bimorph walking robot in HEXAPOD configuration

Fig. 3. 3D model of the hexa-quad bimorph walking robot in QUADRUPED configuration

While designing the construction the choice was to minimize the number of legs so as not to complicate an already complex kinematic structure. Because the body is made of three segments, with active joints between the segments, it is possible to support the machine movement by adequately steering the robot body. Thanks to this, with a smaller number of legs, faster, statically stable gaits are achieved. Adequately using the drives of the body joints it is also possible to surmount obstacles in the form of naturally-occurring terrain or man-made obstacles, e.g. street kerbs.

Transformation into the alternative QUADRUPED robot is executed by elevating the front body by means of the drive in the double axial joint. In this configuration mainly the second key function of the hexa-quad bimorph walking robot is executed - manipulating objects while in motion or at a standstill. The robot can perform the object gripping and moving operations as well as perform operations on the objects, e.g. pressing buttons or pushing. To execute the above mentioned functions locomotive and manipulative legs are used. Moving around on the four remaining legs, the robot is forced to use the only statically stable gait - crawl. As a result, to achieve higher motion speeds in the alternative configuration, it is necessary to use dynamically stable gaits.

2.2. Physical research model

Based on the above described kinematic structure the design of the research model was created. Its 3D model is presented in Fig. 2. The basic function of the designed machine is performing specific analyses and designing motion control algorithms for hexa-quad bimorph walking robots. Due to a testing nature of the design, the machine was designed in a way that ensures simplicity of manufacturing and assembly. This construction is a prototype whose testing will contribute to building walking machines adapted to specific applications, both military (e.g. minesweeping robot) and civilian (e.g. mining machines).

The most important component of every walking robot are pedipulators - that is the legs of the robot executing basic locomotive functions. Their design has an influence on nearly all the features related to stability and generation of robot gait. In the presented design the biological structure of the insect was used. However, the ratio of lengths is different than in the standard insect structure being 1:2,3:4 instead of 1:4:5. Each limb consists of three links, hip segment 35 mm long, thigh segment 80 mm long and shank segment 140 mm long. That size of the leg makes it possible to achieve the step length 66 mm and the velocity of movement 33 mm/s. Kinematic analysis of this type of pedipulator was performed and presented in previous papers (Wojtkowiak, 2016). The foot structure of the insect is much more energy-efficient than the foot structure of reptiles or mammals. The features inspired by this biological structure are a three-segment body with one pair of legs assigned to each segment, and multifunctionality of the feet (Zielińska, 2014 and Morecki et al., 1999).

Pedipulator of the hexa-quad bimorph walking robot (Fig. 4) consists of three links. The first link consisting of two identical elements 1a and 1b is called the hip segment. It is connected with the body by the joint allowing rotation around the vertical axis. The middle link 2, called the thigh segment, and the final link 3, the so-called shank segment, have the ability to rotate around the longitudinal axis. At the end of this link the robot's foot 4 is located. Its main functions are to provide adequate friction between the robot and the surface, necessary to move around, to absorb foot strike and to enable the assembly of pressure sensors needed for testing static stability. The three-segment construction of the walking robot leg ensures that the foot can achieve any position within the working area of the pedipulator. All the segments are made from flat cranks of curvaceous shapes, connected with each other by means of servomotors 5, 6 and 7, which control the angular position of particular links, generating the robot's gait. In order to avoid complicating the design of the research model, the only difference between manipulation and locomotion legs and other pedipulators is the additional reinforcement in the middle segment in the form of the second flat crank to increase the stiffness of the leg. At the end of the shank segment there is a foot embedded on a ball pivot with a spring element 8. To ensure a sufficiently stiff connection between the leg and the body, the upper part 1a of the hip segment is connected to the servomechanism and the lower part 1b can rotate thanks to the axis 9 and the bearing set 10 in the lower plate of the body 11. The shape of each segment was designed based on the FEM analyses together with kinematic analyses, which helped to describe the operation zone of the pedipulator and prevent dangerous collisions during work (Wojtkowiak, 2016). Additionally, authors tried to reduce the weight of the limbs, which decreased the inertia and needed torque.

DOI 10.2478/ama-2018-0010

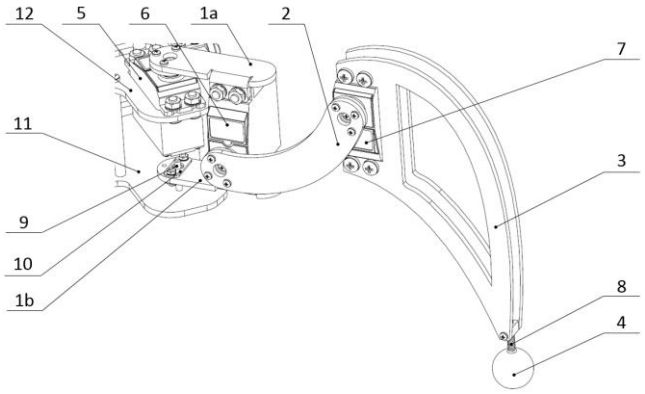

Fig. 4. Pedipulator structure of the hexa-quad bimorph walking robot: 1a – upper part of the hip segment, 1b – lower part of the hip segment, 2 – thigh segment, 3 – shank segment, 4 – foot, 5 – hip segment servomotor, 6 – thigh segment servomotor, 7 – shank segment servomotor, 8 – foot pivot, 9 – axis, 10 – bearing set, 11 – lower plate of the body, 12 – upper plate of the body

Characteristic elements of the hexa-quad bimorph walking robot design are the joints between body segments and the extendable weight system. Single axial joint (Fig. 5), between the middle and the rear body segment consists of the servomotor 1 responsible for rotation around the vertical axis. The motor is based on two C-channels mounted on the lower plate of the middle body 3. The upper plate of the rear body 4 is adequately profiled and mounted directly to the servomotor. In the double axial joint (Fig. 6) that can be found between the front and the middle body segment, rotation around the vertical axis is executed in an almost identical way, the only difference being that the turning plate 4 is mounted on the servomotor 1. The servomotor 5 responsible for rotation around the lateral axis is screwed onto the turning plate. To the servo motor shaft is attached the elevating crank whose tip is connected by means of the C-channel 7 with the upper plate of the front body segment 8.

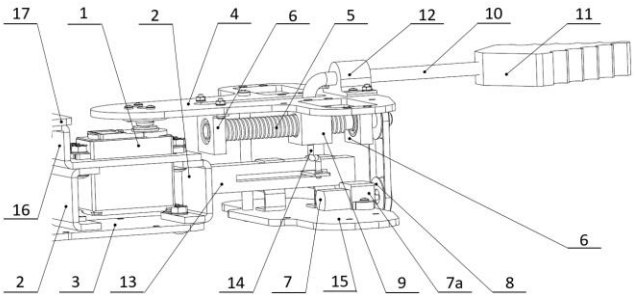

Fig. 5. Structure of the single axial joint and the extendable weight system: 1 – vertical servo motor, 2 – supporting C-channel, 3 – lower plate of the middle body segment, 4 – upper plate of the rear body segment, 5 – trapezoidal thread screw, 6 – bearing support, 7 – DC motor, 7a – motor mount, 8 – transmission belt, 9 – nut, 10 – slider 11 – counterweight, 12 – linear sliding bearing, 13 – sliding potentiometer, 14 – connector, 15 – the lower plate of the rear body segment, 16 – handle of the body servomotor, 17 – the upper plate of the middle body segment

Due to limited enclosure space, the design of the extendable weight system is based on the screw/nut drive mechanism. The system is presented as a schematic in Fig. 7 and its structure is presented in Fig. 5. The screw 5 with the symmetrical trapezoidal thread with support bearings 6 at its tops is driven by the DC motor 7 by means of the belt transmission 8. As a result of the rotary motion of the screw the translational motion of the nut starts. The slider 10 embedded in the linear bearing 12 is rigidly attached to the nut. At the end of the arm is the counterweight 11. This kind of solution excludes the possibility of subjecting the screw to the bending moment. In order to read the current position of the nut it is connected to the sliding potentiometer 13.

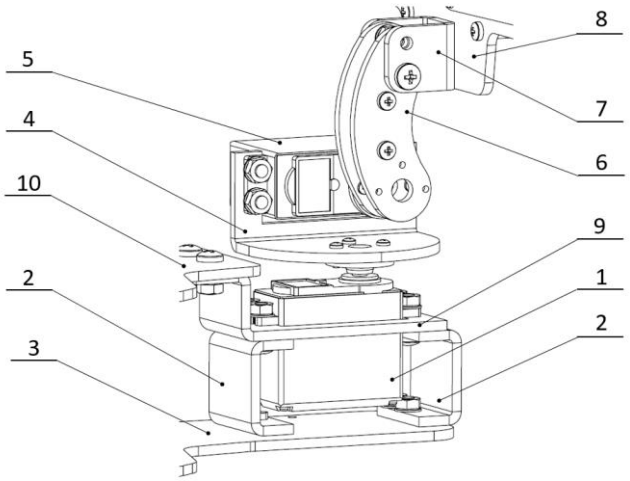

Fig. 6. Structure of the double axial joint of the hexa-quad bimorph walking robot: 1 – vertical servomotor, 2 – supporting C-channel, 3 – lower plate of the middle body segment, 4 – turning plate, 5 – horizontal servomotor, 6 – elevating crank, 7 – angular plate for mounting the elevating crank, 8 – the upper plate of the front body segment, 9 – handle of the body servo motor, 10 – the upper plate of the middle body segment

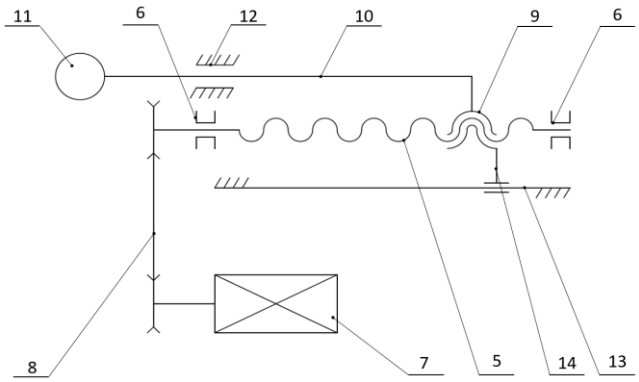

Fig. 7. Kinetic schematic of the extendable weight system: 5 – screw with trapezoidal thread, 6 – bearing support, 7 – DC motor, 8 – belt transmission, 9 – nut, 10 – arm, 11 – counterweight, 12 – longitudinal bearing, 13 – sliding potentiometer, 14 – connector

Apart from the mechanical construction a very important stage in designing walking robots is the choice of actuators, sensors, drivers and power supply systems. 3D model of the testing prototype with necessary electronics is presented in Fig. 8.

In order to select the drives, the analysis of maximum load moments of particular joints of the robot needs to be performed. The following analyses were performed and presented in the previous work (Wojtkowiak, 2017). The presented research model is driven by 21 analogue servomotors with range of motion be-

DOI 10.2478/ama-2018-0010

tween 0° and 180°. Despite small size and weight, they have a relatively big moment and sufficient speed with the 6 V power supply. An additional advantage of choosing these motors is the fact that their components - gears and the serrated output shaft - are made from metal, not plastics. Using metal connectors ensures required stiffness of the serrated connection between the output shaft and the connector. The extendable weight system is driven by the DC motor with the rotational speed of 70 rpm and supply voltage of 6 V.

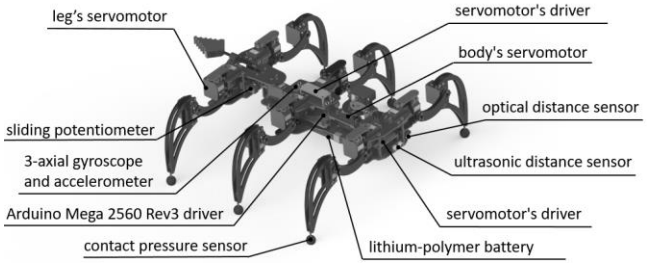

Fig. 8. 3D model of the hexa-quad bimorph walking robot with sensors and drivers

In order to obtain a certain degree of operational autonomy of the tested prototype, it is equipped with a number of sensors. Because of the application of the testing prototype, which is to enable research in order to describe the kinematics and the steering method, the robot was equipped only with the basic sensors. In the front and in the rear of the robot there are two ultrasound distance sensors with a range of 2–400 cm, whose role is to detect obstacles on the robot's path. On the lower plate of the front body segment, from below, the optical distance sensor with a range of 4–30 cm is mounted. In the basic configuration its role is to monitor clearance between the front body segment and the surface providing information about the characteristics of the terrain where the robot is moving. In the alternative configuration its role is to read the position of the objects that are being manipulated. A very important piece of equipment, as far as testing dynamic stability and the influence of terrain slope on the robot's gait, is the three axial accelerometer and gyroscope mounted on the middle body segment. In order to test static stability on the basis of foot pressure, each leg is equipped with the resistance pressure sensor with the measurement range between 0.2 N and 20 N. So as to measure power consumption of the servomechanism the robot is equipped with the power sensor.

In order to control selected actuators and analyze signals from the above described sensors the robot is equipped with Arduino Mega 2560 Rev 3 driver based on ATmega2560 microcontroller. The system contains 54 input/output pins, of which 15 can be used as PWM outputs, 16 analog inputs and 4 UART hardware serial ports, an SPI and I2C. The system is powered with 7–12 V input voltage. In order to control servomotors two 16-channel servomotor controllers Adafruit containing accurate 12-bit PWM signal generator are used. In turn, the DC motor is controlled by the system based on the H bridge allowing the change in rotation direction and speed regulation. In order to separate control systems from servomotors that introduce interferences a separate power supply is used. The testing prototype can be powered from the lithium polymer battery located at the bottom of the front body segment or from separate lab power supplies. The battery that supplies power to the electronic components has the capacity of 1300 mAh whereas the battery that supplies power servomotors has the capacity of 3300 mAh. Both batteries are two cell and have nominal voltage of 7.4 V and big current efficiency (30C). Although this capacity will be enough only for maximum 30 minutes of operation.

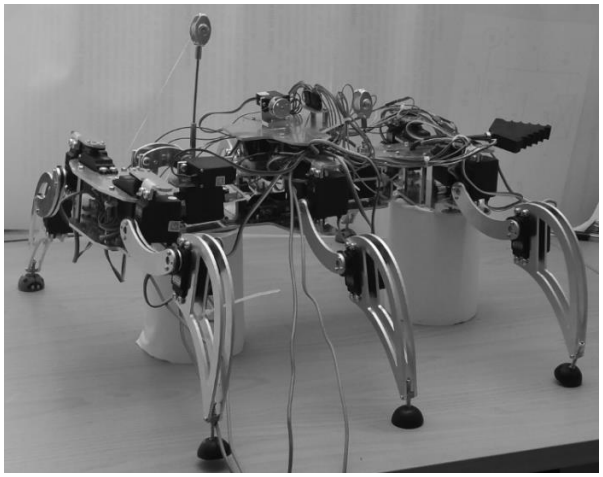

Fig. 9. Hexa-quad bimorph walking robot prototype

On the basis of the formulated design the testing prototype presented in Fig. 9 was built. Its overall dimensions do not exceed 500 mm in length and 300 mm in width. The height of the bimorph hexa-quad walking robot is less than 200 mm in hexapod configuration, measuring from the surface on which it stands to the top plate of the base (without accessories mounted on its back) and rise to 350 mm after changing its configuration to quadruped. Total weight of the robot is approximately 3 kg. The payload of the machine should not exceed 0.5 kg, but could be increased using heavier retractable weight.

3. GAIT STABILITY

Gait stability is one of the most important parameters influencing a number of functional features related to walking robots, from mechanical construction to control algorithms and generating steps. There are two types of stability in walking robots: static stability and dynamic stability. The measurement value to determine stability margin can be distance, angle, energy, moment or force. Many stability criteria have been formulated on their basis. With appropriate assumptions, the same methods can be used to determine both types of stability. One example is the energy stability margin, which involves measuring the difference between the initial potential energy and the actual potential energy. If we consider that all external forces including the force of gravity act on the centre of gravity of the robot we get the dynamic energy stability margin (Hajiabadi, 2013; Hirsoe, 2001).

In the above mentioned research projects attention was focused solely on static stability. The main assumption of static stability of walking robots is retaining centre of gravity or its projection inside the support polygon. This region is defined as a support polygon, a two-dimensional figure created from coordinates of tips of all supporting legs projected onto a support plane. These coordinates can be calculated based on the kinematic model of the leg (Wojtkowiak, 2016). In order to determine which legs are currently in a support phase, pressure sensors can be used. As a quantitative criterion static stability margin (SSM) and

DOI 10.2478/ama-2018-0010

longitudinal static stability margin (LSM) were used – Fig. 10. Longitudinal static stability margin is defined as the shorter one out of the distances between the projection of centre of gravity on the support plane and the edge of the support polygon as measured along the direction of the walking robot's speed vector. In turn, static stability margin is defined as the shortest distance between the aforementioned projection and the edge of the support polygon. (Inagaki, 1998; Hung, 2005). These methods can be used in cases of negligible inertia and absence of forces counteracting the robot's movement. However, irregularities of the surface where the robot is moving around do not have influence on the adequacy of the results obtained by means of one of the above mentioned methods (Garcia, 2002).

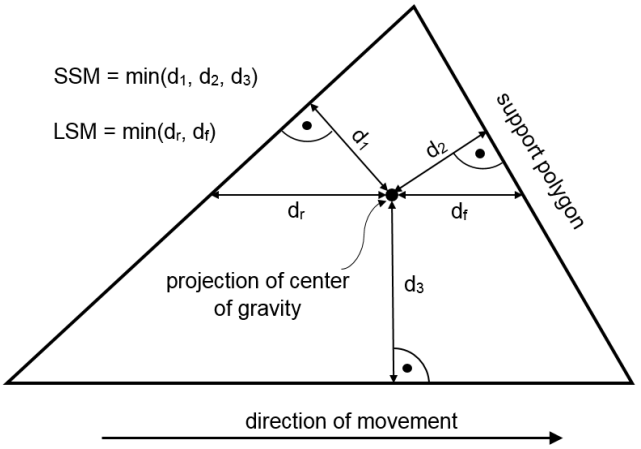

Fig. 10. Support polygon together with indicated stability margins

4. SUMMARY

In this article the design of the hexa-quad bimorph walking robot was presented. The key advantage of this robot is, that it construction provides an ability to move easily from hexapod configuration to quadruped configuration or the other way around. This means, it can combine advantages of both four-legged and six-legged robots. Basically its main function is to achieve the highest possible speed while moving through uneven terrain. Additionally, robot can manipulate objects while being in motion or at a standstill. In order to gain desired parameters of the hexa-quad bimorph walking robot, presented prototype must be tested by making a series of researches, which contain stability and control algorithms tests.

REFERENCES

1. **Bartsch S.** (2012), *Development, control, and empirical evaluation of the six-legged robot SpaceClimber designed for extraterrestrial crater exploration*, dissertation, Bremen, University of Bremen.
2. **Boston Dynamics** website https://www.bostondynamics.com/robots [Access date: 26.10.2017].
3. **Garcia E., Estremera J., Gonzalez-de-Santos P.** (2002) A comparative study of stability margins for walking machines. *Robotica*, 20, 595-606.
4. **Garcia E., Estremera J., Gonzalez-de-Santos P.** (2002), A classification of stability margins for walking robots, *Proceedings of CLAWAR*, Paris, France.
5. **Hajiabadi M.M.A.** (2013), *Analytical workspace, kinematics, and foot force based stability of hexapod walking robots*, dissertation, Worcester: Worcester Polytechnic Institute.
6. **Hirsoe S., Tsukagoshi H., Yoneda K.** (2001), Normalized energy stability margin and its contour of walking vehicles on rough terrain, *International Conference on Robotics & Automation*, Seoul Korea.
7. **Hung M-H., Cheng F-T., Lee H-L.** (2005), Orin DE. Increasing the stability margin of multilegged vehicles through body sway. *J Chin. Inst. Eng*, 28, 39-54.
8. **Inagaki K.** (1998), A gait study for one-leg-disabled hexapod robot, *Advanced Robotics*, 12, 593-604.
9. **Kim J-Y., Jun B-H.** (2014), Design of six-legged walking robot, Little Crabster for underwater walking and operation, *Advanced Robotics*, 28, 77-89.
10. **Kolouche S., Rollinson D., Choset H.** (2015), Modularity for maximum mobility and manipulation: control of a reconfigurable legged robot with series-elastic actuators, *Proceedings of the IEEE International Symposium on Safety*, Security and Robotics (SSRR), 1-8.
11. **Lewinger W.A, Branicky M.S., Quinn R.D.** (2005), Insect-inspired, actively compliant hexapod capable of object manipulation, *Proceedings of CLAWAR*, Londom, 65-72.
12. **Manz M., Bartsch S., Kirchner F.** (2013), MANTIS - a robot with advanced locomotion and manipulation abilities, *Proceedings of Symposium on Advanced Space Technologies in Robotics and Automation*, Noordwijk the Netherlands.
13. **Morecki A., Knapczyk.J.** (1999), Basics of Robotics – theory and elements of manipulators and robots (in polish), Warszawa.
14. **Roennau A., Heppner G., Nowicki M., Dillmann R.** (2014), LAURON V: A versatile six-legged walking robot with Advanced Maneuverability, *IEEE/ASME International Conference on Advanced Intelligent Mechatronics (AIM)*, Besançon, France, 82-87.
15. **Saunders A., Goldman D.I., Full R.J., Buehler M.** (2006), The RiSE climbing robot: body and leg design, *Proceedings of The International Society of Optical Engineering*, Orlando USA, 6230, 623017.
16. **Tang Y., Ma S., Sun Y., Ge D.** (2015), Planar legged walking of passive-spine hexapod robot, *Advanced Robo*tics, 29, 1510-1525.
17. **Todd D.J.** (1985), *Walking machines - An introduction to legged robots*, Springer, London**.**
18. **Wojtkowiak D., Malujda I., Talaśka K., Magdziak Ł., Wieczorek B.** (2017), Influence of the Body Weight Distribution on the Walking Robot's Gait Stability, *Proceedia Engineering*, 177, 419-424.
19. **Wojtkowiak D., Talaśka K., Malujda I.** (2016), Computer analysis of insect-like robot leg structure – part 1 – Static Finite-Element analysis, *Journal of Mechanical and Transport Engineering*, 68(3), 53-62.
20. **Wojtkowiak D., Talaśka K., Malujda I.** (2016), Computer analysis of insect-like robot leg structure – part 2 – kinematic and dynamic analyses, *Journal of Mechanical and Transport Engineering*, 68(3), 63-75.
21. **Wojtkowiak D., Talaśka K., Malujda I.** (2017), The selection of the bimorph walking robot drives based on the dynamic model of its legs (in polish), *Inżynieria wytwarzania*, Wyd. uczelniane Państwowej Wyższej Szkoły Zawodowej w Kaliszu, in press.
22. **Zielińska T.** (2014), Walking robots – basics, design, steering and biological patterns, PWN, Warszawa.

DOI 10.2478/ama-2018-0011

CONSTRUCTIONAL FEATURES OF ROPES IN FUNCTIONAL UNITS OF MINING SHAFT HOIST

Eugeniusz MAŃKA[*], Małgorzata SŁOMION[**], Maciej MATUSZEWSKI[***]

[*]Research and Supervisory Centre of Underground Mining, ul. Lędzińska 8, 43-143 Lędziny, Poland
[**]Doctoral studies, University of Science and Technology, ul. S.Kaliskiego 7, 85-796 Bydgoszcz, Poland
[***]Faculty of Mechanical Engineering, University of Science and Technology, ul. S.Kaliskiego 7, 85-796 Bydgoszcz, Poland

emanka59@wp.pl, m.slomion@yahoo.pl, matus@utp.edu.pl

received 6 June 2017, revised 18 March 2018, accepted 20 March 2018

Abstract: In this paper structural analysis of steel ropes applied in mining shaft hoists was conducted. Functions of the ropes which they fulfilled in these shaft hoists were identified. Expected operational features of ropes were indicated too. An analysis was carried out four identified groups of ropes: hoisting ropes, balance ropes, leading rope and fender ropes. Basic constructional features: geometrical and material of ropes, which they should be characterized in each of mentioned functional groups were indicated. Constructional structures of mentioned steel ropes, the most often applied in domestic mining shaft hoists were described. Observed tendencies in analyzed issues also were shown.

Key words: Shaft Hoist, Steel Rope, Hoisting Rope, Balance Rope, Leading Rope, Fender Rope, Operational Feature, Constructional Feature

1. INTRODUCTION

The ropes as the element or the elements set are appearing in numerous, diverse machines and mechanisms, fulfilling the most different functions in them. They are elements used, for example, as flexible connector in control systems, they are used also for an transfer operation of axial load in changeable directions in transport systems, both horizontal and vertical.

As the constructional element moving axial forces with significant values steel ropes are applied, e.g.: in the construction (goods and personal lifts, reinforcing concrete), in the mining for the vertical and horizontal transport and in other branches of industry, as a different kind of tension members, being used for a transport of materials and people.

Relatively great durability and a reliability are a major advantage of ropes. This second feature results from it, that the rope has a parallel constructional structure what causes, that in case of damage one or a few structural components (wire) loss of the ability of the whole system, in which its is existing isn't taking place (Guo et al., 2017; Olszyna et al., 2013, Peterka et al., 2014; Sioma and Tytko, 2012; Zhang et al., 2017).

2. ROPES IN MINING SHAFT HOISTS

Mining shaft hoists are a very representative example of the object being used for a vertical transport, of both the staff of the mine and winning. Their depth is diversified and in Polish mines of the hard coal is coming up to 1300 meters. Among others for this reason constructional structure of shaft hoists is diversified. In addition, in each of variants existing individual ropes or set of ropes which fulfilling the following functions:

- carrying – moving total axial load coming from hung mass: of hoisting dishes, suspensions, ropes, transported mining, material or people,
- balancing – being used to balance out the static moment resulting from the imbalance of mass on both sides of the driving wheel,
- leading, which providing the free migration of dishes in the mineshaft is a task,
- fender – limiting lateral movements of dishes in the mineshaft.

Situating them in the standard mineshaft was presented in Fig. 1.

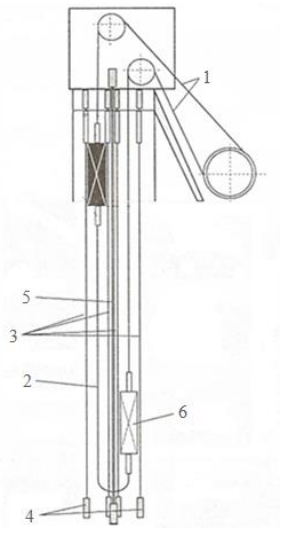

Fig. 1. The ropes in the exemplary mining shaft hoist: 1 – hoisting rope, 2 – balance rope, 3 – leading ropes, 4 – weights of leading ropes, 5 – fender ropes, 6 – hoisting dishes

DOI 10.2478/ama-2018-0011

From the above statement it appears that ropes in mining lifts are fulfilling number of diverse functions. It is a reason, that applied in them ropes have various constructional solutions and the structure. They differ between themselves above all in structural features: geometrical and material what he causes that also their operational features are diversified. Using the rope with the specific construction depends first of all on the function which it is supposed to carry out (Chang et al., 2016; Wang et al., 2015; Zhang et al., 2017).

2.1. Hoisting ropes

Hoisting ropes in mining shaft hoist are working in different layouts, depending on the type of the drive:

- in drum drives – rope working in the overlap or underlap arrangement,
- in drives with the frictional contact (KOEPE system) – in arrangements one-, two- or four-ropes.

In multi-rope systems essentially is that ropes work identically, not entering undesirable disruptions into the system (Chang et al., 2017; Ma and Xiao, 2013; Ma and Xiao, 2016; Styp-Rekowski et al., 2015). For this reason it necessary is to apply in the system the identical number of left- and right-lay ropes, because it allows to minimize tendencies of turning the hoisting dish. Moreover, hoisting ropes in multirope arrangements should be produced from one party of wire rods and in one production cycle. It is stated practically by authors (Mańka, 2013; Mańka and Styp-Rekowski, 2009) that in multi-rope arrangements the use of ropes dating from different supplies in the significant range is shortening the time of their use.

One already stated above that for correct and effective fulfilling assumed functions, selecting the constructional features suitable for the function of ropes was essential.

In case of hoisting ropes first of all one should rank significant material constructional features: the chemical composition of the wire rod which wire is produced from – basic structural element of a steel rope. Tensile strength, that is a quantity determining the basic functional feature of hoisting ropes depend on its chemical composition – acceptable tensile force. On account of the fact that the hoisting rope is repeatedly bent also plastic properties of wire, as well as the whole rope are significant. Such features provides a wire rod of steel contents within carbon in the range of 0.3 ÷ 0.9%, of manganese in the amount 0.3 ÷ 0.8%, and up to the 0.2% of such metals as: chromium, nickel, copper. Such elements as: sulphur and phosphorus should not be altogether more than a 0.05% on account of the fact that they are granting the undesirable brittleness of steel.

A core is an important element of the constructional structure of round hoisting ropes, above all material from which it is made. It is responsible for an appropriate shape of the rope, moreover, it is an axis of the moment of stranding back of the whole rope, resulting from the constructional structure of ropes and from the way of producing them. In hoisting ropes to main objectives of the organic core belong:

- providing the "support" for rope strand so that in operating time contact between them doesn't take place,
- counteraction for considerable radial pressures and minimizing deformations of the section diameter of the rope,
- protecting the inside of the rope (of wire and strands) against the corrosion.

Currently, in the domestic mining shaft hoist round or triangle strand single-layer ropes are applied. Their constructional structures were presented in Figs. 2 and 3.

In Fig. 2 ropes were shown structures of round strand ropes of type Warrington-Seale (WS) and Warrington-Cover (NW).

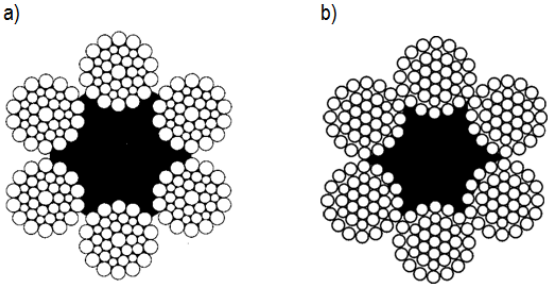

Fig. 2. Examples of structures of round strands hoisting ropes: a) type 6x36WS-FC, b) type 6x35NW-FC (Catalogs of rope manufacturers)

The ropes presented in the picture above (Fig. 2) are made of a round strands which are rising as a result of winding on spinal wire next layers of wire. In Fig. 2a the structure of the rope of the type Warrington-Seale was presented, in which among layers of wires in strands a linear contact of wire is appearing, however in Fig. 2b – the rope of the type Warrington-Cover, in which between last and one before last layer of wires in strands point contact is appearing.

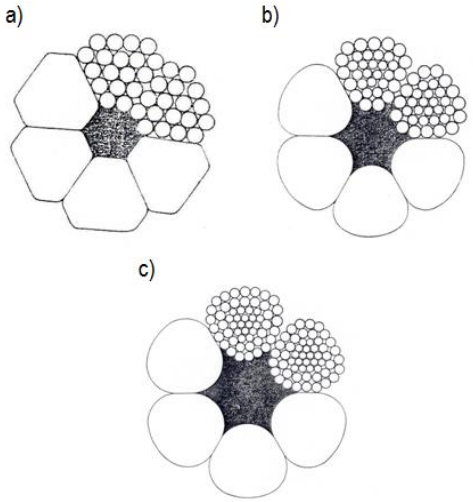

Fig. 3. Examples of structures of triangle strands hoisting ropes: a) type 6xV18B-FC, b) type 6xV33B-FC, c) type 6xV54B-FC (Catalogs of rope manufacturers)

Triangle strand ropes – Fig. 3, are made according to the Polish Standard PN-66/G-46602. In these ropes to the triangular core of strand, made from three pairs of round wire and three wire filling up (3x2+3), is rolled up one (Fig. 3a), two (Fig. 3b) or three (Fig. 3c) the layers of wire of various diameters. Diameter of the triangle strand rope depends on the diameter of wires in particular layers and numbers of wires in strands.

Multilayered hoisting ropes type Notorplast are applied in deep mineshafts. They are screwed together of around strand – Fig. 4. Ropes of the such structure are characterized by great unscrewness, and tensile strength of wire is included in the range of 1770 ÷ 2000 MPa. Between the centre and outer layer they have a greased plait made of sisal fibres. The important task of

DOI 10.2478/ama-2018-0011

plait, apart from the corrosion protection, is reducing surface pressures between the outer and inner layer.

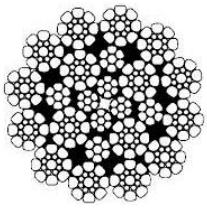

Fig. 4. Structure of multilayer hoisting rope firm ArcelorMittal Wire (France), type Notorplast 12x16 SPC: PWRC [FC-4x7-(4x17S+4x7)] (Catalogs of rope manufacturers)

For a few years a tendency of replacing described higher ropes is being observed, especially a triangle strand ones, by ropes with other constructional structures, first of all with compacted ropes – Fig. 5. Such ropes are built of strands with the linear contact of wire, subjected to plastic forming. After this processing a surface contact of wire in strands is being get.

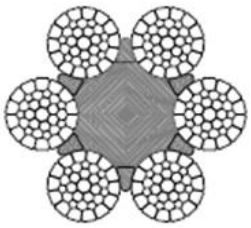

Fig. 5. Structure of hoisting rope type 6xK36WS-FC with surface contact of wires in plastic deformed strands (Catalogs of rope manufacturers)

With advantages of compacted ropes, in comparing to traditional ropes, are among others: greater filling of the diameter, smaller unscrewness moment, the greater resistance to wear, abrasion, the corrosion and the greater tensile strength (Carbogno et al., 2010; Zhao et al., 2017; Peng et al., 2016).

2.2. Balance ropes

In order to protect against the possibility of the appearing of the unchecked slide in the arrangement: hoisting rope – driving wheel (lineshafting), and also for balancing the static moment resulting from the imbalance of mass on both sides of the driving wheel, in mining shaft hoist balance ropes are applied. These ropes should have appropriate mass individual, to be characterized unscrewness, the great durability, but especially a resistance to the effect of the aggressive environment. Based on literature information, e.g. in the papers of authors (Carbogno et al., 2005; Li et al., 2017; Mateja and Pojnar, 2005; Xu et al., 2014), as well as on results of authors own investigations, e.g. (Styp-Rekowski and Mańka, 2010), the time of life of steel balance ropes in the large degree depends exactly on the environment, in which they are operated. In order to minimizing the corrosion effects, wires of round ropes are covered with the protective coating. In domestic ropes to the protective coating of wire zinc is applicable, foreign producers apply also an alloy of zinc and aluminum (galwan).

Direction of a lay of wire in strand and strands in the rope, is a next essential geometrical constructional feature of balance ropes. Flat steel ropes and steel-rubber ropes are built from the same number of the right-lay and left-lay ropes what causes, that ropes of this type are unscrew.

A contact of wire appearing between particular layers in the strands and individual layers of strands in multi-layer ropes is a next important constructional feature of steel balance ropes. On account of the durability of ropes one endeavour to situation, that it will not point contact.

In traditional solutions, as balance ropes round multi-layer ropes are applied – Fig. 6, made according to Polish norms or company conditions of the producer. They were applied in shaft hoist about the depth to 1300 m. Parameters of wire lay in strands and structure of strand in ropes are so well-matched that these ropes aren't having a tendency to the rotation against the own axis. Round strand balance ropes have two (Fig. 6a) or three (Fig. 6b) layers of strands.

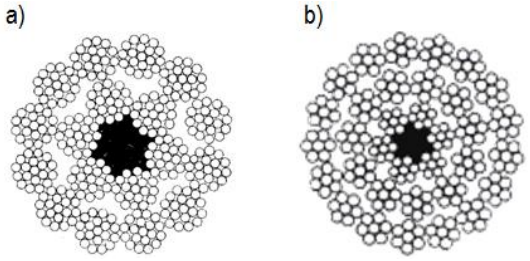

Fig. 6. Examples of round balance ropes structures: a) two-layers type 18x19M-FC, b) three-layers type 33(M)x7-FC (Catalogs of rope manufacturers)

Two-layers round balance ropes of the domestic structure are built from wires of the identical diameter. In mentioned types of ropes a point contact is appearing between wires in strands and between strand layers in whole ropes. In order to getting the optimum shape of strand, three-layers ropes have spinal wire of the diameter 0.1 mm bigger than wire of strand. In foreign ropes as a result of strand making of the various diameter wire and of using inserts of natural or artificial fibres, the contact between wire and layers isn't punctual.

The elasticity of steel ropes with such constructional is possible to obtain thanks to the great number of strands. Multilayer round balance ropes during the operation ought to have ensured a possibility of pivot in rope suspension due to the resultant moment acting there (from the load) twisting off strands.

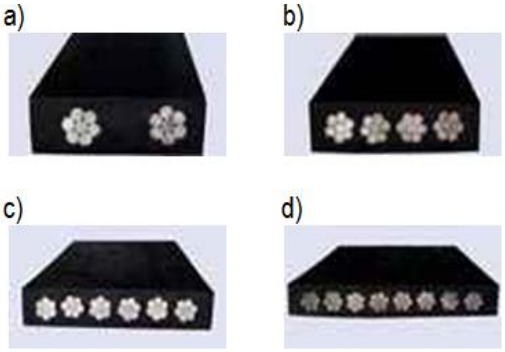

Fig. 7. Structure of steel-rubber balance ropes type SAG: a) 2-ropes, b) 4-ropes, c) 6-ropes, d) 8-ropes (Catalogs of rope manufacturers)

DOI 10.2478/ama-2018-0011

At present, in the predominating number of cases, as balance ropes steel-rubber ropes are used – Figs. 7 and 8, which characterize the great fatigue durability, resistance to action of the corroding environment and on little blows of falling objects (mining). At the appropriate technology of making, they can be applied in shaft hoists depths above 2200 meters.

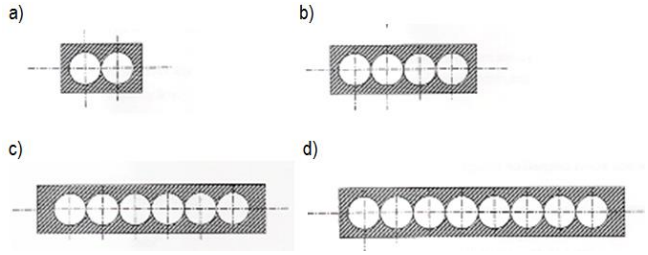

Fig. 8. Steel-rubber balance ropes type ZEP: a) two-ropes, b) four-ropes, c) six-ropes, d) eight-ropes (Catalogs of rope manufacturers)

Basic advantages of steel-rubber ropes, given by authors: (Hansel, 2000; Kwaśniewski, 2010, Milcarz and Fundament, 2005) are following:

- unscrewness,
- the great corrosion resistance and blows of small falling objects,
- possibility of repair of the rubber coating in places of mechanical damages with method of the vulcanization or the adhesive bonding,
- the lack of the need of additional lubrication,
- antistatic-ness, letting for applying in exhaust shaft hoists carrying out air from each type of methane fields,
- possibility of control of the technical condition with applying non-destructive testing with magnetic method at the producing plant and during the operating.

Steel-rubber ropes in their structure have steel cables alternately – right-lay and left-lay ropes, which are in the rubber coating. The weight of the steel-rubber rope depends on the number and the diameter of steel cords and on the thickness of the rubber coating.

Both types of ropes (SAG and ZEP) are usually produced of thicknesses 29 or 35 mm. In order to reach the right specific weight and transverse dimensions of the rope, transverse dimensions of the rope can be changed as a result of arrangements between the producer and the user.

Core in steel-rubber ropes types of SAG and ZEP, which is in the form of steel links strand, is made identically like remaining strands of ropes. It is structure with the linear contact of wire of the type WARRINGTON.

2.3. Leading and fender ropes

Leading ropes are applied in shaft hoists where instead of stiff leading of dishes (steel or wooden guides) a rope guidance was applied. Providing the free, but defined displacement of dishes in the shaft hoist is the main task of these ropes.

Limiting lateral movements of dishes in the shaft hoist is the task of fender ropes. Similar functions of leading and fender ropes in mining hoists causes, that in both cases ropes are applicable with the same constructional structure.

Leading and fender ropes can be applied in shaft hoists of the depth more than 1000 m, in which providing the rectilinearity of stiff leading of dishes is labor consuming and uneconomical. Hoisting dishes are being led by ropes in exchangeable sliding or sliding-rolling tracks attached to dishes.

Leading and fender ropes in shaft hoists have closed or half-closed structure. Ropes of this structure are characterized of "smooth" surface, unscrewness, corrosion and abrasive resistance, great tensile strength, and great crosswise and longitudinal stiffness. The tensile strength of wire in ropes of the closed and half-closed structure should take out from 780 to 1470 MPa. Tolerance of the tensile strength for individual wire of leading ropes according to standard (PN-EN 12385-7:2004) should not cross +250 MPa.

In Fig. 9 two typical solutions of applying leading and fender ropes were presented:

- corner arrangement, in which leading ropes are located in corner of the hoisting dish – Fig. 9a,
- side arrangement, leading ropes are arranged along one side of the hoisting dish – Fig. 9b.

Corner arrangement – Fig. 9a, is more resistant to action of the unscrew moment of hoisting rope. Side arrangement – Fig. 9b, is recommended at multi-ropes system of hoisting ropes, in which unscrew moment, as a result of applying the same number of right- and left-lay, practically is not appearing.

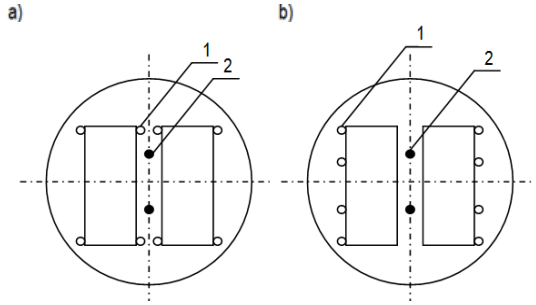

Fig. 9. Location of leading and fender ropes in shaft hoist in arrangements: a) corner, b) side; 1 – leading ropes, 2 – fender ropes

Arranging presented in Fig. 9 of leading ropes around dishes are the most often applying solution in domestic shaft hoists. In the world it is possible to meet a lot of other solutions of these ropes arranging around the dish, it is regarding both the number of ropes and the way of arranging them around the dish.

In newly built or modernized shaft hoists, for leading the dish round strand, ordinary-lay, non-spinning leading ropes are applied. Leading ropes in that kind of hoist, apart from leading the dish are usually also hoisting rope of the service platform hanging in the shaft. These ropes one end are being fixed to the platform and second, through directional wheels on the tower of hoist to the drum situated on the framework. On the drum a remaining rope-length which is used to raise or to leave the working platform. The dish is led by the leading sleigh installed above it on the rope. Tensile strength of wires of this kind of ropes is 1570 MPa and more, depending on requirements ordering.

In mining applicable regulations essential requirements concerning leading and fender ropes operating in domestic shaft hoists were determined. They contain, among others:

- demanded minimal safety factor understood as the quotient of real tensile force of rope in one piece to the maximum of static load,
- number of leading and fender ropes depending on air flow rate in the shaft,

DOI 10.2478/ama-2018-0011

- way of leading ropes arranging around the dish and fender ropes in the shaft,
- the kind, the way and the value of the tension of ropes in sump or in tower of the shaft,
- diameter of fender ropes; it should be 2 mm bigger than leading ropes.

Leading and fender ropes, the most often of closed and half-closed structure, belong to a type of twisted line ropes. Next layers of round wire are being wound on central spinal wire, and then, depending on the structure and donating the rope – shaped wires. For getting almost total unscrewness of that kind of ropes, lay directions of wire in particular layers are closely determined in standard.

Half-closed ropes are built of a few layers of round wires, however outer layer alternately arranged round wire and profile wire.

In ropes of the closed structure according to the standard (PN-EN 12385-7:2004), on layers previously screwed together of round wire, a layer of alternately arranged wire shaped (X) and round is wound, and then layer of other shaped wire (Z).

Using wedge-shaped wire in structures of this type of ropes causes, that they are characterized by an increased stiffness what for the function carried out is not a negative feature. Important factor causing that ropes of the closed and half-closed structure have a abrasive and corrosion resistance there are transverse dimensions of profile wire. Transverse dimensions of profile wires, especially their height and diameter of the wire in the outer layer of the half-closed structure can be into 10 mm. Detailed requirements concerning dimensions of wire of outer layer for ropes of the half-closed structure are given in the standard (PN-EN 12385-7:2004). Dimensions of profile wire in ropes of the closed structure are determined by the producer of the rope. In the outer layer usually they have a height of about 6 mm. It is an essential requirement, if only structure of closed and half-closed structure ropes a creates possibility of keeping cracked wire in the contour of ropes, because cracking and weaving of profile wire can lead to the stop of hoisting shaft.

Round strand leading ropes belong to double-laid ropes. They are made by winding on the fibre core one or more layers of strands. Round strand ropes single-layer are making as ordinary lay with aim of getting the smallest unscrewness. In these ropes laid direction of wire in strands is against to laid direction of strands in the rope.

Conducted analysis of types of leading and fender ropes operating in domestic mining shaft hoists showed that the most often ropes of below described structural solutions were applied. In Figs. 10-12 a few structural solutions were presented. Constructionall structure of ropes of the structure half-closed and closed is more compound than the around strand ones, therefore the marking is more compound. In denotation of ropes symbols according to the applicable standard (PN-EN 12385-2:2008) were accepted.

In Fig. 10 half-closed ropes were shown. Rope of structure 1 + 6 + 7 / 7 H (Fig. 10 a) is a rope having in outer layer alternately, 7 profile wires (H) and 7 round wires. The internal layer of this rope is screwed together from 7 round wire (1 + 6).

Rope of structure 1+6+6/ 6+9/9 H in Fig. 10 b, in outer layer has 9 wires alternately, profile (H) and 9 round wire. The internal layer of this rope is screwed together from round wire in the amount of 1+6+6/6.

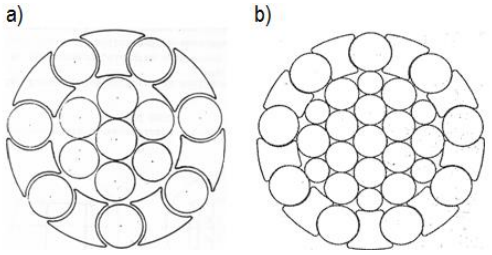

Fig. 10. Exemplary constructional structure of half-closed ropes (Catalogs of rope manufacturers)

In the next picture ropes of the closed structure were presented. The rope produced of LINODRUT company, for which the structure was presented in Fig. 11a, in outer layer has 23 profile wires (Z). Next layer constitutes 17 profile wires (S). Inside of this rope is screwed together from round wire in the number: 1+6/ 6+12+18.

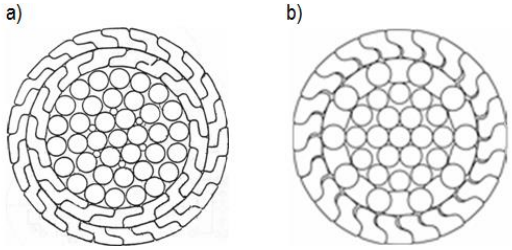

Fig. 11. Exemplary cross section of closed ropes of structures: a) 23Z+17S+18+12+6/6+1, b) 24Z+10/10H+12+6+1 (Catalogs of rope manufacturers)

Rope of the Teufelberger company (Austria) – Fig. 11b, in outer layer has 24 profile wires (Z), next layer it is alternately arranged 10 profile wires (H) and 10 – round wires. The internal layer of this rope is screwed together from round wire in the amount of 1+6+12.

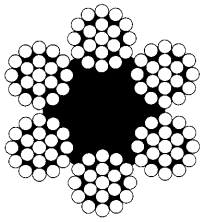

Fig. 12. Cross section of round strand rope, type 6x19M-FC (Catalogs of rope manufacturers)

In Fig. 12 a structure of the round strand rope was shown. This rope is built of 6 strands containing 19 wires with point contact of wire in strands (marked M), with the fibre core (marked FC).

3. CLOSURE

Above, chosen examples of the construction of more often appearing ropes: hoisting, balance, leading and fender were presented. In individual cases, in which different criteria than one gave higher are considered, applied ropes can be of other constructional structure.

DOI 10.2478/ama-2018-0011

On the base of conducted, and described in this work the functional and structural analysis of various constructional solutions of steel ropes applied in shaft hoists, following conclusions were formulated:

- produced ropes are characterized by great structural diversity but simultaneously not very great versatility. Mentioned factors cause, that ropes still are objects of numerous researches fulfilled by scientific and scientific-research centers,
- at depths of shaft hoistings over 500 meters multi-layer ropes, which are characterized of great unscrewness are applied,
- structural diversity of ropes – particularly multi-layers causes, that the evaluation of the current rope technical condition is complicated and requires great experience from conducting an examination,
- discerning, multifactorial analysis preceding the decision to use the rope in the mechanism of the determined structural form is contributing undoubtedly to increase the effectiveness of carried out action, among other thanks to the possibility of the optimization of choice in this range, at logistic criteria.

REFERENCES

1. **Carbogno A., Fundalewicz Z., Mateja S.** (2005), Safety of the round balancing rope type „SUPERFLEX", *Proceedings of International Conference* „Shafts Transport 2005", Institute of Mining Technology „KOMAG", Gliwice – Zakopane, 221-232 (in Polish).
2. **Carbogno A., Żołnierz M., Mateja S.** (2010), Rope with surface contact of wires used in mining transport equipment, *Proceedings of International Conference* „Safety Operation of Mining Transport Equipment" Research and Supervisory Centre of Underground Mining, Lędziny – Ustroń, 45-55 (in Polish).
3. **Catalogs of rope manufacturers:** ArcelorMittal, Bourg-an-Bresse Wire, Polish Ropes, Sosnowiec, Teufelberger, Wels, SAG, Katowice, SILTrade (in Polish).
4. **Chang X.D., Peng Y.X., Zhu Z.C., Gong X.S., Yu Z.F., Mi Z.T., Xu C.M.** (2017), Effects of strand lay direction and crossing angle on tribological behavior of winding hoist rope, *Materials*, 10, 630.
5. **Chang X.D., Peng Y.X., Zhu Z.C., Wang D.G., Gong X.S., Zou S.Y., Sun S.S., Mi Z.T., Xu W.X.** (2016), Tribological properties of winding hoisting rope between two layers with different sliding parameters, *Advances in Mechanical Engineering*, 8(12), 1-14.
6. **Guo Y.B., Zhang D.K., Yang X.H., Feng C.N., Ge S.R.** (2017), Experimental research on effect of wire rope transverse vibration on friction transmission stability in a friction hoisting system, *Tribology International*, 115, 233-245.
7. **Hansel J.** (ed.) (2000), Steel-rubber balances ropes SAG. Scientific and Technical Papers KTL – AGH Kraków, 19, 1-125 (in Polish).
8. **Kwaśniewski J.** (2010), Magnetic steel ropes tests. AGH Publishers, Kraków (in Polish).
9. **Li S.L., Hu P.Y., Zhao X.F., Chen K.J., Li J.K.** (2017), Atmospheric corrosion performance of wire rope sling in a sulfur dioxide-polluted environment, *Advances in Mechanical Engineering*, 9(6), 1-12.
10. **Ma C., Xiao X.M.** (2013), Kinetic analysis of a multi-rope friction mine hoist under overload conditions, *Journal of Vibroengineering*, 15(2), 925-932.
11. **Ma Y.S., Xiao X.M.** (2016), Dynamic analyses of hoisting ropes in a multi-rope friction mine hoist and determination of proper hoisting parameters, *Journal of Vibroengineering*, 18(5), 2801-2817.
12. **Mańka E.** (2013), *Comparative analysis of ropes test methods in terms of increasing accuracy and informativeness of the tests*, Doctor's dissertation, Faculty of Mechanical Engineering, University of Science and Technology in Bydgoszcz (in Polish).
13. **Mańka E., Styp-Rekowski M.** (2009), Diagnostic tests of balance ropes of mining hoist, *Proceedings of International Conference „TEMAG"* 2009, Silesian Technical University, Gliwice – Ustroń, 185-195 (in Polish).
14. **Mateja S., Pojnar A.** (2005), Analysis of the technical condition of the multi-layer balance rope Ø49 mm type NRHD-24 after the operation, *Proceedings of International Conference* „Shafts Transport 2005", Institute of Mining Technology „KOMAG", Gliwice – Zakopane, 241-251 (in Polish).
15. **Milcarz T., Fundament K.** (2005), Repair of flat steel-rubber balance rope SAG built in the hoist shaft IV N KWK „Sośnica, *Proceedings of International Conference* „Safety Operation of Mining Transport Equipment" Research and Supervisory Centre of Underground Mining, Lędziny – Szczyrk, 307-313 (in Polish).
16. **Olszyna G., Sioma A., Tytko A.** (2013), Assessment of the condition of hoisting ropes by measuring their geometric parameters in a three-dimensional image of their surface, *Archives of Mining Sciences*, 58(3), 643-654.
17. **Peng Y.X., Chang X.D., Zhu Z.C., Wang D.G., Gong X.S., Zou S.Y., Sun S.S., Mi Z.T., Xu W.X.** (2016), Sliding friction and wear behavior of winding hoisting rope in ultra-deep coal mine under different conditions, *Wear*, 368, 423-434.
18. **Peterka P., Kresak J., Kropuch S., Fedorko G., Molnar V., Vojtko M.** (2014), Failure analysis of hoisting steel wire rope, *Engineering Failure Analysis*, 45, 96-105.
19. **PN-EN 12385-2:2008,** Steel ropes. Safety. Part 2: Definitions, markings and classification (in Polish).
20. **PN-EN 12385-7:2004,** Steel ropes. Safety. Part 7: Ropes closed construction for mining shafts (in Polish).
21. **Sioma A., Tytko A.** (2012), Vision methods for assessing the geometrical parameters of steel ropes, *Acta Mechanica et Automatica*, 6(1), 63-67.
22. **Styp-Rekowski M., Mańka E.** (2010), Environmental factors of rope hoisting shaft wear and reliability, *Proceedings of Xth International Conference „Tribology and Reliability"*, Petersburg State Transport University Publishing, St. Petersburg (Russia), 245-257.
23. **Styp-Rekowski M., Mańka E., Matuszewski M., Madej M., Ozimina D.** (2015), Tribological problems in shaft hoist ropes wear process, *Industrial Lubrication and Tribology*, 67(1), 47-51.
24. **Wang X.Y., Meng X.B., Wang J.X., Sun Y.H., Gao K.** (2015), Mathematical modeling and geometric analysis for wire rope strands, *Applied Mathematical Modelling*, 39(3-4), 1019-1032.
25. **Xu L.M., Zhang D.K., Yin Y., Wang S.Q., Wang D.G.** (2014), Fretting wear behaviors of hoisting rope wires in acid medium, *Materials & Design*, 55, 50-57.
26. **Zhang D.K., Feng C.A., Chen K., Wang D.G., Ni X.** (2017), Effect of broken wire on bending fatigue characteristics of wire ropes, *International Journal of Fatigue*, 103, 456-465.
27. **Zhang J., Wang D., Zhang D., Ge S.R., Wangb D.** (2017), Dynamic torsional characteristics of mine hoisting rope and its internal spiral components, *Tribology International*, 109, 182-191.
28. **Zhao D., Liu S.G., Xu Q.T., Shi F., Sun W.Y., Chai L.Q.** (2017), Fatigue life prediction of wire rope based on stress field intensity method, *Engineering Failure Analysis*, 81, 1-9.

RADIATION-STIMULATED CHANGES IN THE CHARACTERISTICS OF SURFACE-BARRIER AL–SI–BI STRUCTURES WITH DIFFERENT CONCENTRATIONS OF DISLOCATIONS AT THE CRYSTAL SURFACE

Bohdan PAVLYK[*], Markijan KUSHLYK[*], Dmytro SLOBODZYAN[*], Igor MATVIJISHYN[*], Roman LYS[*], Marek JAŁBRZYKOWSKI[**]

[*]Faculty of Electronics, Lviv Ivan Franko National University, Drahomanova Street 50, 79005 Lviv, Ukraine
[**]Bialystok University of Technology, Faculty of Mechanical Engineering, ul. Wiejska 45C, 15-351 Bialystok, Poland

pavlyk@electronics.lnu.edu.ua, kushlykmarik@gmail.com, slobodzyan_d@ukr.net,
matvijishyn@ukr.net, lys_r@ukr.net, m.jalbrzykowski@pb.edu.pl

received 6 June 2016, revised 19 March 2018, accepted 22 March 2018

Abstract: We report the results of studies for the radiation-stimulated changes in electro-physical characteristics of surface-barrier Al–Si–Bi structures based on p-Si. We demonstrate that the X-ray irradiation is accompanied by different processes which depend on the density of the dislocations in the original silicon crystals. A usual evolution of the existing structural defects and their radiation-stimulated ordering dominate when the concentration remains low enough. Increase in the concentration causes the increasing role of generation of additional radiation defects. Modelling of the underlying physical processes has testified that the near-contact Si layers are strained. They act as getters for the structural defects and impurities.

Key words: Silicon, Dislocations, Surface-Barrier Structures, Surface Layers, Radiation-Stimulated Reconstruction of Defects

1. INTRODUCTION

Fabrication of reliable electronic systems with well-predicted characteristics, which are able to work in extreme conditions (e.g., in a wide temperature range, under the influence of irradiation, atmosphere or magnetic fields), is one of the urgent problems of modern electronics engineering. The external factors induce a number of changes in electro-physical and optical characteristics of crystals such as silicon and corresponding devices made on their basis.

In the recent years there have appeared a significant number of publications devoted to the regularities of changes occurring to the parameters and characteristics of surface-barrier structures (SBSs) made of silicon, as well as to diode structures subjected to the magnetic and irradiation fields (Borkovska et al., 1984; Mahkamov et al., 1999; Nikolaev et al., 2003; Marchenko et al., 2010; Kalinina et al., 2010; Dolgolenko et al., 2006; Makara et al., 2008; Skvortsov et al., 2009; Mudriy et al., 2010). It is now well established (Borkovska et al., 1984; Mahkamov et al., 1999; Nikolaev et al., 2003; Marchenko et al., 2010; Kalinina et al., 2010; Dolgolenko et al., 2006) that the irradiation stimulates evolution of defect structure of crystals and so can lead to either deterioration or improvement of many characteristics of the silicon structures. Though being somewhat unusual, the latter effect really exists and is known as an 'effect of small doses'.

There is fewer works devoted to combined influence of the mentioned fields on the processes of defects evolution in silicon, as well as to the corresponding stimulated changes in the parameters of structures on its basis (Mudriy et al., 2010). A path from microelectronics to nanoelectronics makes the studies in this field more urgent, since they can enable predicting and governing the changes occurring in the parameters of many devices of the modern electronics.

The aim of this work is to study the influence of concentration of surface dislocations on the efficiency of radiation-stimulated reconstruction of defects located in the near-surface layer of the SBSs made of p-Si.

2. EXPERIMENTAL TECHNIQUES

In our experiments we used p-Si samples with the specific resistance of ρ_1 = 24 Ohm·cm, which had been grown with the Czochralski technique. Contacts at the crystal surfaces were made with the aid of a Vacuum Universal Post device VUP-5 under the pressure of 10^{-5} Pa. A nitric-trap technique was used according to standard procedures described earlier by Pavlyk et al. (2012). A 240–250 nm thick aluminum film was coated, using thermal vacuum sputtering, on the (111) silicon surface, which had been preliminarily polished chemically and degassed in a vacuum (the pressure 10^{-5} Pa) at 320°C. The corresponding coating rate was equal to 15 nm/s. After that the samples were subjected to a necessary thermal treatment and cooled down to the room temperature. The other contact was a 90 nm thick bismuth film. It was coated with the same rate. Considering a technological peculiarity of the evaporation process consisting in Bi contacts being deteriorated, the samples were not treated thermally in the latter case. All the procedures involved in the formation of our SBSs were performed in a single production cycle.

For the microscopic studies of defect state of our crystals covered by the metal films, we etched the samples chemically in the two following stages: at the first one the metal film was etched using the hydrochloric acid and, at the second, the samples were

DOI 10.2478/ama-2018-0012

subjected to standard etching with a selective etchant. To determine the concentration of etching pits, we used an light microscopy based upon a microscope LUMAM I-3 and an atomic force microscopy facilitated by a Solver P-4 device.

The samples were irradiated by X-ray beams, using an X-ray equipment URS.1.0 (the Mo anode, U = 45 kV, and I = 10 mA). Finally, the volt-ampere (VAC) and the high-frequency (125 kHz) capacity-voltage (CVC) characteristics of our Al–Si–Bi SBSs were measured with a capacitive modulation spectrometer URAN-1. The data collected in this manner were processed using a personal computer. To provide different dislocation concentrations on the (111) surface of each experimental sample, we carried out controlled plastic straining of the silicon crystals at the temperature of 1000 K.

3. EXPERIMENTAL RESULTS AND DISCUSSION

In order to confirm experimentally the availability of defects in the near-surface layer of our silicon crystals and determine their compositions qualitatively and quantitatively (the types of the defects, their energy levels, etc.), we measured both the VAC and the high-frequency CVC. Fig. 1a displays the VACs obtained for the SBS sample having the barrier contacts located in the areas with the concentrations of dislocations 10^2, 10^4 and 10^5 cm^{-2}. As seen from Fig. 1b, introduction of dislocations into the p-Si crystals results in decreasing direct current flowing through the SBS under direct voltage. This is mainly caused by the effect of gettering of the majority charge carriers at the dislocations.

According to a standard and well-known theory, the following relation holds true for the total current I_{pn} through the p-n-junction:

$$I_{pn} = I_s\left(e^{-\frac{eU}{kT}} - 1\right) + I_R\left(e^{-\frac{eU}{2kT}} - 1\right). \quad (1)$$

Here $I_S = \frac{eDSP_{n0}}{L \cdot th(\frac{\omega}{L})}$ is the diffusion current and $I_R = \frac{\frac{kT}{e}P_{n0}D\omega}{(\Delta\varphi_0 - U_{pn})L^2}$ the recombination current, e the electron charge, U the electric voltage, k Boltzmann constant, and T the absolute temperature. In the formulas defining the I_S and I_R parameters, S denotes the p-n-junction area, D the diffusion coefficient, P_{n0} the concentration of impurities injected into the base, L the diffusion path length, $\Delta\varphi_0$ the potential barrier, ω the thickness of the base, and U_{pn} the voltage applied to the p-n-junction.

The total reverse current can be presented as a sum of the diffusion current in the neutral area and the current thermally generated inside the barrier region.

The concentration of the intrinsic charge carriers in the crystals under test is small, so that the contribution of the diffusion component is minimal and the reverse current is described well by the Shockley law. An increase in the concentration of minority carriers takes place in the course of uniaxial straining of the crystal. This factor explains the increased reverse current (see Fig. 1b).

Fig. 2a depicts the CVC for the SBSs with different concentrations of dislocations at their surfaces. It is apparent that increasing dislocation concentration decreases the capacity both near its maximum and in the region of positive bias voltages. This means that the generation-recombination processes in the space-charge region cause a decrease in the positive charge located inside the insulating substrate. In other words, the contribution of charge carriers to the capacity of the space-charge region decreases due to gettering of charge carriers at the dislocations.

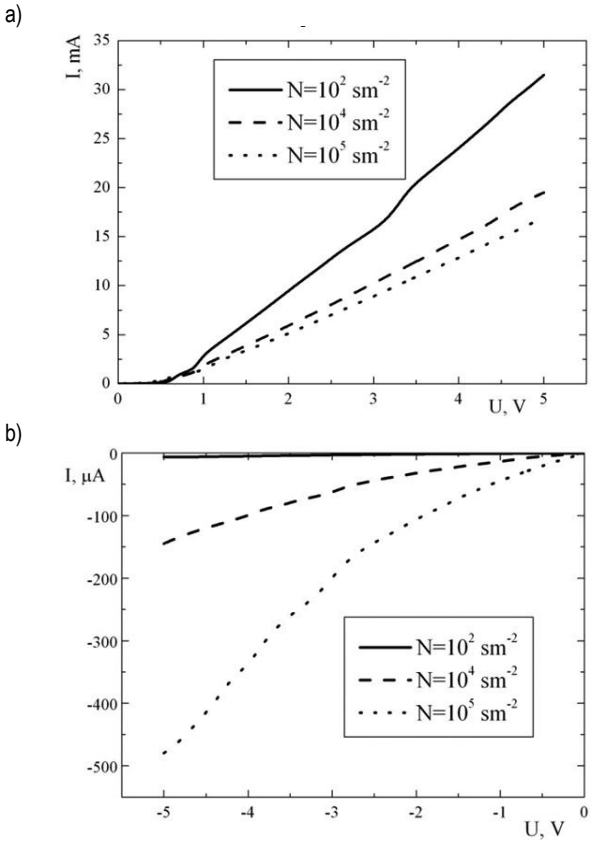

Fig. 1. Direct (a) and inverse (b) regions of VAC for the SBSs with different dislocation concentrations at their surfaces

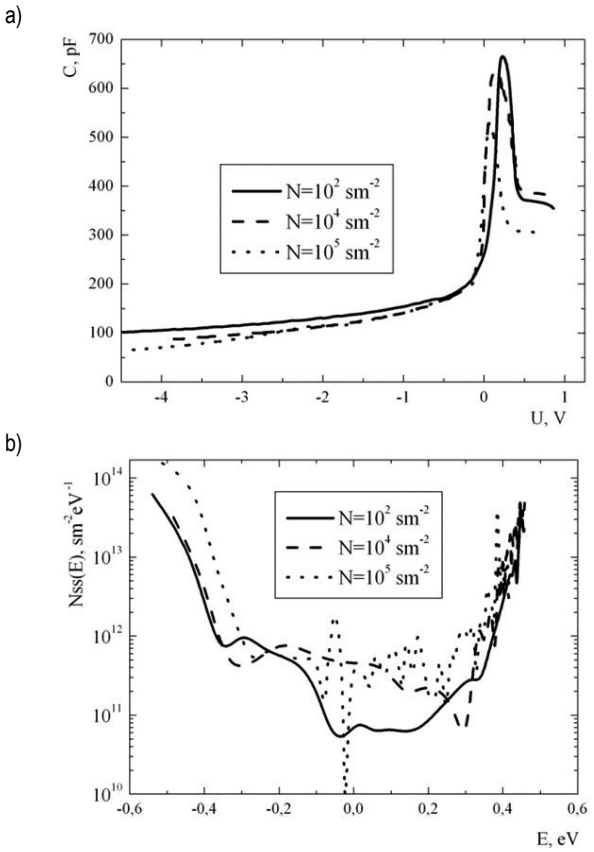

Fig. 2. CVC (a) and concentration distribution of the surface states inside the silicon bandgap (b) for the SBSs with different dislocation concentrations at their surfaces

As shown by Slobodzyan et al. (2015), the maximum efficiency of generation of the surface states is peculiar for the defective near-surface layers where the mechanical strains are maximal. The source of these strains can be dislocations which contribute notably to the energy spectrum of the surface, thus changing the concentration distribution of the surface states inside the bandgap of silicon (see Fig. 2b). As a consequence, we have a change in the slope of the linear region of the CVC curve occurring at the positive voltages (see Fig. 2a).

Fig. 3 illustrates the radiation-stimulated changes typical for the direct region of VAC measured for the SBS created on the basis of silicon crystals. As seen from Fig. 3, the X-ray irradiation changes the slopes of this characteristic. Initially, we observe an increase in the direct current through the metal–semiconductor contact, though the doses of 390 Gy or higher cause decreasing VAC slope.

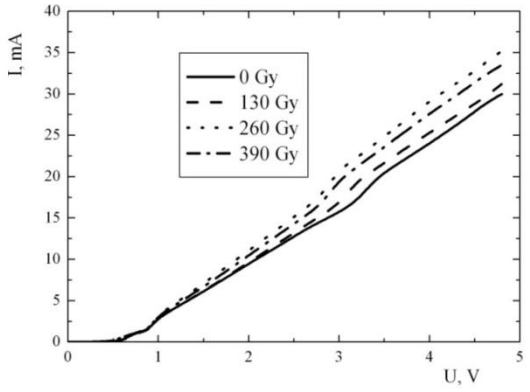

Fig. 3. Changes in the direct region of VAC for the SBS based on a dislocation-free silicon, which are induced by X-ray irradiation of different doses shown in the legend

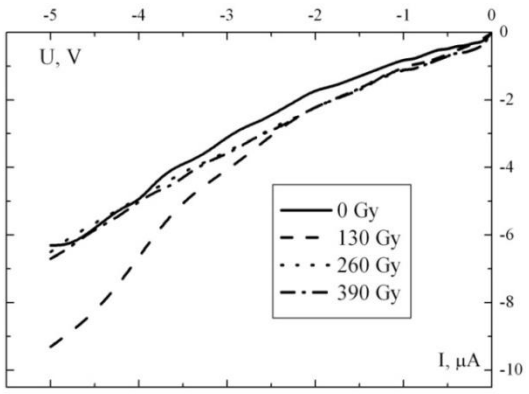

Fig. 4. Changes in the reverse region of VAC for the SBS based on a dislocation-free silicon, which are induced by X-ray irradiation of different doses shown in the legend

It is often assumed (Peka and Strikha, 1992) that the local areas are formed at the surface and in the near-surface layer of the crystal, which reveal higher contents of oxygen–vacancy and vacancy–impurity complexes. Some of these defects are in metastable states. This is because of differences among the charges localized at the vacancies and the impurities.

While analyzing the results obtained by us, it is necessary to consider the fact that generation of additional defects is not the only consequence of the irradiation. In addition, a process of radiation-stimulated 'ordering' of the defect structure takes place, which is known as 'the effect of small doses' (Pavlyk et al., 2012). On the initial stages of irradiating the SBS, there occurs partial reordering of the metastable near-surface defects. Then their charge state changes, together with the charge associated with the surface energy states. As a result of these changes, the concentration of charge carriers and the current associated with the direct VAC region increase. Further increase in the irradiation dose (> 390 Gy) is accompanied by a domination of defect-generation effect and so by gettering of the majority carriers at these defects. In its turn, this decreases the direct current.

As seen from Fig. 4, the radiation-stimulated changes occurring in the reverse region of the VAC are smaller. This fact can be explained by increasing probability of tunneling of the minority carriers through the barrier, with their subsequent localization at the imperfections of crystalline lattice.

As for the X-ray stimulated changes observed in the CVC of the SBS under study, Fig. 5a testifies that the increase in the absorbed dose (from 0 to 390 Gy) imposes decreasing amplitude of a characteristic maximum typical of the CVC curve. Hence, the positive charge in the dielectric layer located between the metal and the semiconductor decreases. We notice that the mentioned layer could not be got rid of in the process of manufacturing the SBS.

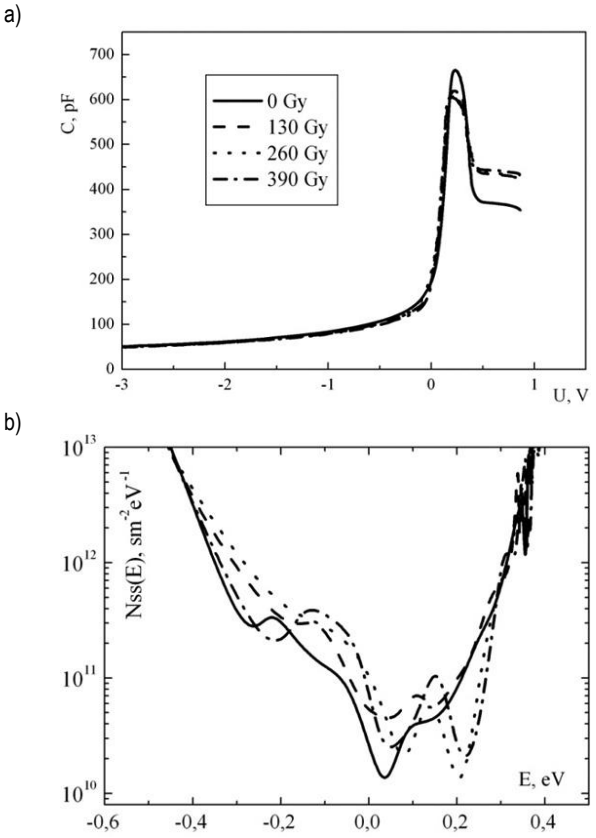

Fig. 5. Radiation-stimulated changes in CVC (a) and surface-state density (b) observed for the SBS based on dislocation-free silicon

Gradual capacity changes in the region of positive voltages occur whenever the absorbed dose increases. This reflects the changes in the charge of the space-charge region happening under the irradiation (i.e., a 'shelf' on the CVC). A 'critical' dose for the capacity dependence is 390 Gy, since the capacity decreases under further increasing dose. These data correlate well with the

DOI 10.2478/ama-2018-0012

radiation-stimulated changes seen in the VAC of our SBSs. They serve as a confirmation of reconstruction of the metastable defects, with the charge at these defects forming the region of the space charge.

It is known that the defects create additional discrete states at the surface of semiconductor crystals and contribute notably to the total spectrum of the surface-state density. Under X-irradiation, some reconstruction of the metastable defects can occur at the surface of the p-Si:B structure (ρ = 24 Om.cm). Moreover, additional defects are formed, of which occurrence depth only slightly differs from that of the former defects. Therefore the total spectrum of the surface states does not change in practice, though it shifts towards higher energies (see Fig. 5b).

Thus, the initial stages of irradiation (D < 390 Gy) of the SBSs based on dislocation-free silicon are governed by the mechanism of irradiation-induced ordering of the defect structure inside the near-surface silicon layers. The doses higher than 390 Gy change the prevailing mechanisms of interaction among the defects available in the structure and the radiation-stimulated defects.

The analysis of the radiation-stimulated changes in the VAC observed for the SBSs with different concentrations of dislocations suggests the following:

- A weak (D < 290 Gy) irradiation treatment of our Si samples with the dislocation concentration of $N_d = 10^2$ cm^{-2} leads to relatively small changes in both the direct and reverse VAC regions.
- The same treatment of the samples with $N_d = 10^4$–10^5 cm^{-2} imposes a decrease in the direct current. The reason is increasing probability of scattering of carriers at the dislocations. Besides, the probability of gettering of the majority carriers at the dislocations increases with increasing coefficient of radiation-stimulated diffusion (Pavlyk et al., 2012).
- For the structures with $N_d = 10^4$–10^5 cm^{-2}, further increase in the absorbed dose up to 400 Gy is accompanied by increasing direct current, when compared with its initial value. The increase of the current may be explained by the effect of radiation-stimulated ordering of structural defects available in the crystal.
- Radiation-stimulated decrease in the reverse current, which is proportional to the density of the dislocations, is stipulated by generation of the minority carriers and their partial localization at the vacancies and dislocations.

That is why one can say that the defect state of the near-surface layer of the silicon crystals where the SBSs are formed represents a crucial factor in the process of radiation-stimulated changes of their electro-physical characteristics (Pavlyk et al., 2013). The processes associated with the effect of X-rays are less important.

Figs. 6a and 6b show the radiation-stimulated CVC changes observed for the SBSs with different dislocation concentrations at the crystal surface. Regardless of the quantity of dislocations under the barrier electrode, a peculiar feature of the radiation-stimulated CVC changes is a decrease in the amplitude of a characteristic maximum observed in the region of positive voltages and, additionally, a lack of any changes in the density of surface states under the doses less than 390 Gy. These features are the same as in the previous case of SBSs based on dislocation-free silicon. However, the capacity at the characteristic maximum begins to increase under the doses higher than 390 Gy. As for the capacity corresponding to the space-charge region, it decreases at first and then starts to increase at the absorbed doses as low as 130 Gy. The values of the characteristic doses for this structure correlate well with those causing the corresponding VAC changes.

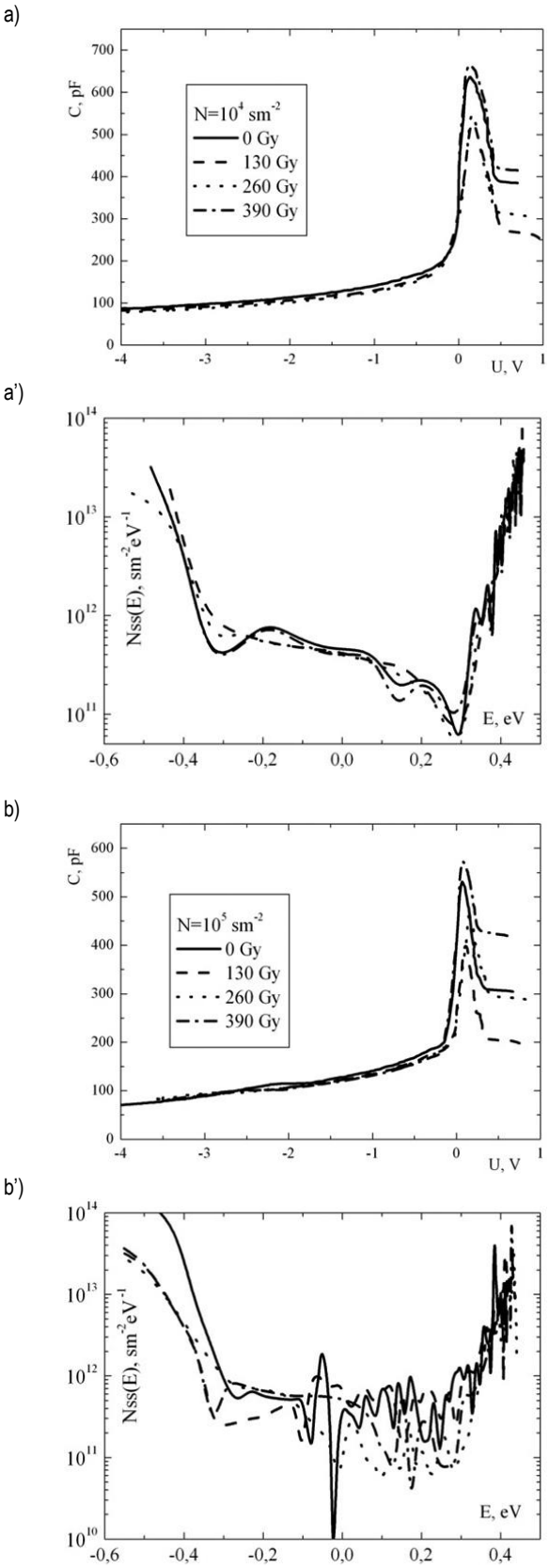

Fig. 6. Radiation-stimulated changes in CVC for the SBSs with different dislocation concentrations at the silicon surface (a, b) and density distributions for the surface states inside the bandgap of silicon (a', b')

As seen from Fig. 6a', Fig. 6b', the dislocations contribute essentially to the energy spectrum of the surface states, of which charge changes after irradiation. It also accompanies the evolution of defect structure of the near-surface layers in the silicon crystals. Thus, we conclude that the increase in the density of the dislocations present in the near-surface crystal layer of p-Si stimulates efficient reconstruction of metastable and radiation-induced defects in the SBS.

The modeling of the underlying physical processes carried out by Pavlyk et al. (2013) has shown that the near-contact layers of Al and Si in the SBS are strained. Having performed similar calculations for the bismuth films, we arrive at considerably smaller mechanical tensions in the contact areas of the bismuth–silicon structures. This is a result of smaller differences between the corresponding lattice parameters and thermal expansion coefficients, as well as lower-temperature regime of Bi-film formation, when compared with Al films. In other words, the thickness of the strained layers is an order of magnitude smaller, being about one or two atomic layers in the contact region of silicon. Then the depth of capture of the defects from the crystal bulk is also smaller for this region. The results of our modeling are shown in Fig. 7.

a)

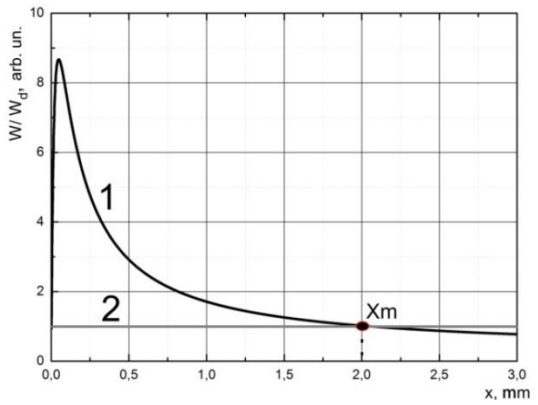

b)

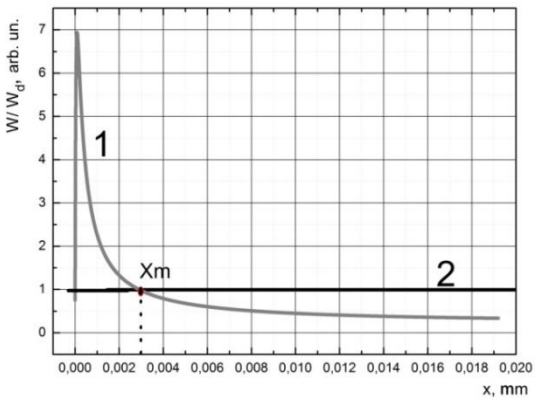

Fig. 7. Dependences of total energy of the strained Al–Si (a) and Si–Bi (b) layers (curve 1) and dislocation energy (curve 2) on the distance from the crystal surface: Xm is the maximal depth of defect capture from the crystal volume

The studies of the surface structure performed after chemical etching of the metal films and further selective etching have shown that, in practice, there is no defect layer under the bismuth films. Since the dislocations impose mechanical tension fields in their vicinities, they represent efficient gettering centers for different types of point defects and impurities in the crystal. Application of external mechanical field or temperature treatment of the samples stimulate a motion of dislocations, which migrate through the crystal lattice (e.g., the loop-shaped dislocations with fixed ends can become curved) and capture defects from the crystal bulk. The dislocations move inside the near-surface layer subjected to mechanical tensions, which are caused by a difference in the lattice parameters of silicon and the aluminum film. There they leave the defects localized around the dislocation cores. After the tension is unloaded, the dislocation is becoming 'straightened' and turns back to its initial state. The defects captured remain to be in the deformation-potential field of the near-surface layer.

It is important that the defect-type near-surface layer is formed only under the aluminum films at high enough temperatures, and precipitated aluminum is not saturated by silicon up to its maximal solubility of 1.6 %. Then one can assume a low-temperature diffusion of the silicon atoms into the polycrystalline Al film. This assumption is confirmed by the fact that, during the formation of SBSs, a significant amount of defects (e.g., dislocations, grain boundaries, etc.) is formed in the bulk of the film. These defects act as pathways of accelerated diffusion. Moreover, it is necessary to take into consideration that the mechanical tensions in the contact area weaken interactions of silicon atoms located in the crystalline lattice sites. As a result of all of these processes, a layer is formed in the region of silicon nearby the boundary, which is enriched with vacancies, interstitial silicon atoms and the other impurity atoms.

4. CONCLUSIONS

1. As a result of mechanical tensions present in the strained defect layer, the defects are captured from the crystal bulk, thus leading to the changes observed in electro-physical characteristics of the SBS samples.
2. The irradiation triggers the two competing processes: the generation of additional defects and the change in charge state of the existing defects. Depending on the defect structure of the silicon crystals, one of these mechanisms can prevail on a particular stage of irradiation.
3. Dislocations act as getters for charge carriers, thus resulting in significant differences observed for the characteristics of electronic devices made on the bases of dislocation-including and dislocation-free silicon crystals.

REFERENCES

1. **Borkovska O.Y, Dmitruk P.L., Litovchenko V.H.** (1984), Effect of radiation ordering in heterojunctions of (n-Si)-(p-GaP), *Semiconductors,* 18(10), 1808-1810.
2. **Mahkamov S., Tursunov N.A., Ashurov M.** (1999), About the peculiarities of formation of radiation defects in silicon structures, *Technical Physics,* 69(1), 121-123.
3. **Nikolaev D.V., Antonova I.V., Naumova O.V.** (2003), Charge accumulation in oxide and interface states of silicon-on-insulator structures after irradiation by electrons and γ-rays, *Semiconductors,* 37(4), 443-449.
4. **Marchenko I.G., Zhdanovich N.E.** (2010), Influence of irradiation by electrons on the electrical parameters of silicon p-n-structures, weakened by aluminum screens, *Technical Physics,* 36(10), 45-51.
5. **Kalinina E.V., Kossov V.G., Yafaev R. R.** (2010), High-temperature radiation-strong rectifier based on 4H-SiC alumimium ion implanted p^+-n-junctions, *Semiconductors,* 44(6), 807-815.

DOI 10.2478/ama-2018-0012

6. **Dolgolenko A.P., Litovchenko P.G., Varentsov M.D.** (2006), Particularities of the for-mation of radiation defects in silicon with low and high concentration of oxygen, *Physica Status Solidi,* 243(8), 1842-1852.
7. **Makara V.A., Vasiliev M.A., Steblenko L.P.** (2008), Caused by magnetic field changes of impurity composition and microhardness of silicon crystals, *Semiconductors,* 42(9), 1061-1064.
8. **Skvortsov A.A., Orlov A.M., Solov'ev A.A.** (2009), Magnetoplastic effect in silicon: the search for new methods of management of structure-sensitive properties of elemental semiconductors, *Physics of the Solid State*, 51(12), 2304-2308.
9. **Mudriy S.I., Kulyk Y.O., Steblenko L.P.** (2010), Change of internal stress and lattice parameter of silicon crystals, stimulated by the combined influence of X-ray irradiation and a magnetic field, *Physics and Chemistry of Solid State,* 11(2), 334-337.
10. **Slobodzyan D.P., Pavlyk B.V., Kushlyk M.O.** (2015), Features of influence of x-radiation and magnetic field on the electrical characteristics of barrier structures based on p-si with dislocation, designed for solar energy, *J. Nano- Electron. Phys.,* 7(4), 04051-1 - 04051-5.
11. **Peka G.P., Strikha V.I.** (1992), *Surface and contact phenomena in semiconductors*, Kyiv, Lybid.
12. **Pavlyk B.V., Slobodzyan D.P., Kushlyk M.O.** (2012), Quality of the *p*-Si crystal surface and radiation-stimulated changes in the characteristics of Bi-Si-Al surface-barrier structures, *Semiconductors,* 46(8), 1017-1021.
13. **Pavlyk B.V., Slobodzyan D.P., Kushlyk M.O.** (2013), Electrophysical characteristics of near-surface layers in p-si crystals with sputtered al films and subjected to elastic deformation, *Ukr. J. Phys.,* 58(8), 742-747.

DE GRUYTER
OPEN

DOI 10.2478/ama-2018-0013

COMPENSATING POSE UNCERTAINTIES THROUGH APPROPRIATE GRIPPER FINGER CUTOUTS

Adam WOLNIAKOWSKI*, Andrej GAMS, Lilita KIFORENKO***, Aljaž KRAMBERGER**, Dimitrios CHRYSOSTOMOU****, Ole MADSEN****, Konstantsin MIATLIUK*, Henrik Gordon PETERSEN***, Frederik HAGELSKJÆR***, Anders Glent BUCH***, Aleš UDE****, Norbert KRÜGER*****

*Faculty of Mechanical Engineering, Bialystok University of Technology, ul. Wiejska 45C, Białystok 15-351, Poland
**Department for Automation, Biocybernetics and Robotics, Jožef Stefan Institute, Jamova cesta 39, 1000 Ljubljana, Slovenia
***The Maersk Mc-Kinney Moller Institute, University of Southern Denmark, Campusvej 55, DK-5230 Odense M, Denmark
****Robotics and Automation Group, Aalborg University, Fibigerstraede 14, DK-9220 Aalborg East, Denmark

adam.wolniakowski@gmail.com, andrej.gams@ijs.si, lilita@mmmi.sdu.dk, aljaz.kramberger@ijs.si, dimi@m-tech.aau.dk, om@m-tech.aau.dk, k.miatliuk@pb.edu.pl, hgp@mmmi.sdu.dk, frederikhagel@gmail.com, anbu@mmmi.sdu.dk, ales.ude@ijs.si, norbert@mmmi.sdu.dk

received 27 October 2016, revised 19 March 2018, accepted 22 March 2018

Abstract: The gripper finger design is a recurring problem in many robotic grasping platforms used in industry. The task of switching the gripper configuration to accommodate for a new batch of objects typically requires engineering expertise, and is a lengthy and costly iterative trial-and-error process. One of the open challenges is the need for the gripper to compensate for uncertainties inherent to the workcell, e.g. due to errors in calibration, inaccurate pose estimation from the vision system, or object deformation. In this paper, we present an analysis of gripper uncertainty compensating capabilities in a sample industrial object grasping scenario for a finger that was designed using an automated simulation-based geometry optimization method (Wolniakowski et al., 2013, 2015). We test the developed gripper with a set of grasps subjected to structured perturbation in a simulation environment and in the real-world setting. We provide a comparison of the data obtained by using both of these approaches. We argue that the strong correspondence observed in results validates the use of dynamic simulation for the gripper finger design and optimization.

Key words: Grasping, Uncertainties, Gripper Design, Simulation

1. INTRODUCTION

The most common type of grippers utilized in automated robotic workcells (the robotic setup including the robot, the sensors (typically a vision system) and the environment) in the industry are simple parallel-finger grippers. Such grippers are relatively cheap, easy to control, and any adaptation required by changing the application at hand can often be achieved by replacing the disposable fingers. The finger design has to accommodate the shape of the object to be grasped taking into account the task constraints and the unavoidable process uncertainties, such as pose estimation errors due to shortcomings of the vision system, or variations in the objects properties.

Nowadays, this gripper design procedure usually involves empirical trials, which require substantial time, expertise, and material costs. The solution to these problems may be found in employing simulation to obtain the feedback on choices made in the design process. In our previous work, we have been interested in utilizing dynamic simulation to accelerate the design process by removing these obvious obstacles. The development of fast and accurate physics engines (a computer software that provides routines for the simulation of physical systems) over the last years, e.g. (Thulesen and Petersen, 2016), and the constant increase of the available computational power makes the use of simulation a feasible alternative to physical testing.

In this work, we first present the use case of an industrial object grasping scenario, to which we apply our simulation-based gripper optimization method introduced in (Wolniakowski et al., 2013, 2015, 2017). As compared to these works, we show in this paper the optimization process and the optimal finger geometry computed for the task context, and provide in-depth analysis of our gripper optimization method performance with regard to expected alignment of the objects. We then perform experiments to confirm our approach of using the simulation to obtain feedback on the design choices by comparing the simulated gripper performance with the real world results. Finally, we discuss the obtained results and the usage of simulation in the real-world optimization problems. We conclude with ideas on the improvement of the simulation to better reflect the real-world conditions.

2. STATE OF THE ART

2.1. Gripper design in industry

Grasping accounts for much of the workload associated with assembly, pick-and-place actions and palletizing. Still, the need of frequent setup changes associated with context switching (such as introducing a new product) provide an interesting challenge in terms of gripper design. The optimal gripper design is a persisting problem, which is currently solved by a procedure that in-

DOI 10.2478/ama-2018-0013

volves a costly and time-consuming trial-and-error process. The engineering expertise necessary to produce proper finger designs is based on heuristics, collected in general guidelines, such as (Causey, 2003; Monkman et al., 2007; Wolf et al., 2005; Tarnowski, 1997; Siiliano and Khatib, 2008; Carbone, 2013; Causey and Quinn, 1998). The guidelines stress the importance of minimizing gripper weight and footprint to increase the system throughput and decrease the cost, and to provide secure grasping of the handled parts.

These aims are solved by introducing gripper design features, such as cutouts (A slot in the finger surface designed to interact with the grasped objects) that embrace the grasped parts, or chamferings to reduce the gripper interference. A body of work focused on gripper design utilizing these features is present, and several overviews, such as (Boubekri and Chakraborty, 2002), have been published. Additionally, a lot of research has been devoted to the design of gripper mechanisms (Krenich, 2004; Cuadrado et al., 2004; Lanni and Ceccarelli, 2009; Ceccarelli et al., 2002). Some work has been done on the topic of gripper jaw design (Zhang et al., 2001; Zhang and Goldberg, 2006).

2.2. Gripper learning in simulation

The established gripper design and development process based on iterative resource and time-consuming real-world testing makes it prohibitively expensive for implementation in industrial ventures which require frequent context switching.

The usage of simulation in the design process of object aligning gripper jaws has been previously discussed in (Ellekilde and Petersen, 2006).

In (Wolniakowski et al., 2013), we have presented a general and flexible method that allows to compute an array of gripper Quality Indices based on statistical analysis of the simulated grasp outcomes. In (Wolniakowski et al., 2015) and (Wolniakowski et al., 2017), we have extended our method with additional alignment quality assessment, proposed the gripper finger parametrization, and shown an optimization procedure that yields gripper designs optimized for specific.

3. METHODS

3.1. Gripper evaluation

The gripper evaluation method based on dynamic simulation (in dynamic simulation, the object movements are calculated based on the object contacts, forces and torques, as opposed to kinematic simulation, which uses velocity and position trajectories) of grasps has been introduced and described in detail in our previous works (Wolniakowski et al., 2013, 2015, 2017). We will, however, present the key concepts here for the sake of completeness.

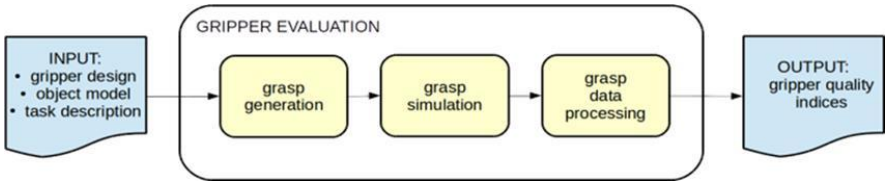

Fig. 1. Overview of the gripper evaluation procedure based on dynamic simulation of the grasping

An overview of our evaluation process is presented in Fig. 1. The input of the procedure consists of the proposed gripper design, the object model, and the task context. The context includes the description of the environment, and the grasping process to be simulated, together with the task constraints.

The evaluation process starts with the generation of a set of candidate grasps to be simulated in the surrogate scenario. The grasps are either planned, or drawn from a random distribution based on the predicted noise levels. The grasps are then executed in simulation and the statistics and the data collected. Based on these, several Quality Indices are calculated:

- *Success Index* (S) – quantifies the percentage of succesfully executed grasps,
- *Coverage Index* (C) – describes the gripper versatility in approaching the object,
- *Alignment Index* (A) – describes the gripper ability to force predictable poses on the grasped object countering the pose estimation uncertainty,
- *Wrench Index* (W) – defines how secure the grasps executed by the gripper are,
- *Robustness Index* (R) – quantifies the gripper performance in the presence of process noise,
- *Stress Index* (T) – illustrates the structural robustness of the design,
- *Volume Index (*V) – defines the cost of the gripper design (in the case of printed fingers (printed fingers are produced using additive manufacturing processes)).

3.2. Gripper optimization

Gripper design optimization builds on the evaluation method described above. A numerical optimization algorithm performing iterative evaluation of the gripper design paramatrized by a vector of design variables gradually approaches the best solution. In this work, we have solved the problem of optimizing the gripper cutout for the task of grasping a small metal object – the magnet. The target object and the task environment in both reality and in simulation are presented in Fig. 2.

The optimization problem is formulated as follows. The goal is to find the values of the parameters of the finger geometry, which yield the maximum value of the selected objective:

$$x_{opt} = \underset{x \in \mathbb{R} | x_{min} \le x \le x_{max}}{argmax} f(x), \quad (1)$$

where x is the vector of the design parameters, x_{min} and x_{max} are the limits on the parameter values and $f(x)$is the objective:

$$f(x) = (\prod_{i=1}^{n} q_i w_i)^{1/\Sigma_{i=1}^{n} w_i}, \quad (2)$$

where **q** = [S, C, A, W, R, T, V] is the vector of Quality Indices, and **w** = [w_1, w_2, ..., w_n] is the vector of individual weights.

Adam Wolniakowski, Andrej Gams, Lilita Kiforenko, Aljaž Kramberger, Dimitrios Chrysostomou, Ole Madsen, Konstantsin Miatliuk,
Henrik Gordon Petersen, Frederik Hagelskjær, Anders Glent Buch, Aleš Ude, Norbert Krüger
DOI 10.2478/ama-2018-0013
Compensating Pose Uncertainties through Appropriate Gripper Finger Cutouts

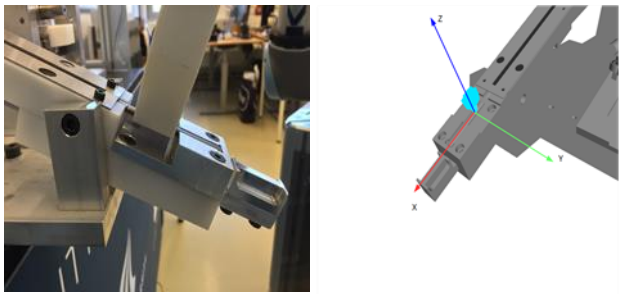

Fig. 2. The magnet grasping task: real setting (on the left) and the simulated scenario (on the right)

The Fig. 3. presents the parametrization of a simple trapezoidal cutout for the gripper finger. The vector x of the design variables controls the shape of the cutout:

$$x = [\mathrm{d},\mathrm{w},\alpha_1,\alpha_2], \tag{3}$$

where d is the *cutout depth*, w is the *cutout width*, α_1 is the *cutout angle #1*, and α_2 is the *cutout angle #2* (as indicated in Fig. 3). The values for the lower and upper bounds on the parameter values x are presented in Tab. 1.

Tab. 2. presents the values of the individual Quality Index weights used in this work in the computation of the objective function $f(x)$.

Tab. 1. Bounds of the design variables

parameter	d [m]	w [m]	α1 [°]	α2 [°]
min	0	0	0	0
max	0.01	0.01	180	180

Tab. 2. Weights w_i assigned to the individual Quality Indices in the objective function calculation

QI	S	C	A	W	R	T	V
w_i	0.1	0	1	0.1	0	0.01	0.01

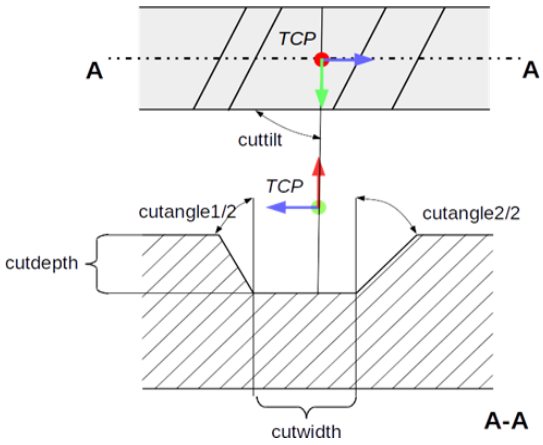

Fig. 3. The parametrization of the trapezoidal cutout. Top: the view of the inner surface of the finger. Bottom: the length-wise crossection of the finger. The coordinates are defined with respect to the TCP frame shown

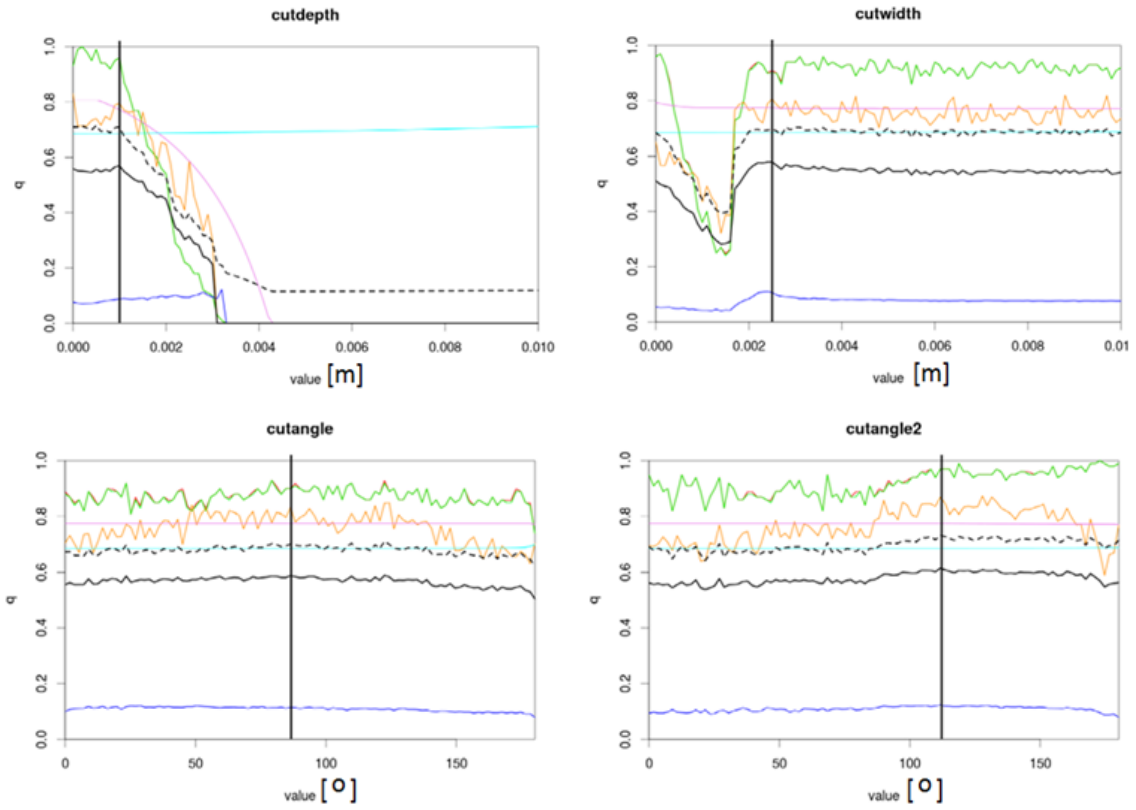

Fig. 4. The shape of the QI evaluations for the trapezoidal cutout parameters during the optimization process. Top row: quality evaluation for the change in cutout depth (on the left) and cutout width (on the right). Bottom row: evaluations for cutout angle #1 (on the left) and cutout angle #2 (on the right). Vertical black lines indicate the optimal values chosen for the individual parameters. Green line – Success Index, orange – Alignment Index, blue – Wrench Index, solid black – f(x)

DOI 10.2478/ama-2018-0013

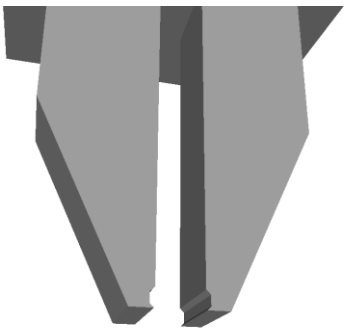

Fig. 5. The optimized trapezoidal cutout for the magnet object

In this work, we have used a simplified coordinate descent optimization method to find the optimal values for the design variables, by examining the shape of Quality Index evaluation functions across the slices of the parameter space. Fig. 4. presents the successive QI evaluations for the following order of parameters: cutout depth, cutout width, cutout angle #1, and cutout angle #2. The optimization criterion was to maximize in order: Alignment Index, Wrench Index, and Success Index, as reflected by the choice of weights (Tab. 2). The small weights imposed on the Stress (T) and Volume (V) objectives are in order to force the selection of a physically feasible design (in case either of these Indices equal to zero, the geometric mean would force the whole objective to 0).

The values chosen for the individual parameters of the design variables vector are:

$$\mathrm{d}{=}0.001[m], \mathrm{w}{=}0.0024[m], \alpha_1 = 90[º], \alpha_2 = 110[º] \quad (4)$$

The optimized trapezoidal cutout shape found for the magnet is presented in Fig. 5.

4. EXPERIMENTS

4.1. Setting and the protocol

The feasibility of using simulation in order to obtain feedback used to optimize gripper designs can only be asserted if the simulation yields results comparable to those obtained from the real-world testing. After computing the optimal finger design suitable for the magnet grasping in the considered scenario, we have performed a set of experiments to confirm the validity of our approach.

We have designed a set of experiments to test whether the real and simulated grasps yield the same outcome when the reference grasp is altered with increasing offsets. Since the exhaustive exploration of the *SO(3)* pose offset space is prohibitive for such an experiment, we have decided to test and compare the offsets along the five axis of the magnet object: *y, z, Rx, Ry*, and *Rz*, where *R* indicates a rotation around the axis (see Fig. 2. on the right).

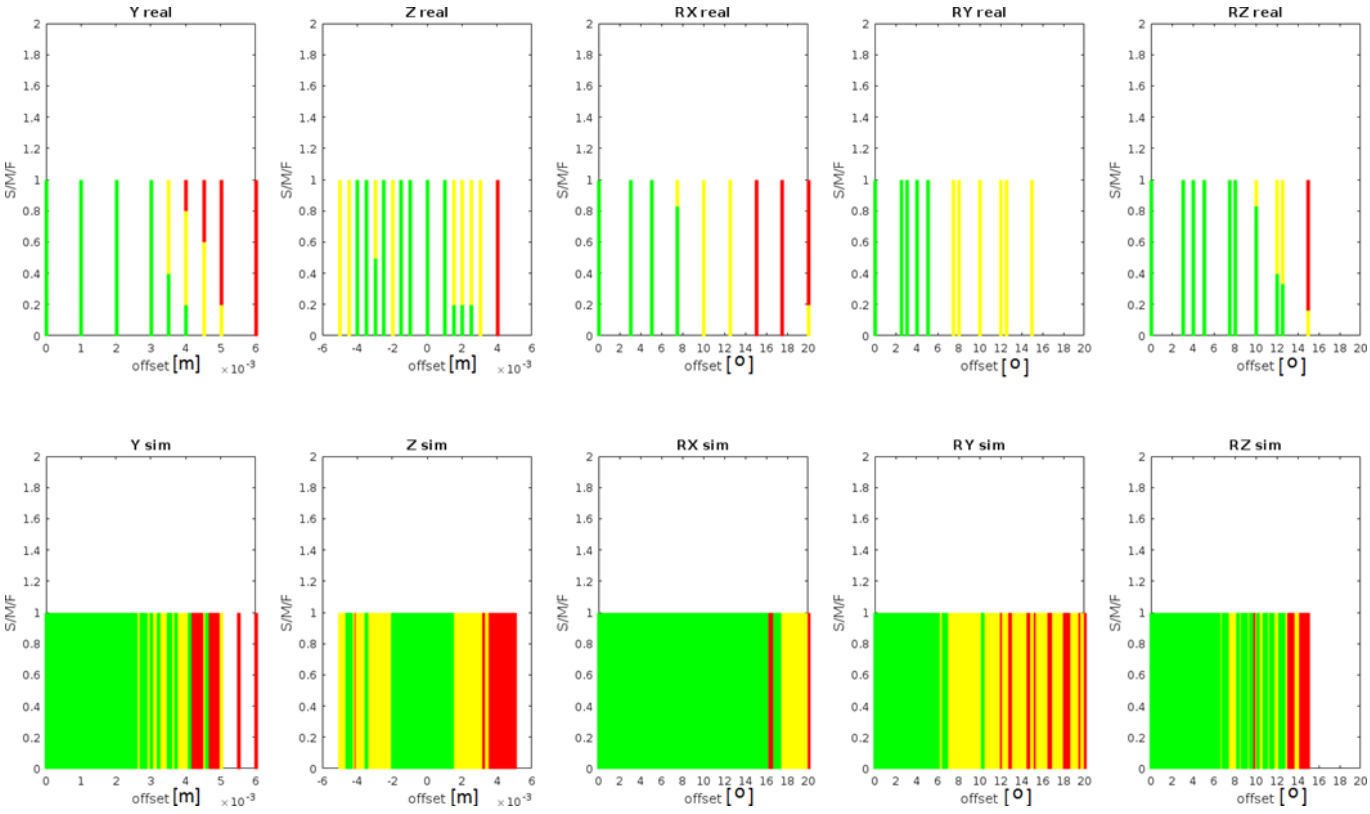

Fig. 6. The comparison of the real grasping outcomes (top) and the simulated results (bottom) – raw results. Green bars illustrate the percentage of successes, yellow – the percentage of misaligned grasps, and red – failures

Adam Wolniakowski, Andrej Gams, Lilita Kiforenko, Aljaž Kramberger, Dimitrios Chrysostomou, Ole Madsen, Konstantsin Miatliuk,
Henrik Gordon Petersen, Frederik Hagelskjær, Anders Glent Buch, Aleš Ude, Norbert Krüger
DOI 10.2478/ama-2018-0013

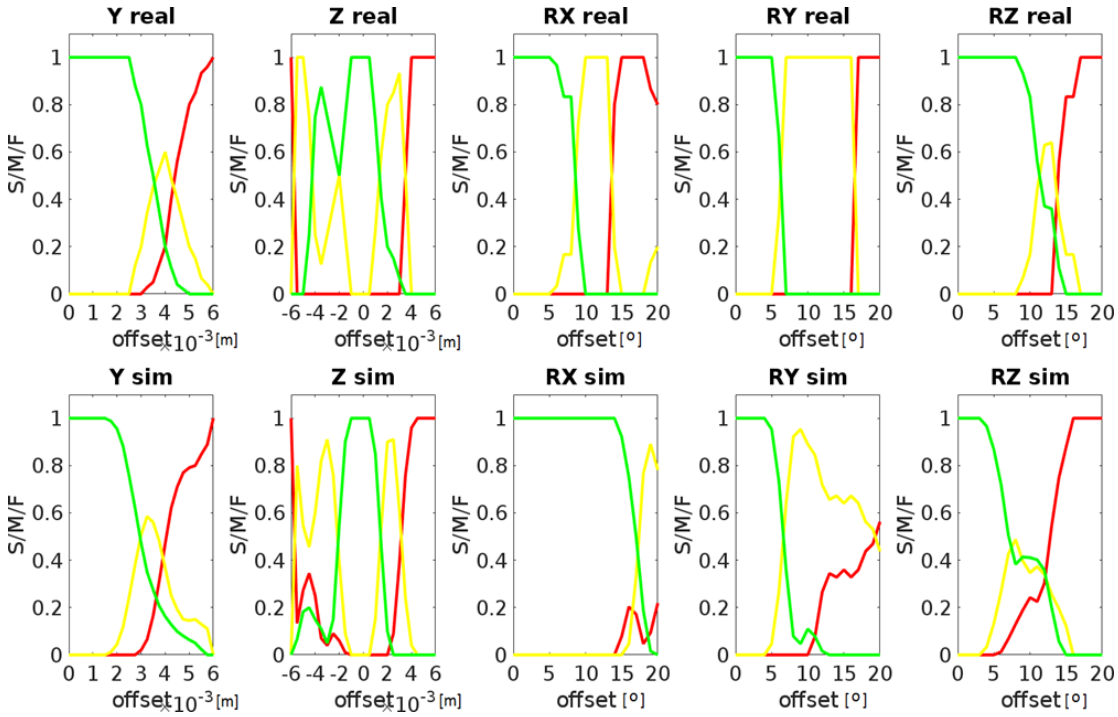

Fig. 7. The comparison of the real grasping outcomes (top) and the simulated results (bottom). Green lines illustrate the percentage of successes, yellow - the percentage of misaligned grasps, and red – failures

4.2. Results

In the course of the performed experiments, we tested the correspondence between the results obtained from simulation and from real-world testing. The ranges of the offsets tested along the selected axes and the comparison of the outcomes is presented in Fig. 6.

Because of the fundamental difference between the stochastic nature of the real version of the experiment and the deterministic nature of the simulation, and due to the disparity in the sample coverage of the offset space, it was necessary to process the raw data obtained from the testing.

Fig. 7. presents the data processed with a median filter in order to compare the probability of grasp success in both simulation and reality. The filtering was done with a window of size 1 mm for the linear offsets, and 2 degrees for the angular offsets.

The results show a decent match between the simulated and the real-world outcomes. In some of the cases (Rz) the simulation yields a more conservative limit on gripper success than real-world experimentation. This can be explained by insufficient modelling of friction and compliance in our physics engine. Additionally, some artifacts have been found in the simulation results, which are due to unknown software bugs.

5. CONCLUSION

In this paper, we have presented the usage of a novel, simulation-based gripper optimization method in a real industrial grasping scenario. We first introduced and described our evaluation procedure, upon which the optimization method is based. We then proposed a gripper cutout parametrization, which we then optimized for a magnet grasping context. We then performed a set of experiments in both a simulated and the real-world setting, in order to confirm the validity of our approach. Finally, we discussed the obtained results.

The obtained results show a good match between the simulation and reality. The residual errors, and a number of artifacts found in simulation give us an indication of the issues and improvements that we still have to implement. Future work will involve the extension of presented methods, the fixing of aforementioned issues, and the implementation of compliance modelling.

REFERENCES

1. **Boubekri N., Chakraborty P.** (2002), Robotic grasping: gripper designs, control methods and grasp configurations – a review of research, *Integrated Manufacturing Systems*, 13, 520–531.
2. **Carbone G.** (2013), *Grasping in robotics*, Springer-Verlag London.
3. **Causey G.** (2003), Guidelines for the design of robotic gripping systems, *Assembly Automation*, 23(1), 18–28.
4. **Causey G.C., Quinn R.D.** (1998), Gripper design guidelines for modular manufacturing, *IEEE International Conference on Robotics and Automation*, 2, 1453–1458.
5. **Ceccarelli M., Cuadrado J., Dopico D.** (2002), An optimum synthesis for gripping mechanisms by using natural coordinates, Proceedings of the Institution of Mechanical Engineers, Part C: *Journal of Mechanical Engineering Science*, 2016(6), 643–653.
6. **Cuadrado J., Naya M.A., Ceccarelli M., Carbone G.** (2002), An optimum design procedure for two-finger grippers: a case of study, *IFToMM Electronic Journal of Computational Kinematics*, 15403(1).
7. **Ellekilde L.-P., Petersen H.G.** (2006), Design and test of object aligning grippers for industrial applications, *IEEE/RSJ International Conference on Intelligent Robots and Systems*, 5165–5170.
8. **Krenich S.** (2004), Multicriteria design optimization of robot gripper mechanisms, *Solid Mechanics and Its Applications*, 117, 207–218, Springer Netherlands.

DOI 10.2478/ama-2018-0013

9. **Lanni C., Ceccarelli M.** (2009), An optimization problem algorithm for kinematic design of mechanisms for two-finger grippers, *Open Mechanical Engineering Journal*, 3, 49–62.
10. **Monkman G., Hesse S., Steinmann R., Schunk H.** (2007), *Robot grippers*, Wiley.
11. **Siciliano B., Khatib O.** (2008), *Springer handbook of robotics*, Springer Verlag Berlin Heidelberg.
12. **Tarnowski W.** (1997), Foundations of engineering design, *CAD, CAM*, Wydawnictwa Naukowo-Techniczne, Warszawa.
13. **Thulesen T.N., Petersen H.G,** (2016), RobWorkPhysicsEngine: A new Dynamic Simulation Engine for Manipulation Action, *IEEE International Conference on Robotics and Automation (ICRA)*, 2060-2067.
14. **Wolf A., Steinmann R., Schunk H.** (2005), *Grippers In Motion*, Springer Berlin Heidelberg.
15. **Wolniakowski A., Jorgensen J.A., Miatliuk K., Petersen H.G., Krüger N.** (2015), Task and Context Sensitive Optimization of Gripper Design Using Dynamic Grasp Simulation, *20th International Conference on Methods and Models in Automation and Robotics*, 29-34.
16. **Wolniakowski A., Miatliuk K., Gosiewski Z., Jørgensen J.A., Bodenhagen L., Petersen H.G, Krüger N.** (2017), Task and Context Sensitive Gripper Design Learning Using Dynamic Grasp Simulation, *Journal of Intelligent and Robotic Systems*, 87(1), 15-42.
17. **Wolniakowski A., Miatliuk K., Krüger N., Rytz J.A.** (2013), Automatic Evaluation of Task-Focused Parallel Jaw Gripper Design, *International Conference on Simulation*, Modelling and Programming for Autonomous Robots, *LNCS*, 8810, 450-461.
18. **Zhang M.T., Goldberg K.** (2006), Designing robot grippers: optimal edge contacts for part alignment, *Robotica*, 25, 341-349.
19. **Zhang T., Cheung L., Goldberg K.** (2001), Shape tolerance for robot gripper jaws, *IEEE/RSJ International Conference on Intelligent Robots Systems*, 1782–1787.

Acknowledgement: The research leading to this publication has been funded by the EU FoF Project ReconCell (project number 680431). This research has been funded in part by the GOSTOP programme C3330-16-529000, co-financed by Slovenia and EU under ERDF.